The Influence of Accurate Attenuation Correction on Quantitative Gamma Camera Imaging

by

Helen Louise Blundell

Cardiff University, School of Engineering

PhD Thesis

2012

DECLARATION

This work has not previously been accepted in substance fro any degree and is not concurrently submitted in candidature for any degree.

Signed…….. (candidate) Date ……

STATEMENT 1

This thesis is being submitted in partial fulfillment of the requirements for the degree of PhD.

Signed …… (candidate) Date ……

STATEMENT 2

This thesis is the result of my own independent work/investigation, except when otherwise stated. Other sources are acknowledged by explicit references.

Signed …….. (candidate) Date …….

STATEMENT 3

I hereby give consent for my thesis, if accepted, to be available for photocopying and for inter-library loan, and for the title and summary to be made available to outside organizations.

Signed…….. (candidate) Date……..

Abstract

Gamma camera systems are used in a variety of diagnostic applications to image and in some cases measure, the physiological uptake of a radioactive tracer within the body. A number of factors, particularly attenuation and scatter of photons within the body tissues can cause degradation of image quality and inaccuracies in the measurement of tracer uptake. Single photon emission tomography (SPECT) systems which incorporate an x-ray computed tomography (CT) facility have enabled accurate transmission images of the patient to be obtained. These 'attenuation maps' can be used to correct the SPECT images for the effects of attenuation.

The aim of this project was to investigate the use of an x-ray CT based attenuation correction (AC) system in SPECT gamma camera imaging. The use of AC with other physical parameters of the imaging process including scatter was firstly examined in order to determine the optimum imaging parameters required to maximise image quality. The influence of attenuation, scatter and other imaging parameters on the accuracy of absolute and relative quantitative measurements was then investigated.

The methodology involved using the GE Millenium Hawkeye gamma camera system to obtain images of a range of phantoms filled with various concentrations of radioactivity; from simple point sources to phantoms which simulate organs of the body.
An attempt was made to establish SPECT sensitivity values that would allow accurate determination of activity in a region of interest. These sensitivity values were applied to all subsequent measurements and a measure made of quantitative accuracy.

The results showed that the sensitivity value used for quantitative SPECT measurements must reflect the reconstruction method and corrections used in the acquisition. Attenuation correction proved to be more significant than scatter correction in quantitative accuracy, with activity results being within 30% of expected values in all cases where AC was used.

Acknowledgments

I am grateful to all in the Department of Medical Physics and Clinical Engineering for allowing me to do this project, especially Professor Wil Evans for much needed support and guidance. Thanks also to Professor Peter Wells for helpful comments on my thesis.

With love and thanks to all my family and friends.

Contents

Abbreviations

The following is a list of abbreviations used in this thesis:

AC	Attenuation Correction
ASNC	American Society of Nuclear Medicine
BEM	Bulls Eye Map
BNMS	British Nuclear Medicine Society
CDR	Collimator Detector Response
CFOV	Central Field of View
COR	Centre of Rotation
Cor	Coronal
cps	Counts per second
CT	Computed Tomography
CZT	Cadmium-Zinc-Telluride
DEW	Dual Energy Window
DMSA	Dimercaptosuccinic Acid
ECG	Electro cardiogram
EDTMP	Emthylene diamine tetramethylene phosphonate
FBP	Filtered Back Projection
FOV	Field of View
FWHM	Full Width Half Maximum
Gd-153	Gadolinium-153
GFR	Glomerular Filtration Rate
HLA	Horizontal Long Axis

IPEM	Institute of Physics and Engineering in Medicine
IRAC	Iterative Reconstruction with Attenuation Correction
IRACSC	Iterative Reconstruction with Attenuation and Scatter Correction
IRNC	Iterative Reconstruction No Corrections
IRSC	Iterative Reconstruction with Scatter Correction
LSF	Line Spread Function
LT	Left
MCA	Multi Channel Analyser
MDP	Methylene Diphosphonate
MIBI	methoxyisobutylisonitrile
MLEM	Maximum Likelihood Expectation Maximisation
Mo-99	Molybdenum-99
MPI	Myocardial Perfusion Imaging
NaI(Tl)	Sodium Iodide Thallium Doped
NEMA	National Electrical Manufacturers Association
NPL	National Physical Laboratory
OSEM	Ordered Subsets Expectation Maximisation
PET	Positron Emission Tomography
PHA	Pulse Height Analyser
PMT	Photomultiplier Tube
PSF	Point Spread Function
PVC	Partial Volume Correction
PVE	Partial Volume Effect

QC	Quality Control
ROI	Region of Interest
RR	Resolution Recovery
RT	Right
SA	Short Axis
Sag	Sagittal
SD	Standard Deviation
SDS	Summed Difference Score
Sm-153	Samarium-153
SNM	Society of Nuclear Medicine
SPECT	Single Photon Emission Computed Tomography
SRS	Summed Rest Score
SSS	Summed Stress Score
Tc-99m	Technetium-99m
TEW	Triple Energy Window
Trans	Transaxial
TRT	Targeted Radionuclide Therapy
UFOV	Useful Field of View
VLA	Vertical Long Axis

Chapter 1

Introduction

1.1 Background

Diagnostic nuclear medicine involves visualisation of both anatomy and physiological processes via the administration of a small amount of a radioactively labelled tracer to a patient. The labelled tracer is commonly known as a radiopharmaceutical and is, as the name implies, a pharmaceutical agent labelled with a radionuclide. The pharmaceutical chosen governs the body organ or system to be imaged through physiological uptake mechanisms e.g. methylene diphosphonate is absorbed onto the surface of bone via osteoblastic and vascular mechanisms. The radionuclide used for the majority of diagnostic studies is technetium Tc-99m, the properties of which will be discussed in section 2.2. Gamma photons emitted by the decay of the Tc-99m within the patient are detected using a gamma camera, the detailed operation of which is described in Section 2.4.

The distribution of the radiopharmaceutical, and hence the image that will be produced, depends entirely on its physiological uptake within the body and so will be different in a normal healthy state compared to a diseased state. For example, a cancerous tumour which has an increased rate of cell turnover may take up more of a radiopharmaceutical, than the surrounding healthy tissue. The difference in the number of detected gamma photons from abnormal and normal regions is what provides

contrast in nuclear medicine images. For this reason it is evident that nuclear medicine images provide physiological information as well as anatomical information, whereas imaging modalities such as x-ray computed tomography provide primarily anatomical information. As will be described later, modern developments in imaging technology have led towards multi modality imaging, where anatomical and physiological information is gained from different modalities in the same imaging procedure.

1.2 Quantitation in nuclear medicine

Due to its physiological nature, the ability to derive functional parameters from nuclear medicine images is a useful adjunct to visual interpretation. For example, in renography a sequence of images following the administration of the tracer may be analysed to give a number of indices of kidney function such as the rate of renal blood flow, the relative renal clearance rate and individual renal excretion. Furthermore, quantitation of images enables their interpretation to be more objectively based and therefore adds confidence and reproducibility to clinical reporting.

In general, quantitative measurements may be classified into two groups, relative and absolute. In relative quantitation, the derived physiological parameters are based on the comparison of count rates in different parts of the image. For example, this approach may be used to derive the relative function of the left and right kidneys in renography. Absolute measurements of radiopharmaceutical uptake involve converting count

rate to activity, thereby enabling quantification of uptake as a fraction of the total amount administered to the patient. The conversion of countrate in an image region to an accurate measure of absolute uptake could be described as the ‘holy grail’ of nuclear medicine. This has particular application in targeted radiotherapy dosimetry (Fleming and Perkins, 2000). Unfortunately, there are a number of factors which make accurate quantitation difficult as will be discussed.

The basis of gamma camera imaging is the planar (projection) image, which is a two dimensional representation of the three dimensional distribution of radioactivity within the body. A major disadvantage of planar imaging is that there is no inherent depth information. This is a problem since radiation from an organ of interest will be attenuated (absorbed and scattered) by overlying tissues. Thus regions with similar radiopharmaceutical concentration closer to the surface of the body give a greater signal than those deeper within the body. Furthermore, activity in tissues underlying and overlying the organ of interest will contribute to the overall signal. In other words, each pixel of a planar image can be considered as a projection of the counts due to activity in a rod of tissue through the patient.

A simplistic approach to this problem is to acquire planar images in orthogonal views to give qualitative depth information. Where quantitation is required, an approximate correction for depth can be made by acquiring images in opposed views and taking the geometric mean of

background corrected counts in the relevant image region of interest. Careful thought needs to be given to the best method of background subtraction – for example, in dynamic planar renography correction needs to be made for both intra-vascular and extra-vascular activity. Background regions can be drawn manually or automatically (e.g. using edge detection techniques) and must be positioned so as to avoid other image regions for which the counts are not representative of the background for the organ of interest.

Three dimensional imaging was made possible by the development of single photon emission computed tomography (SPECT), a concept applied to medical imaging by Shepp and Logan in 1974 (Shepp and Logan 1974). Essentially SPECT imaging involves the tomographic reconstruction of a set of two dimensional slice images from a series of projection images acquired at a sufficient number of positions around the object being imaged. The projection images are generally acquired along an arc spanning at least 180°. This reconstruction may be carried out using filtered back projection or iterative reconstruction techniques as described in section 2.5. The three dimensional images of activity distribution obtained in SPECT give the potential for more accurate quantification than planar imaging, because each voxel in the image provides an estimate of the activity at a specific spatial location. Accuracy of quantification, however, remains limited by physical factors including photon attenuation, photon scatter, the partial volume effect (finite spatial resolution) and depth dependant collimator response. These factors and

methods for correcting for them within the SPECT reconstruction process will be discussed individually in sections 3.2 to 3.7.

1.3 Aim

In recent years, manufacturers of SPECT imaging systems have provided correction techniques for attenuation, scatter and, more recently, depth dependent spatial resolution. Whilst these systems have been shown to provide superior image quality and have thus been widely accepted into clinical practice, their influence on quantitation is less clear. For quantitative clinical applications as described, it is obviously necessary to obtain accurate quantitative results and so the efficacy and necessity of such corrections must be validated. The hypothesis to be tested by this project is ***"accurate attenuation correction is essential for quantitative gamma camera imaging".***

In order to test this hypothesis, the quantitative effects of attenuation and scatter on SPECT images acquired with the GE Hawkeye gamma camera system (GE Medical Systems) will be investigated by using a series of phantom measurements. All SPECT images will be reconstructed and analysed, in terms of derived quantitative parameters, both with and without manufacturer supplied corrections for attenuation and scatter. The parameters used will include image uniformity, image contrast, count rate sensitivity (in terms of cps/MBq) and a measure of absolute uptake. Measurements will be carried out on both single and double regions of activity within the image, so that absolute and relative quantitation can be investigated. Where applicable, planar images with no

corrections applied will be analysed to assess the overall impact of SPECT imaging with and without corrections on quantification, when compared to the more simple planar case. Finally, conclusions will be drawn on the relative impact of attenuation correction, scatter correction and a combination of both, on quantitative SPECT imaging. Recommendations for its clinical application, particularly in relative quantitative measurements (e.g. relative renal uptake) will be considered.

Chapter 2

Planar and SPECT Gamma Camera Imaging

2.1 Introduction

Images of radiopharmaceutical distribution within the body are acquired using a gamma camera. Before understanding how this is achieved however, it is necessary to understand the fundamental processes by which gamma photons emitted from a radionuclide interact with matter both within the patient and the camera. The radionuclide used exclusively in this study is technetium 99m (Tc-99m), so this chapter begins with a description of its properties. The chapter then moves on to describe the processes by which gamma photons are absorbed and scattered in a material, with particular regard to photoelectric absorption and Compton scattering. Absorption and scattering together result in the attenuation of photons and it is this combined attenuation that is of relevance in later parts of this study.

The operation of the gamma camera is then described and the way in which it may be used to produce two dimensional planar images and three dimensional SPECT images. The process of filtered back projection (FBP) for SPECT reconstruction will be described and the basis of iterative techniques introduced.

2.2 Technetium-99m (Tc-99m)

A radiopharmaceutical used in clinical nuclear medicine comprises a pharmaceutical labelled with a radionuclide tracer. The radionuclide chosen to be this tracer should have several desirable properties;

- it should be a pure gamma emitter, since alpha and beta particles are absorbed within a very short path length within tissue and would therefore be totally absorbed in the patient.
- the gamma photons should have sufficient energy to pass through the patient and be detected by an external detector.
- the half life of the radionuclide should be sufficiently long to allow physiological uptake and imaging to occur but short enough that the patient does not receive an unacceptably high radiation dose.
- the radionuclide must be able to be chemically linked to a range of pharmaceuticals without altering their chemical properties.

The radionuclide that best fulfils these criteria is technetium-99m (Tc-99m). This metastable isotope was isolated for the first time in 1938 by Segrẻ and Seaborg (Segrẻ and Seaborg 1938), but not used as a medical tracer until the 1960s (Sorensen et al. 1963, Herbert et al. 1965). Tc-99m is a pure gamma emitter of 140 keV photon energy and has a half life of 6.01 hours for its decay to Tc-99 via the process of isomeric transition, as shown in Fig. 2.1.

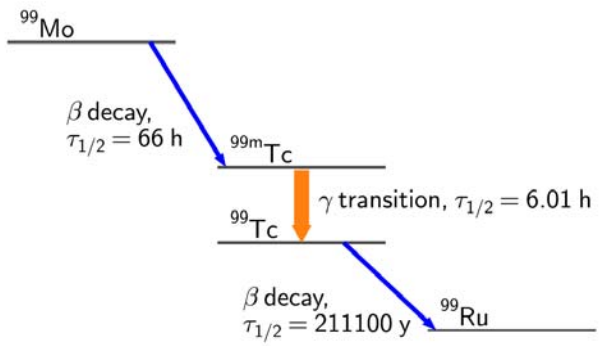

Fig. 2.1 Tc-99m decay scheme, showing the decay of Tc-99m to Tc-99 via isomeric transition with a half life of 6.01 hours.

Tc-99m also has the advantage of being produced in a table top generator from its parent Mo-99 and so it is relatively cheap and readily available. In its chemically reduced form, it can combine with a wide range of compounds without altering their properties. As a result, Tc-99m is used for the vast majority of diagnostic nuclear medicine imaging studies and will be the radionuclide utilised in this project.

2.3 Interaction of photons with matter

In order to understand the physical processes that occur in gamma camera imaging, it is necessary to understand the underlying processes by which photons interact with an absorbing material, both within the patient and the gamma camera itself. There are four interactions that can occur; elastic scattering, the photoelectric effect, Compton scattering, and pair production, the probability of each being governed by the energy of the incident photons

and properties of the absorbing material. It is important to remember that the term scattering simply refers to the change in direction of the initial photon, whereas absorption refers to the transfer of energy from the photon to the absorbing material. A combination of scatter and absorption results in attenuation, that is a reduction in intensity of the incoming photons as shown in Eqn. 2.1.

$$I = I_0 e^{-\mu x} \quad \text{Eqn. 2.1 (Dendy and Heaton 2012)}$$

where I_0 and I are the incident and transmitted photon intensities and x the thickness of absorbing material. The parameter μ is the linear attenuation coefficient, which is a measure of the fraction of gamma rays that are lost in each centimetre of material.

In theoretical 'narrow beam' conditions, it is assumed that the source and detector are small and so any scattered photons are undetected. For 140 keV gamma photons in body tissue, this results in a theoretical attenuation coefficient of 0.15 cm^{-1}. However, in nuclear medicine imaging the source is usually extended, referred to as 'broad beam' conditions, which means that some scattered photons are detected. This results in a lower measured value of the attenuation coefficient, dependent on the scatter conditions. Typical values for 140 keV photons in tissue are in the range 0.11 to 0.13 cm^{-1}.

At low energies, photons may be scattered without any absorption. This process is called elastic or coherent scattering and is caused by photons passing close to an atom causing resonance of bound electrons. The probability of elastic scattering increases with increasing atomic number of the scattering material ($\propto Z^2$) and decreases as the energy of the photon increases ($\propto 1/ h\upsilon$ where h is Planck's constant and υ is the frequency of the photon). Although a certain amount of elastic scattering occurs at all photon energies, it never accounts for more than 10% of the total interaction processes in nuclear medicine. Also, the very low energy scattered radiation is heavily absorbed in the patient, so the contribution to image formation is very low (less than 1%)(Dendy and Heaton 2012). For this reason elastic scattering will not be considered further here.

Pair production occurs for photons with energies >1.02 MeV and results in the conversion of a photon to an electron and a positron. The positron then interacts with an electron in an annihilation reaction to produce two 511 keV photons which move apart at 180° to each other. Due to its energy requirement, pair production it is relevant to positron emission tomography (PET) imaging, but not standard gamma camera imaging and will not be considered further here.

The two interactions that are most relevant to nuclear medicine imaging are the photoelectric effect and Compton scattering.

2.3.1 The Photoelectric effect

In photoelectric interactions, the energy of the incident photon is completely absorbed by an atom and one of the atomic electrons, known as the photoelectron is released.(Fig. 2.2)

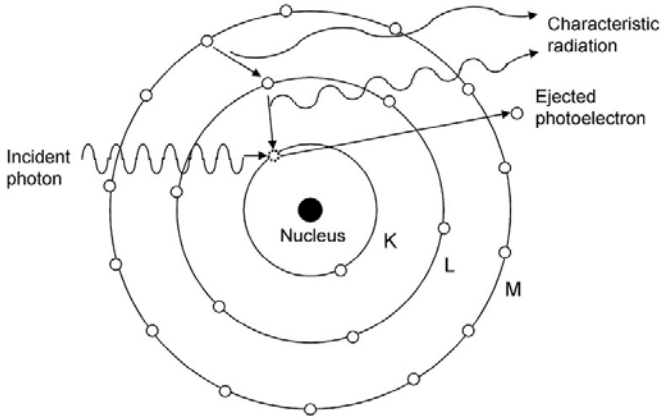

Fig. 2.2 The photoelectric effect

The kinetic energy of the electron is equal to the photon energy less the binding energy of the electron.

$$\frac{mv^2}{2} = h\upsilon - \phi$$

Eqn. 2.2 (Dendy and Heaton 2012)

where $mv^2/2$ is the kinetic energy of the photoelectron, $h\upsilon$ is the energy of the incident photon and φ is the binding energy.

The resultant gap in the electron shell is filled by an electron moving typically from the higher energy L shell. In moving from a higher to a lower energy shell the excess energy is radiated as a characteristic x-ray.

The probability of a photon undergoing a photoelectric interaction is proportional to the density of the absorbing material and highly dependent on its atomic number, being proportional to Z^3. This interaction is also more likely to occur at low energies (< 0.2 MeV), as it is proportional to $1/E^3$.

2.3.2 Compton scattering

Compton scattering is an inelastic scattering process by which a photon scatters from a loosely bound atomic electron, resulting in a less energetic photon and a scattered electron as shown in Fig. 2.3.

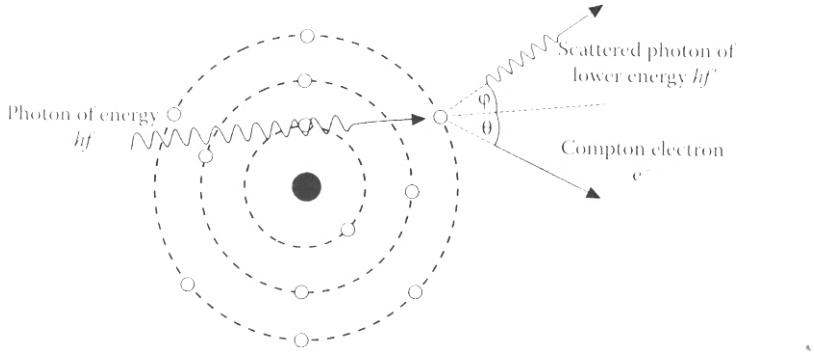

Fig. 2.3 Schematic representation of the Compton effect (Diagram physics for Diagnostic Radiology 3rd Ed Dendy and Heaton.)

As in the photoelectric effect, a characteristic x-ray is emitted, as the vacancy in the electron shell is filled by an electron from a higher energy shell. The kinetic energy of the Compton electron is dissipated by ionisation and excitation and eventually as heat within the medium, whereas the

scattered photon emerges from the medium with a lower energy than the initial photon, or goes on to be fully absorbed by the photoelectric effect.

The distribution of energy between the scattered and original photon is given by equation 2.3.

$$E'\gamma = \frac{E\gamma}{1 + (E\gamma / mc^2)(1 - \cos\varphi)}$$ Eqn. 2.3 (Dendy and Heaton 2012)

where $E\gamma$ is the energy of the original photon, $E'\gamma$ that of the scattered photon, m is electron mass, c the speed of light and φ the angle by which the direction of the original photon is altered.

As can be seen from the equation, the loss of energy of the scattered photon depends on the incident energy and the angle of scatter. For a 140 keV photon, the loss of energy corresponding to 30° scattering is only about 5 keV, which makes scattered photons hard to distinguish from primary photons with the limited energy resolution of the gamma camera. Scattered photons carrying incorrect positional information are therefore detected, causing a loss of resolution and contrast in the projection images. In addition, it is possible for a photon to undergo several Compton interactions before being fully absorbed via the photoelectric effect, so photons with a range of energies from close to zero to the photopeak energy can be detected as shown in Fig. 2.4.

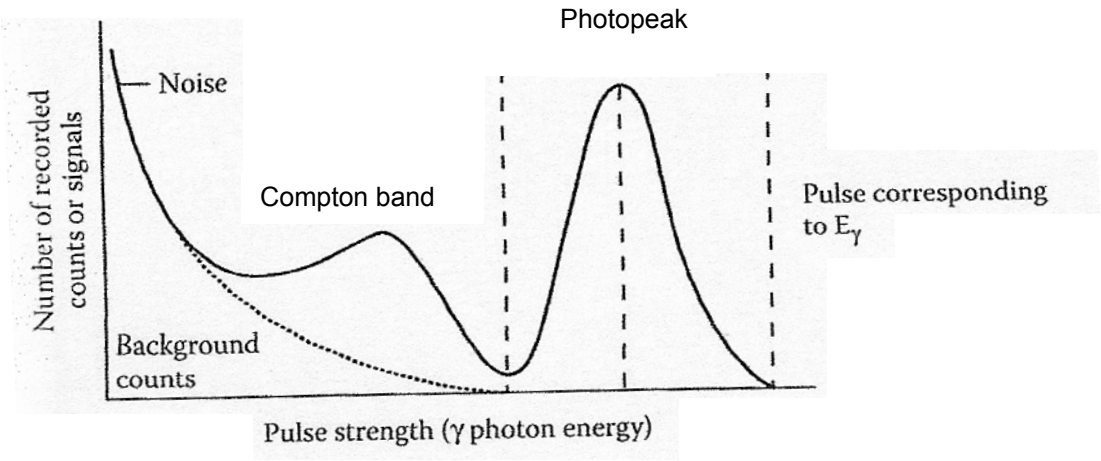

Fig 2.4 Energy spectra showing Compton band and photopeak. Since pulse strength is proportional to photon energy, noise in the detection process results in a large peak recorded at very low photon energies. (For Tc-99m this peak occurs at energies less than 40 keV and is often omitted from idealised spectra). (Diagram Physics for Diagnostic Radiology 3rd Ed. Dendy and Heaton).

For free electrons, the probability of a Compton interaction decreases with photon energy ($\propto 1/E$), However in practice sufficient energy is required for electrons to break away from other atoms, so the probability of this interaction occurring remains essentially constant in the 10 -100 keV range and then decreases with energy above this. The variation in the probability of a Compton event occurring (expressed as the Compton cross-section area) is shown in Fig. 2.5

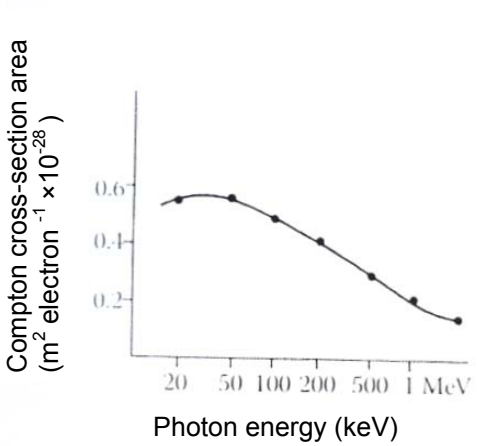

Fig 2.5 Variation of Compton cross section with photon energy (Diagram Physics for Diagnostic radiology 3rd Ed. Dendy and Heaton).

Compton scattering is the predominant interaction within the patient for 140 keV photons used for imaging in nuclear medicine.

With regard to absorbing material, the Compton effect is almost independent of the atomic number. This is because the probability of the Compton effect occurring, defined as the Compton coefficient σ, is proportional to the number of electrons in the material. Therefore, if the Compton mass attenuation coefficient is defined as σ/ρ, where ρ is density, this will be proportional to electron density. For any material, the number of electrons is proportional to the atomic number Z and the density is proportional to atomic mass A. Hence $\sigma/\rho \propto Z/A$. Z/A is almost constant for a wide range of elements.

2.4 Gamma camera image formation

The basic principles of using scintillation detectors to count and image radioisotopes were investigated in the 1960's. Since that time instrumentation has developed through small collimated imaging devices and rectilinear scanners to the Anger type gamma camera (Anger 1958; Anger 1964) the components of which are outlined in Fig. 2.6.

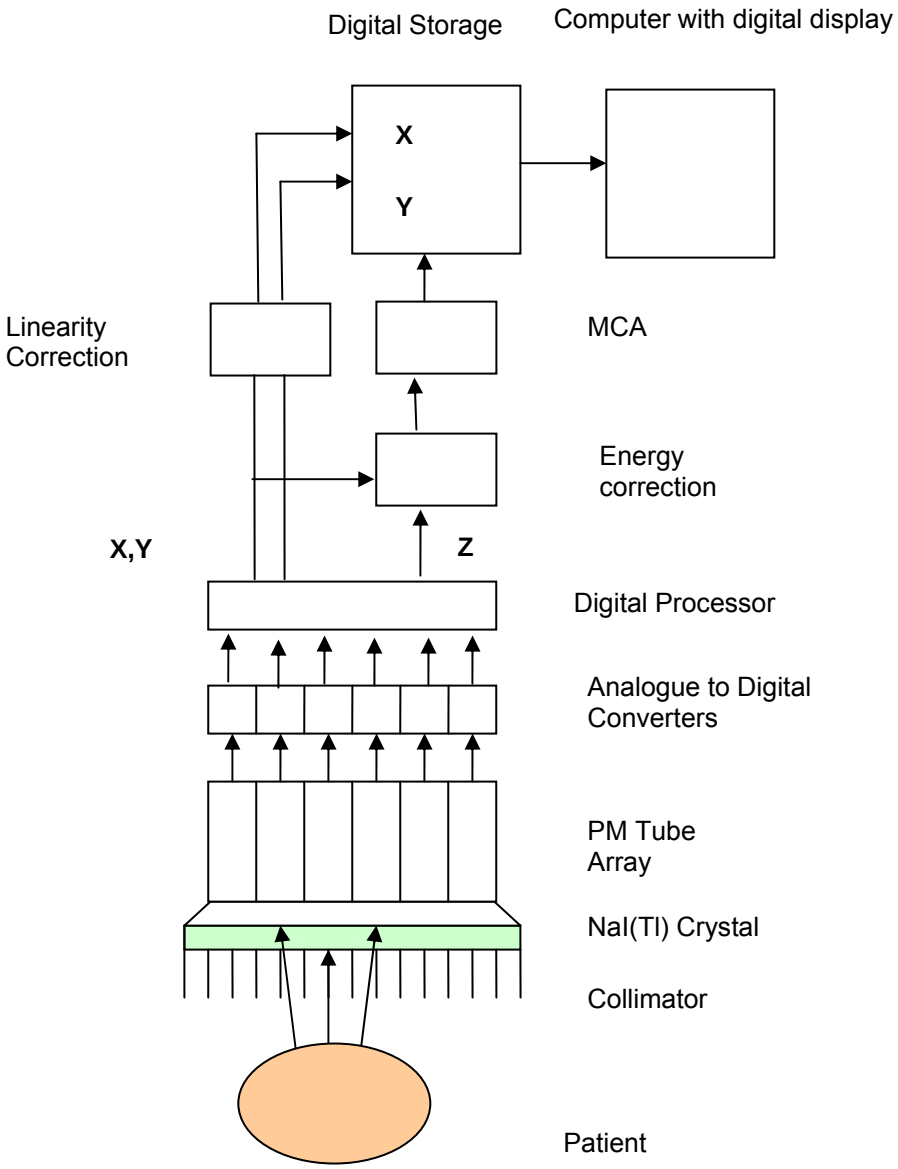

Fig 2.6 Components of an Anger gamma camera

2.4.1 The collimator

Gamma rays emitted from the patient are formed into an image of the distribution of the radiopharmaceutical by use of a collimator. The parallel hole collimator as used in this project, is a 'honeycomb' array of several thousand holes separated by lead septa. These septa absorb all gamma rays except those passing straight through the holes (subject to <1 % septal penetration for low energy collimators). The energy of gamma photon emission for which the collimator can be used is determined by the septal thickness. The properties of the collimator in terms of spatial resolution and sensitivity are determined by the diameter of the holes and the length of the septa. For a parallel hole collimator, the resolution is governed by the expression:

$$Rc = d(1 + b/h) \qquad \text{Eqn 2.4}$$

where d is the hole diameter, h is the hole length and b is the distance from the radiation source to the face of the detector.

It can be seen from this expression that for the best resolution, collimator holes should be long and of small diameter and the object to be imaged should be as close as possible to the gamma camera face.

For this project, a low energy, high resolution collimator was used; which has a septal thickness of 0.2mm a hole diameter of 1.5mm and a hole length of 35mm.

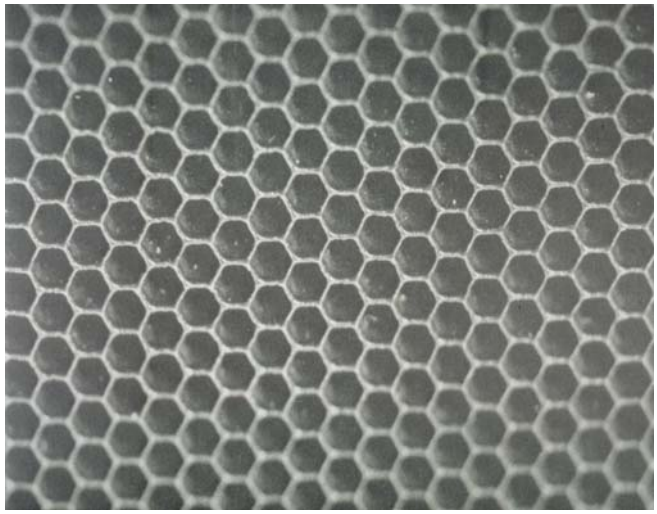

Fig 2.7 Magnified view of a parallel hole collimator. Hexagonal array.

2.4.2 The scintillation crystal

Some of the rays that pass through the collimator interact with a large area crystal of sodium iodide doped with thallium (NaI(Tl)) to produce photons of light at a wavelength of 410 nm via the process of scintillation. In a modern camera the crystal is typically 9.5 mm thick and has dimensions of 600 $\times$ 405 mm giving a field of view of about 550 $\times$ 400 mm. Desirable properties of the scintillation crystal are;

- high efficiency for absorbing gamma photons.
- attenuation of light should be minimal.
- high conversion of gamma photon energy into light.
- wavelength of light should match the response of the photomultiplier tubes.
- crystal should be mechanically robust.
- length of scintillation should be short.

The process of scintillation can be thought of in terms of energy levels within the crystal structure. Normally, electrons reside at the ground (lowest) energy state bound to the sodium and iodine atoms in the crystal. Photon interactions in the crystal transfer their energy to the bound electrons, causing them to jump and reside at the excited (highest) energy level. Light emission (scintillation) occurs when the excited electrons lose their energy and become bound once again. A pure crystal of NaI reabsorbs much of its own light emissions. To improve the efficiency of light emission, the NaI crystal is doped with Tl. This introduces activator (trapping) site for electrons of intermediate energy. When electrons that occupy the activator sites return to ground level, light emission also occurs. Although the energy gap between the bound and excited state is 6 eV, it takes an average of 20 eV to create one excited electron. Approximately 7000 electrons become excited in the case of total absorption of a photon of 140 keV. With a concentration of 0.1% Tl however, the process of light emission in NaI (Tl) is only about 10% efficient (Dendy and Heaton 2012). Thus for 7000 excited electrons, only 1050 light photons are emitted, most originating from the Tl activator sites.

To maximise the efficiency of the transfer of light photons from the scintillation crystal to the photomultiplier tubes a light guide is used, in the form of a slab of Perspex (Lucite). Silicone grease is used to maintain good optical contact between the light guide and both the exit window of the detector and the entrance window of the photomultiplier tubes.

2.4.3 The photomultiplier tubes (PMTs)

The light photons are converted into electrical signals by an array of photomultiplier tubes (PMTs), optically coupled via the light guide to the back of the crystal. For the crystal size discussed, ~60 PMTs are used to cover the area of the crystal. The photomultiplier tube is a vacuum tube that detects the very small amount of light produced in the scintillation. The light energy releases electrons from a photocathode deposited as a thin layer on the inside of the entrance window. Inside the tube are a series of electrodes called dynodes that are held at increasing positive potential to each other by a high voltage supply. The electrons are accelerated from the photocathode to the first dynode by the potential difference and gain kinetic energy, thus releasing further electrons.

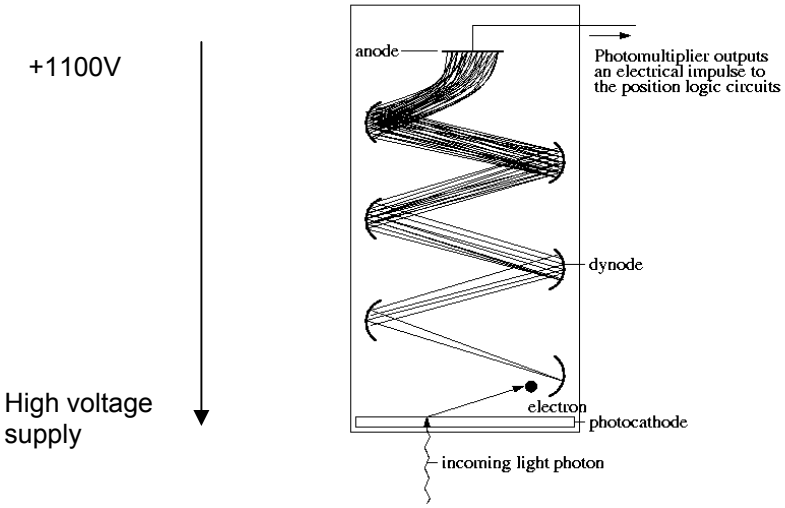

Fig 2.8 A photomultiplier tube. Its basic structure is an evacuated cylinder enclosed in glass, with a photocathode on one end, an anode at the other end and small curved dynodes in between. The electrical potential to the dynodes is what causes multiplication of the electrical signal created at the photocathode.

The electrical signal produced at the photocathode of each PMT tube, is magnified within the tube by a factor of 10^7 to give an electrical charge large enough for the subsequent electronics, although further amplification is still required.

The amplification (gain) of a PMT, and hence the amount of charge produced at the anode, is strongly influenced by the high voltage. In a gamma camera, the gain of each PMT must be matched to that of the other tubes in the array and this requires fine adjustment of the high voltage applied to each one.

2.4.4 Signal processing

In a modern gamma camera, the outputs from each PMT are digitised by use of an analogue to digital converter located after the preamplifier. For this reason scintillation crystal based gamma cameras cannot be described as truly digital, unlike solid state systems such as the GE Discovery NM 530c dedicated cardiac camera (GE Healthcare, Haifa, Israel) (Esteves et al. 2009). In solid state gamma cameras, semiconductors such as Cadmium-Zinc-Telluride (CZT) are used as the detector. Semiconductors directly produce electron current in response to gamma photons and so combine the functions of the scintillation crystal and photomultiplier tubes (Sharir et al. 2010).

In the scintillation crystal based gamma camera, once digitised the outputs from the PMTs are converted into three signals, two of which (X and Y) give the spatial location of the scintillation, while the third (Z) represents the energy deposited in the crystal by the gamma ray. Spatial information is obtained since the amount of light received by a particular PMT depends on the inverse square of the distance from the scintillation to that PMT. Once the electrical charge pulse has been converted to a voltage pulse by the pre-amplifier, the distribution of pulse heights carries information about the position of scintillation in the plane of the crystal. Information about the energy of the interaction is obtained because the sum of pulse heights is proportional to the total amount of light produced and hence the energy absorbed from the gamma photon by the crystal.

Suppose there are n PMTs and that any particular one is designated as i, with Xi,Yi being the position of the ith PMT. The X and Y co-ordinates of the scintillation are given by:

$$X = \frac{\sum V_i X_i}{\sum V_i}$$

Eqn 2.5 (a)

$$Y = \frac{\sum V_i Y_i}{\sum V_i}$$

Eqn 2.5 (b)

where Vi is the height of the voltage pulse from the ith PMT (in volts). Here Σ indicates a sum over all the PMTs i.e. from i=1 to i=n. The absorbed energy is proportional to:

$$Z = \Sigma V_i \qquad \text{Eqn 2.6}$$

The fact that Z appears in the denominators of the expressions for X and Y means that their values do not depend on the gamma photon energy. Thus a 140 keV photon and a 364 keV photon that are completely absorbed at the same position in the crystal generate different values of Vi and hence Z, but identical values of X and Y.

2.4.5 Energy discrimination

The value of Z measured, even for an isotope with a monoenergetic gamma photon emission such as Tc-99m, will not have a single value due to the nature of the photon interactions that occur within the crystal. As has already been discussed, the photon may interact via the photoelectric effect or Compton scattering. If it interacts via the photoelectric effect all of its energy is absorbed (through the photoelectron) whereas if the photon suffers one or more Compton interactions within the crystal (with the singly or multiply scattered photon escaping from the crystal) only part of its energy will be absorbed through the scattered electrons. A third possibility is that the photon undergoes one or more Compton interactions followed by a photoelectric interaction, in which case its full energy will again be absorbed. Therefore, even if all the gamma photons leaving the patient have the same energy, interactions within the crystal will produce different amounts of scintillation light and hence different Z values. Successive gamma

interactions produce a range of Z values from the very small to a maximum representing the total absorption of the gamma photon energy. As already shown in Fig 2.4 the photon energy spectrum is therefore comprised of a Compton ‘band’ and a narrow photopeak. Theoretically the photopeak should be very narrow, but because of various factors such as light production, transmission and detection this has a measurable width usually expressed as full width at half maximum (FWHM). As will be seen in chapter 4, calculation of FWHM as a percentage of the energy of the photopeak is a measure of the energy resolution of the gamma camera which is tested routinely as part of a quality control programme.

For nuclear medicine imaging, the scattered photons are unwanted, since they degrade image quality. Therefore, in order to reject photons from the Compton band, the Z signal is passed through a multi-channel analyser (MCA), which tests whether the energy of the gamma ray is within the range of values expected for the photopeak of the particular radionuclide being imaged. Typically values within a 20% window ($\pm$10%) of the energy at the centre of the photopeak in the pulse height spectrum are accepted. More than one window may be used to accommodate isotopes with more than one gamma ray emission. If the signal has an acceptable value, then the system records that a gamma ray interaction has occurred at the position given by the X and Y signals.

2.4.6 Linearity, energy and sensitivity corrections

Finally, before the image is produced, electronic corrections are made for linearity, energy and sensitivity. Spatial non-linearity is caused by systematic mispositioning of counts i.e. errors in the calculation of X and Y values. In particular, the locations of individual counts tend to be shifted towards the centre of the nearest PMT. Thus a straight line source of radioactivity tends to give a wavy line image and there is an increased count density at the locations of the PMTs when a uniform source is used. Errors in measurement of energy may be caused by the Z value varying with position due to factors such as variation in light production, light transmission, light detection and residual PMT gain. This can result in the fraction of counts rejected by energy discrimination varying from one area of the crystal to another. Positional variation in sensitivity (count rate per unit activity) may be due to manufacturing defects in the crystal and/or collimator.

2.4.7 Image display

Once these final corrections have been made, an image is built up of usually several hundred thousand detected interactions or counts. The signals are most commonly acquired in matrix mode, where the camera's field of view is divided into a regular matrix of picture elements or pixels. This matrix is usually square with the number of locations along each edge being a power of 2 e.g. 256 x 256 (2^8 x 2^8); the maximum is usually 1024 x 1024 (2^{10} x 2^{10}).

Each pixel is assigned a unique memory location in the computer. The value stored in this location is the number of gamma photon interactions that have been detected in the corresponding location on the camera face. The array of numbers is then converted into a viewable image by a lookup table which links the number of counts to a specific value of displayed image intensity. Lookup tables may use monochrome or colour scales to display this intensity.

2.5 Single photon emission computed tomography (SPECT) imaging

The basis of nuclear medicine imaging is the planar image, which is the projection of a three dimensional radionuclide emission distribution onto a two dimensional detector plane at one angle of view. This has the dual disadvantages that no information is available regarding the depth in the patient at which gamma photons are emitted and that activities originating from more than one structure can overlap with each other, resulting in a low contrast image. As elegantly described by Bruyant (2002), “With only 1 projection image it is impossible to determine the activity distribution because an infinite number of distributions can yield the same projection. It is as difficult as to find 2 values knowing only their sum.” This situation is improved by acquiring projection images at a number of angles of view around the subject. In principle, if a sufficient set of projection images are acquired, it becomes possible to reconstruct the corresponding activity distribution. The principle of tomographic acquisition is shown in Fig 2.9 for the gamma camera in one angle of view. From the dashed line it can be seen that photons emitted at different depths, but along the same direction can produce scintillations at the same point in the crystal, so several angles of view are required to build an image.

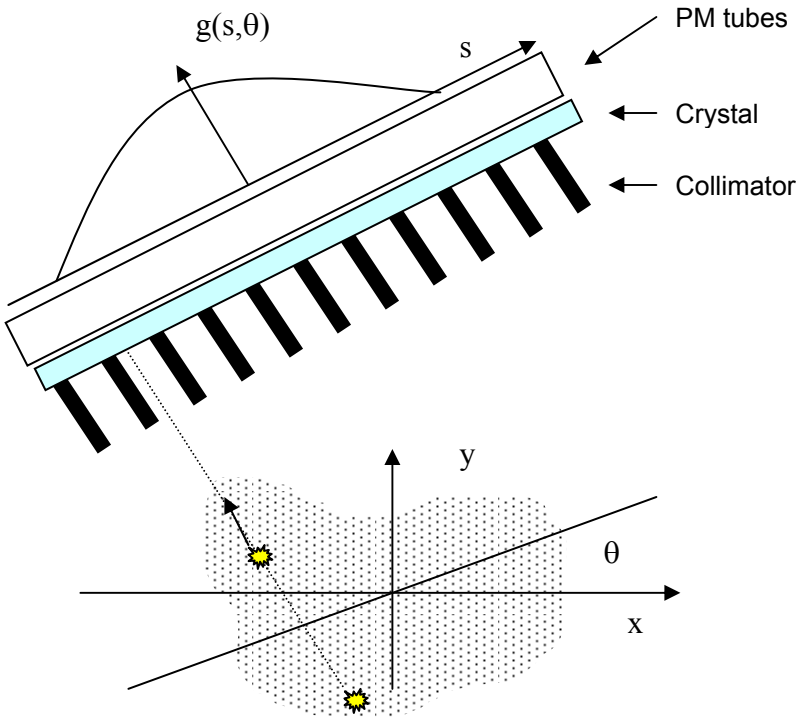

Fig 2.9 Principle of tomographic acquisition and geometric considerations. For each angle of acquisition (θ), g (s,θ) is the sum of radioactive counts recorded in any time interval at point s on the detector. The location of any scintillation onto the crystal allows one to find out the direction of the incident photon (dashed line) but not to know the distance between the detector and the emission site of the photon.

In this representation g(s,θ) is the number of gamma photons detected at any location s along the detector, when the detector head is at an angular position θ. f(x,y) is the estimated number of photons emitted at any point (x,y) of the transverse slice in the field of view. The function g is the projection of f onto the crystal as allowed by the collimator. A common representation for the projection data g corresponding to a slice is the

sinogram Fig 2.10 This is a two dimensional image where the horizontal axis represents the location of the detected gamma photon on the detector and the vertical axis corresponds to the angular position of the detector.

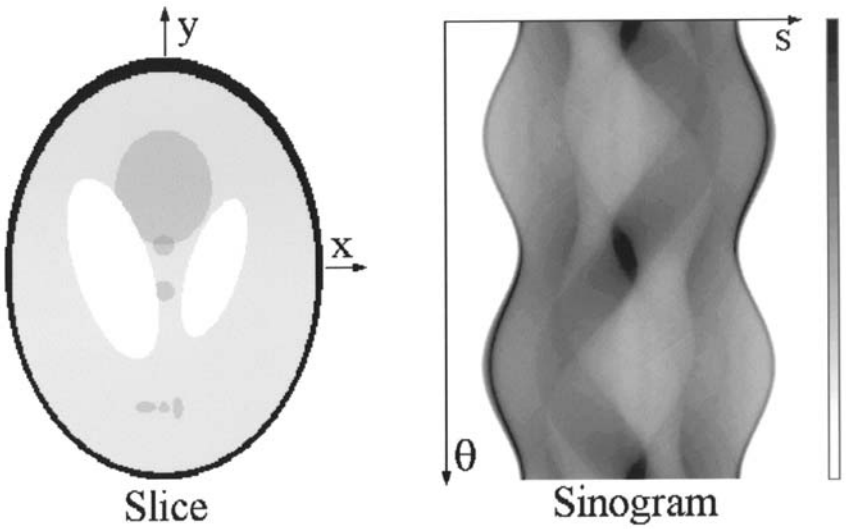

Fig 2.10 (Left) Shepp-Logan phantom slice (256× 256 pixels). (Right) Corresponding sinogram with 256 pixels per row and 256 angles equally spaced between 0° and 359° (Image Bruyant 2002).

Therefore the problem to be solved by any reconstruction algorithm is “Given a sinogram g, what is the distribution of radioactivity f in the slice of interest?”

2.5.1 Back projection and filtered back projection

Until recently, filtered back-projection was the most common method of SPECT reconstruction implemented on commercial nuclear medicine computer systems (Greaves, 2011). Before considering back projection, we must consider the projection operation (or forward projection operation). This gives the number of counts detected in any point of the line $g(s,\theta)$ as a

function of the number of counts f(x,y) emitted in any point of the field of view. Mathematically this can be described by the Radon transform first described in 1917 (Radon 1917).

$$g(s, \theta) = \int f(s \cos\theta - u \sin\theta , s \sin\theta + u \cos\theta)du \qquad \text{Eqn 2.7}$$

Essentially this means that $g(s,\theta)$ is the sum of values f(x,y) along a line perpendicular to the profile (parallel to the holes of the collimator). For this reason $g(s,\theta)$ is known as the ray-sum. The variable u defines the location of the points to be summed along the perpendicular line.

Fig 2.11 shows a distribution of two point sources and their profiles for three positions of the camera. Each element in each profile represents the sum of values at that point of measurement (s) on the detector. (These points of measurement are sometimes referred to as bins – the total number of bins equals the number of points of measurement along the detector multiplied by the number of angles).

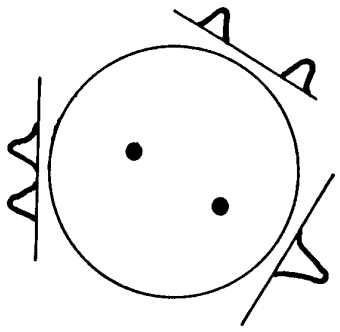

Fig 2.11 Projection profiles for two sources of radiation at three gamma camera positions.

In order to reconstruct the object distribution from a known profile, the back projection operation is then used. This is known as the summation algorithm and is defined mathematically as:

$$b(x,y) = \int g(s,\theta)d\theta \qquad \text{Eqn 2.8}$$

Essentially b(x,y) represents the summation of the ray-sums of all the rays that pass through a given point on the x,y plane.

In ideal conditions (i.e. without attenuation) the projections acquired at angles between π radians (180°) and 2π radians (360°) do not provide new information because they are symmetrical to the projections acquired at angles between 0 and π and so back projection can be carried out over 180°. Back projection of profiles leads to a rough image being built up, but with a lot of background and 'star' artefacts as shown in Fig. 2.12.

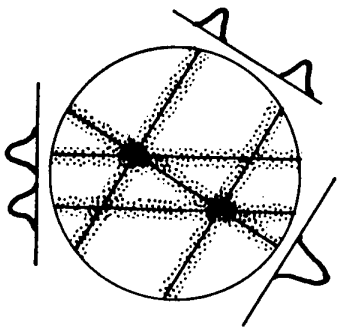

Fig. 2.12 The process of back projection of line profiles leading to star artefacts

These artefacts can be reduced by filtering each line of the sinogram and back projecting these filtered projections. In order to understand filtering, we

need to consider that an image can be described in terms of a combination of spatial frequency (cm^{-1}) components that can be found using the Fourier transform. The effect of filtering is to alter the proportion of high and low spatial frequency components of an image e.g. to reduce the amount of high frequency ‘noise’ or low frequency ‘blur’. The filters themselves are also usually described in terms of spatial frequency. If described in terms of the profiles, the effect of filtering is to generate negative numbers adjacent to the positive numbers, so when back projected these cancel out some of the artefacts as shown in Fig. 2.13

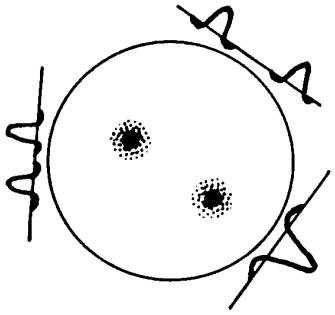

Fig. 2.13 Filtered profiles showing a reduction in star artefacts

The process of projection/back projection filters the image by a factor of 1/f where f is the spatial frequency. This causes unwanted smoothing of the image which is overcome by using a ramp filter which amplifies each frequency proportionally, as shown in Fig 2.14 up to the Nyquist frequency (0.5 cycles per pixel).

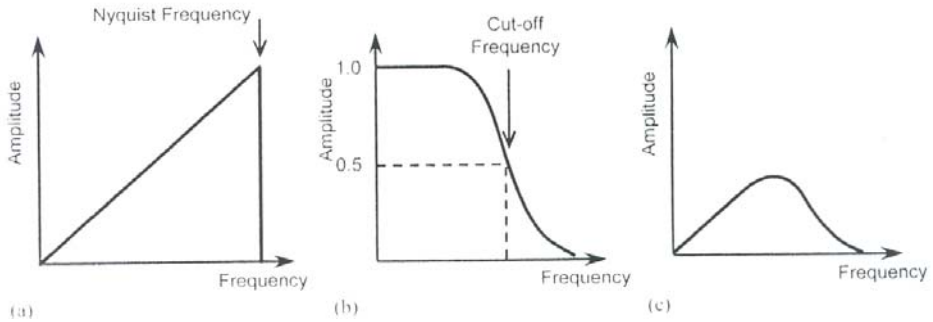

Fig 2.14 Frequency response of a practical SPECT filter; a) the ramp filter; b) a smoothing window; c) the practical filter which is the product of a) and b). (Greaves 2011).

Unfortunately this leads to amplification of high frequency noise and the sharp cut off leads to 'ringing artefacts'. This is solved by using a smoothing window to reduce the noise, but this also has the effect of reducing resolution. The product of the ramp filter and smoothing window is a practical SPECT filter that is a compromise between noise and resolution. A range of filters are available such as the Hanning filter (also known as the Hann or the Chesler filter (Chesler et.al. 1975)) and the commonly used Butterworth filters (Butterworth 1930). These allow parameters to be changed to alter the amount of smoothing such as the cut-off value, which is the frequency above which all spatial content is removed. Mathematically they are described by equation 2.9 (a) and (b)

$$\text{Hanning}(f) = 0.5 + 0.5\cos(\pi f/f_c) \text{ for } f \leq f_c$$

$$= 0 \qquad \text{for } f > f_c \qquad \text{Eqn 2.9 (a)}$$

$$\text{Butterworth}(f) = 1/\left[1 + (f/f_c)^{2N}\right]^{1/2} \qquad \text{Eqn 2.9 (b)}$$

where f_c is the cut-off frequency and N is a variable parameter called the order. By adjusting these parameters, the user may alter the range of frequencies allowed through the filter and therefore the amount of smoothing of the reconstructed images. The best filter to use in a given situation will depend on several parameters including the amount of fine detail required in the image, the number of counts in the image and operator preference, as discussed by Van Laere et al. (2001).

2.5.2 Iterative reconstruction techniques

Today the reconstruction algorithm of choice in SPECT is based on one of the statistical iterative methods (Bailey 2013). Iterative reconstruction works on the premise that during SPECT acquisition, what are actually measured are projection profiles. Therefore, if estimated profiles are generated by forward projecting an initial estimate of the image, these estimated profiles can be compared with the real profiles, to generate a profile error. By back projecting the profile errors, image errors can be generated to update the original image estimate. The process is then repeated until the best possible solution is reached.

There are several types of iterative reconstruction algorithm available. A standard statistical method, is the expectation maximization (EM) algorithm for computing maximum likelihood (ML) estimates of the radioactivity distribution(Shepp and Vardi 1982). The basis of this technique is the

Poisson model that allows one to predict the probability of a number of detected counts, given the mean number of disintegrations. This can be expressed as:

$$prob[c/r] = \frac{e^{-r} r^{c}}{c!} \qquad \text{Eqn. 2.10}$$

where c= count and r = expected measurement

Using this Poisson model, the probability of acquiring the projection count distribution that was measured, P, given an estimated distribution of activity in the emission object f, can be represented by the product of probabilities for individual projection pixels. This term is the 'likelihood' L(P | f) and can be expressed as:

$$L(P \mid f) = prob[P \mid f] = \prod_i \exp\left[-\sum_j a_{ij} f_j \right] \left(\sum_j a_{ij} f_j \right)^{Pi} \left(p_i ! \right)^{-1} \qquad \text{Eqn 2.11}$$

Mathematically we can say that maximising prob [P| f] provides the most likely distribution of emissions that represents the original activity distribution, given the measured projections.

The algorithm is implemented in several stages. Firstly an estimate is made of the activity distribution in the patient (either uniform pixels or FBP image). This is then forward projected to estimate what the detectors would measure given the initial object i.e. estimate the corresponding projection images. In order for this to occur accurately, a model of the emission and detection

process must be incorporated, the 'system matrix' (a_{ij}) into which alterations for attenuation, scatter and loss of resolution with depth can be included. The estimated projections are then compared with the measured projections and any discrepancies in projection space are back-projected to give discrepancies in image space. These are used to update the estimated image. The process is repeated until the estimated and acquired projections agree with one another or until a fixed number of iterations have been achieved.

The ML-EM algorithm can be summarised as shown in Fig. 2.15

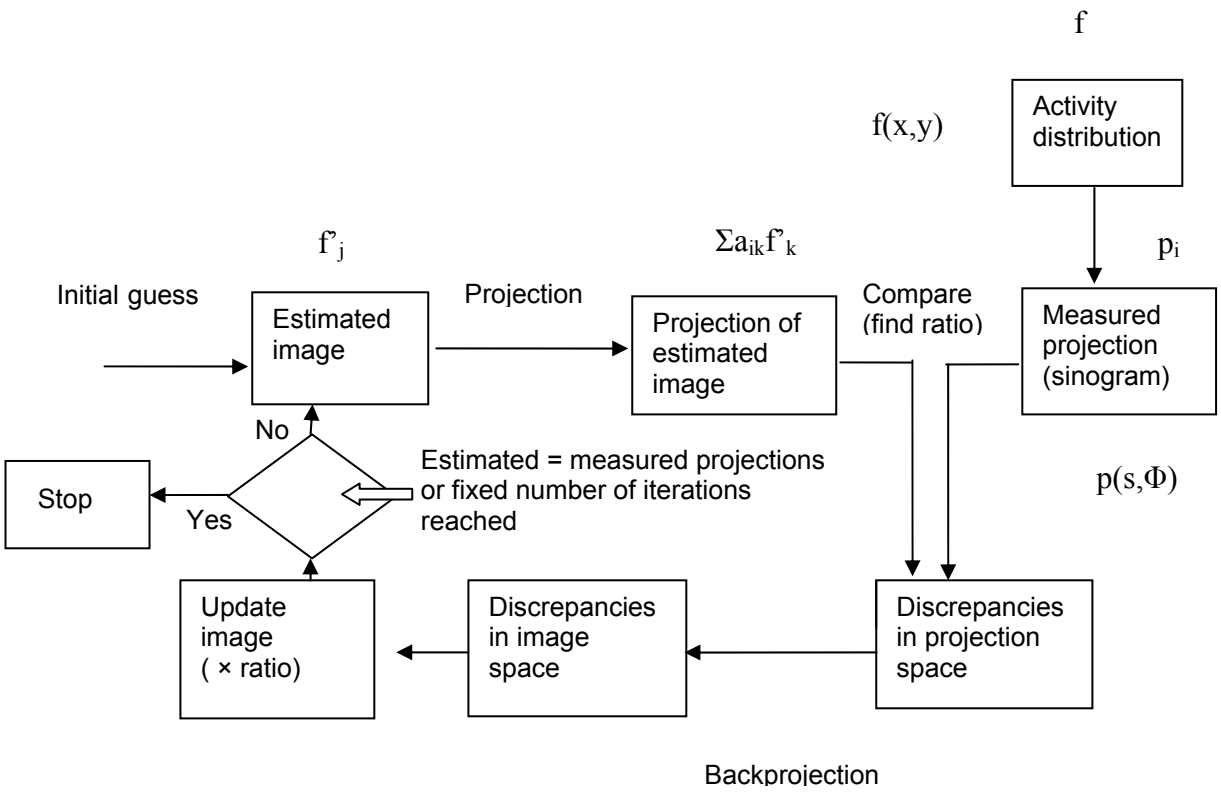

Fig. 2.15 Flow chart of a loop in the ML-EM iterative process

In simple terms :

$$New\_estimate = old\_estimate \times backprojection\_of \frac{measured\_projections}{forward\_projections\_of\_old\_estimate}$$

This can be expressed mathematically as:

$$f_j^{new} = \frac{f_j^{old}}{\sum_l a_{lj}} \sum_i a_{ij} \frac{p_i}{\sum_k a_{ik} f_k^{old}} \qquad \text{Eqn 2.12}$$

where aij is the system matrix.

The system matrix (a_{ij}) essentially defines the probability of detecting an emitted photon originating from location j at any particular position i on the detector, which will depend upon many factors including detector geometry, attenuation and resolution. By altering values within the system matrix, the effects of attenuation and finite resolution can be modelled, allowing images to be reconstructed with these effects corrected for. A full description of the system matrix and its utilisation in correcting for attenuation, scatter and finite resolution within an iterative reconstruction algorithm will be given in section 3.6.

In ML-EM each update involves BP and FP for all projections, which is a very slow process. An accelerated version of the EM algorithm is the ordered subsets EM (OSEM) algorithm. (Hudson and Larkin 1994) Here each update uses only a subset of projection angles, such that the total number of EM

iterations is the number of OS-EM iterations multiplied by the number of subsets e.g. 10 subsets ×2 iterations = 20 EM iterations. The choice of how many subsets and iterations to use is governed by speed and accuracy of convergence and noise considerations. Noise is proportional to signal in EM, so although theoretically the more iterations the more accurate the estimated image would be, in practice the image reaches an optimal visual quality at typically around 16EM iterations and appears noisy at higher numbers of iterations. Clinically it is therefore common to use only a small number of iterations, but this runs the risk of reducing reconstruction accuracy. A better solution may be to use a larger number of iterations with post reconstruction smoothing to reduce the noise.

2.6 Conclusions

This chapter has outlined the underlying physical processes involved in the creation of planar and SPECT gamma camera images. Particular relevance has been placed on the gamma photon interaction processes of photoelectric absorption and Compton scatter, which combine to cause attenuation of photons. The next chapter will build upon this theory to describe the processes which influence quantitative accuracy in SPECT imaging which include; attenuation, scatter, the partial volume effect and depth dependent collimator resolution.

Chapter 3

Corrections for Quantitative Gamma Camera Imaging

3.1 Introduction

Although simple quantitative measurements can be carried out on planar images, such as relative uptake measurements in static renal imaging, it is accepted that planar imaging is limited by its inherent lack of depth information and that for accurate quantitation three dimensional SPECT imaging is required. In this chapter, factors affecting the accuracy of SPECT quantitative gamma camera imaging, namely photon attenuation, scattered photons, the partial volume effect and depth dependent collimator response will be discussed, together with a review of methods of correcting for these effects from the earliest attempts to those used today.

In many cases the application of these correction methods is dependent on the SPECT reconstruction algorithm being used, so this will also be described in some detail. Finally, the clinical applications for which correction techniques are used, particularly in SPECT imaging where quantitation is required, will be discussed. Although to date much of this work has been applied to nuclear cardiology, there are many other applications (targeted radiotherapy dosimetry), where accurate quantitation has been found to be of great clinical benefit.

3.2 Attenuation correction

Some of the most basic calculated methods for SPECT attenuation correction assume uniform attenuation for a body contour defined either manually or by automatic edge detection methods.

A widely used early method was the Chang (Chang 1978) method. This is a post processing method in which the transverse section is first reconstructed by filtered back projection and then corrected pixel by pixel using a correction matrix. This correction matrix is obtained by calculating the attenuation of a point source at each point in the matrix and requires knowledge of the body outline and the attenuation coefficient. It also assumes narrow beam conditions. This is “first order Chang”. Being based on the point source response, this method is limited for larger sources which will be over-corrected or under-corrected depending on their position in the image. To compensate for this, a second stage can be included where the first order correction image is re-projected to form a new set of profiles. These are subtracted from the original profiles to form a set of error profiles. Filtered back projection of this error set produces an error image that must be attenuation corrected as in first order Chang. The corrected error image is then added to the first order image to obtain the final image.

Several methods of determining the body outline have been proposed including; using data acquired in the Compton scatter window (Ben Younes,

Mas et al. 1988; Wallis, Miller et al. 1995), directly from photopeak data only (Hosoba, Wani et al. 1986; Tomitani 1987; Herbert, Gopal et al. 1995) or by using both scatter and photopeak window emission images (Pan, King et al. 1997).

For clinical applications, none of the above methods are satisfactory due to the inhomogeneous nature of the human body and transmission images must be generated to accurately determine the attenuation map. Early work on simultaneous emission and transmission tomography was carried out using a radionuclide flood source of gadolinium-153 (Gd-153), attached to a rotating gamma camera (Bailey, Hutton et al. 1987). Scatter from the emission source into the transmission window (for Tc-99m emission) was removed by subtracting the predicted scatter distribution. Since that time a variety of radionuclide sources and geometries have been used. A major step was the development of the scanning Gd-153 line source (Tan, Bailey et al. 1993), a modification of which was the multiple line source array (Celler, Sitek et al. 1998), where 20 collimated Gd-153 line sources were used, with activity in the central lines higher than at the edges. In the same year, Beekman et al. used 2 Gd-153 point sources positioned to move along the focal lines of 2 half-fanbeam collimators on a dual headed gamma camera, with the heads at 90°. Using a gantry rotation of 180° they reported higher sensitivity, reduced noise, reduced downscatter and improved

resolution compared with multiple line source methods (Beekman, Kamphuis et al. 1998)

The most commonly implemented commercial configuration for external radionuclide transmission scanning proved to be the scanning Gd-153 line source, as implemented on the Philips Vantage system (Philips Medical).

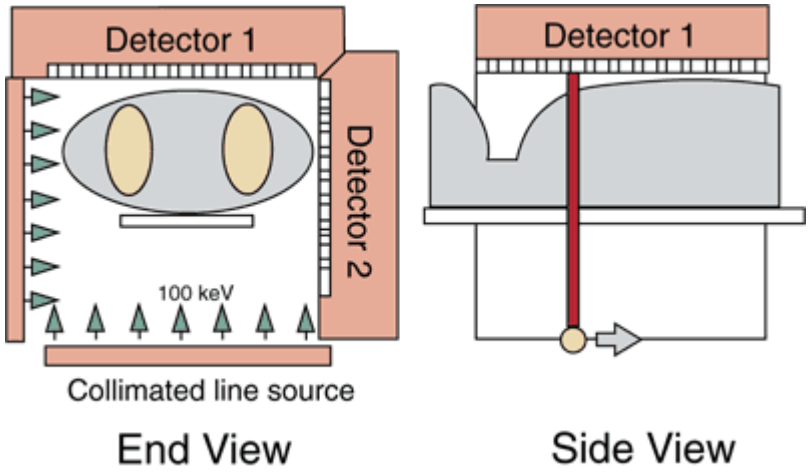

Fig. 3.1 Philips Vantage system (image Philips Medical) Two collimated line sources of Gd-153 move across the field of view of each detector during SPECT acquisition.

The next development in transmission imaging was the use of x-ray computerised tomography (CT) generated transmission images." CT images can generate a patient specific attenuation map since they contain pixel values that are related to the linear attenuation coefficient (μ) at that point in the patient, calculated for the mean energy of the x-ray photons used to generate the CT image. At first CT images were acquired by scanning the patient in a separate scanner and then moving them to the gamma camera for the emission imaging. The two sets of images were registered using

external markers and image registration software (Fleming 1998; Hutton, Braun et al. 2002) More recently dual-modality imaging systems have been developed incorporating CT and SPECT or PET capabilities. Early results from a combined SPECT/CT system were presented by Bocher et al. in 2000. Their system (GMAXT) was composed of an X-ray transmission system mounted onto the slip ring gantry of a GEMS Millennium VG gamma camera. The x-ray system comprised an x-ray tube and set of 384 cadmium tungstate detectors located on opposite sides of the gantry. This is the same configuration used by the Hawkeye scanner used in this project. The cross-sectional anatomical transmission map is acquired as the system rotates around the patient in a manner similar to a third generation CT scanner.

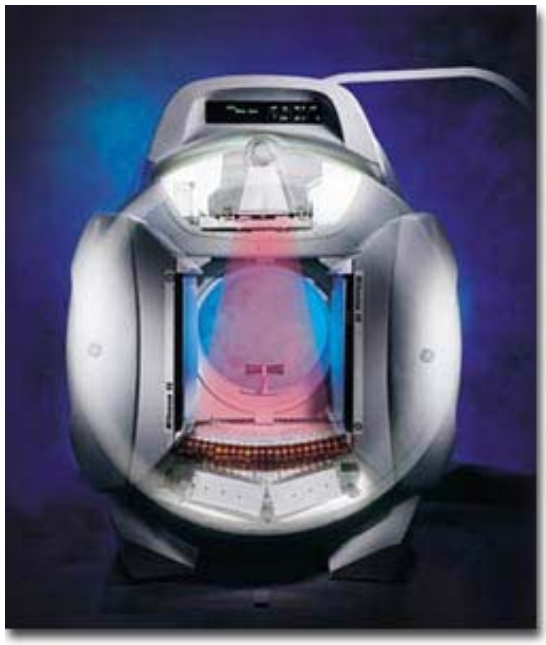

Fig. 3.2 GE Hawkeye Gamma camera SPECT/CT system (image GE Medical Systems)

Since the linear attenuation coefficient is calculated at the x-ray energy rather than the energy of the photon emitted by the radionuclide, a calibration curve is required to convert the linear attenuation coefficients obtained from the CT scan to those corresponding to the energy of the emission photons (Blackenspoor, Xu et al. 1996). This is done by taking CT scans of a phantom containing tissue equivalent calibration materials and plotting the measured CT number against the known attenuation coefficient at the photon energy of the radionuclide used in the emission study. This calibration means that CT scans can be used to correct emission images for a variety of different radiopharmaceuticals.

The other point to consider when using CT images is that CT has a higher spatial resolution and is reconstructed in a finer image matrix than SPECT, so the CT image must either be averaged to a coarser matrix, or the scanner must be designed with a lower spatial resolution specifically for attenuation and atomic mapping purposes.

Currently, x-ray CT attenuation systems have replaced radionuclide line sources as the method of choice for the reasons shown in Table 3.1

Advantages of x-ray CT compared with radionuclide sources	**Disadvantages of x-ray CT compared with radionuclide sources**
High count density transmission maps	Sequential imaging- chance of malregistration
No cross-talk compensation required	High initial cost
Replacement of source not required	Need for room shielding

Table 3.1 Relative advantages and disadvantages of x-ray CT compared with radionuclide sources for attenuation correction

O’Connor et al.(2002) compared the performance of several commercial systems for attenuation in cardiac SPECT and concluded that systems that generated high quality attenuation maps yielded the best results.

The most recent generation of SPECT/CT hybrid systems can incorporate four or sixteen slice spiral CT or cone beam CT attenuation systems. The Philips Brightview XCT system for example incorporates a cone beam CT tube opposite a flat panel detector. This allows 140 ×1 mm thick slices to be acquired simultaneously, so that high resolution attenuation maps can be acquired quickly and with very low patient dose.

Fig. 3.4 Philips Brightview XCT (image Philips Medical)

3.3 Scatter correction

The physical principles of Compton scattering are described in chapter 2. As explained, the loss of energy for a Tc-99m photon scattered through 30° is only 5keV, which makes scattered photons difficult to differentiate from unscattered events, given the finite energy resolution of the gamma camera. For this reason, in most clinical situations scattered photons account for 30-40% of the photons detected in the photopeak energy window of a SPECT system (Hutton et al. 2011).These photons, having originated at a spatial location within the object removed from the spatial location at which they are detected, have the effect of degrading image quality. Unfortunately, following the scatter history of each photon is implausible in practical terms due to the large number of parameters involved. These include; the emission energy of the radioisotope, the spatial distribution of the tracer, the composition and geometry of the object and features of the imaging system such as the thickness of the crystal, the density and geometry of the light guide and photomultiplier tubes and the distance between the collimator and the object. Several methods of correcting for scatter have been developed over the years. Although not all will be discussed here, those most commonly used can be grouped under the following sub-headings;

1) limitation of detection of scattered photons

2) compensation for effects of scatter

3) elimination of scattered events.

1) Limitation of detection of scattered photons

The most basic method of limiting the detection of scattered photons is the use of the standard 20% photopeak window, centred on the emission energy. This removes lower energy scattered photons, but due to the finite energy resolution of the camera, photons which have been Compton scattered once or even twice may still be detected. It is generally accepted that for a Tc-99m planar acquisition of a normal sized patient, 30% of the photons detected within the 20% window have been scattered at least once (Buvat 1994). This could be improved by narrowing the window, but with a corresponding drop in efficiency. A further improvement can be made by shifting the window towards higher energies, although the optimal shift is not standard, but is specific to the radioisotope and object being imaged. This method is also particularly sensitive to the electronic stability of the detector and the gain of the photomultiplier tubes.

Although the above methods have the advantage of simplicity, which makes them suitable for clinical practise, the proportion of removed scattered and unscattered photons is not estimated, so accurate quantitation is impossible.

2) Compensate for effects of scatter

If it is recognised that a percentage of detected events are due to scatter, different methods can be used to compensate for this. A crude method is multiplication of the image by a factor calculated from an estimate of the

mean scatter fraction, defined as the ratio of scattered to unscattered photons. This method may improve activity quantification, but does not solve the problem of the incorrect location of scattered events (Buvat 1994).

A more commonly used method is based on taking scatter into account during attenuation correction. Although theoretically, the number of photons detected passing through a medium decreases by an exponential factor due to attenuation, in reality, scatter increases the number of photons that can be detected from a specific point, due to the contribution of photons not emitted at that point. This is known as the build-up function which is extremely difficult to determine since it depends on the same numerous parameters as scatter. The simplest approach to take this into account is to use an effective attenuation coefficient μ_{eff} measured for broad beam geometry i.e. including the detection of scattered events, rather than the theoretical value of μ corresponding to a narrow beam geometry measurement. Typically, in water and for an energy equal to 140 keV, μ_{eff} =0.12 cm^{-1} and μ = 0.15 cm^{-1} Unfortunately this method may lead to significant errors(Jaszczak, Greer et al. 1984) and so is not suitable for quantitation. It is also incorrect to use a single attenuation coefficient, especially in parts of the body such as the thorax which incorporates a variety of tissues of differing densities. A more accurate approach would be to estimate the build-up function either experimentally(Wu and Siegel 1984; Siegel, Wu et al. 1985) or using Monte Carlo simulations (Dewaraja and Koral 2001).

Despite the above mentioned drawbacks of this method, the “use of effective attenuation correction coefficients in conjunction with Chang attenuation correction continues to be a commonly used approach in clinical practice to roughly correct for the apparent reduction in reconstructed activity from deep structures. It should also be noted that although this approach compensates for the effect of scatter, it cannot be considered a scatter correction technique as it does not remove photons that are at a wrong location.

3) **Elimination of scattered events:**

Another widely used methodology relies on estimation of the spatial distribution of the scattered photons in order to remove them from the acquired data. Several methods have been developed for doing this:

Early work by Logan (Shepp and Logan 1974) was based on the proposal that the shape of the scatter spectra is essentially constant in the spectral range of the photopeak. Therefore the photopeak can be divided into two adjacent subwindows such that the number of scattered events detected in the two subwindows are the same. Simple subtraction of the two windows for each pixel can therefore yield the unscattered photons. Unfortunately, some unscattered photons are also removed from the image, which results in a loss of efficiency and prevents precise quantitation. In Logan’s study, about 20% of unscattered photons were removed.

The method described by King et al. (1992) also divides the 20% photopeak window into two equal non-overlapping energy windows and then finds a regression relationship between the ratio of the number of counts within these subwindows R(i) and the scatter fraction within the photopeak window SF(i). Early results in phantoms using this method were encouraging, although it is very susceptible to uniformity artefacts, and due to the noisy low count density nature of SF(i), pre-low pass filtering is required.

A variation on this method is the channel ratio method (Pretorius, van Rensburg et al. 1993) where it is assumed that the "ratio of the number of unscattered photons detected in the two subwindows is constant as well as the ratio of the number of scattered photons ie:

$$U_{lw}(i)/\ U_{uw}(i) = k_1 \text{ and } S_{lw}(i)/S_{uw}(i) = k_2 \quad \text{Eqn. 3.1}$$

where U and S stand for unscattered and scattered respectively and lw and uw stand for lower window and upper window respectively. The disadvantage of this method is that " the experimental determination of k_1 and k_2 is not easy, since $U_{lw}(i)$, $S_{lw}(i)$, $U_{uw}(i)$ and $S_{uw}(i)$ are not directly measurable so further assumptions must be made. The method also fails for pixels containing only scattered photons and yields negative values in this instance.

A more familiar method is the dual energy window (DEW) method, where a fraction k of the events recorded in a secondary window is subtracted from the photopeak window. This method was first applied to planar images, before Jaszczak et al. (Jaszczak, Greer et al. 1984) developed the technique for scatter correction in SPECT. In their study a secondary energy window of 92- 125 keV was used for Tc-99m. The value of k was first determined by comparing the integral of counts in a line source imaged in air using planar imaging i.e. non-scatter geometry, and in a water filled cylinder using SPECT imaging i.e. scatter geometry. SPECT images of the line source in water and air and placed both on and off axis were evaluated. The value of k that gave the best agreement between the non-scatter and scatter geometry counting rates was found to be k~0.5. This resulted in scatter geometry count rates within 10% of non-scatter geometry count rates. The second method of determining k was to use Monte -Carlo simulations which resulted in a value of 0.56. Jaszczak found that this method resulted in qualitative and quantitative improvements for the limited source geometries investigated. However, the value of k has been shown to depend on many factors, including the object, the acquisition geometry, the SPECT reconstruction algorithm used and whether projection images or reconstructed slices are subtracted, so although easy to implement, the quantitative accuracy of this method must be called into question.

A development of this technique is the Triple Energy Window (TEW) method (Ogawa et al 1991). This uses a narrow energy window placed on either side of the photopeak. The scatter estimate is obtained on a pixel by pixel basis using:

$$SE = (C_l/w_l + C_u/w_u) \times w_p/2 \qquad \text{Eqn 3.2}$$

where C_l and C_u are the pixel counts measured in the lower and upper energy windows respectively and w_l, w_u and w_p are the window widths for the lower, upper and photopeak energy windows.

This method has the advantage that it can be applied to situations where there is down scatter from higher energy emissions as well as the identified photopeak. (For isotopes with only single energy emission, the technique effectively simplifies to a dual window technique.) Once the scatter estimate has been determined, it is subtracted from the photopeak projection image on a pixel by pixel basis.

This method has the advantage over the Jaszczak dual window method that the value of k does not have to be calculated, but the disadvantage that the low counts acquired in narrow energy windows lead to poor noise characteristics.

The above methods of removing scattered events rely on the use of the photopeak. Another category of methods use data acquired in a wide energy

window. The spectrum of the photons detected in each pixel is then analysed to deduce the contribution of scattered photon on either a pixel-by-pixel, or global basis. Due to their relative computational complexity, these are not used clinically in favour of the simpler to implement TEW method.

3.4 Correction for the partial volume effect

The partial volume effect (PVE) is a consequence of the finite spatial resolution of the gamma camera due to detector blurring and non-ideal collimation. (The contribution of collimation effects will be discussed independently in section 3.5) The partial volume effect tells us that in SPECT, if an imaged object is smaller (in any of its three dimensions) than approximately two FWHMs of the system's point spread function (PSF), the regional maximum counts per pixel in the resulting image will no longer represent a linear relationship with the radionuclide concentration at that location, but will vary with the size (or thickness) of the object. Objects small compared to the system resolution will appear to be less bright than larger objects, even if the tracer concentration is the same. In simple terms, objects smaller than the resolution volume will have all their counts detected but over a larger volume- the counts will be 'spread out' thus the recorded concentration of activity will be lower than the actual concentration. (Fig. 3.5) The ratio of these concentrations is the recovery coefficient.

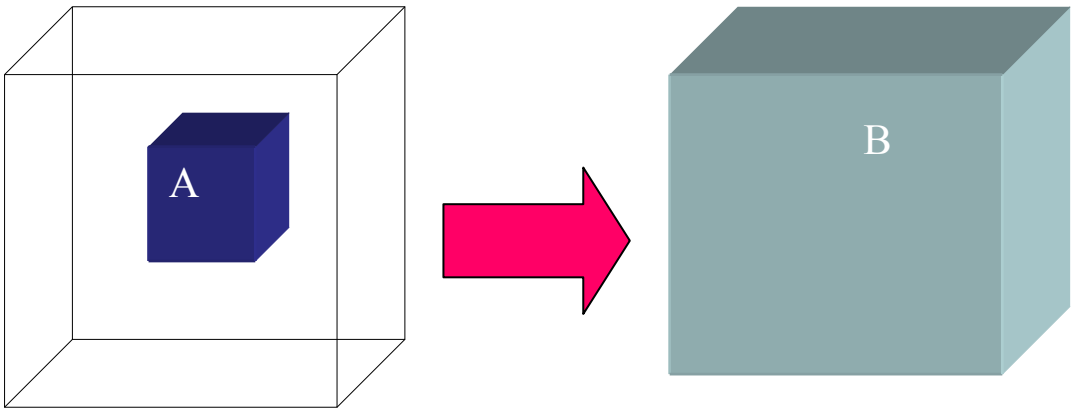

Fig. 3.5 The partial volume effect. All of the counts in object volume A, where A is smaller than the voxel volume of the imaging system are detected in image voxel volume B. The count density measured in the voxel B, is therefore lower than that in the object volume A.

The situation is further complicated by counts ‘spilling in’ from areas of neighbouring activity. The goal of partial volume correction (PVC) is therefore to be able to account for both the loss of signal due to the limited size of the object with respect to resolution and the signal contamination coming from the rest of the images.

The need to correct for the partial volume effect was first noted in PET studies. Early work by Hoffman (Hoffman, Huang et al. 1979) into PVC was based on the computation of resolution recovery coefficients from the known geometry of the objects being imaged and their position relative to the centre of a given PET slice. Since then it has been shown that the PVE is an important issue in clinical SPECT applications, for example in the

determination of myocardial wall thickness (Hutton 1998), in quantitative brain studies where activity concentrations in small structures may be underestimated (Soret et al. 2003) and in dosimetry for radionuclide therapy where uptake by small tumours may be important for accurate dose assessment (Dewaraja et al. 2001).

Early correction methods were based on physical phantom measurements. These empirical methods modelled the object (radioactivity distribution) by a series of simple geometric shapes (cylinders, spheres) to derive correction factors for actual anatomical structure that could be approximated by a simple shape or a linear combination of simple geometrical shapes. Jaszczak investigated using these techniques in SPECT(Jaszczak, Coleman et al. 1981). This approach has been applied to myocardial perfusion imaging and has been shown to be feasible for PET data down to ~ 1.5 FWHM.

A more widely accepted method of correction today is to use a reconstruction based technique. As will be discussed in section 3.6 the algorithm for ML-EM or OSEM iterative reconstruction, can model the imaging system by varying parameters in the system matrix. In this way account can be taken of attenuation, scatter and also the variation of the system's point spread function (PSF) to account for limited resolution. As will be seen full 3D iterative reconstruction is required for effective correction.

3.5 Correction for depth dependent collimator response

Another factor that limits resolution that is sometimes included in discussions of the partial volume effect is finite resolution due to collimator response. Gamma camera imaging relies on the use of collimators to limit the range of directions from which photons can reach the scintillation crystal and hence improve spatial resolution. However, due to the need for acceptable sensitivity, the angular range of photons accepted by each collimator hole obviously cannot be reduced to zero. This finite range of directions results in a finite resolution of the imaging system and hence causes blurring of the projection data and the final image. This spatial blurring is distance dependent as can be seen in Fig. 3.6. As the source moves further from the collimator, the fan-beam of photons that can pass through the collimator widens, resulting in an increase of the full width half maximum (FWHM) of the line spread function. As with the partial volume effect described in section 3.4, the result of finite resolution is that the image of a small source is a larger but dimmer source.

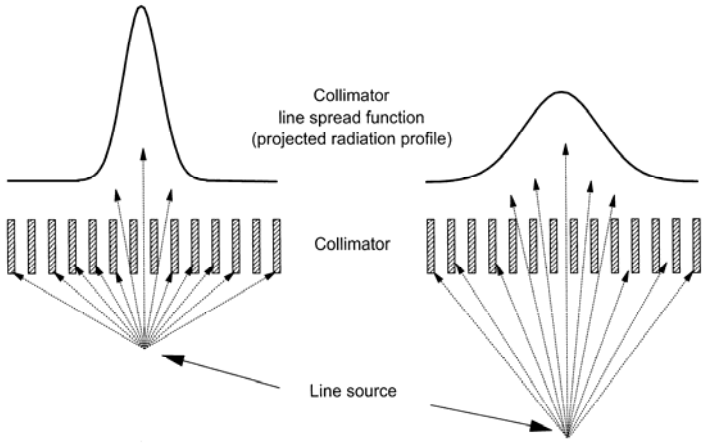

Fig 3.6 Effect on line spread function of distance from the collimator.

Fig 3.6 shows this effect in 1D, although the effect is actually in 3D. This is illustrated beautifully by Soret et.al (2007) in their paper on the partial volume effect on PET tumour imaging. (Fig. 3.7)

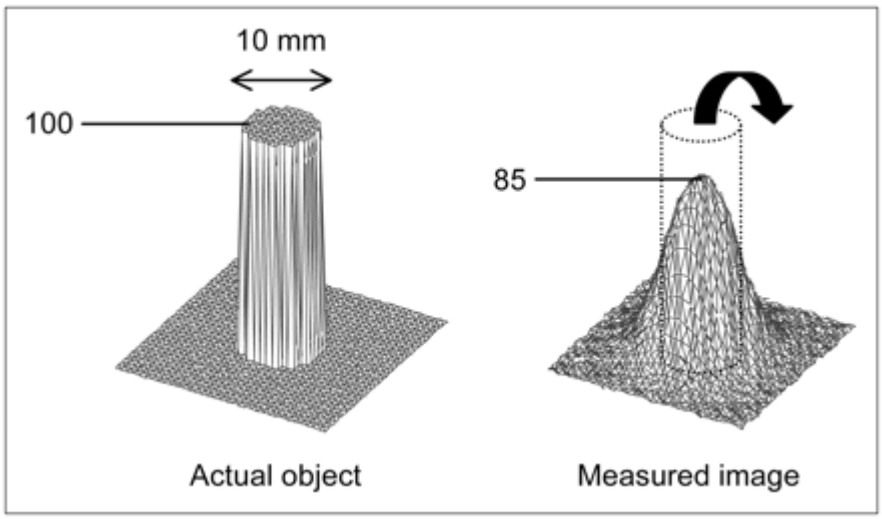

Fig. 3.7 Circular source (diameter of 10 mm) of uniform activity (100 arbitrary units) in nonradioactive background yields measured image in which part of signal emanating from source is seen outside actual source. Maximum activity is reduced to 85. (Soret et al. 2007)

Standard filtered back projection reconstruction methods take no account of this ‘spreading’ of the line spread function or projected radiation profile; it is an implicit assumption that the projection rays are perfectly narrow. Another feature of the FBP algorithm is that it gives equal weight to all pixels along the projection ray irrespective of distance, whereas in fact gamma rays originating close to the camera contribute more information than those that originate from far away. Therefore, an early, approximate way of dealing with the deterioration of resolution with distance was to use a distance weighted

back projection (Nowak et. al 1986). In this method instead of placing back projected counts equally in all pixels along the projection ray, more emphasis is placed on pixels close to the camera.

The next method of correcting for finite resolution in FBP that found more widespread use, was to use a resolution recovery filter such as the Metz or Weiner filter, during the FBP process. Since poor resolution results in a loss of fine detail in the image, resolution recovery requires an amplification of medium and high frequencies. However, in order to avoid amplification of noise, practical resolution recovery filters must be limited to amplifying medium frequencies and be rolled off at high frequencies. Both the Metz and Weiner filters have a frequency response that starts with amplitude 1.0 at low frequency and rises to a peak at medium frequencies before falling to zero at high frequencies. It must be remembered when using these filters that the collimator response changes as a function of distance so in practice it is usual to use a collimator detector response for an average distance from the face of the collimator, for example equal to the radius of rotation.

In modern camera systems, the effect of depth dependent collimator response can be more accurately modelled by incorporation into the system matrix of an iterative reconstruction algorithm, as described in section 3.6. This method allows for the probability of photons being detected in pixels adjacent to the pixel of interest. The contribution of each pixel needs to be

calculated from the known resolution of the camera and collimator combination at any given distance. Modification of the projection matrix in this way takes account of loss of resolution within each transaxial slice. However, loss of resolution also causes counts to be spread between slices as well as within slices, so use of a full 3D reconstruction algorithm as described in section 3.7 is required for accurate correction.

In a study by Kalantari et al. (2012) a variety of digital phantoms were used to investigate the quantitative errors associated with poor SPECT resolution and the effects of 2D and 3D resolution recovery, by modelling system response during iterative image reconstruction. Gaussian functions of varying widths were used to model collimator detector response (CDR). The results showed that even with noise-free projections, the conventional OSEM iterative reconstruction algorithm provided limited quantitative accuracy compared to both 2D and 3D resolution recovery, especially when the size of the of the object was comparable with the spatial resolution of the system. The 3D resolution recovery gave superior results to the 2D in both visual quality and quantitative accuracy.

Today, gamma camera manufacturers include Resolution Recovery packages on most modern systems. An example is the GE Evolution resolution recovery method (GE Healthcare) developed at UNC Chapel Hill and Johns Hopkins University and then optimised by GE Healthcare. This

method uses 3D modelling of the CDR including the intrinsic system response and the collimator specific response. Accurate predictions of the geometric response function for various collimator designs had already been derived (Metz 1980, Tsui 1990) and penetration and scatter components of the CDR were obtained using Monte-Carlo simulation methods. In order to incorporate the obtained CDR into the reconstruction algorithm, the following information is then used:

- Collimator design parameters: hole length and diameter, septal thickness
- Detector characteristics: intrinsic resolution, crystal thickness, collimator-detector gap
- Acquisition parameters: centre of rotation to collimator face distances for every projection view acquired.

When in use, the collimator design parameters and detector characteristics are retrieved from a look-up table within the software, and the acquisition parameters are retrieved from raw projection data.

3.6 Incorporation of corrections in iterative reconstruction

In order to correct for attenuation, scatter and finite resolution within SPECT reconstruction, iterative reconstruction techniques are necessary. The most common iterative algorithm used is OSEM (Hudson and Larkin, 1994) as described in section 2.5.2. This allows physical characteristics of the acquisition process to be modelled in the system matrix (a_{ij}).

The system matrix defines the probability of detecting an emitted photon originating from location j at any particular position i on the detector, which will depend upon many factors including detector geometry, attenuation and resolution. In order to understand the system matrix, consider a simple image as a 3×3 array of pixels. If this is imaged at 8 angles, we have 8 1D line profiles, or 8 sets of 3 projection 'bins' that can be arranged into a sinogram e.g. 3×8 bins. The system matrix, gives the probability of a given image pixel contributing to a given projection bin.

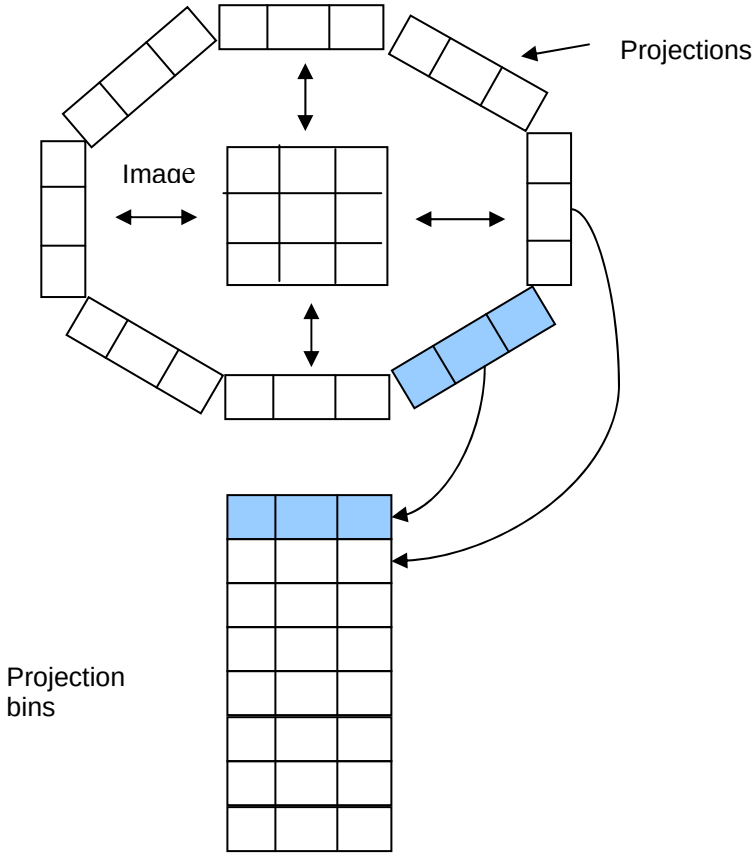

Fig. 3.8 Creation of an image sinogram for an image of 3×3 pixels imaged at 8 angles.

In this case, the system matrix would include (3× 3) × (3× 8) = 216 numbers. Fig. 3.9 shows a simplified system matrix for a 3×3 image with pixels labelled a to i. This is imaged at 4 angles labelled 1 to 4, with 3 projection bins at each angle, resulting in 12 bins labelled O to Z. The values in the system matrix represent the probabilities of a given pixel contributing to a given projection bin, which in this idealised case of no attenuation and scatter and perfect resolution, just represent geometry.

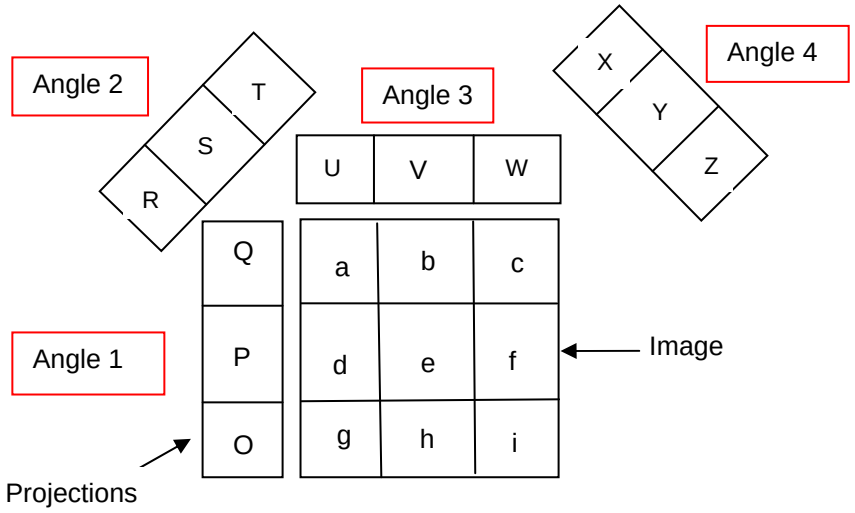

		a	**b**	**c**	**d**	**e**	**f**	**g**	**h**	**i**
Angle 1	**O**							1	1	1
	P				1	1	1			
	Q	1	1	1						
Angle 2	**R**				0.8				0.8	
	S	1	0.2		0.2	1	0.2		0.2	1
	T		0.8				0.8			
Angle 3	**U**	1			1			1		
	V		1			1			1	
	W			1			1			1
Angle 4	**X**		0.8		0.8					
	Y		0.2	1	0.2	1	0.2	1	0.2	
	Z						0.8		0.8	

Fig. 3.9 System matrix with no corrections for a 3×3 image imaged at 4 angles with no attenuation or scatter and perfect resolution. The values in the matrix represent the probability of each pixel (a to i) contributing o each projection bin (O to Z) which in this case just represent geometry.

However as mentioned, an advantage of the iterative technique is that corrections for attenuation, scatter and resolution can be incorporated. In the case of attenuation, the system is modelled by altering values of aij such that if a photon passes through a long distance of tissue its probability of detection and hence its' weighting factor within the matrix will be lower. The weighting factors are based on the attenuation map acquired using an external transmission source or CT.

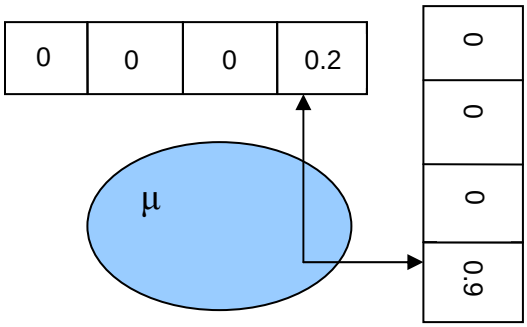

Fig. 3.10 Incorporation of attenuation into the system matrix.

This adjustment to the projection matrix only needs to be carried out once, before reconstruction starts. Since the forward-projection step now includes the effects of attenuation, the estimated projections will be attenuated. These are then compared with the measured projections which already include real attenuation, and so when the iteration completes, the final estimated image should be automatically corrected for attenuation (Greaves 2011).

In a similar way, the imperfect resolution of the imaging system can be modelled, by allowing the probability of photons being detected in adjacent pixels to the pixel of interest as in Fig. 3.11.

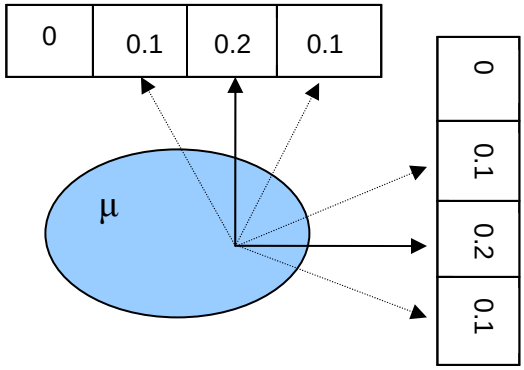

Fig 3.11 Incorporation of resolution model into the system matrix

There are two ways in which scatter can be corrected for. Either by modification of the system matrix to include a model of scatter in a given body outline, or by measuring scatter data from a scatter window and either subtracting this from the observed projections or adding it to the estimated projections. It has been found that adding the scatter contribution to the estimated projections helps to minimise noise and so is the preferred option (Greaves 2011).

3.7 Three dimensional (3D) reconstruction

As previously mentioned, the loss of resolution of a gamma camera with distance of the object from the collimator, results in counts being spread between transaxial slices as well as within slices. For this reason, in order for this loss of resolution to be corrected for, full 3D reconstruction must be carried out- a process that deals with all slices simultaneously.

Although this process is similar to 2D reconstruction, we now need to deal with a 3D set of projection bins (2D projection images at a range of angles) and a 3D set of reconstructed image voxels. This requires a 6 dimensional reconstruction matrix as opposed to the 4 dimensional matrix used in 2D reconstruction.

The method of 3D resolution recovery is essentially an extension of the method described in 2D. As long as the point spread function of the camera is known then the projection matrix can be modified to take account of the probability that gamma rays originating from slightly off the projection ray can still reach a given projection bin. The PSF can be approximated by a Gaussian shaped profile with a given FWHM. This will increase with increasing distance from the collimator, but this can easily be measured or calculated if the parameters of the collimator (hole size and length etc.) are known. Therefore, as long as the properties of the collimator and the distance of the patient from the collimator are known, the projection matrix

can incorporate the actual image blurring caused by limited resolution. This means that the image can be reconstructed without this blurring appearing.

In practice, this process is still limited by image noise particularly in studies with low counts per pixel. A way of minimising the noise without affecting the resolution is to smooth the acquired projection images with a low-pass filter. The loss of resolution that this causes can be compensated for by including the same smoothing function during the forward projection step of iterative reconstruction. The projection matrix does not need to be modified, so it gives an estimate of the unsmoothed projection. This can then be smoothed and compared with the smoothed versions of the acquired projections.

Until recently, full 3D iterative reconstruction was not commonly used due to the large amount of computing power required. However, today with more powerful computers available, 3D iterative reconstruction is available on commercial systems for routine nuclear medicine use.

3.8 Clinical applications of correction techniques

Since the introduction of SPECT/CT hybrid imaging systems with iterative reconstruction techniques, their advantages of providing correction for attenuation, scatter, partial volume and depth dependant collimator response together with increased specificity and accurate localisation of disease have led to many clinical applications. In the area of oncological diseases alone SPECT/CT is now used to localise endocrine and neuroendocrine tumours, solitary pulmonary nodules and lung cancers, brain tumours, lymphoma, prostate cancer, malignant and benign bone lesions and infection (Bockisch et al. 2009; Mariani et al. 2010). These applications however, all rely on the ability of SPECT/CT to enable accurate image fusion rather than its capability for quantitative corrections and so will not be considered further here.

In their recent review of quantitative SPECT imaging and potential clinical applications, Bailey and Willowson (2013) recognised that SPECT is often regarded as secondary to PET when it comes to absolute quantitation and also suffers from poorer sensitivity and spatial resolution. However, SPECT does have the advantages of utilising longer lived radionuclides that are readily available without close proximity to a medical cyclotron which makes SPECT/CT more readily available than PET/CT. Their group have carried out two studies using Tc-99m and SPECT/CT with in-vivo validation in a clinical setting. The first involved Tc-99m MAA lung imaging and will be

referred to in section 3.8.5. The second was in subjects undergoing left ventricular ejection fraction measurements using Tc-99m labelled erythrocytes. The activity concentration of Tc-99m in a peripheral venous whole blood sample at the time of the SPECT scan was measured in a gamma counter and compared with the concentration of the radiolabelled blood pool in the images reconstructed with CT based attenuation and scatter correction (Willowson et al. 2010). The average error in estimated activity concentration was + 1.3%, with a range of -6.3% to +4.9%. A further study by Zeintl et. al (2010) investigated the accuracy of quantitative Tc-99m SPECT measuring the activity concentration of urine in the bladder of subjects undergoing Tc-99m methylene diphosphonate (MDP). Their reported average error was +1.1%.

Tc-99m is not the only radionuclide that has been used in investigations of quantitative SPECT/CT. As will be seen, I-123 has been used in thyroid studies for diagnosis and dosimetry for targeted radionuclide therapy (TRT), as has I-131 and a range of more novel therapeutic radionuclides as described in section 3.8.1.

In diagnostic nuclear medicine to date correction techniques have been utilised most widely in myocardial perfusion imaging (MPI), where image artefacts due to attenuation lead to the possibility of misdiagnoses being made. However, correction techniques are also finding a role in other areas

of diagnostic SPECT imaging including skeletal, renal, lung and brain studies, to improve quantitative accuracy and confidence in clinical reporting.

3.8.1 Internal dosimetry for targeted radionuclide therapy

An important field where there is a need for accurate quantitation of nuclear medicine images is dosimetry for targeted radionuclide therapy (TRT) (Loke et. al 2011). Absorbed dose calculations based on modelled bio-distribution data and serial planar quantitative imaging procedures have given unsatisfactory results in the past, with the consequence that TRT treatments today are still often based on empirical fixed administered activities, modified by clinical and/or pathological findings (Flux 2006). It is recognised that targeted radionuclide therapy ought to be based on patient specific dosimetry in a manner analogous to external beam therapy (Stabin et al. 2008), but there are difficulties specific to internal radionuclide dosimetry such as: lack of radionuclide homogeneity within the tissues, tracer amounts of isotope used for uptake measurements with different biokinetics to the full therapeutic dose and a lack of uniformity in the reporting of internal dose results (Meredith et al. 2006). As a result, errors in internal dosimetry calculations as high as 30-100% have been reported (Flux et al. 2006). Although biokinetic data is important, Flux stated that the most significant barrier to routine accurate dosimetry is that of image quantification, by which the counts recorded in an image may be converted to absolute values of activity. He listed the main corrections needed for absolute quantification as:

attenuation, scatter, collimator efficiency, detector sensitivity, septal penetration and high count rate. With the incorporation of these corrections and the customisation of the actual patient size and organ weight, the overall uncertainty of an organ dose estimate can be reduced to about ±30% (Fisher et al. 2000).

A frequently used tool in dosimetry studies is Monte Carlo modelling (Tsougos et al. 2010). In general terms, Monte Carlo is a mathematical technique in which physical systems are simulated by statistical methods employing random numbers. A model is created as similar as possible to the real physical system of interest and interactions are created within that system based on known probabilities of occurrence, with random sampling of the probability density functions (PDFs) (Zaidi 2006). For simulation of imaging systems, radiation transport is simulated by the creation of charged particles or photons from a defined source region. These are tracked as they travel through the system with the PDFs of their interactions sampled to evaluate their trajectories and energy deposition at different points in the system. Importantly, the energy deposition during each interaction gives the radiation absorbed dose when divided by the appropriate values of mass, so with sufficient numbers of interactions, the mean absorbed dose at points of interest is given with acceptable uncertainties (Zaidi 2006). The overall technique for patient specific dosimetry can therefore be summarised in three steps:

i) SPECT images are reconstructed into transverse slices, to produce a count density map of source regions

ii) The count density is converted to an activity map using the sensitivity derived from a calibration phantom

iii) The activity distribution is converted to a dose map, either by convolving the activity distribution with dose point kernels or by direct Monte Carlo calculations.

The Monte Carlo approach has been used in several dosimetric studies and research continues in this area (Ljungberg et al. 2002; Ljungberg et al. 2003; Haidi et al. 2003; Ljungberg et al. 2011; Saeedzadeh et al. 2012).

An example of targeted radiotherapy, where traditionally standard activities have been given (IPEM Report 83) is I-131 treatment for differentiated thyroid cancer. Several dosimetric studies have been carried out to establish a more patient specific method of treatment planning (Dewaraja 2009; Wong 2011). In a recent study Saeedzadeh et al. (2012) used Monte Carlo modelling to carry out voxel-level radiation dosimetry for organ activities in an anthropomorphic phantom representing an I-131 treated thyroid cancer patient. This approach allowed incorporation of the size, shape and composition of organs and intra-organ and intra-tumour inhomogeneities in the activity distributions. The total activities of the tumours and their heterogeneous distributions were measured from SPECT images. The

results showed that due to the non-uniform distribution of tracer within the tumour, some areas of the tumour received a lower dose than others. In this case it would be misleading to quote the mean or maximum absorbed dose, because overall treatment response would be limited by the tumour volume that received low (i.e. non-lethal) doses. Saeedzadeh concluded that three dimensional radiation dosimetry and calculation of tumour dose-volume histograms could lead to the derivation of clinically reliable dose-response relationships and therefore may ultimately improve treatment planning as well as response assessment for radionuclide therapy.

In recent years, further therapeutic radiopharmaceuticals have found clinical applications, necessitating dosimetric studies, either using tracer amounts of the therapeutic radiopharmaceutical to produce the count density map, or an alternative with a similar biodistribution. For example, tumour dosimetry based on quantitative analysis of Tc-99m macroaggregated albumin SPECT/CT images has been shown to be predictive of progression free survival and overall survival of patients with hepatocellular carcinoma treated with Y-90 microspheres (Diedonne et al. 2011; Garin et al. 2012). Other dosimetry studies that have been carried out involve I-131-tositumomab or Y-90-ibritumomab tiuxetan for treatment of non-Hodgkin lymphoma (Dewaraja et al 2010; Amro et al. 2010; Wiseman et. al 2003), I-131-MIBG therapies for metastatic neuroblastoma, phaeochromocytoma and paraganglioma (Sudbrock et al. 2010) and Sm-153 ethylene diamine

tetramethylene phosphonate (EDTMP) for palliative treatment of malignant bone disease (Vanzi et al. 2009).

3.8.2 Myocardial perfusion imaging (MPI)

It is widely recognised that the specificity of planar and SPECT myocardial perfusion imaging can be seriously affected by image artefacts. The most common causes of these artefacts include breast and 'diaphragmatic' attenuation, patient and respiratory motion, obesity, left bundle branch block and photon scatter from adjacent structures. Artefacts from breast and diaphragmatic attenuation are often suspected because of their typical locations and shapes relative to the heart. Fixed defects in the anterior and inferior walls may be distinguished from infarction by the identification of normal wall motion with gated SPECT imaging, but reversible defects are more difficult to interpret. In their review article, Corbett et al. (1999) stated that photon attenuation is the single most important variable in influencing the specificity of SPECT perfusion imaging, with references to other work which provided quantitative evidence for the contribution of attenuation to regional myocardial activity variations and reduced test specificity (Frey, Tsui et al. 1992; Jaszczak, Gilland et al. 1993; Tan, Bailey et al. 1993).

Patterns of attenuation in the thorax are highly variable from patient to patient, so although SPECT perfusion scans routinely show variable areas of breast, diaphragmatic and lateral attenuation in female, male and obese

patients respectively, their locations and magnitudes can be very different. This makes the clinical differentiation of artefacts from true perfusion defects difficult, so simply recognising the patterns that occur should not be relied upon. Corbett and Ficaro (1999) refer to a multi- centre study carried out by the Cedars Sinai group (Van Train et al. 1993, Van Train et al. 1994) in which a sensitivity of 89% was achieved, but specificity was a poor 36%.

Although the important role attenuation correction could play in SPECT myocardial perfusion imaging was recognised, early studies carried out with a variety of methodologies gave variable results. Such was the uncertainty and confusion surrounding attenuation correction systems that by 1996 Ficaro and Fesler (1996) concluded that 'At the present time it is unclear whether attenuation correction of cardiac SPECT will remain the emperor's new clothes or will develop into a fashionable Armani suit. Until further progress has been made, one cannot recommend attenuation correction devices for routine clinical practice'. In 1999 an editorial was published in the Journal of Nuclear Medicine entitled 'Attenuation correction, or the emperor's new clothes?' (Wackers 1999). In an overview of experience with attenuation correction up to that date, he quoted the paper by Ficaro et al. (1996) as giving very encouraging results, where-as other papers, including work by Vidal and Buvat (1999), highlighted problems. In this particular study, the investigators tested a commercially available attenuation correction method in patients with documented coronary artery disease. In

the inferior wall, specificity was improved by >12% for detection of right coronary disease. However, in the anterior wall, attenuation correction resulted in a reduction in sensitivity of >20% for detection of left anterior descending coronary artery disease, with preserved specificity. This paper also stated that new learning is necessary to interpret attenuation corrected images. For example, on normal attenuation corrected images substantial apical defects may be present and should be ignored. The problem of ‘apical thinning’ on attenuation corrected images was reported as early as 1995 when Stewart et al. (1995) described apical anterior defects in 16 of 18 attenuation corrected SPECT studies in comparison with attenuation-corrected PET studies. Another early study by Ficaro et al. (1996) concluded that after attenuation correction the apex and distal inferior segments had reduced counts compared with the rest of the myocardial segments. However, differences between male and female activity distributions were removed and the ratios of septal to lateral and anterior to inferior walls were approximately equal. Apical thinning has been investigated more recently by Okuda et al. (2011), who found that even in patients with normal myocardial perfusion, low apical activity is frequently observed after attenuation correction. They concluded that this in fact is not an artefact caused by AC processing, but the myocardial count is actually low based on the thinning of the myocardial apex.

A more difficult problem to allow for even on modern systems is that of mis-registration of hybrid SPECT/CT images leading to artefactually reduced counts in the anterior and antero-septal walls. Tonge et al. (2006) reported that in a group of ninety-four patients (64 men, 30 women) where stress and rest MPI was carried out using CT attenuation correction, mis-registration could be classed as severe in 35% of cases. Where this mis-registration resulted in heart tissue being corrected by the attenuation coefficient of lung tissue, artefacts in the anterior and apical segments became likely. In previous work (Tonge et al. 2005) it had been shown that mis-registration by as little as 1 pixel can create a defect in the anterior or apical wall. Software to allow correction of mis-registration before attenuation correction is now becoming available to help combat this problem and has been seen to reduce the incidence of anterior/apical defects (Tonge et al. 2006).

Despite some seemingly negative results, attenuation correction does have a role in clinical diagnosis, particularly in ‘difficult’ groups such as women or obese subjects. Women with known or suspected coronary artery disease have traditionally been a difficult group to diagnose, partly due to the wide variability of breast attenuation and the increased frequency of relatively small heart sizes. Ficaro et al. (1996) studied 59 women, 43 with insignificant coronary artery stenoses. Although attenuation corrected studies showed no significant increase in sensitivity (0.93 vs 0.86, p=NS), they did show a

significant increase in specificity (0.88 vs. 0.68, p= 0.03) which would lead to improved confidence in clinical diagnoses in women.

It is accepted that if attenuation correction is carried out correctly, there should be no difference between male and female activity distributions. In a study by Grossman et al. (2004), a gender independent normal database was developed in an obese population. Attenuation correction was carried out using Gd-153 line sources. These studies were processed twice, once using conventional reconstruction and gender specific database quantification and a second time using attenuation correction and a gender-independent attenuation-corrected normal database. As expected, when comparing attenuation corrected perfusion distributions of men and women, no statistically significant differences were found whereas significant differences were found in the same uncorrected studies.

A further adjunct to attenuation correction in the processing of myocardial perfusion studies has been physiological gating. This method uses the R wave of the patient's electrocardiogram (ECG) to trigger each acquisition. Each heart beat is then acquired into 8 or 16 frames, so that by the end of the study a rough 'beating' image of the heart can be reconstructed. From these gated images, software can be used to calculate an estimated ejection fraction, and a cine loop of the images can be viewed to assess wall motion and thickening. An area of healthy myocardial tissue will move in phase with

the rest of the heart and thicken on contraction. Therefore if an area of seemingly reduced perfusion is seen to be moving and thickening normally, the reduction is likely to be artefactual. In a study by Heller et al. (2004), 90 consecutive stress-only ECG gated Tc-99m methoxyisobutylisonitrile (MIBI) images were interpreted by 10 independent nuclear cardiologists. The studies were interpreted sequentially with myocardial perfusion imaging (MPI) alone, MPI plus ECG gated data and attenuation corrected MPI with ECG-gated data. Attenuation correction was carried out using Gd-153 line sources (VantagePro/ExSPECT II/ ADAC/Philips Laboratories). The studies were interpreted on a five point scale for diagnostic certainty (normal, probably normal, equivocal, probably abnormal, abnormal) and the perceived need for rest imaging. With stress MPI data alone, the interpretation categories were relatively equally divided across the 5 categories. Only a small proportion of studies were interpreted as definitely normal or abnormal (37%, 41%) with a very high perceived need for rest imaging (77%). The addition of gating did not significantly alter the interpretations. However, attenuation-corrected gated data significantly increased the number of studies categorised as definitely normal or abnormal (84%, $p<0.005$) and significantly reduced the perceived need for rest imaging (43%, $p<0.005$). This study also investigated the effect of body habitus (obese or non-obese) on clinical interpretation. Results showed that, the percentage of definite interpretation with attenuation correction was high and independent of body habitus (86.5% vs 78.6%, p= NS). For both body

habitus groups, attenuation correction resulted in a significant increase in definite categorisation and a reduction in the need for rest imaging. A more recent study by Giubbini et al. (2011) used gated SPECT with CT attenuation correction (Infinia VG Hawkeye or Infinia VG Hawkeye 4, General Electric Healthcare), to investigate the effect of AC on infarct size quantification in male patients with previous inferior myocardial infarct. Uncorrected and corrected SPECT images were analysed for perfusion using a 5 point segmental scoring scale as above and the summed stress score (SSS), summed rest score (SRS) and summed difference score (SDS) of the left inferior wall were determined and compared with the regional wall motion score from uncorrected gated SPECT images. The results showed that differences between SSS and SRS for the uncorrected and corrected groups were statistically significant, but not in the case of the SDS. From this it was concluded that the combination of diaphragmatic attenuation and inferior myocardial infarction leads to an artifactual overestimation of infarct size. The AC resting perfusion score (SRS) correlated well with the regional wall motion score, but other than this AC did not effect the detection and apparent size of residual ischaemia.

Despite some promising results, by 2003 the British Nuclear Medicine Society was still cautious, concluding that “Although initial results are encouraging, each method behaves differently and none overcomes artefacts entirely, some even introducing new forms of artefact from

overcorrection. The effectiveness of these techniques in routine clinical practice is currently uncertain. They should be used only in experienced centres and preferably as part of a formal evaluation of their value. Corrected images should not be used without review alongside the uncorrected images" (Anagnostopoulos et al. 2003). A joint statement issued the year previously by the Society of Nuclear Medicine (SNM) and the American Society of Nuclear Cardiology (ASNC) (Hendel et al. 2002) had been more optimistic concluding that "incorporation of attenuation correction in addition to ECG gating with SPECT myocardial perfusion images will improve image quality, interpretive certainty, and diagnostic accuracy. These combined results are anticipated to have a substantial impact on improving the effectiveness of care and lowering health care costs." However, they stipulated that attenuation correction should be used in conjunction with motion correction, scatter correction and resolution recovery and also that physicians should view and interpret both uncorrected and corrected images.

In recent years, worldwide problems with the supply of Tc-99m have led to an interest in using the improvement in image quality offered by resolution recovery software to allow myocardial perfusion imaging to be carried out with a reduced amount of administered activity. Armstrong et al. (2012) carried out a study where half-count SPECT data were derived from full count data sets for 53 stress and rest routine myocardial perfusion studies on a GE Infinia camera. Full count data were reconstructed using standard

non resolution recovery (RR) OSEM, whereas half-count data were reconstructed using GE Evolution RR software. Myocardial function values, image quality and clinical report outcomes of the full count and half count reports were compared. Sequential full-time and half-time myocardial SPECT acquisitions were also carried out for 15 stress and rest studies on a Siemens c.cam dedicated cardiac camera (Siemens Medical Solutions). Half-count data were reconstructed using Siemens Flash 3D RR software. The results showed that no degradation in image quality was found when comparing full-count and half-count studies from the Infinia. Ten percent of the half-count studies from the c.cam were considered slightly worse than the full count data. Statistically significant differences in some full count versus half-count functional values were found, but the actual mean differences were not considered clinically significant.

3.8.3 Skeletal studies

Case et al. (1999) carried out an early comparison of attenuation correction techniques in bone SPECT of the cervical spine, a region where variable attenuation in the head, neck and shoulders leads to an artefactual reduction in counts in the upper cervical and thoracic regions relative to the neck region. The methods they compared were:

i) a downscatter method where the body outline was determined using a combination of the photopeak and Compton scatter window

ii) the Chang method, where the body outline was determined from photopeak data

iii) a transmission method using Gd-153 line sources and fan-beam collimators on a triple head gamma camera system.

For the mathematically calculated methods, a uniform attenuation coefficient of $\mu = 0.15cm^{-1}$ was used. The results were compared using the transmission corrected results (adjusted for truncation effects) as the 'gold standard'. It was found that with no correction, cervical spine counts were overestimated by 30-50%. Chang AC led to an underestimation in cervical spine counts of the same amount, due to problems locating the patient boundary. The downscatter correction method gave count values ranging from 90% of the transmission method results to indistinguishable from the transmission method. It was concluded that in the cervical spine the most important factor in determining patient attenuation is the accurate estimate of the patient boundary, with variable attenuation within that boundary being less important. Clinically, patient studies using downscatter AC showed significant improvement in the uniformity of estimated cervical spine uptake in normal patients and of the lower back in obese patients.

With regard to scatter correction however, a study by Stark et al. (2003) concluded that scatter correction using a 3 window technique did not improve the image quality in SPECT of the spine. They surmised that this was due to a lower signal to noise ratio in the scatter corrected images,

which contained 30-35% fewer counts than the non-scatter corrected images.

Of particular interest in bone scinitgraphy has been the use of 3D resolution recovery. Stansfield et al. (2010) carried out a preliminary evaluation of image quality of paediatric Tc-99m MDP SPECT studies acquired on the Siemens ECAM (Siemens Medical Solutions) and reconstructed using Flash 3D (Siemens Medical Solutions) OSEM-3D resolution recovery software. The aim of the study was to assess whether improvements with the use of this technique could lead to a reduction in patient dose or a shortening of imaging time. Fifty SPECT studies of the spine were evaluated with each data set having been reconstructed three times. The three methods of reconstruction were: FBP with data from two detectors, OSEM 3D with data from two detectors and OSEM 3D with data from a single detector to simulate half count data. To review the data, two nuclear medicine physicians assessed the images for image quality in four categories using a four point scale. The categories were: artefact detection, lesion detection, image noise and image sharpness. The results showed that compared with FBP, images reconstructed by using OSEM 3D with one or two detectors showed significant improvement in image quality with respect to lesion detection, image noise and image sharpness ($p<0.02$, 0.01 and 0.001 respectively). With OSEM 3D no significant differences were observed when either one or two detectors were used. It was concluded that improved

quality of skeletal SPECT with either a 50% reduction in radiation dose or a 50% reduction in acquisition time or a combination of the two can be achieved by using OSEM 3D reconstruction.

3.8.4 Renal Studies

An early SPECT technique for absolute quantitation of radiopharmaceutical in patients was derived by Front et. al (1987) This technique involved defining regions of interest using a thresholding technique. A threshold value of 43% of the maximum pixel, was found to give the most reliable results. Reconstruction was carried out using filtered back projection for this study, with no corrections made for attenuation, scatter or limited resolution. Results in phantoms were encouraging and the method was subsequently applied to quantitation of renal uptake using Tc-99m dimercaptosuccinic acid (DMSA) SPECT. Calibration results using kidney phantoms were applied to the assessment of renal uptake of Tc-99m DMSA in 25 normals, 16 patients with single normal kidney, 30 patients with unilateral nephropathy and 17 patients with bilateral nephropathy. An excellent correlation was found between SPECT measured concentration and actual concentration in kidney phantoms.

Kojima et al. (2000) later devised a method for accurately measuring renal activity by using a static emission image corrected for attenuation using transmission data from an external Tc-99m array line source and corrected

for scatter using a triple energy window method. In their idealised phantom study they found that accurate background correction taking into account attenuation and kidney volume, together with scatter correction, could give depth independent count rates and could estimate the true count rate with errors of <5% for all kidney to background activity concentrations. However if either background or scatter correction was performed alone, the absolute error increased to about 50% for the smaller concentration ratios.

The use of resolution recovery in paediatric bone imaging has already been discussed in section 3.8.3 where it was seen to offer improved image quality even at lower counts. In 2009, the same group at the Children's Hospital, Boston (Sheehy et al. 2009) compared reconstructing Tc-99m DMSA SPECT studies with FBP and with OSEM 3D in terms of improving image quality and reducing the radiopharmaceutical activity and radiation dose. Fifty paediatric patient Tc-99m DMSA studies of 98 kidneys were reconstructed using FBP and OSEM 3D with data from one detector to simulate half count data. Two nuclear medicine physicians scored the studies in terms of image quality, renal size, relative function and detection of renal cortical defects. The results showed that image quality was significantly enhanced with half count OSEM 3D resconstruction ($p<0.001$). Cortical defects were identified better on half count OSEM 3D images than on FBP images with four kidneys displaying defects with half count OSEM 3D that were not seen with FBP. No significant difference in relative renal

function between the two methods was found. It was concluded that OSEM 3D resolution recovery in Tc-99m DMSA SPECT offers the potential for improved image quality with reduced radiation doses and/or reduced scanning time for patients.

3.8.5 Lung Studies

An area where quantitative nuclear medicine has a particular application is the assessment of the *in vivo* distribution of a drug administered by inhalation. In particular it has been used to assess the percentage of total deposition of activity in the lung. Early work used planar gamma camera imaging to visualise aerosol deposition (Dolovich et al. 1976). Subsequently planar imaging continued to be used to quantify aerosol deposition. In a study carried out on dogs, Itoh et al. (1985) investigated aerosol deposition in the lungs by 3 independent methods:

i) tyndallometry (continuous concentration in the mouth)

ii) planar gamma camera imaging

iii) filter collection of exhaled aerosol.

For the gamma camera images, counts were converted to deposited activity and correction was made for attenuation using a perfusion image derived calibration factor. The results showed close agreement between the gamma camera data and the other two methods. However, animal experiments may not always extrapolate to human studies and some early human studies

showed that uncorrected planar gamma imaging is inclined to slightly overestimate the amount of lung deposition when compared with independent pharmokinetic measurements (Borgstrom et al. 1992, Newman et al. 1995). In view of this finding, Pitcairn et al. (1997) investigated the use of attenuation correction applied to aerosol deposition studies and Lee et al. (2001) carried out a comprehensive investigation into the effect of scatter and attenuation correction on aerosol deposition as determined by gamma scintigraphy. Two methods of scatter correction were investigated:

i) Jaszczak method

ii) factor analysis.

Scatter was shown to account for 20% of raw data in the whole lung, 20% in the oropharynx and 43% in the central airways and oesophagus. Three methods of attenuation correction (all utilising the geometric mean of anterior and posterior images) were investigated and compared:

i) uniform attenuation correction

ii) broad beam attenuation correction (with no *a priori* scatter correction)

iii) narrow beam attenuation correction using fused CT image attenuation maps and *a priori* scatter correction.

The three methods differed significantly, but all indicated that attenuation is a severe quantification problem. The narrow beam attenuation correction

with scatter correction showed that raw data underestimated tracer deposition by 44% in the lung, 137% in the oropharynx and 153% in the trachea/oesophageal region.

In 2003, Fleming et al. compared planar imaging using quantitative methods for attenuation and scatter correction with SPECT imaging, where SPECT quantitation measurements were used as the gold standard. The planar attenuation methods used were thickness measurement and transmission measurement, with and without *a priori* scatter correction. The two scatter correction techniques investigated were reduced attenuation coefficient (i.e. broad beam assumption) and line source scatter function convolution subtraction. Thickness measurements for the planar corrections and the attenuation map for the SPECT attenuation correction were obtained from fused MR images. Activity in the right lung was calculated in terms of MBq, using a measured planar sensitivity factor. Results showed that when the thickness measurement and transmission techniques were applied with scatter compensation using a reduced attenuation coefficient, activity was systematically overestimated by 5% in both cases. Separate scatter correction reduced these systematic errors significantly to -1.5% and 2.7% respectively. All techniques provided assessment of total lung activity with an accuracy and a precision that differed by less than 10% compared to SPECT values, which led Fleming

to conclude that “Planar gamma camera imaging provides a good method of assessing total lung deposition of inhaled aerosol”.

More recently however, Nunez et al (2009) carried out a simulation study to evaluate the influence of AC on defect to normal ratios (D/N) for lung SPECT. Attenuation correction was carried out by use of a synthetic map derived from the emission data and the results compared with those obtained using a CT map. The role of attenuation correction in reprojected SPECT data (i.e. ‘planar- like’ images generated from the SPECT images) was also investigated. Phantom studies showed that AC markedly affects the D/N ratio. However, variations in μ values typical of those found in clinical studies resulted in relatively small changes in results. Clinical SPECT/CT data reconstructed with CT attenuation maps and simulated maps showed an excellent correlation between the two methods, implying that the use of a synthetic map in lung SPECT is feasible, avoiding the need for extra radiation dose to the patient. Planar-like images generated from the reprojected SPECT data were well matched to normal planar images provided that AC was performed.

In the case of lung perfusion using Tc-99m MAA, Willowson et al. (2008) examined the accuracy of *in vivo* activity measured in the lungs using SPECT/CT, based on the assumption that 100% of the radiopharmaceutical is trapped in the lungs after intravenous injection of a

calibrated amount of the radiopharmaceutical. The total activity in 12 subjects was estimated to be, on average, in error by -1% with a range of -7% to +4%.

3.8.6 Thyroid Studies

Quantitative gamma camera imaging with I-123 or Tc-99m pertechnetate is a sensitive and specific technique for the diagnosis of thyroid malignancy especially in diagnosis and risk stratification of spontaneous or iodine-induced hyperthyroidism (Meller and Becker 2002). At present, a simple planar method of thyroid imaging is still recommended (Sharp 2005). Background corrected counts in a region of interest drawn around the thyroid are compared with an aliquot of known activity measured in a neck phantom, designed to give an approximation of the attenuation and scatter conditions found in the patient. Work remains to be done on the use of SPECT imaging incorporating accurate corrections for attenuation, scatter and partial volume in thyroid uptake values in thyroid uptake values. As seen with dosimetric studies, more accurate uptake values could lead to patient specific therapies for hyperthyroidism.

In thyroid cancer patients, radioiodine has been used diagnostically and therapeutically for over 50 years on the basis of the ability of the thyroid gland to accumulate iodine through the sodium iodide (Na+/ I-) symporter. (Barwick 2012). Treatment for differentiated (follicular and papillary) thyroid

carcinoma in the majority of cases consists of total thyroidectomy, followed by radioiodine (I-131) ablation of thyroid remnants and thyroid-stimulating hormone (TSH) suppressive thyroid hormone therapy (British Thyroid Association 2007). The utilisation of quantitative SPECT imaging to improve individual patient treatment planning has been considered in section 3.8.1. with several studies having been carried out on accurate dosimetry in I-131 radionuclide therapy (Dewaraja 2009; Wong 2011, Saeedzadeh 2012). In one example, Dewaraja et al. used clinically realistic phantom simulations to model SPECT projections, using a Monte Carlo code. Within the model, SPECT reconstruction was performed using OSEM with the incorporation of corrections for attenuation, scatter and 3D detector response. Based on the SPECT image and a patient specific density map derived from CT, 3D dosimetry was performed using Monte Carlo modelling as previously described. Dosimetry was evaluated by comparing mean absorbed dose estimates calculated directly from the defined phantom activity map with those calculated from the SPECT image of the phantom. Finally, the 3D methods were applied to a real I-131 therapy patient and the mean tumour absorbed dose from the new calculation was compared with that from dosimetry using conjugate view imaging. Overall the percentage error of the SPECT based absorbed dose estimates in the phantom was <12% for targets of volume down to 16 ml, but up to 35% for the smallest 7 ml tumour, due to partial volume effects. For the patient, the mean tumour absorbed dose estimate from the Monte

Carlo calculation was 7% higher than that from conventional dosimetry, demonstrating the value of accurate 3D dosimetry in patient management (Dewaraja 2009).

Post therapy, the use of combined SPECT/CT has been advocated only in the follow- up of patients defined clinically as at high risk of recurrence (Pacini et al. 2008). Barwick et al. (2012) recently carried out a review of the use of SPECT/CT in a range of differentiated thyroid cancer studies. These studies assessed:

i) post ablation imaging

ii) mixed post-first-ablation imaging and subsequent therapy

iii) mixed post therapy and diagnostic imaging

iv) diagnostic imaging either with I-131 or I-123.

Overall, additional diagnostic information was provided by SPECT/CT over planar imaging for 34-74% of patients, with the wide spread of results attributed to varied patient selection and imaging times in the studies considered. This review however, only involved the use of SPECT/CT for improved localisation rather than measurement of absolute quantitation - corrections for attenuation, scatter and partial volume effect were not included.

3.8.7 Brain Studies

SPECT imaging of the dopaminergic system using I-123 labelled ioflupane (DaTSCAN) has been found to have significant clinical benefit in the evaluation of Parkinsonian syndromes (Catafau et al. 2001; Vlaar et al. 2007). Visual assessment alone has been used to evaluate the normality of DAT binding and has been found to be sufficient in differentiating Parkinsonism from essential tremor (Benamer et al. 2000). However, a semi-quantitative approach using ROI comparisons with age-matched controls is now recommended for an objective measure of DAT binding in the striatum and striatal sub-regions (caudate, nucleus, pitumen) (Darcourt et al. 2009). A quantitative approach is particularly relevant for indications such as measurement of disease progression (Chouker et al. 2001) the assessment of Lewy body dementia (Walker et al. 2002) and the monitoring of neuroprotective treatments (Fahn et al. 2004; Schillaci et al. 2005). Several studies have shown that values from semi-quantitative analysis are strongly dependent on the corrections performed. A significant problem with accurate quantitation in this area is that the small size of the striata means that the partial volume effect (PVE) becomes significant. In I-123 brain SPECT, radioactivity concentration in the striata can be underestimated by more than 50% if no correction for PVE is used (Buvat et al. 2000, Soret et al. 2003). Soret et al. (2003) investigated the combined effect of attenuation, scatter and partial volume effect corrections on quantitation using a Monte Carlo simulation and brain phantom experiments. SPECT scans were performed

using a triple headed camera, with Tc-99m line source attenuation correction. Scatter correction was carried out using a triple energy window method and partial volume correction (PVC) was performed by use of a method derived from the region-of-interest technique proposed by Rousset at al. (1993) for PET. Without any correction, brain activity was underestimated by at least 65% and absolute striatal activity measured in regions corresponding to the anatomic contours of the striate was underestimated by about 90%. With scatter and attenuation corrections only, estimated brain activity was accurate within 10%, but striatal activity remained underestimated by about 50%. When combined with AC and SC, anatomically guided PVC reduced the underestimation to about 10%, despite small errors in registering SPECT images with anatomic data or in segmenting the striata.

3.9 Conclusions

This chapter has reviewed the methods employed to improve the quantitative accuracy of gamma camera SPECT imaging by correcting for the physical processes of attenuation, scatter, partial volume effect and depth dependent collimator response. Some of the applications of these corrections in clinical nuclear medicine have been outlined, though the list considered is by no means exhaustive and there are likely to be further applications in the future.

This study will go on to consider two of these corrections in depth, namely attenuation correction and scatter correction and investigate their effect on the SPECT images acquired using the Hawkeye gamma camera system. Corrections for partial volume and depth dependent collimator response will not be included in this study, since the software for carrying out these corrections is not currently available on this system. However, inclusion of all four relevant corrections to ascertain their relative importance in accurate quantitative imaging will definitely be considered as further work in the future.

Chapter 4

Baseline Characteristics of the Hawkeye Gamma Camera

4.1 Introduction

The Hawkeye gamma camera system (GE Medical Systems, Milwaukee) used in this study was installed in the Medical Physics department of the University Hospital of Wales in January 2003. The system comprises a dual headed large field of view VG Millennium gamma camera and a low dose CT scanner mounted onto a slip-ring gantry. The processing workstation is the GE eNTEGRA software version 2.5302.

The gamma camera detector heads each contain a 9.5 mm thick, 600×500 mm NaI(Tl) crystal, giving rise to a useful field of view of 540×400 mm. Both crystals are backed by 59 photomultiplier tubes, each connected to an ADC. The collimators used during this study were low energy, high resolution collimators with septal thickness 0.2 mm, hole diameter 1.5 mm and hole length 35 mm.

The CT scanner comprises a X-ray tube operating at 140 keV, 2.5 mA, mounted opposite an array of 384 cadmium tungstate detectors. The X-ray tube aperture is mechanically collimated to a fixed slice thickness of 10 mm.

Before investigating the influence of different factors on quantitation, it was important to establish the baseline performance characteristics of the Hawkeye gamma camera in planar and SPECT operation. Once baseline

performance had been established and verified as being within manufacturers specifications, quality control (QC) tests were repeated on a regular basis throughout the duration of the study to ensure consistency of performance. The performance of the SPECT reconstruction software on the eNTEGRA workstation was verified by comparing results with known data supplied by the Institute of Physics and Engineering in Medicine (IPEM) Nuclear Medicine Software group as part of a national audit in 2002 (Jarritt et al. 2002) as described in section 4.4.

Quantitative SPECT performance was then further investigated using SPECT performance phantoms – namely a Jaszczak phantom and an anthropomorphic torso phantom (Data Spectrum) as described in section 4.5.

4.2 Measurement of planar gamma camera performance

Planar physical performance characteristics of the gamma camera include intrinsic uniformity, system uniformity, energy resolution, system spatial resolution and sensitivity. These parameters were measured using the methods outlined below in order to establish baseline performance indices of the Hawkeye gamma camera.

4.2.1 Method

4.2.1.1 Uniformity

Uniformity refers to the ability of the gamma camera to record an equal number of counts in each pixel of the image, when irradiated with a uniform source of radiation.

Two measures of uniformity are intrinsic and system uniformity. The intrinsic uniformity measurement was carried out with the collimators removed, so that the performance of the NaI(Tl) crystal and subsequent imaging system was tested. The test was carried out by placing a point source of 10 MBq Tc-99m at the centre of the field of view (FOV) of the gamma camera head at a distance of 2.5 m from the detector face. This distance is used to ensure that there is a less than 1% variation in radiation flux reaching the face of the camera (Bolster 2003). For establishment of performance, 30 M counts were acquired into a 256× 256 matrix. For system uniformity measurements, the gamma camera collimators were in place so that the overall performance of the gamma camera was tested. This test was carried out using a Co-57 flood source (376 MBq, reference date 09.10.06) with a gamma photon emission of 122 keV. Again 30 M counts were acquired into a 256 ×256 matrix.

The integral and differential uniformity were calculated as follows:

$$\text{Integral uniformity} = \text{max-min} / \text{max} + \text{min} \qquad \text{Eqn 4.1}$$

where max = maximum pixel count in the image and min = minimum pixel count in the image (Bolster 2003);

and

$$\text{Differential uniformity} = H + L / H - L \qquad \text{Eqn 4.2}$$

where H = maximum count in five consecutive pixels and L = minimum count in five consecutive pixels (Bolster 2003).

Differential uniformity is measured in both the X and Y directions.

In order to discount edge effects, uniformity results were quoted for the central field of view (CFOV), which is 75% of the useful field of view (UFOV).

4.2.1.2 Energy resolution

For mono-energetic photons incident on the gamma camera crystal, the pulse height energy spectrum has the shape already seen in Fig. 2.4 with a broad Compton band and a narrow photopeak. Energy resolution is a measure of the width of the photopeak measured at half of the maximum amplitude, expressed as a percentage of the photopeak energy. This was measured on the Hawkeye gamma camera by acquiring a spectrum containing 300k counts using the pulse height analyser (PHA) facility, as shown in Fig. 4.1. This facility enables the calculation and display of the full width at half maximum of the photopeak on completion of acquisition.

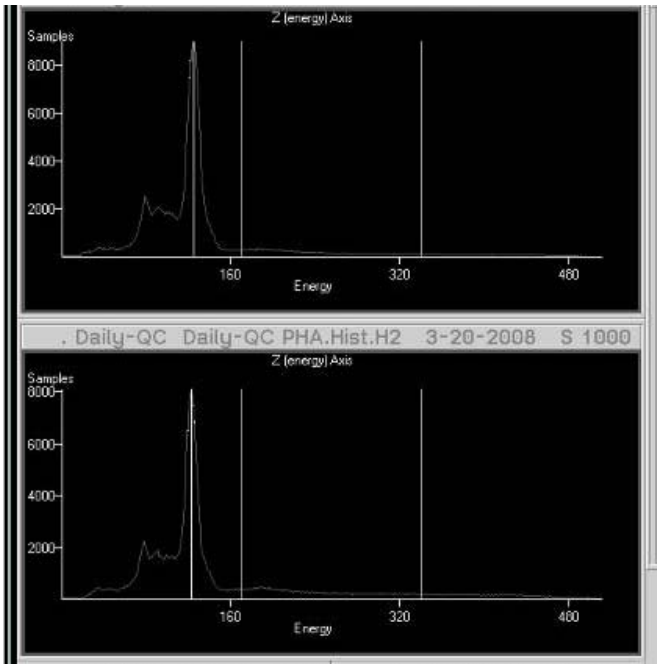

Fig 4.1 Pulse height energy spectrum used to measure energy resolution on the Hawkeye gamma camera. The X axis shows energy in keV and the Y axis shows number of counts. In this example, the energy resolution of Head 1 (upper spectrum) is 10.35% and the energy resolution of Head 2 (lower spectrum) is 9.75%.

4.2.1.3 System spatial resolution

System spatial resolution is a measure of the sharpness of the image produced by the gamma camera.

A quantitative measurement of spatial resolution was made by imaging a capillary line source containing 40 MBq of Tc-99m, positioned on the camera collimator in both the X and Y directions. The spatial resolution was measured as the full width at half maximum (FWHM) of a profile taken through the image, defined as the line spread function (LSF). The FWHM is equal to the minimum separation required between two line sources if they are just to be resolved.

4.2.1.4 Sensitivity

Sensitivity is a measure of the proportion of gamma photons emitted from a radionuclide source which is detected within the photopeak of the collimated gamma camera. This was measured by imaging a 10×10 cm phantom containing 70 MBq of Tc-99m, for 300 seconds at a distance of 10 cm from the camera collimator. The sensitivity was expressed as counts per second per MBq (cps/MBq) after correction for background.

4.2.2 Results

The results of the planar baseline performance measurements are given in Table 4.1.

Property	Results	
	Head 1	Head 2
Intrinsic uniformity CFOV 30M counts	Integral 2.38% X diff 1.69% Y diff 1.46%	Integral 2.07% X diff 1.40% Y diff 1.43%
Energy resolution	9.47%	9.48%
System uniformity CFOV 30M counts	Integral 3.14% X diff 1.48% Y diff 1.84%	Integral 3.09% X diff 1.71% Y diff 1.65%
System spatial resolution at 10cm air	X direction 8.6± 1.1 mm Y direction 7.8± 1.1 mm	X direction 7.9± 1.1 mm Y direction 8.0± 1.1 mm
Sensitivity phantom at 10cm air	65.42±0.01 cps/MBq	65.27±0.01 cps/MBq

Table 4.1. Planar baseline performance characteristics for the GE Hawkeye gamma camera

These results are all within the limits recommended by the British Nuclear Medicine Society (BNMS) for guidance when purchasing a gamma camera (BNMS 2004), manufacturer specifications (Millennium VG Operators manual 2002) and National Electrical Manufacturers Association (NEMA) standards (1980).

4.2.3 Planar Quality control measurements

4.2.3.1 Method

Measurements of system uniformity (made by acquiring 4M counts) and energy resolution were carried out on each day that the camera was used, for the duration of this project as part of a routine quality control programme. The acceptable limit of system uniformity had been previously determined using the system uniformity measurements of the first 3 months use of the camera post installation. At this time the mean value of system uniformity was found for each head and limits of acceptable performance set at two standard deviations above this value. This gave a result of 4% for each head. Above this 'action level' corrective action would need to be taken to improve performance before the camera could be used.

To ensure that the system uniformity of the camera remained stable and within the acceptable limit over the time for which measurements were made for this study, trend analysis on daily uniformity results was carried out. This was done for each head by plotting a sample uniformity result selected at random once a month for a 3 year time period and carrying out linear regression analysis on the resultant scatter plot.

Energy resolution was also measured and recorded daily as part of the routine quality control programme. A scatter plot of these results, selected as for the daily uniformity measurements, was generated to ensure that the energy resolution was within the manufacturer's specified limit at all times.

Intrinsic uniformity and sensitivity were measured annually as part of the extended quality control programme.

4.2.3.2 Results

The results of daily integral uniformity trend analysis are shown in Fig. 4.2 a) and b).

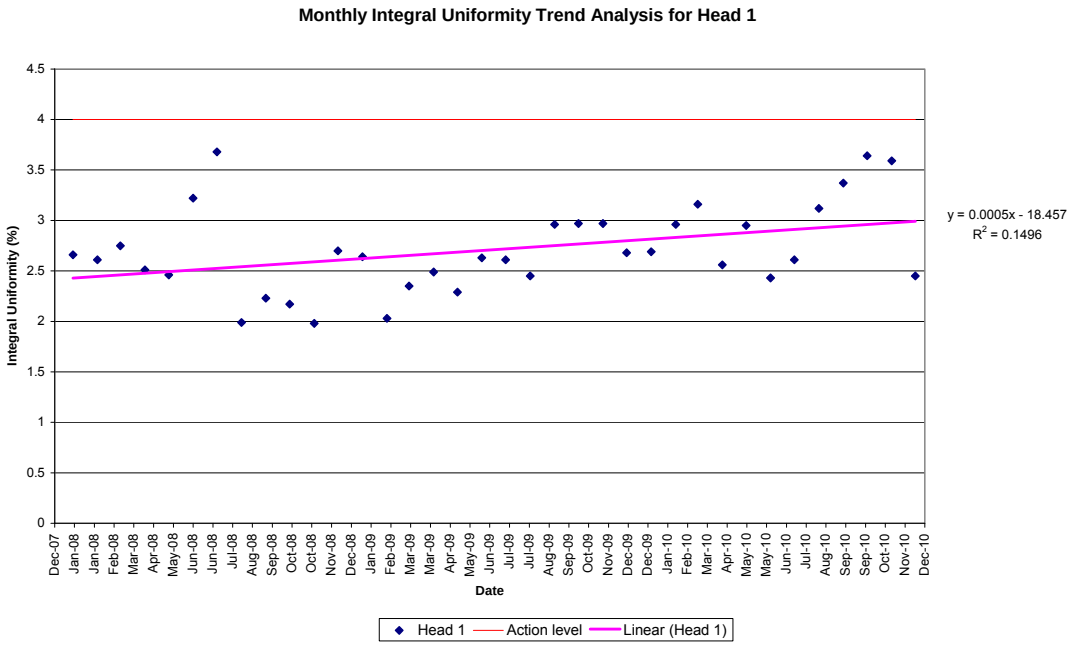

(a)

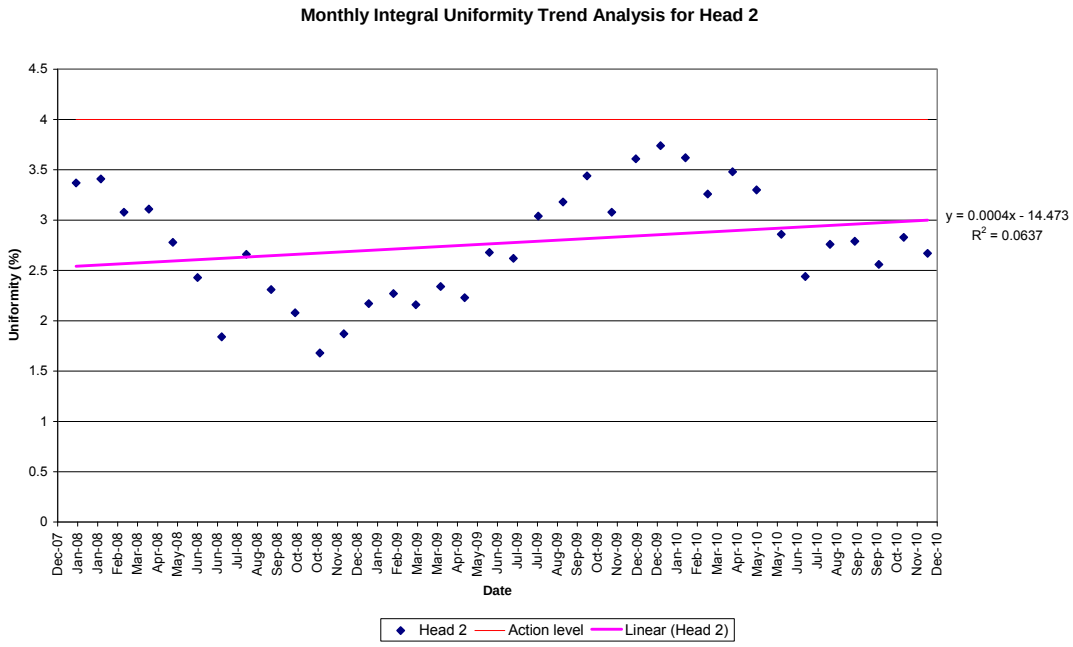

(b)

Fig. 4.2 Monthly integral system uniformity trend analysis for (a) head 1 and (b) head 2 on the Hawkeye gamma camera.

The results show that despite daily variation, there is no significant linear degradation with time and all results are well within the action level set.

The results of the daily energy resolution measurement are shown in Fig. 4.3 (a) and (b) and show that the value remained lower than the manufacturer's limit of 11% outlined in the Millennium VG Operators Manual (2002), for the duration of the study.

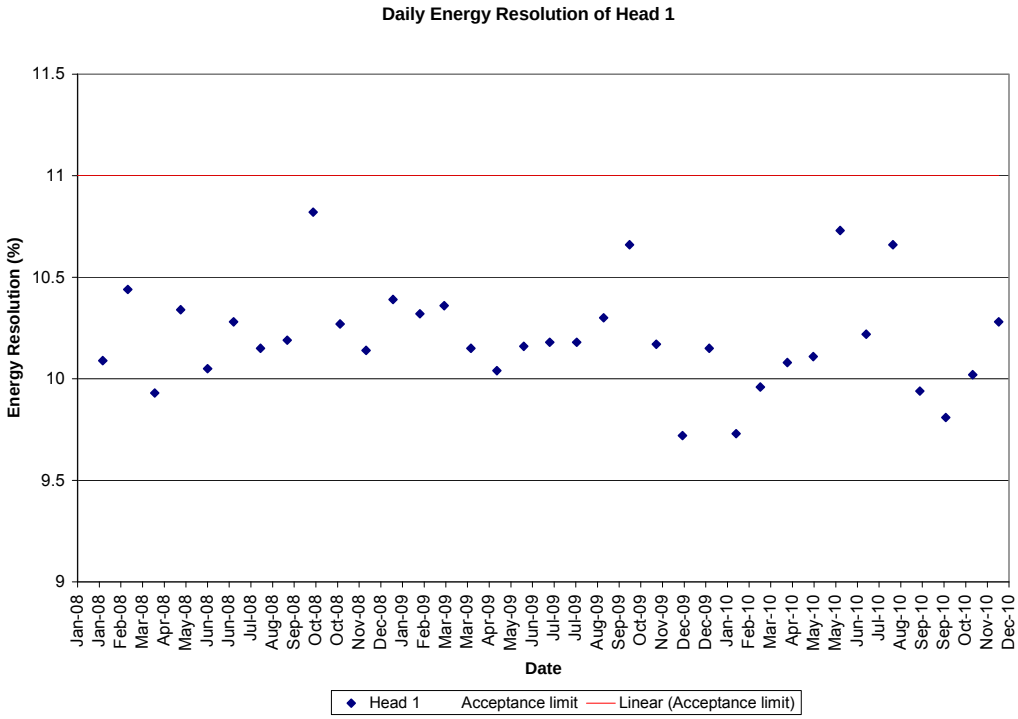

(a)

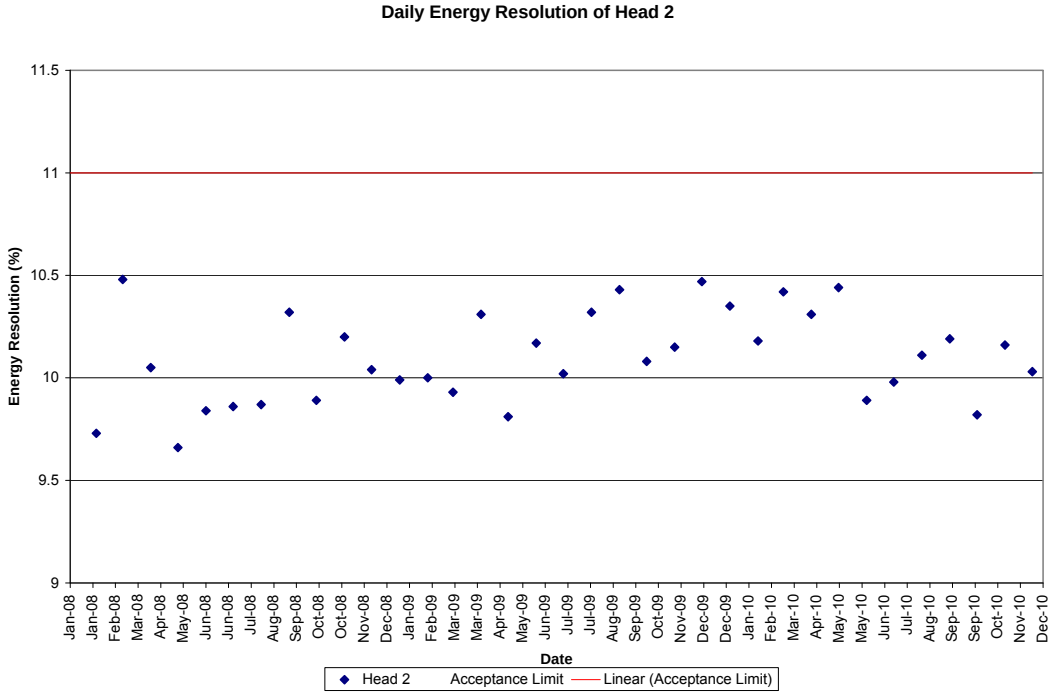

(b)

Fig. 4.3 Daily energy resolution for (a) head 1 and (b) head 2 on the Hawkeye gamma camera.

The results of the annual extended QC tests are shown in Table 4.2 and show that the results were all within manufacturer's specified limits for the duration of the study and showed no degradation in performance from the measured baseline characteristics.

		2008	2009	2010
Intrinsic Uniformity (%)	Head 1	2.87	1.94	2.42
	Head 2	3.33	2.17	1.99
Sensitivity (cps/MBq)	Head 1	68.98± 0.01	68.40± 0.01	72.70± 0.01
	Head 2	69.59± 0.01	68.40± 0.01	72.30± 0.01

Table 4.2 Results of annual extended quality control tests for the Hawkeye gamma camera.

4.2.4 Investigation of change in planar spatial resolution with source-camera separation

To investigate the effect of spatial resolution with distance from the collimated camera face, a capillary line source was filled with ~40 MBq Tc-99m (concentration 100MBq/ml). Acquisitions were carried out with the line source placed centrally on the collimator in the x direction. The distance between the source and the camera head was increased sequentially to 30cm. This was repeated for each camera head and for the line source placed in the y direction. The line spread function was calculated as the FWHM of the profile across the centre of the line source image. The results are shown in Figs. 4.4 to 4.7.

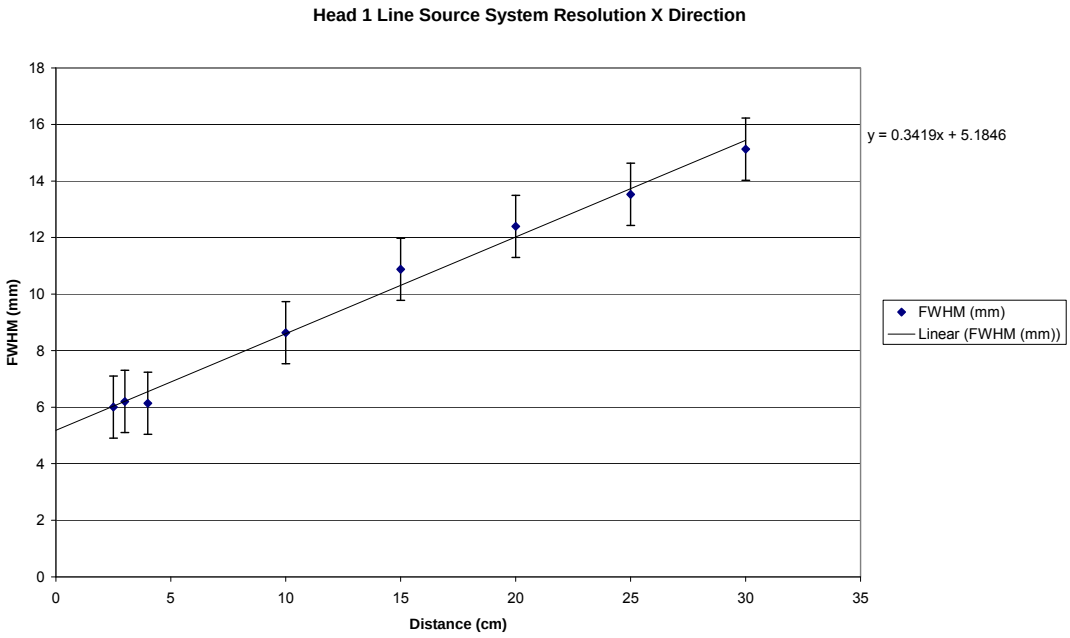

Fig. 4.4 Head 1 line source resolution in air with line source in x direction

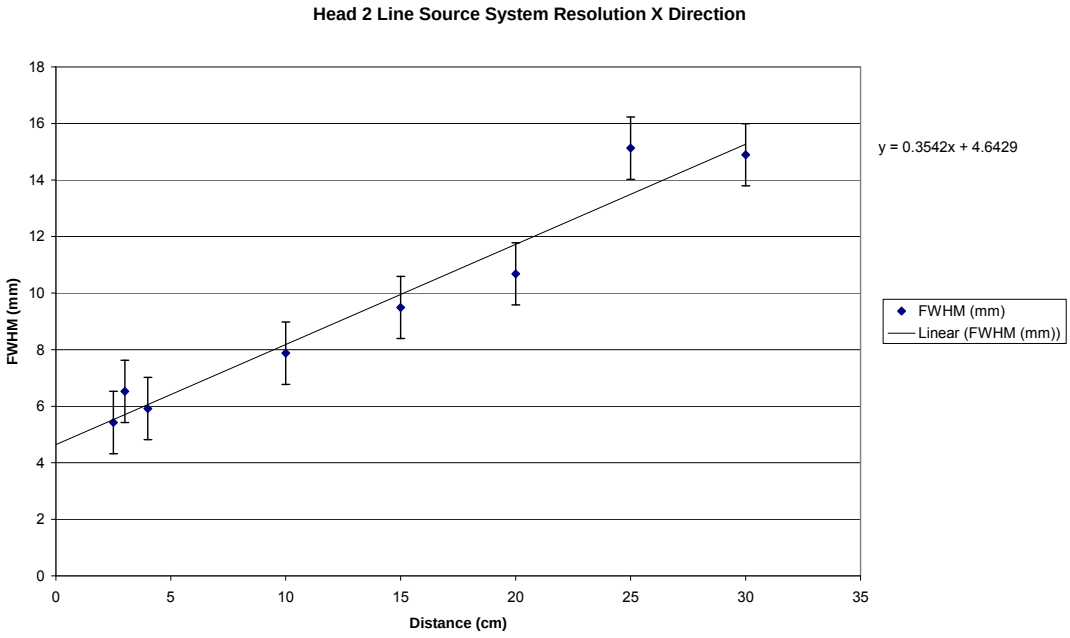

Fig. 4.5 Head 2 line source resolution in air with line source in x direction

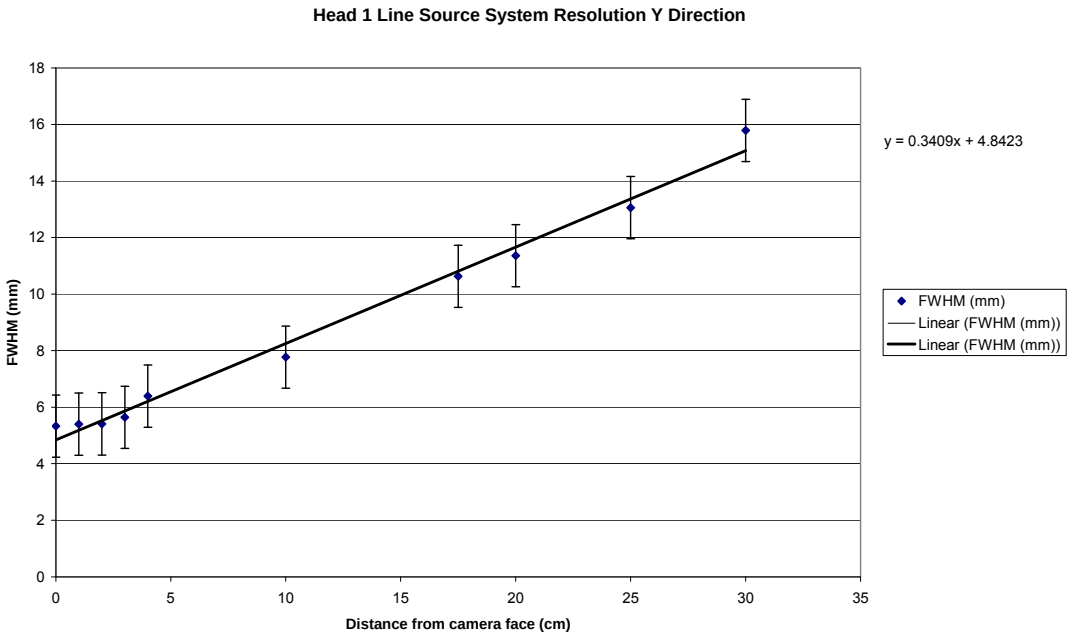

Fig. 4.6 Head 1 line source resolution in air with line source in y direction

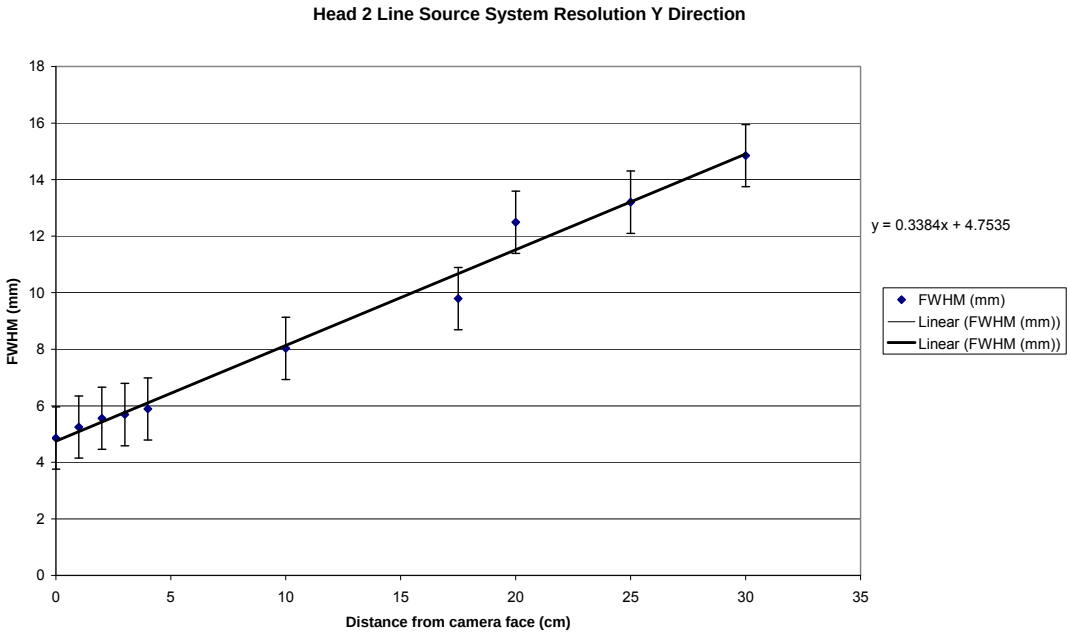

Fig 4.7 Head 2 Line source resolution in air with line source in y direction

The mean spatial resolution at the camera face is 4.9±1.1 mm in the x direction and 4.8±1.1 mm in the y direction. At 10cm from the camera face, the values are 8.3±1.1 mm and 7.9±1.1 mm respectively which correspond

well with the measured baseline values. The relationship between resolution and distance is linear, given by the equations:

$y = 0.35x + 4.97$ x direction

$y = 0.34x + 4.80$ y direction

4.2.5 Conclusion

The planar performance measurements show that the gamma camera was performing at an acceptable and consistent level with respect to image uniformity, energy resolution and camera sensitivity in line with BNMS guidelines (2004), NEMA standards (1980) and manufacturer specifications (GE 2002). The spatial resolution has been shown to vary linearly with distance in air, with FWHM varying at a rate of 0.35 mm/cm in the x direction and 0.34 mm/cm in the y direction.

4.3 CT performance measurements

4.3.1 Method

Performance measurements were carried out on the CT component of the Hawkeye system as part of a routine quality control programme. Quality control tests were carried out using the manufacturer supplied water filled phantom and pre-set acquisition protocols. The phantom incorporates a uniform water section and the following tests patterns:

- A range of water/plastic bar patterns placed diagonally across the phantom. The bar patterns represent spatial frequencies of 2.0, 2.5, 3.0, 3.5 and 4.0 line pairs/cm. as shown in Fig. 4.8

- A slice width gauge consisting of four inclined rows of holes drilled at 63.4 degrees to the horizontal.
- A low contrast resolution test plate, consisting of a thin plastic plate with an image density 2.5% greater than water when imaged with a 10 mm slice thickness. The plate has several holes of different diameter which are filled with water as shown in Fig. 4.9.

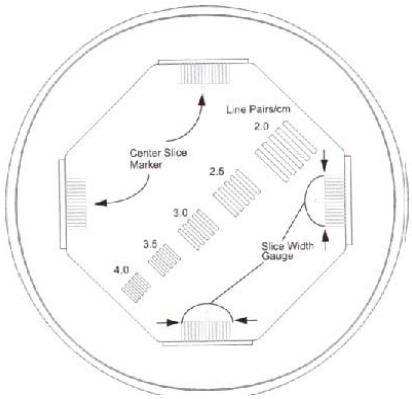

Fig. 4.8 Alignment and resolution section (image GE Medical Systems Training in Partnership)

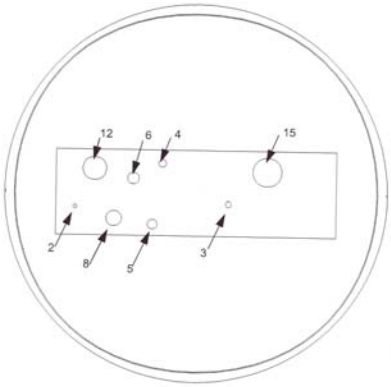

Fig. 4.9 Low contrast section showing hole diameters (mm) (image GE Medical Systems Training in Partnership)

Daily QC tests were carried out by acquiring a single slice in the uniform water section of the phantom and carrying out the X-ray daily QC protocol provided on the workstation. This automatically assigns 6 ROIs to the slice:

centre, top, bottom, right, left and a large ROI covering the whole of the water area, as can be seen in Fig. 4.10. Pixel values were expressed as the CT number plus 1000, so that air has a value of 0 and water 1000. The mean and standard deviation of the pixel values, was found for all of the ROIs and uniformity expressed as the difference between each small ROI average and the average of the large ROI i.e. the whole water slice.

As part of the extended QC program, 3 CT slices were acquired: one in the uniform section, one encompassing the resolution bars and slice width gauges and one encompassing the low contrast test pattern. Analysis was carried out using the Weekly X-ray QC protocol provided on the workstation.

4.3.2 Results

An example of a set of Daily X-ray QC results is shown in Fig 4.10. The quality control tests passed every day during the duration of this study.

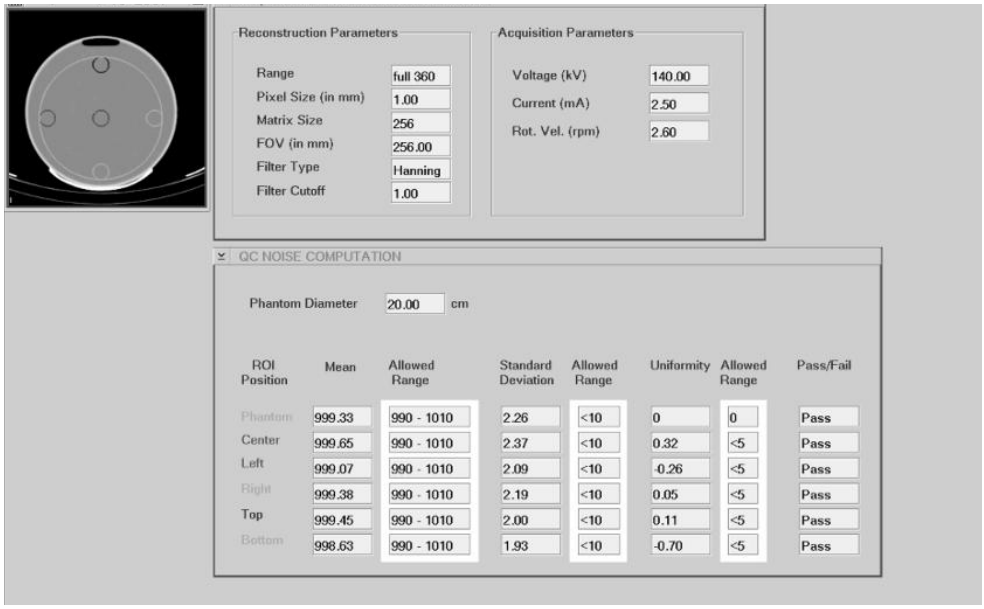

Fig 4.10 Daily X-ray QC results; showing the positions of the ROIs, reconstruction parameters, mean pixel values and uniformity values.

The results show that all of the mean pixel values were within the acceptance range of 990-1010 with a standard deviation <10. All of the uniformity values for the small circular ROIs were within 5% of the uniformity of the large circular ROI.

An example of a set of extended X-ray QC results is shown in Figs. 4.11 to 4.14. The extended tests passed throughout the duration of this study.

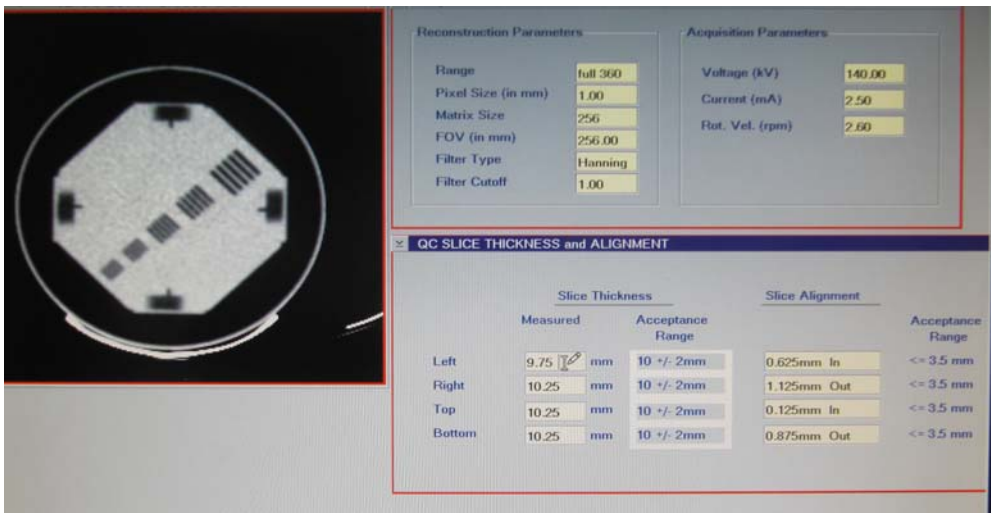

Fig 4.11 X-ray CT slice thickness and alignment results

The left, right, top and bottom slice thicknesses are all within the acceptance range of 10±2 mm and the slice alignment values are all within the acceptance range of ≤3.5 mm.

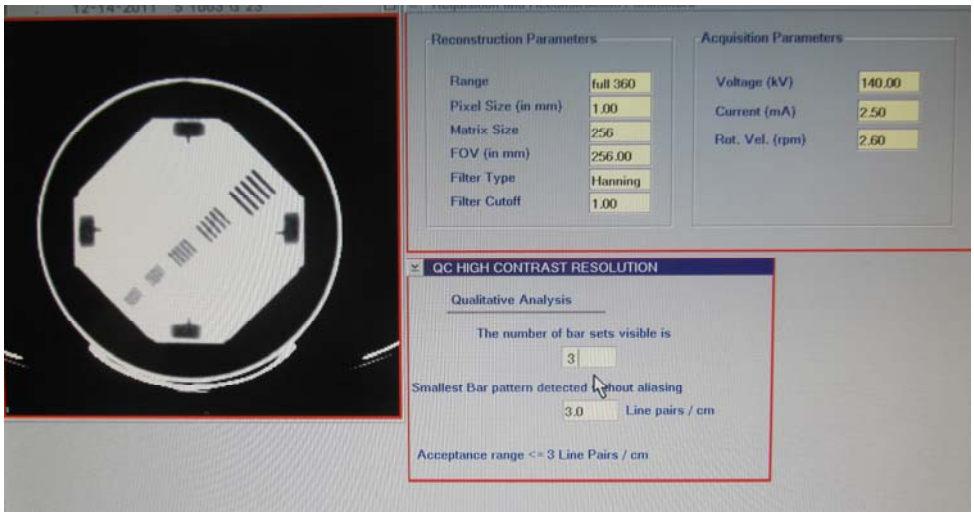

Fig. 4.12 X-ray CT high contrast resolution results

The results show that 3 bar sets can be resolved, which means that the high contrast resolution is 3.0 line pairs/cm which is within the acceptance range of $\leq$ 3 line pairs/cm.

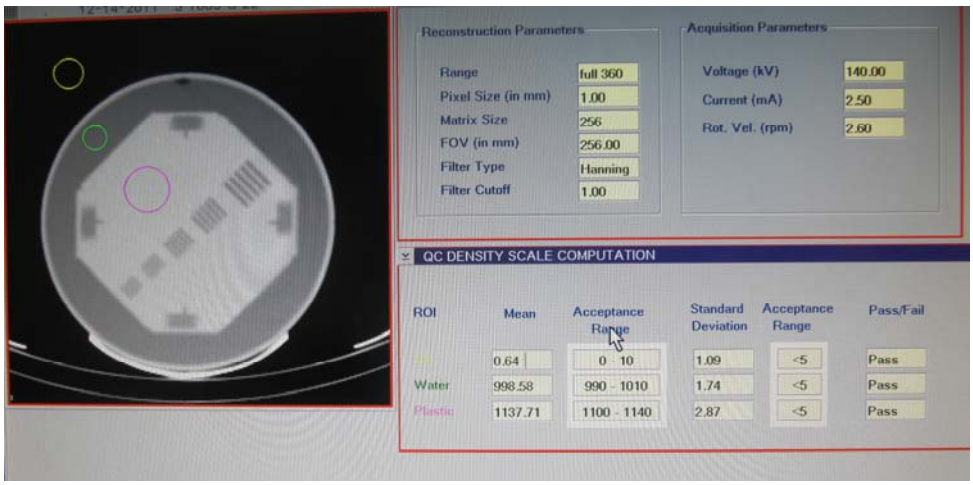

Fig. 4.13 X-ray CT density scale results

The measured CT density for air lies between 0 and 10, that for water between 990 and 1010 and that for plastic between 1100 and 1140.

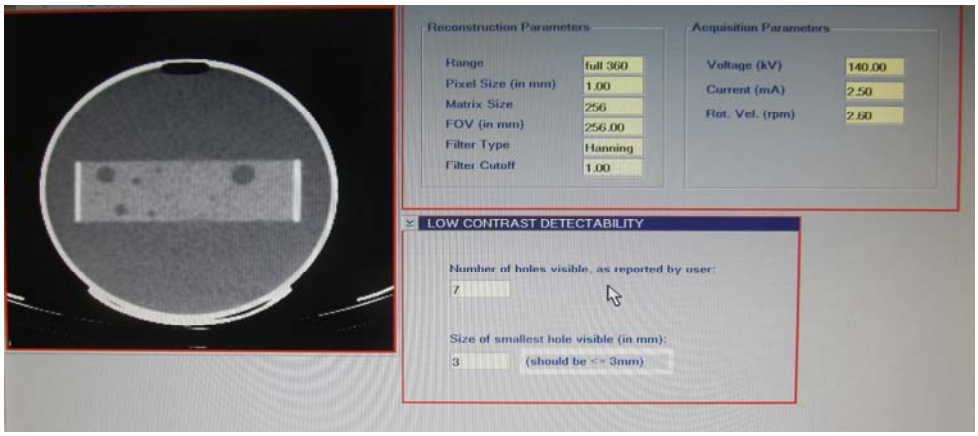

Fig. 4.14 X-ray CT low contrast detectability results

The number of holes that can be detected is 7, corresponding to a diameter of 3 mm which is within the detectability acceptance limit of ≤ 3 mm .

4.3.3 Conclusions

The results of the uniformity, slice width and alignment, high and low contrast and CT density scale results show that the system was operating within the manufacturers specifications for the duration of the study.

4.4 SPECT reconstruction software performance

When a gamma camera and image processing system is used for SPECT imaging, an important part of performance evaluation, is that of the software used for image reconstruction. This is to ensure that quantitative errors are not introduced into SPECT images by the reconstruction process itself. In 2002 the software group of IPEM carried out a nationwide audit of quantitative characteristics of SPECT software using projection data from an

analytically generated software phantom and a measured line source (Jarritt et. al. 2002). The phantom consisted of three structures:

(1) a uniformly filled cylinder labelled region A

(2) a series of active cylindrical rods of various diameters in a background activity with a rod to background ratio of 2:1

(3) a set of three concentric rings of activity in the ratio 1:0:1 labelled H, I and J.

The uniform cylinder had a radius of 56 pixels and height of 42 pixels in a 128×128 matrix. The rods were generated at equi-angular positions around the centre of the simulation at a radial distance of 27 pixels. Counting anti-clockwise from the top centre of the reconstructed axial data, the rods were of radii 0.0, 1.0, 1.5, 3.0, 6.0 and 9.0 pixels. The concentric rings were created by generating a uniform cylinder of radius 56 pixels and height 42 pixels, with an annular defect for which the inner and outer radii were 18 and 36 pixels respectively. The phantom contained no added statistical noise and no attenuation was imposed on the data. The phantom was simulated with projection data at six different count densities as shown in Table 4.3. A single set of projections from a thin line source was also distributed.

SPECT Dataset	Count density
1	0.898
2	1.201
3	2.567
4	4.000
5	5.000
6	8.640

Table 4.3. Count densities of simulated SPECT data sets. The count densities correspond to counts per voxel in a 128×128 matrix, before forward projection.

4.4.1 Method

For evaluation of the reconstruction software supplied on the eNTEGRA workstation, the audit data were reconstructed using;

1. general SPECT FBP software, with and without filters
2. iterative reconstruction Auto OSEM software with no corrections.

The measurements carried out were; mean and standard deviation of counts in the uniform cylinder, maximum counts in each cylindrical rod and mean counts in regions placed within the concentric rings. The positions of the ROIs used for processing are shown in Fig. 4.15. For the line source, the full width at half maximum and peak pixel counts for a profile through the reconstructed line were measured.

The results were then compared with the known true values.

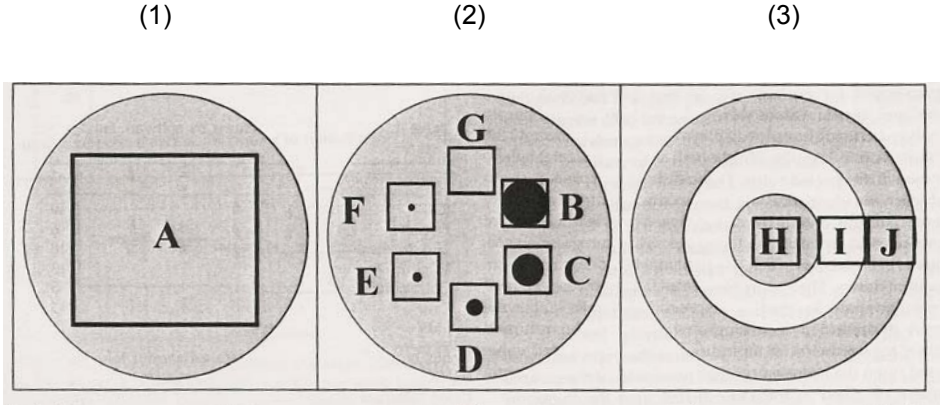

Fig 4.15 Analytical cross section images used to generate projection images for the software phantom, overlaid with region of interest placements required for data analysis.(1) uniform cylinder; (2) hot rods; (3) concentric rings. (Jarritt 2002).

4.4.2 Results

The results of analysing the data are shown below.

4.4.2.1 Uniform cylinder

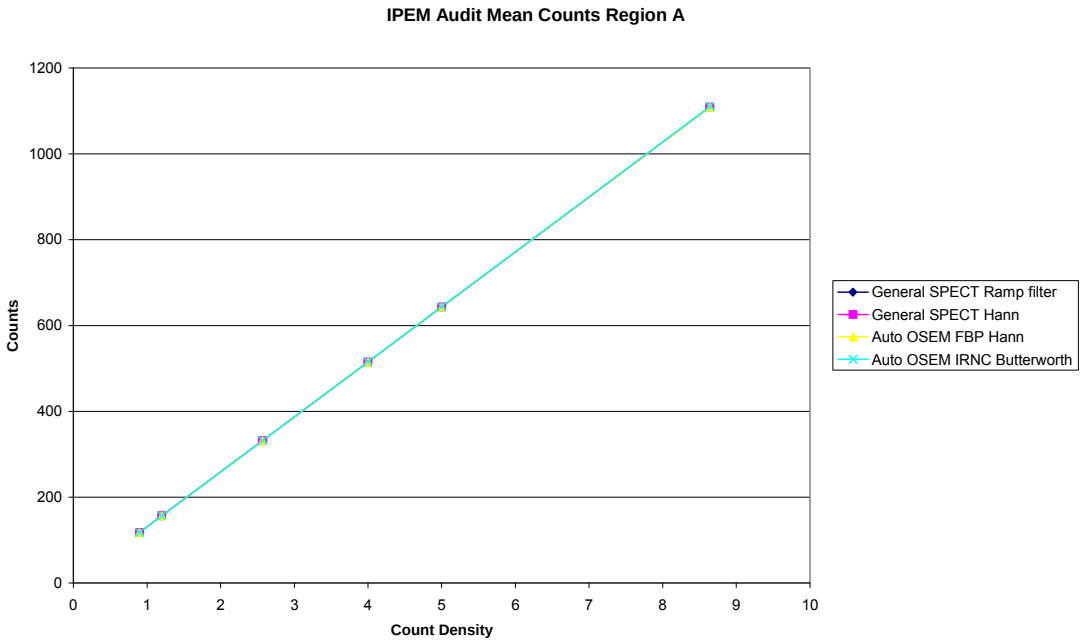

Fig . 4.16 Graph of mean counts in the uniform image against count density for varying reconstruction methods.

The results show that the relationship between count density and reconstructed counts is linear as would be expected for all of the reconstruction methods investigated.

4.4.2.2 Hot rods

When the ratio of rod: background was compared to the true ratio of 2:1, the results showed that all reconstruction methods perform badly for the region of the smallest diameter rod. The ratio fell to 1.5 or below in 19/30 (63%) of cases. This could be due to the partial volume effect giving an underestimation of counts at small volumes.

With General SPECT ramp filter only, the ratio increased above 2.5 in 9/30 (30%) of cases. This occurred in hot rods of all diameters.

The reconstruction method that performed best was Auto OSEM FBP with filter, where the ratio was below 1.5 in 4/6 cases for the smallest diameter rod, but in all other cases was between 1.5 and 2.5.

4.4.2.3 Concentric rings

The true values for the ratios should be 1,0,1. The results shown in Table 4.4 are for the mean ratio values of SPECT data sets 1 to 6.

	H/A	I/A	J/A
General SPECT Ramp Only	1.048	0.035	0.999
General SPECT with Filters	1.047	0.034	1.008
Auto OSEM FBP Ramp Only	1.047	0.034	1.008
Auto OSEM IRNC with Filter	1.039	0.180	0.978
Auto OSEM FBP With Filter	1.047	0.035	1.007

Table 4.4 Mean ratio results for concentric rings

The results show that on average the Auto OSEM IRNC reconstruction method does not get as close to zero for the central ring as the other reconstruction methods do. Therefore the contrast between the rings is poorer. The best contrast is achieved with General SPECT with filters.

4.4.2.4 Spatial resolution with a line source

Using General SPECT ramp filter only, the FWHM was 8.96 mm. This is less than the expected value of 9.5 mm based on the planar resolution of the gamma camera. The published NEMA standard for SPECT resolution is that the reconstructed resolution should be no greater than 110% of the planar value – the assumption being made that the SPECT resolution should not be lower than the planar.

4.4.3 Conclusions

Analysis of the analytically generated SPECT data sets showed that the General SPECT and Auto OSEM SPECT reconstruction packages provided on the eNTEGRA workstation were both able to generate a linear response between projection count density and reconstructed counts, as would be expected. When comparing the reconstruction method alone, with no modelling of attenuation or scatter, the best detection of the rods was achieved with iterative reconstruction. The best contrast between concentric rings was achieved with filtered back projection. This implies that the iterative reconstruction process itself results in images that are smoother or more ‘blurred’ than images resulting from FBP even with the use of filters.

4.5 SPECT performance measurements

Due to its more mechanically complex nature, there is a more stringent requirement for quality control in SPECT imaging than in planar imaging. In addition to the tests outlined in section 4.2.3, a centre of rotation offset measurement was carried out on a regular basis as outlined below. SPECT performance measurements in terms of uniformity and contrast were also carried out using a cylindrical performance phantom and an anthropomorphic phantom as described in sections 4.5.2 and 4.5.3 respectively.

4.5.1 Centre of rotation offsets

4.5.1.1 Method

During SPECT imaging, the detectors rotate about a line in space called the axis of rotation. The reconstruction process assumes that a perpendicular line drawn from a location on the detector equivalent to a parameter called the centre of rotation (COR) should pass through the axis of rotation. The COR is typically set to the X pixel location 32.5 in a 64×64 matrix and 64.5 in a 128×128 matrix. Where the perpendicular line does not pass through the axis of rotation, a COR offset is defined by the separation between them. COR measurements were made by positioning a point source of ~20 MBq Tc-99m in the centre of the field of view, offset by ~15 cm from the axis of rotation. Care was taken that the point source had a volume of no more than 0.1 ml in a 1 ml syringe. As the camera rotates, the point source maps out a sinusoidal curve as given by the function:

$$y = A + B\sin(\theta + \varphi) \quad \text{Eqn 4.4}$$

where A, B and φ are constants and θ is the angle of the detector head (Sharp 2005).

The 'DROT' processing package on the Hawkeye gamma camera measures the displacement A of the sine curve from its expected position in the centre of the matrix in the X and Y directions and plots these displacements as a function of the angle of rotation.

4.5.1.2 Results

A sample set of COR offset measurements is shown in Table 4.5.

	Head1	Head 2
COR offsets	0.18 mm	0.32 mm

Table 4.5 Centre of rotation offset results

All results are well within the acceptance value of ±0.5mm.

A review of COR offset measurements made during the duration of this study, showed that offsets remained within limits at all times as shown in Fig. 4.17.

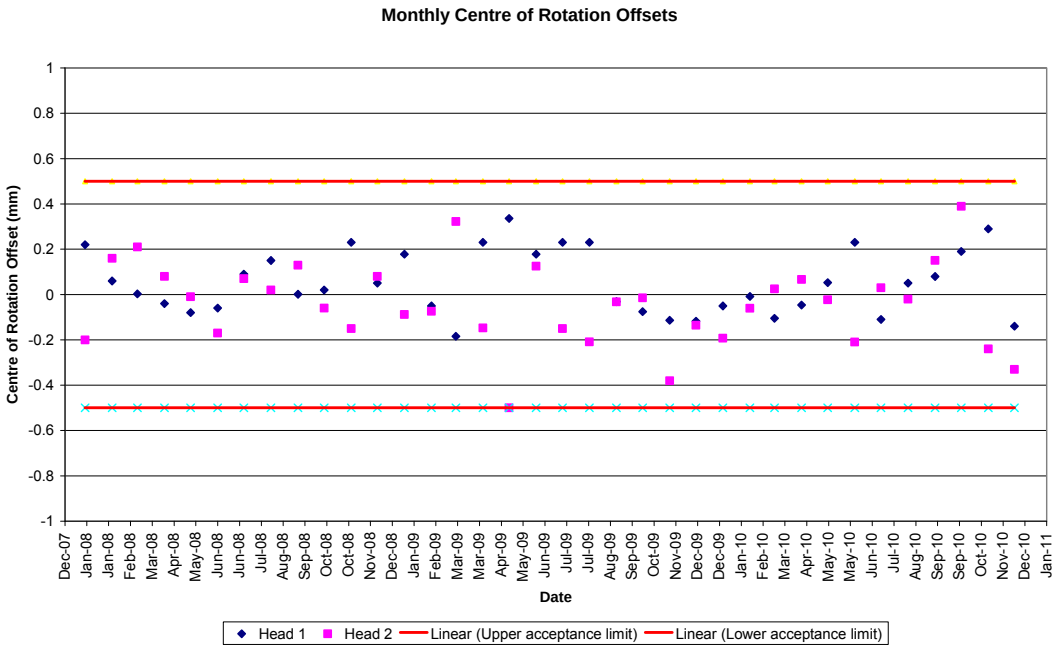

Fig 4.17 Monthly COR offset measurements for the Hawkeye gamma camera

4.5.2 SPECT performance phantom measurements

The phantom used for the establishment of SPECT performance for this study was the Jaszczak SPECT performance phantom (Data Spectrum) as shown in Fig. 4.18.

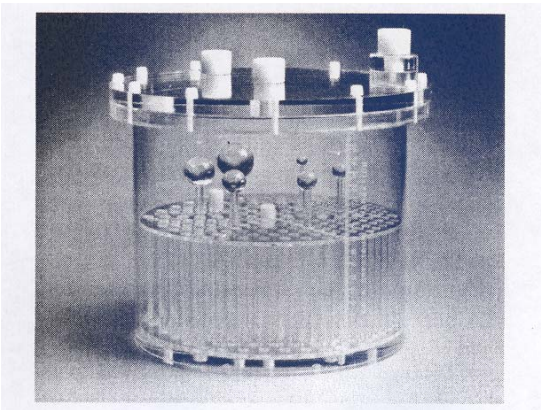

Fig. 4.18 Jaszczak SPECT performance phantom (photograph Data Spectrum)

This is a cylindrical water filled phantom (volume 6.5 litres) which can be used with or without a resolution pattern of rods and spheres of varying volumes. The dimensions are as shown in Fig 4.18.

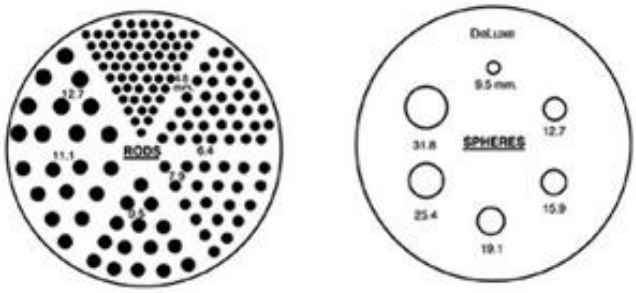

Fig 4.18 Jaszczak phantom rod and sphere inserts (image Data Spectrum)

4.5.2.1 Conservation of counts measurements

Using the Jaszczak phantom with no inserts (i.e. a uniform cylindrical phantom), a series of 12 acquisitions were carried out with activities in the phantom ranging from 94 MBq to 978 MBq corresponding to activity concentrations from 0.01MBq/ml to 0.15 MBq/ml. These concentrations were chosen to mimic those found in clinical practice.

Projection data were reconstructed using the Auto OSEM iterative reconstruction package on the GE eNTEGRA processing system to yield sagittal, coronal and transverse data sets for: filtered back projection (FBP) (default Hann filter), iterative reconstruction with attenuation and scatter correction (IRACSC), iterative reconstruction with no correction (IRNC), iterative reconstruction with attenuation correction (IRAC) and iterative reconstruction with scatter correction (IRSC).

For each reconstruction method, total counts in the reconstructed image were determined from a composite image of the transaxial slices. To investigate the effect of the reconstruction process on projection counts, the projection data (120 frames) were summed to give total projection counts.

4.5.2.2 Effect of FBP filters on conservation of counts

Using the same set of acquisitions as above, the projection data were reconstructed using filtered back projection with a varying filter. The filters used were:

- ramp only
- Butterworth (cut-off 0.25, 0.5, 1.0 power 10)
- Metz (cut-off 1.0, power 3.0)
- Weiner (cut-off 1.0, power 0.1).

The effect of the filter on total counts was found by summing the transaxial slices.

4.5.2.3 Cylindrical phantom uniformity measurements

Using the same set of phantom data, composite images were generated of the uniform cylindrical phantom. Integral uniformity was calculated from a circular region of interest on each composite image using Eqn 4.1. A circle of 24 pixels diameter (80% full diameter) was chosen to avoid edge artefacts. Integral uniformity was also calculated in each case by generating count profiles across each composite image and finding the maximum and minimum count values. Uniformity measurements were repeated 5 times in order to carry out statistical analysis using the Student's t test.

4.5.2.4 Results

The conservation of counts results in Fig. 4.20 show that with an activity less than 475 MBq in the phantom, the relationship between counts and activity is linear as would be expected. Above this activity, the curve becomes a plateau for the IRACSC and IRAC reconstruction methods, indicating count saturation. Compared with the projection data (P) attenuation correction increases counts by a factor of 2.2 with and without scatter correction. This factor remains essentially constant over all activities below the plateau (Fig. 4.21). Filtered back projection with the Hann filter, and iterative reconstruction with scatter correction reduce counts in the reconstructed data by a factor of 1.3. Iterative reconstruction with no corrections reproduces the number of counts in the projection data almost exactly.

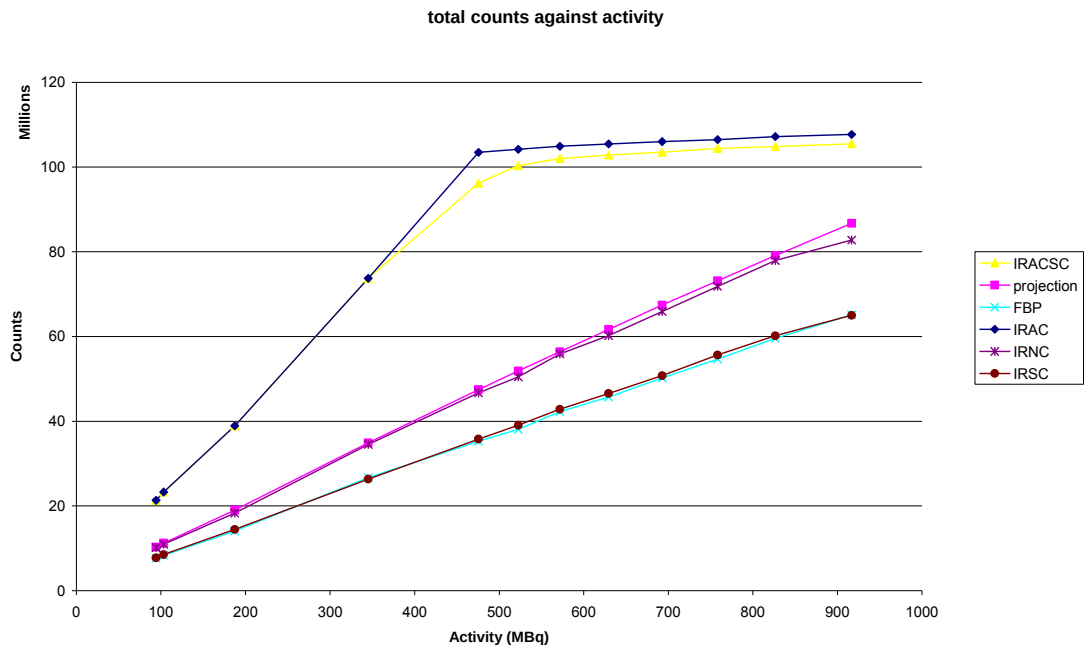

Fig. 4.20 Graph of counts against activity in reconstructed images. Projection counts are shown for comparison.

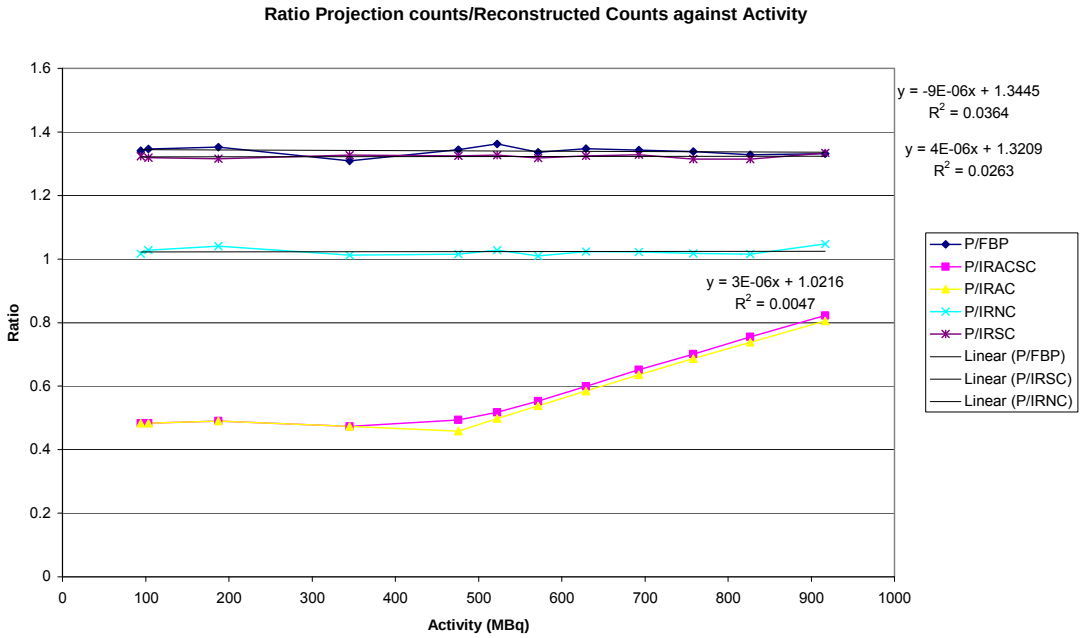

Fig. 4.21 Graph of ratio of projection counts to reconstructed counts against activity.

There is no significant difference between counts in the data reconstructed with the range of Butterworth filters or the ramp filter (Fig. 4.22). This group of filters are also closest to the actual value of the projection reconstructed counts. The Weiner and Hann filter reduce the number of counts by factors of 0.89 and 0.75 respectively.

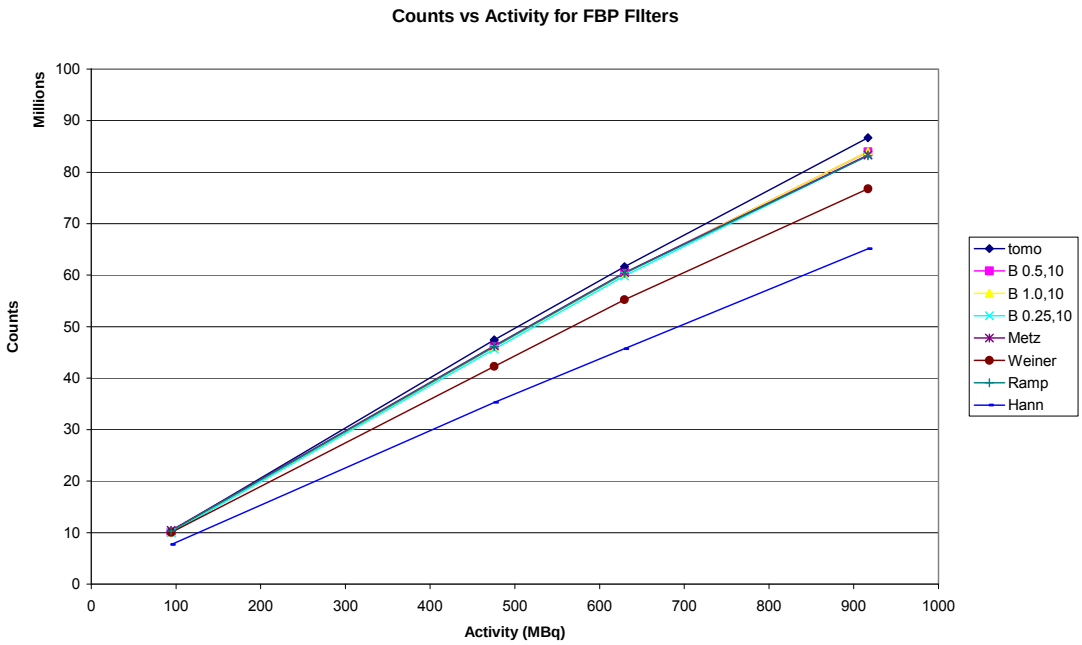

Fig. 4.22 Graph of reconstructed counts against activity for a variety of FBP filters. Summed projection counts are shown for comparison.

The results of the uniformity measurements are shown in Figs. 4.23 and 4.24. With ROI analysis IRAC gives the best uniformity (mean 6.67%). Using the paired samples t test, there is a statistically significant difference between IRNC and FBP ($P<0.001$) with mean uniformities of 21.75% and 26.00% respectively. There is also a statistically significant difference between IRACSC and IRAC ($P<0.001$) with mean uniformities of 9.00% and 6.67% respectively. This suggests that adding scatter correction to attenuation correction does not improve uniformity. The results with profile analysis give the same overall pattern of uniformities, with IRAC giving the best and IRSC giving the poorest uniformity. I consider that the results using ROI analysis are the more reliable, since the profile analysis did not take edge effects into account.

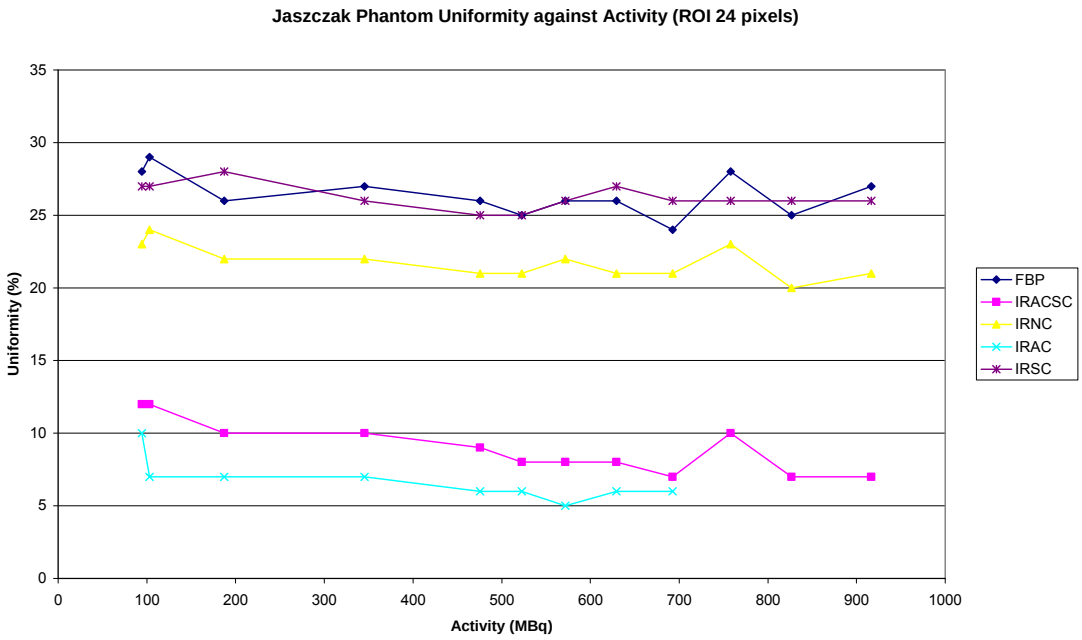

Fig. 4.23. Cylindrical phantom uniformity against activity using circular ROI.

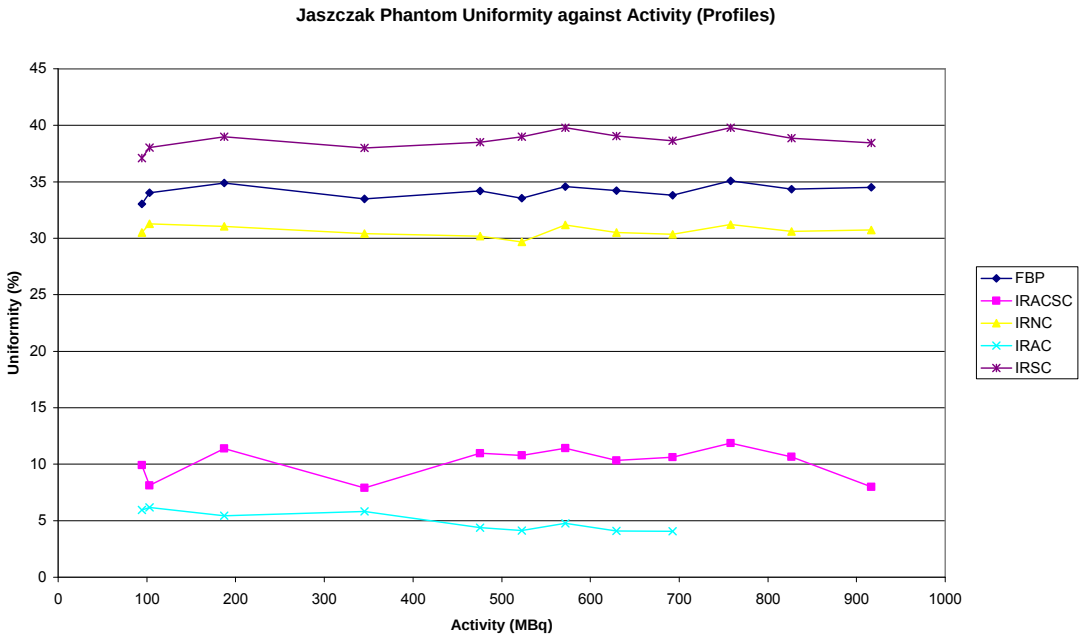

Fig. 4.24 Cylindrical phantom uniformity against activity using profile measurements.

For a cylindrical phantom imaged in air, self attenuation towards the centre of the phantom does significantly degrade uniformity, whereas in the absence of an external scattering medium the effect of scatter on image uniformity is not significant.

4.5.3 Anthropomorphic phantom measurements

4.5.3.1 Method

The anthropomorphic phantom (Data Spectrum) is shown in Fig.4.25. This phantom comprises a large, body shaped cylinder with lung, liver, cardiac and spine inserts. The lung inserts can be filled with polystyrene beads and water to simulate lung density and the liver insert can be individually filled so that background/liver activity ratios can be varied. The cardiac insert can also be filled individually, and additional inserts used to model cardiac defects.

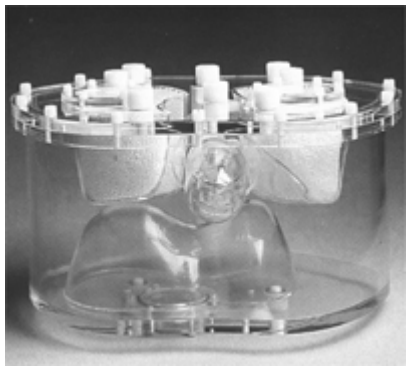

Fig. 4.25 The anthropomorphic phantom. (photograph Data Spectrum)

For these measurements, the cardiac insert was filled with 23 MBq Tc-99m with no activity in liver or background. This activity was chosen to be of a similar order of magnitude to the activity in the myocardium during clinical myocardial perfusion imaging. A SPECT acquisition was carried out and images were reconstructed using FBP, IRNC, IRSC, IRAC and IRACSC as previously. A cardiac processing package on the eNTEGRA was used to generate the following slices:

- horizontal long axis (HLA)
- vertical long axis (VLA)
- short axis (SA).

Bull's eye maps (BEM) (Garcia et.al. 1985) were generated from the SA slices (using in-house software) and used to assess uniformity. A bull's eye map is a method of displaying all of the data from the short axis slices in one image. Each short axis slice was assumed to be annular in shape, so that the counts in each slice could be analysed radially. Thirty radii at 6° intervals were analysed and maximum count circumferential profiles generated and formed into a circular annulus. Starting with the apical slice, each of the generated annuli had an increasing radius so that they all fitted together concentrically with the apex in the middle and the data from the basal slice at the outer edge. The derivation of bull's eye maps is shown diagrammatically in Fig. 4.26.

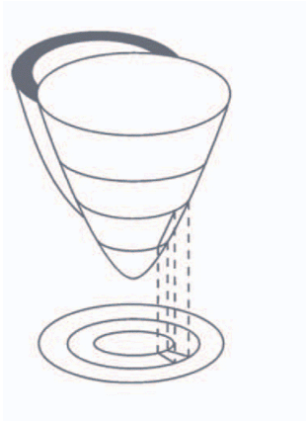

Fig. 4.26 Derivation of the bull's eye map based on the maximum radial values obtained from each short axis slice. The data are then plotted circumferential for each slice starting with the apex data at the centre.

In order to investigate contrast in the images, regions of interest were drawn over the wall and cavity of the cardiac short axis slices and contrast was calculated using the expression:

Contrast = (wall counts – cavity counts)/ wall counts Eqn 4.3

4.5.3.2 Results

The results of bull's eye map uniformity and short axis wall to cavity contrast measurements are shown in Tables 4.6 and 4.7.

	Uniformity %
FBP	30.31± 5.49
IRNC	29.68± 5.44
IRSC	32.17± 5.75
IRAC	15.30± 2.19
IRACSC	15.74± 2.52

Table 4.6 Bull's eye map uniformity results

	Contrast %
FBP	72.23± 10.53
IRNC	59.57± 11.56
IRSC	68.37± 10.77
IRAC	58.51± 2.50
IRACSC	64.99± 2.93

Table 4.7 Short axis wall to cavity contrast results

4.5.3.3 Conclusion

For a cylindrical phantom imaged in air, attenuation correction increased counts in reconstructed images and provided the best uniformity results of the reconstruction methods investigated (an approximate 20% improvement on FBP). For the cardiac phantom bull's eye maps (BEM), uniformity was also best with IRAC.

Scatter correction reduced the counts in the reconstructed data as would be expected. In the absence of an external scattering medium scatter correction was not found to improve uniformity, which may be due to the lower counts giving poorer count statistics. Where no corrections were applied, iterative reconstruction was found to generate more uniform images than filtered back projection. For both Jaszczak and cardiac phantom, the order of uniformity values can be summarised as follows (a lower value indicates better uniformity):

IRAC < IRACSC < IRNC < FBP <IRSC.

For contrast measurements on the short axis cardiac phantom scatter correction was the most significant correction. The contrast with FBP was

better than any of the iterative reconstruction data sets. The iterative techniques benefit image uniformity, but there is a slight trade off with respect to image contrast.

4.6 Discussion

These preliminary results have shown that both the hardware and software components of the Hawkeye gamma camera system used for this study were operating within national and local guidelines and performance remained consistent throughout the study.

The SPECT performance phantom measurements showed that below an activity concentration of 0.07 MBq/ml, attenuation correction increased counts in the reconstructed images by a factor of 2.2 (increase of 120%) compared with the projection data, where-as scatter correction reduced counts by a factor of 1.3 (reduction of 23%).

Attenuation correction alone provided the best uniformity results, with an approximate 20% improvement over FBP. Scatter correction alone offered no improvement in uniformity compared with FBP and in conjunction with attenuation correction gave poorer uniformity results than AC alone.

The anthropomorphic phantom measurements showed that AC alone gave the best uniformity results for the bull's eye maps of the cardiac insert, with an approximate 15% improvement over FBP. Scatter correction as with the Jaszczak phantom, offered no improvement in uniformity but gave the best

results for contrast, with an improvement of approximately 4% over FBP and 10% over IRAC.

These relative impacts of the applied corrections agree largely with data published by El Fahkri et al. (2000) who investigated bull's eye map (BEM) uniformity and contrast between the left ventricular wall and cavity using both simulated data sets and real cardiac phantom data. In their study scatter correction was performed using: Jaszczak subtraction, the triple energy window method and a spectral factor analysis method. Attenuation correction was performed using a Chang correction combined with FBP and transmission imaging using a Gd-153 line source combined with an iterative reconstruction. Uniformity of the bull's eye map was calculated by dividing each BEM into 9 regions. The calculated activity in each region was then normalised to the maximum value and a uniformity index was defined as the mean of these normalised values. Using this method, the ideal uniformity index is 100%. Contrast was calculated between two 3 dimensional volumes of interest (VOIs) drawn inside the LV wall and cavity. The mean number of counts $mean_1$ and $mean_2$ were calculated and the contrast expressed as $100\times(mean_1-mean_2)/(mean_1+mean_2)$. Using this method the ideal contrast is also 100%. The results showed that attenuation correction was the major correction effecting BEM uniformity: uniformity was 78% with FBP compared with 88% with Chang corrections and 89% with Gd-153 corrections i.e. a maximum improvement of 11%. Scatter correction alone significantly improved contrast from 60% with no corrections to 68% or 69% with scatter correction.

In contrast to the results of this study, El Fahkri found a small but systematic improvement of BEM uniformity when scatter correction was combined with attenuation correction compared with attenuation correction alone. This difference could be due to the different methodologies employed in these studies, in particular the method for calculation of uniformity. In this study uniformity was calculated by effectively using counts from just two pixels in the BEM (max and min) whereas El Fahkri used values from 9 segments to give a more globally representative value.

In summary, attenuation correction added counts globally to reconstructed images, resulting in a significant improvement in uniformity. Scatter correction reduced counts in reconstructed images, which is probably the cause of its small but significant degrading of uniformity values. Scatter correction improved contrast, which would imply that the use of this correction is successful in removing scattered and therefore mispositioned counts from background areas such as the myocardial cavity modelled in this study. I therefore conclude that for the most accurate quantitative results in terms of uniformity and contrast in any clinical application, attenuation and scatter correction should be used together.

Chapter 5

Validation of Method

5.1 Introduction

Subsequent to the initial baseline characteristics of the imaging system being established, it was necessary to determine and validate the experimental set-up to be used for both relative and absolute quantitative measurements in later stages of this study. The experimental set-up in question was a phantom based approach, using two plastic bottles placed inside the cylindrical Jaszczak phantom (with inserts removed) to model organs within the body. Two volumes of bottles were investigated referred to as ‘source A’ and ‘source B’. The bottles were cylindrical with volumes of 50 ml (diameter 33.6 mm, height 56.4 mm) and 100 ml (diameter 43.0 mm, height 68.9 mm) respectively without the neck of the bottle accounted for, and 56 ml and 112 ml respectively with the neck of the bottle included. These volumes were chosen to mimic the volumes of the paediatric and adult kidneys for renal studies. For an imaging system with a FWHM of 12 mm at 20 cm, both sources were large enough to avoid partial volume effects. This simple phantom based approach was similar to that used by Shcherbin et al. (2008) who used two cylindrical bottles (diameter 26 mm, height 60 mm, volume 32 ml each) placed inside an anthropomorphic phantom (Data Spectrum) to model oncological tumours.

Decisions to be made about this set-up included:

- suitability of the use of a positioning jig for the phantom
- determination of regions of interest (ROIs) on the reconstructed image

- establishment of errors to include the systematic and random errors inherent in the study
- determination of the rotational orientation to position the phantom during later measurements.

This chapter describes the measurements carried out in this validation process.

5.2 Use of positioning jig

For many of the measurements to be undertaken, in this study, the cylindrical Jaszczak phantom (Data Spectrum) was chosen, as described in chapter 4. For the purposes of this study, the resolution rods and spheres were removed from the phantom to give a uniform cylindrical phantom. This has a 'lip' (Fig 5.1) where the lid is attached to the body of the cylinder of depth 18 mm. In order to lie the phantom flat on the imaging couch in a reproducible position during acquisitions, there were two alternatives;

i) use a specially constructed jig to position the phantom on
ii) position the phantom slightly over the edge of the scanning couch, secured with a strap.

The jig was constructed of polyethylene 8.5 mm thick. These two alternatives are shown in Figs 5.1 and 5.2. SPECT acquisitions were carried out in both of these configurations to ascertain whether the inevitable attenuation caused by the jig itself, would have any effect on quantitative measurements carried out and whether this would contra-indicate its use as a positioning aid for the rest of the study.

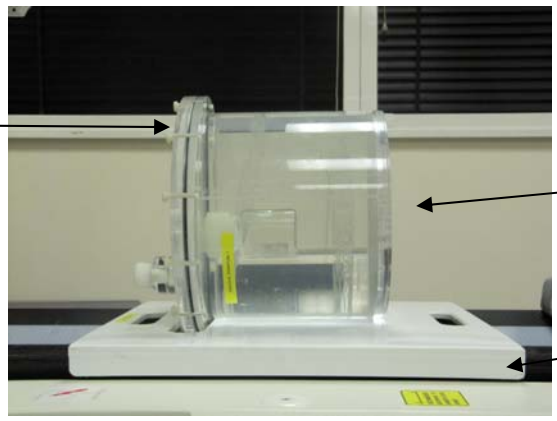

Fig 5.1 Position of cylindrical phantom with jig

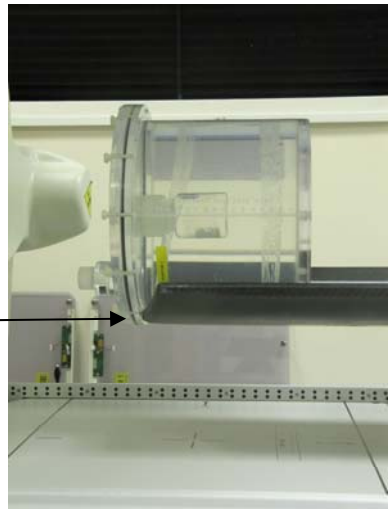

Fig 5.2 Position of cylindrical phantom without jig (strap not shown)

5.2.1 Method

In order to determine the most appropriate method of positioning the phantom, SPECT acquisitions of different phantom configurations were taken with and with out the jig. These were:

a) source A (56ml) only in the centre of the uniform cylindrical phantom

b) source B (112 ml) only in the center of the uniform cylindrical phantom

c) uniform cylindrical phantom only.

In all cases, acquisitions were carried out using autocontouring to keep the heads of the detector as close as possible to the object. This resulted in an elliptical orbit of maximum radius 20.8 cm and minimum radius 11.6cm. Based on measurements in chapter 4, an activity of approximately 180 MBq was used in the cylindrical phantom to avoid count saturation occurring with attenuation corrected reconstructions. This gave an activity concentration of approximately 0.03 MBq/ ml. For sources A and B an activity concentration of approximately 0.1 MBq / ml was used, resulting in activities of approximately 5.6 and 11.2 MBq respectively. The choice of activity concentration was based on the work of Yani et al. (2005).

All geometries were acquired using H mode acquisition into a 128×128 matrix with frame time 30s and zoom 1. Data for scatter correction were acquired using a ±10% energy window centered at 122 keV and a CT transmission image for use as an attenuation map was acquired immediately after the emission images. Tomographic slices were reconstructed using OSEM iterative reconstruction, resulting in FBP, IRNC, IRSC, IRAC and IRACSC data sets. These acquisition parameters were set as the standard parameters to be used for the remainder of the study, and are summarised in Table 5.1.

Camera set up	H mode
Matrix	128 ×128
Frame time	30s
Zoom	1.0
Reconstruction	OSEM 2 iterations 16 sub sets
Data sets	FBP, IRNC, IRSC, IRAC, IRACSC

Table 5.1 Standard SPECT acquisition parameters

Effective volumes of interest were generated by summing the slices containing the source of activity i.e. the 'hot object' and generating a region of interest (ROI) on the summed image in the transverse, sagittal and coronal reconstruction planes. For the phantom and source images, the ROI was drawn as a circle or rectangle just large enough to include the entire visible image. Results were expressed as counts per second per MBq, using an effective acquisition time of 3600 seconds.

Planar posterior acquisitions were then acquired of the cylindrical phantom with and without the jig in place in order to calculate the attenuation due to the jig. Counts were acquired for 300s into a 128×128 matrix. The camera heads were brought in as close as possible to the phantom for these measurements.

5.2.2 Results

The results of determining cps/MBq for sources A and B and the cylindrical phantom with and without the jig are shown in Figs 5.3 to 5.5. In all cases, results for the transaxial (Trans) sagittal (Sag) and coronal (Cor) reconstruction planes are shown for each of the five reconstruction data sets under consideration.

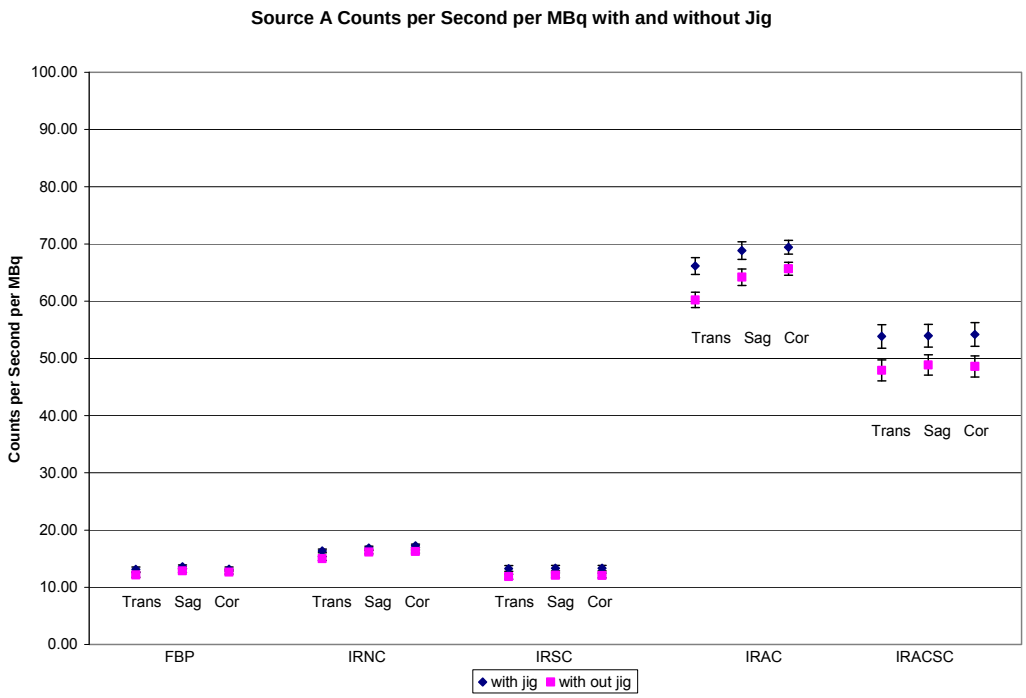

Fig 5.3 Source A counts per second per MBq with and with out jig

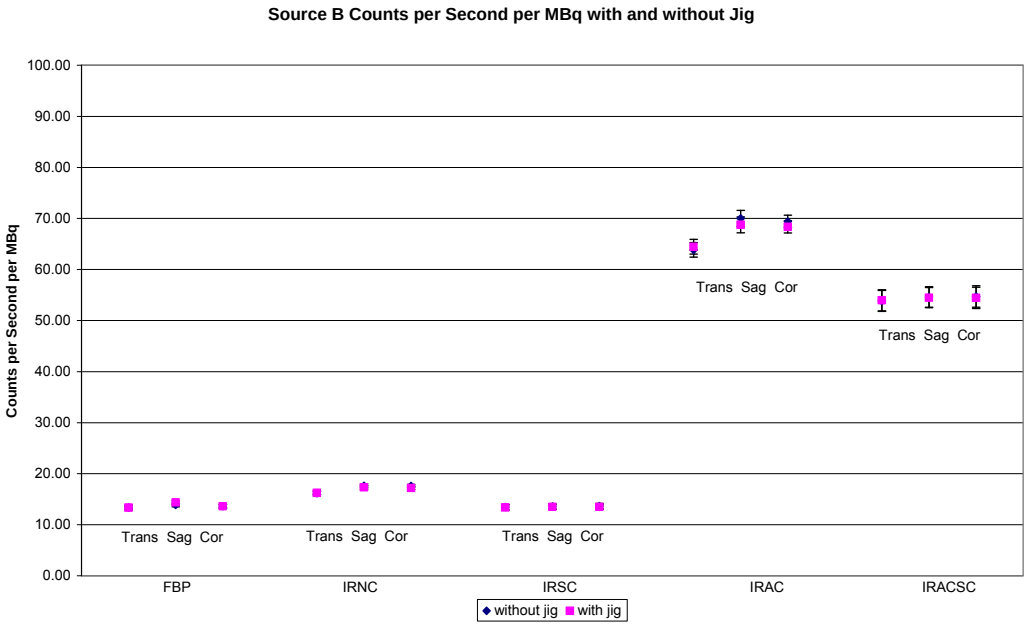

Fig 5.4 Source B counts per second per MBq with and with out jig.

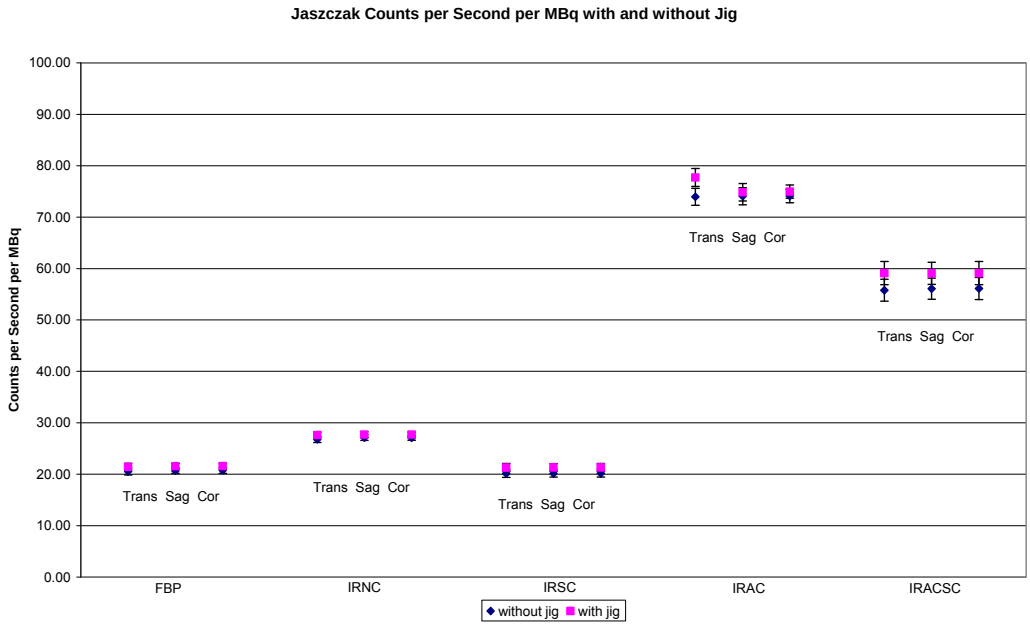

Fig 5.5 Cylindrical phantom counts per second per MBq with and without jig.

When acquiring and reviewing the images of the phantom with the jig in place, it was evident that the effect of the jig was visible on the raw projection data as a reduction in counts on half of the projection images as shown in Fig 5.6. However, the graphs of cps/MBq with and without the jig for the reconstructed images show that the results are within the error range of each other. (The error bars for these graphs of results were added retrospectively after the assessment of errors performed in section 5.4)

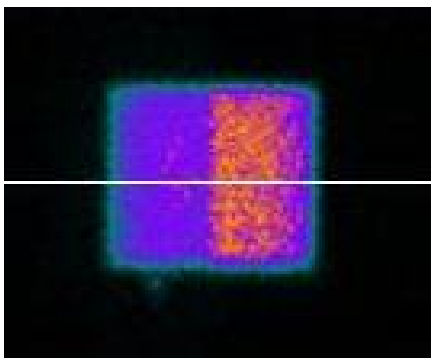

Fig 5.6 Projection image of cylindrical phantom showing the influence of the positioning jig.

The results of acquiring posterior planar images with and without the jig are as shown in Table 5.2

	With Jig	Without Jig
Counts per Second/ MBq	25.02	27.79
Difference (cps/MBq)	2.77	

Table 5.2 Results of cps/MBq Measurements with and without jig for posterior planar images.

Using the equation for linear attenuation:

$$A = A_0 e^{-\mu t} \quad \text{Eqn 5.1}$$

where A is counts, A_0 is original counts, μ is the linear attenuation coefficient and t is the thickness of material, the attenuation factor due to the jig ($e^{-\mu t}$) was calculated as 0.9. From these measurements, the linear attenuation coefficient of the polyethylene is 0.12 cm^{-1} which agrees well with the published figure of 0.14 cm^{-1} (NISTR 1996) These results show that only 90% of the true count rate reaches the posterior head of the gamma camera in the 180° position, where the effect will be greatest. It can be inferred that the jig will have some attenuation effect on the posterior head for all angles of acquisition excluding the true laterals. Although the SPECT acquisition results showed that overall this effect is not significant in SPECT once reconstruction has taken place, it was decided to acquire all future results without the jig present in order to exclude this potential for uncertainty.

5.3 Establishment of Region of Interest (ROI)

In order to record counts from the 'hot objects' on the reconstructed images in a reliable way, with all of the relevant counts included, it was necessary to establish a reliable, consistent and reproducible method of drawing regions of interest around these objects. This was particularly pertinent in this study, since the ease with which the edge of the object could be defined, varied with the reconstruction method chosen. The shape of the bottles used as sources also meant that the narrow neck of the bottle which contained activity and therefore needed to be incorporated, was sometimes difficult to discern. An accurate and reproducible method of establishing ROIs has been recognised as an important step in accurate quantitation of activity and volume. Scherbinin et al. (2008) used a method of applying 3D threshold values to reconstructed SPECT images based on the maximum average over eight voxels in the volume of interest (VOI). The total activity was measured by integrating all counts inside the VOI determined by a threshold set at a level of 1%. In this way, all the counts from a given object were included. In clinical situations however, it is recognised that fixed thresholds cannot account for the variety of situations in which organs and tumours with different sizes and activities are surrounded by other tissues containing different levels of background activity (Grimes et al. 2012). Adaptive thresholding techniques have therefore been devised where a threshold is chosen that takes into account source-to-background ratio (SBR) of activity concentrations. Grimes et al. (2012) developed an iterative adaptive thresholding technique, where a semi-automatic background region was generated to allow reproducible and reliable measurements of

the SBR and hence the threshold for generation of the VOI. By applying this method they found that in phantom experiments source volumes and activities agreed with the true values to within 4%.

For ease of application in this phantom study, where only two volumes of cylindrical sources were to be considered in a fixed geometry, advanced adaptive thresholding techniques were not considered necessary. The choices considered were therefore:

(1) drawing a manual region of interest

(2) using the auto-contour method offered by the eNTEGRA workstation (GE Medical Systems).

The latter method finds the edge of an object by identifying pixel values a certain percentage of the maximum pixel count within the frame.

5.3.1 Method

The manual region was drawn as a circular region on the transaxial images and as a rectangular region on the sagittal and coronal images just large enough to encompass all of the cylindrical source image (including the neck of the source) such that the minimum count in the ROI fell to zero. In this way it could be guaranteed that all of the counts in the image were included. A size of ROI was established on the IRACSC images, where the edges were easiest to determine manually, and this region was applied to all subsequent images for all reconstruction methods.

5.3.2 Results

The results of using the autocontour function are shown in Table 5.3 and indicate that even for the 10% contour, when compared with the rectangular, manually drawn ROI, the number of counts in each region is slightly underestimated. For a contour set to less than 10%, the system failed to define the edge of the object.

	Auto-Contour			
	10%	15%	20%	25%
FBP				
Trans	98.43	97.00	95.53	92.80
Sag	97.36	96.04	95.47	93.04
Cor	97.17	96.17	95.02	93.01
IRNC				
Trans	96.02	92.68	88.99	87.08
Sag	96.11	93.51	90.47	87.98
Cor	94.95	92.48	89.23	87.21
IRSC				
Trans	96.40	98.60	97.47	95.21
Sag	98.18	97.60	96.11	94.71
Cor	98.54	97.87	96.30	94.46
IRAC				
Trans	96.00	92.67	89.76	87.41
Sag	96.42	93.70	90.27	88.87
Cor	93.62	91.46	88.02	86.85
IRACSC				
Trans	97.52	95.34	93.64	91.54
Sag	97.26	95.75	94.25	91.41
Cor	97.38	96.16	95.06	99.75

Table 5.3 Establishment of ROI. Results expressed as percentage of counts in manually drawn region

Visually, the autocontour method identified the edges of the image of the main body of each source correctly, but was prone to error and inconsistency with the narrow neck of the bottle as can be seen in Fig 5.7 For this reason it was decided to use the simpler manually drawn region of interest method for the remainder of this study. Errors inherent in this approach are considered within the error analysis in section 5.4

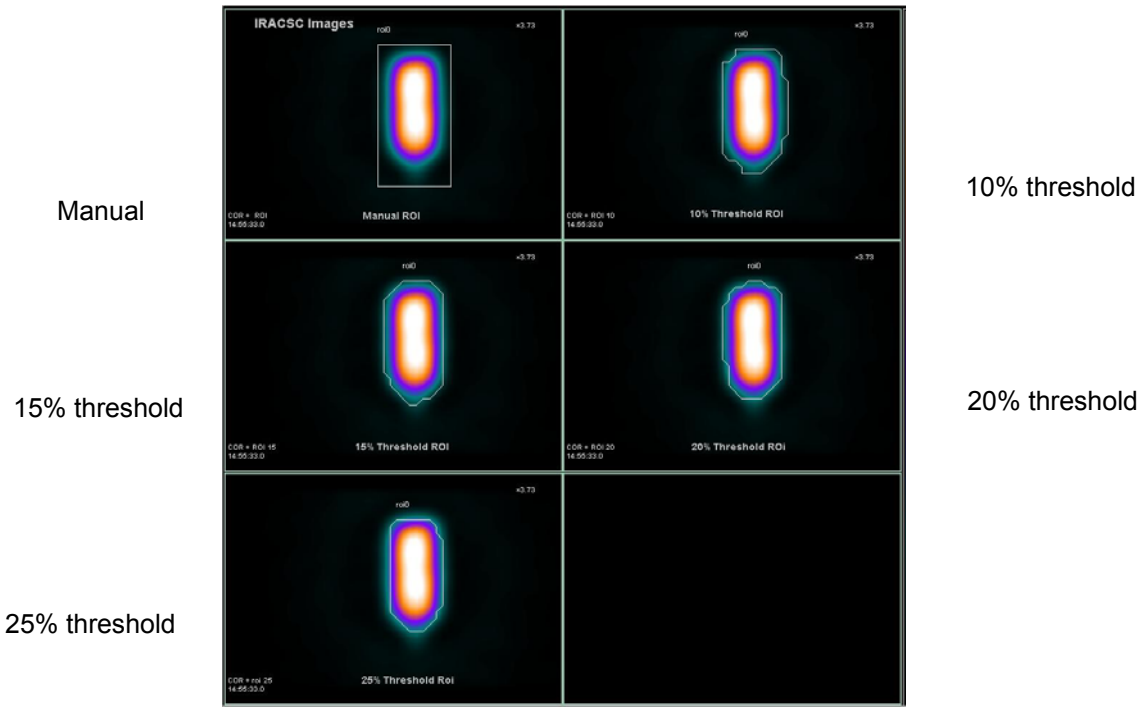

Fig 5.7 Regions of Interest drawn on IRACSC images. The neck of the bottle is to the bottom of each image.

5. 4 Repeat measurements for error analysis

The potential sources of error when carrying out these acquisitions arise at all stages of the process. Principal areas of potential error are;

- measuring the activity in the radionuclide calibrator
- measuring volumes within the phantoms
- accurate filling of the phantoms
- positioning of phantoms on the scanning couch
- drawing reproducible regions of interest on reconstructed images.

For measurement of activity, a Capintec CRC 15-R radionuclide calibrator was used (Capintec Inc. NJ). This is an ionisation chamber, calibrated annually against a secondary standard calibrator (Fidelis), which is in turn

directly traceable to the primary standard calibrator at the National Physical laboratory (NPL). The Fidelis calibrator has been specifically designed to meet the requirements of the NPL Measurement Good Practice Guide No. 93 (Gadd, Baker et al. 2006) . The annual calibration results (using standard activities from NPL) have shown that all readings on the local calibrator are all within ±2% of the secondary standard, which is in turn within ±2% of the primary standard. A repeat set of 20 measurements on the local calibrator showed that the standard deviation was equivalent to a percentage error of 1.14%. Throughout this study, all activities were measured in standard 1ml or 2 ml syringes, held in a jig within the calibrator to minimise errors due to spatial positioning and residues remaining in the syringe once the activity had been used were measured and accounted for.

The volumes of the phantoms and filling of the phantoms were measured using standard laboratory equipment.

Positioning the phantom on the scanning couch and positioning the ROIs on the reconstructed images were both carried out manually. For this reason these are seen as the principal sources of error within this study and as sources of random error are difficult to quantify. It was therefore decided to use a percentage error approach to defining the errors in this study.

5.4.1 Method

Error analysis for this study was carried out by carrying out repeat measurements for the case of Source A only in the cylindrical phantom, with the entire process from measurement of activity to final image processing repeated. The standard error of these measurements was then found and expressed as a percentage of the measured counts. Error bars were added to graphs as ±2 SEM.

5.4.2 Results

The results of carrying out repeat measurements for establishment of percentage errors are shown in Table 5.4

		Mean of 5 measurements (cps/MBq)	2* Standard Error	2SEM as % of mean cps/MBq
FBP	Transverse	12.63	0.41	3.25
	Sagittal	13.16	0.32	2.46
	Coronal	12.98	0.36	2.74
IRNC	Transverse	15.32	0.34	2.20
	Sagittal	16.51	0.33	2.01
	Coronal	16.41	0.28	1.69
IRSC	Transverse	12.52	0.46	3.71
	Sagittal	12.67	0.44	3.46
	Coronal	12.63	0.44	3.50
IRAC	Transverse	61.61	1.37	2.23
	Sagittal	65.69	1.47	2.24
	Coronal	66.10	1.15	1.73
IRACSC	Transverse	50.39	1.93	3.83
	Sagittal	51.04	1.86	3.65
	Coronal	51.06	1.96	3.83

Table 5.4 Establishment of errors

The results show that despite the manual processes inherent in this methodology, the percentage errors in the final values expressed in terms of cps/MBq range between 1.69% and 3.83% which were felt to be acceptable levels of error for this study.

5.5 Determination of rotational orientation

To enable relative quantitation measurements to be made at a later point in this study, more than one source was to be inserted into the cylindrical phantom. It follows that either one or both source inserts would need to be positioned towards the edge of the cylindrical phantom, rather than the centre. It was therefore necessary to establish whether the orientational positioning of the phantom on the scanning couch had an effect on the results and to establish which orientation should be used for further measurements.

5.5.1 Method

Further to the initial quantitation measurements that were made using the cylindrical phantom and single source inserts, the phantom was modified such that sources of volumes 56 ml (A) or 112 ml (B) could be inserted in central position 1 or symmetrically to each side of the centre in positions 2 or 3 as shown in Fig 5.8.

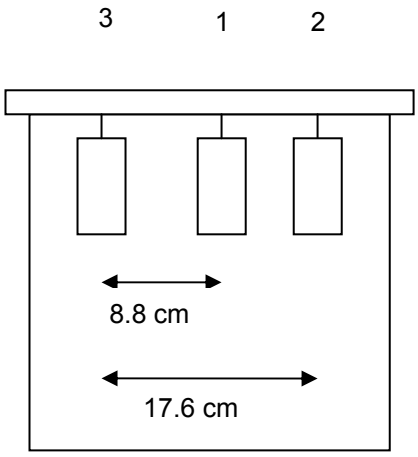

Fig. 5.8 Cylindrical phantom with inserts in central or edge positions.

For the first set of measurements, source A was imaged in positions 2 and 3 shown in Fig 5.8 in a range of rotational orientations as shown in Fig 5.9 to establish whether quantitation has a positional dependence within the transverse plane, for the symmetrical case.

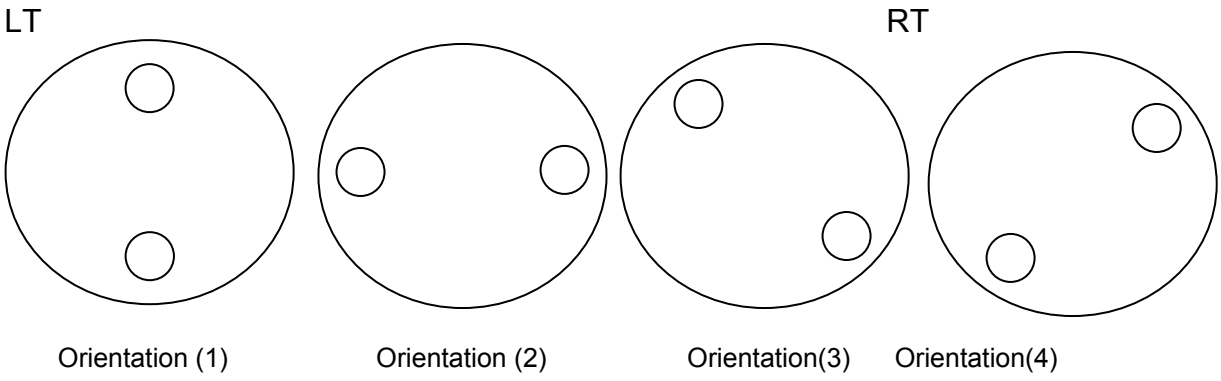

Fig. 5.9 Transverse view of orientations of source A for the symmetrical phantom

For all SPECT acquisitions, the standard acquisition and reconstruction parameters were used as in Table 5.1. To avoid count saturation, an approximate concentration of 0.1 MBq per ml was used in each of the sources resulting in an activity of approximately 5.6 MBq. In all cases an

equal activity was used in each source, such that the true ratio of activities was 1:1 and no activity was present in the background.

Planar acquisitions were also carried out on this set of measurements. With the camera in H mode, anterior and posterior images were acquired for 300s into a 128×128 matrix. Background corrected counts were obtained from ROIs drawn on the anterior and posterior images and used to calculate anterior, posterior and the geometric mean of absolute and relative cps/MBq.

Measurements were then carried out for symmetrical orientation (2) ie. a horizontal orientation, where the ratio of activities in the two sources was changed such that the ratio was 2:1. With the phantom in the same orientation, Source B (112 ml) was then placed in the edge position 3. The activity concentration in Source B was ~0.1 MBq/ml resulting in an activity of ~11 MBq. Finally, with Source A in both positions, the activity concentration of the background was increased from zero to 0.005 MBq/ml. For all experimental arrangements planar images were also acquired as described above. All SPECT results were expressed in terms of (1) cps/MBq, (2) the ratio of cps/MBq in the two sources and (3) deviation from the expected activity, for FBP, IRNC, IRSC, IRAC and IRACSC reconstruction groups in the appropriate orthogonal planes.

The phantom was then modified such that source A was in positions 1 and 2 simultaneously. Once again a range of acquisitions were carried out, with the phantom at different rotational positions as shown in Fig 5.10.

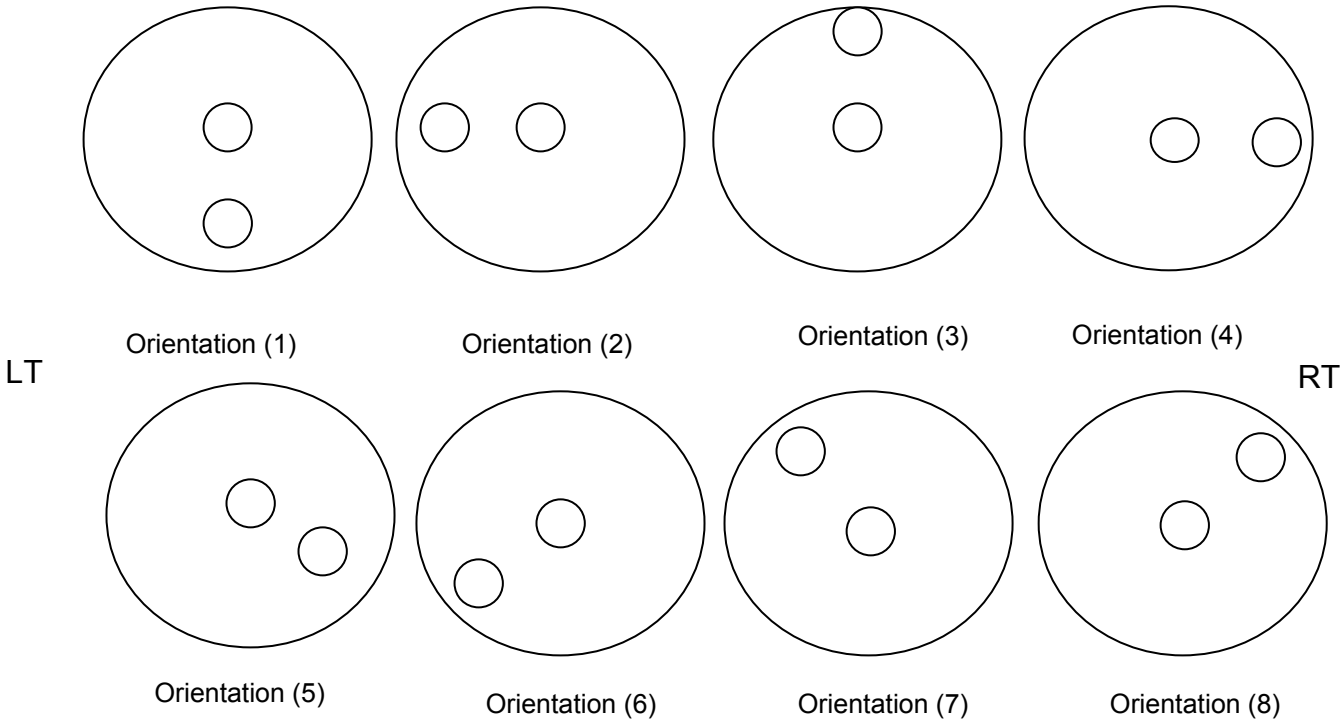

Fig. 5.10 Transverse view of orientations of source A for the non-symmetrical phantom

The set of experiments described above for the symmetrical case was repeated, with all ratios being expressed as counts at the edge;counts at the centre. For the change in activity concentration experiment, the higher activity concentration was positioned in the edge position and for the change in source volume experiment, source B was placed in the edge position. The results were expressed in the same way as the symmetrical results.

5.5.2 Results – Symmetrical phantom

The results in cps/MBq of varying the orientation of the edge source between symmetrical orientations 1 and 4 are shown in Figs 5.11 to 5.14.

Orientation (1)

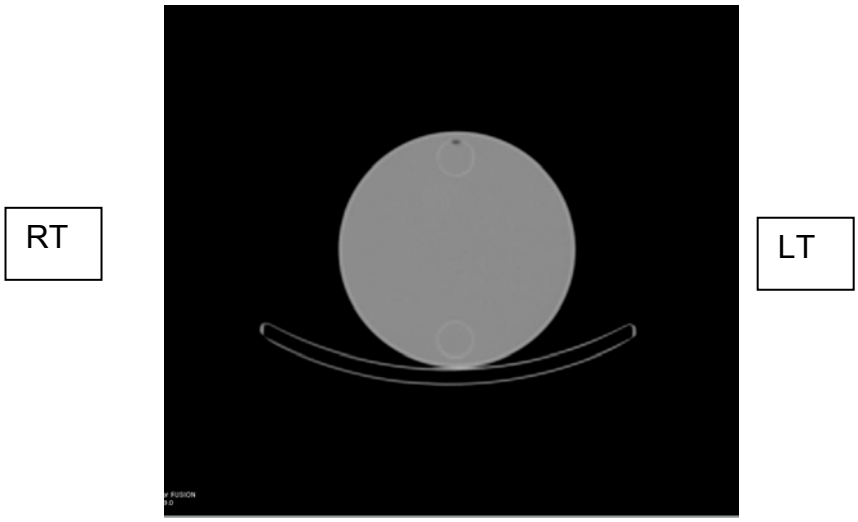

a)

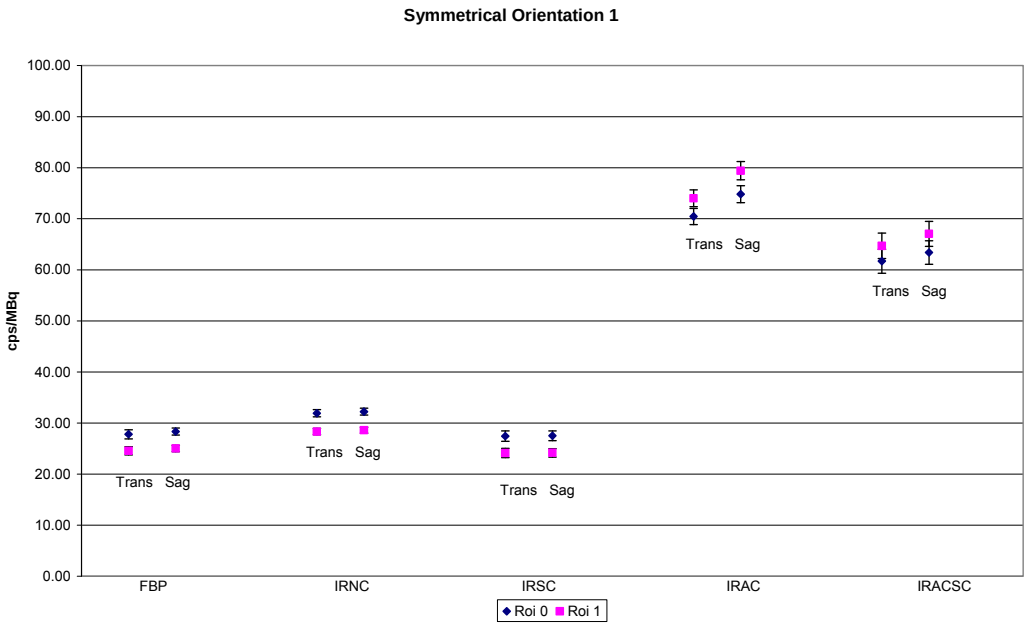

b)

Fig 5.11 a) CT image showing orientation of sources b) cps/MBq for sources in Orientation (1)

Orientation (2)

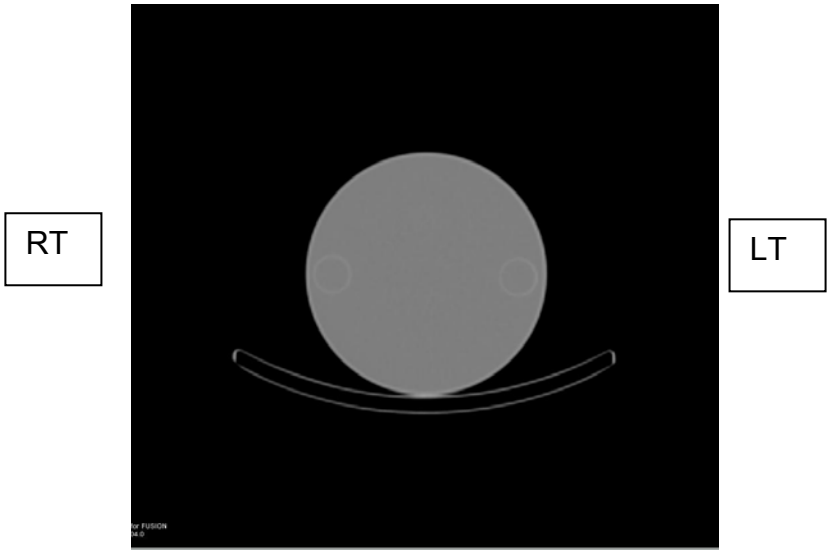

a)

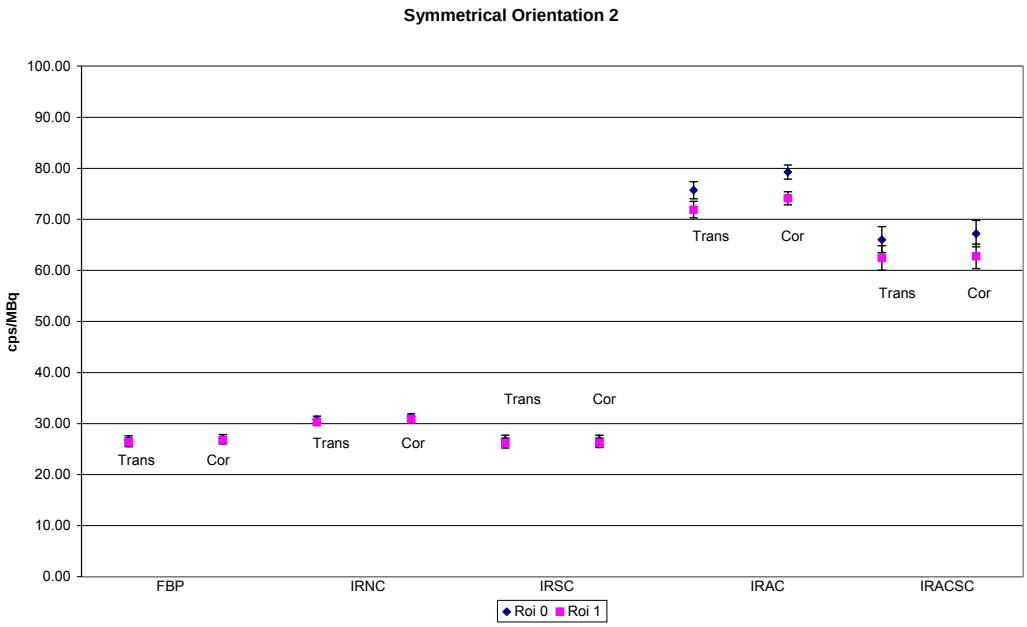

b)

Fig 5.12 a) CT image showing orientation of sources b) cps/MBq for sources in Orientation 2

Orientation (3)

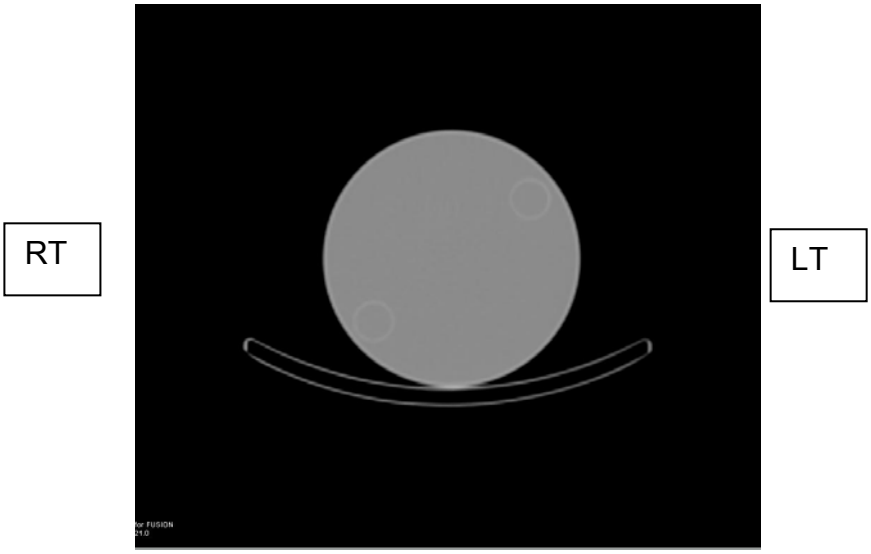

a)

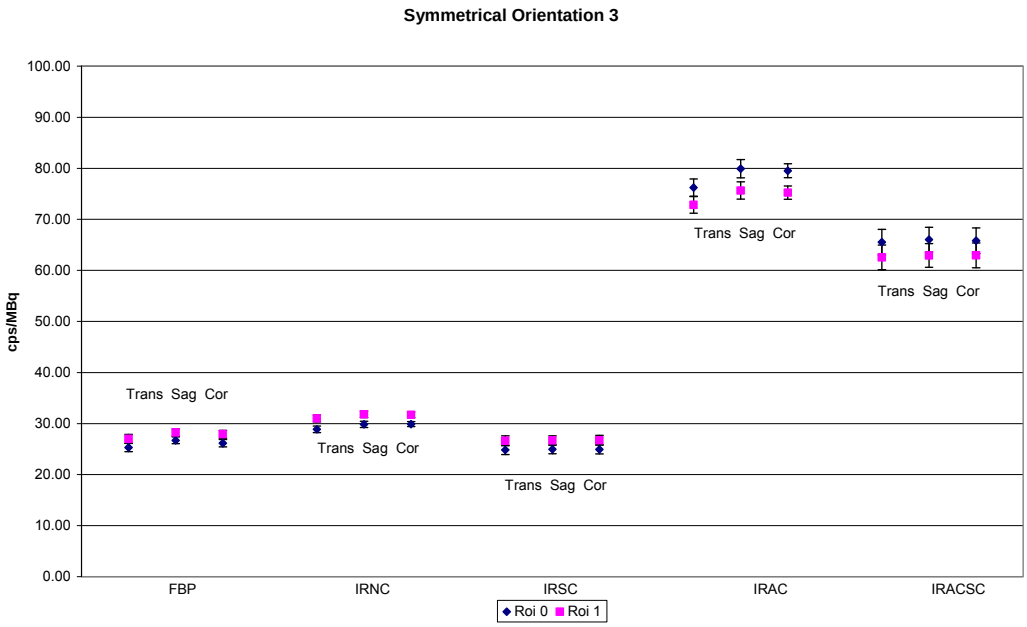

b)

Fig 5.13 a) CT image showing orientation of sources b)cps/MBq for sources in Orientation 3

Orientation (4)

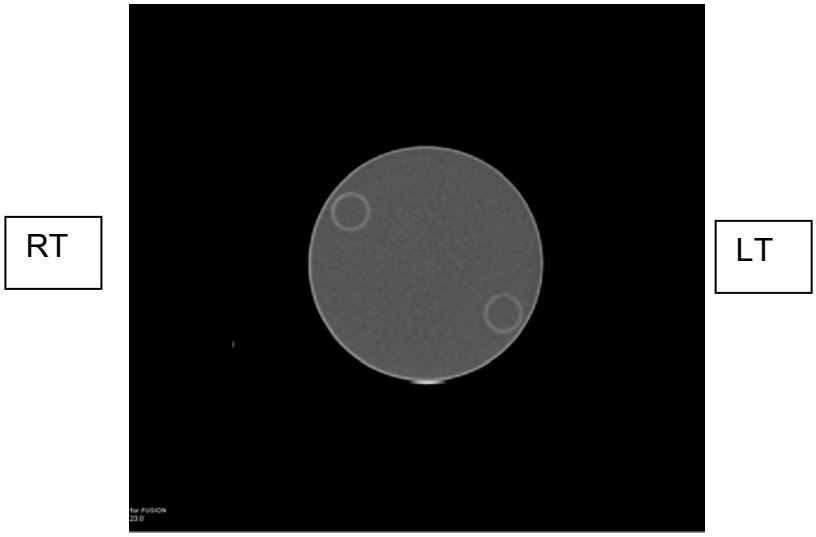

a)

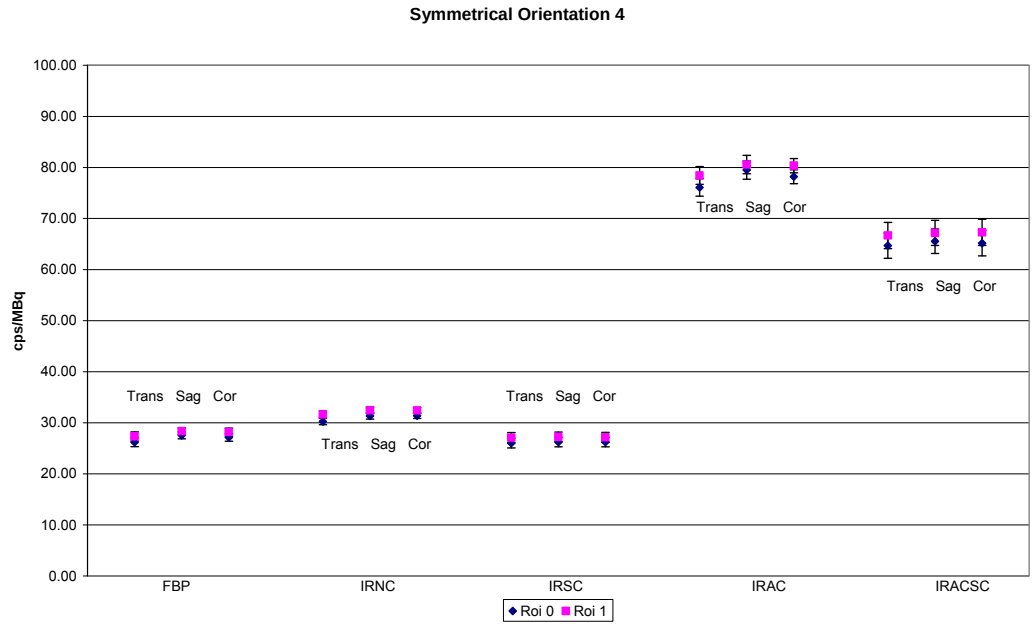

b)

Fig 5.14 a) CT image showing orientation of sources b) cps/MBq for sources in Orientation (4)

The results of finding the ratio of cps/MBq between ROI1 and ROI0 are shown in Fig 5.15.

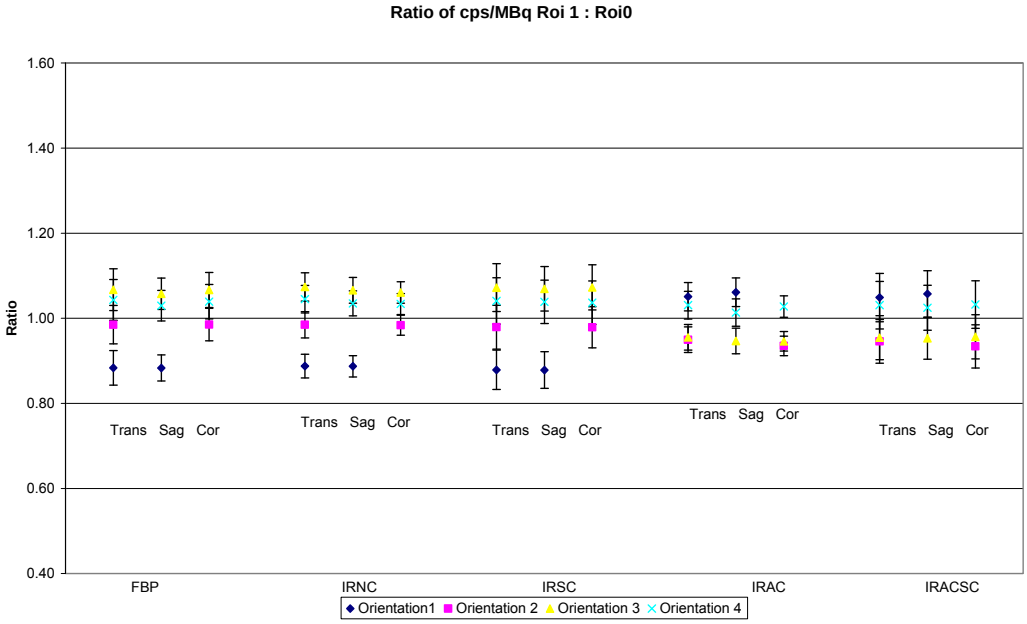

Fig 5.15 Ratio of cps/MBq ROI 1: ROI 0 (edge:centre)

A ratio close to 1.0 is found in all cases, with the horizontal orientation (orientation 2) achieving the most accurate results in the non attenuation corrected cases. This could be due to the attenuation correction magnifying the effect of a slight error in positioning the phantom.

The effect of the rotational orientation is summarised for the transaxial reconstruction plane in Fig 5.16. Note that the results are expressed here as a function of the angle of rotation, with the 0 degree position being taken as the 12 o'clock position (orientation 1 as shown in Fig 5.9).

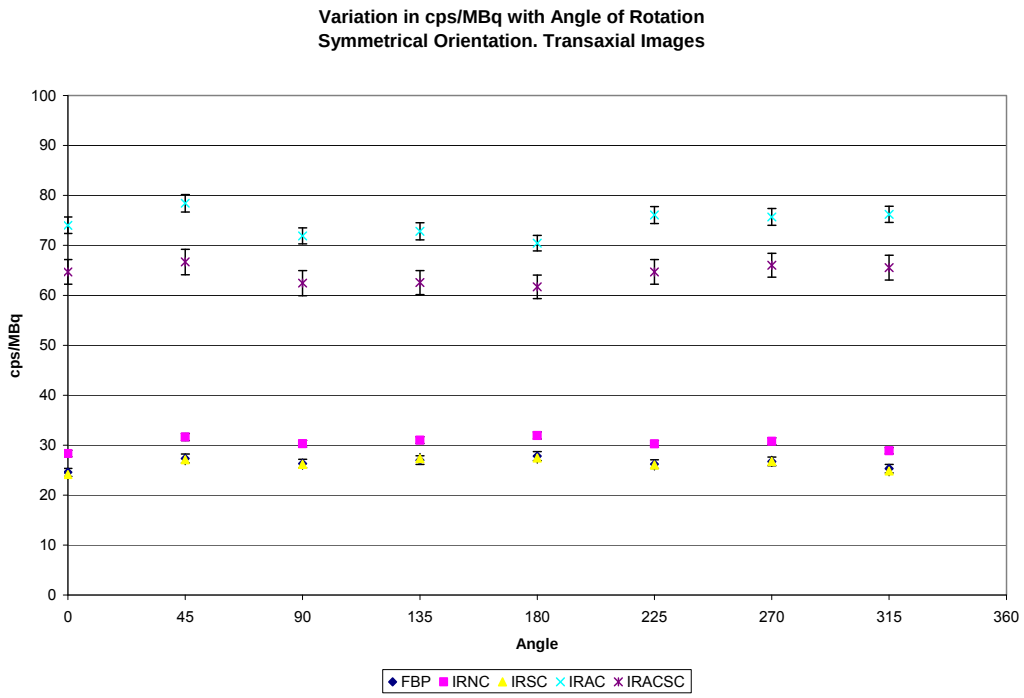

Fig 5.16 Variation in cps/MBq with orientation on transaxial images

The planar results for the symmetrical orientations are shown in Table 5.5

		ROI 0 cps/MBq	ROI 1 cps/MBq	Ratio 1:0
Orientation 2	Head 1	32.46	33.10	1.02
	Head 2	30.63	30.83	1.01
	Geometric mean	31.53	31.94	1.01
Orientation 3	Head 1	12.45	52.67	4.23
	Head 2	49.30	11.58	0.23
	Geometric mean	24.77	24.70	1.00
Orientation 4	Head 1	15.39	53.39	3.47
	Head 2	46.55	13.28	0.29
	Geometric mean	26.77	26.62	0.99

Table 5.5 Planar results for symmetrical orientations 2 to 4.

The addition of AC increases the cps/MBq measured by 2 to 3 times. As before, the addition of scatter correction reduces this by a small but statistically significant amount. The cps/MBq with and without scatter correction were compared and found to be significantly different using a 2 tailed Students t test $p<0.001$ for ROI 0 and $p<0.001$ for ROI 1. The noticeable difference between this case and the non-symmetrical case is that there is very little difference (within experimental error) between the two sources even for the non AC corrected groups. The Students t test gives a value of $p >0.1$ for all reconstruction groups. This is as expected since in this geometry the two sources are an equal distance from the edge of the phantom and therefore subject to the same amount of attenuation. The ratio results confirm this finding, with all the results lying within experimental error of the true value of 1.0. The static results also show that for this phantom geometry, the simple method of using the geometric mean to calculate relative uptake can be used successfully.

5.5.3 Results – Non- symmetrical phantom

The results in cps/MBq of varying the orientation of the edge source between non-symmetrical orientations 1 and 8 are shown in Figs 5.17 to 5.24.

Orientation (1)

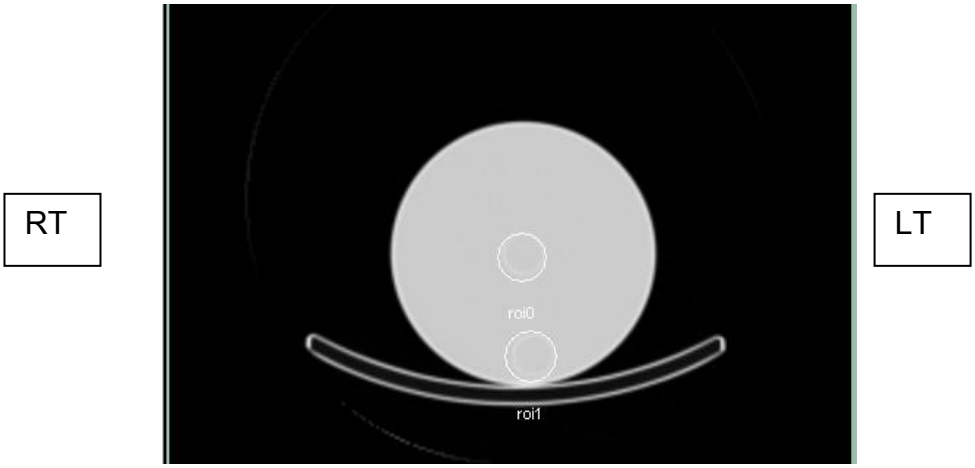

a)

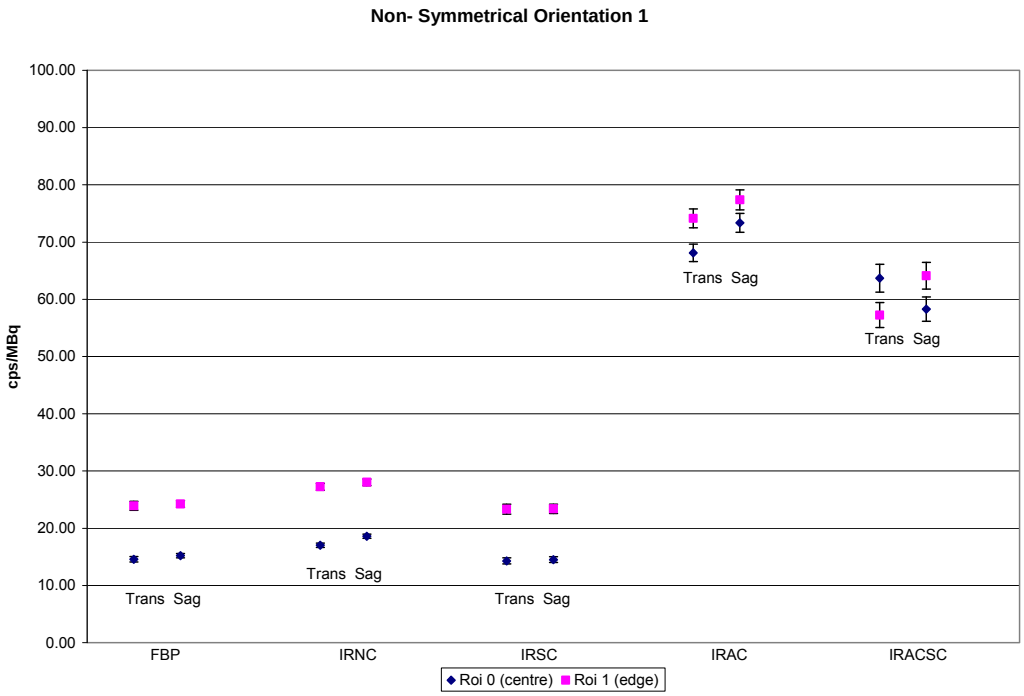

b)

Fig 5.17 a) CT image showing orientation of sources b) cps/MBq for Sources in Orientation (1)

Orientation (2)

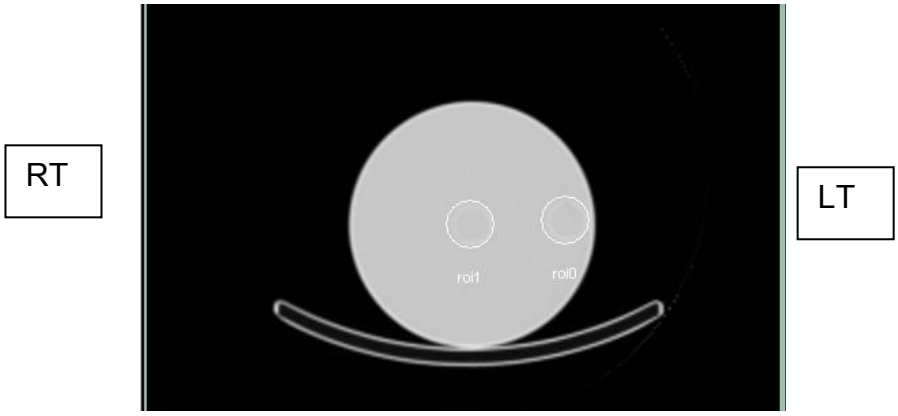

a)

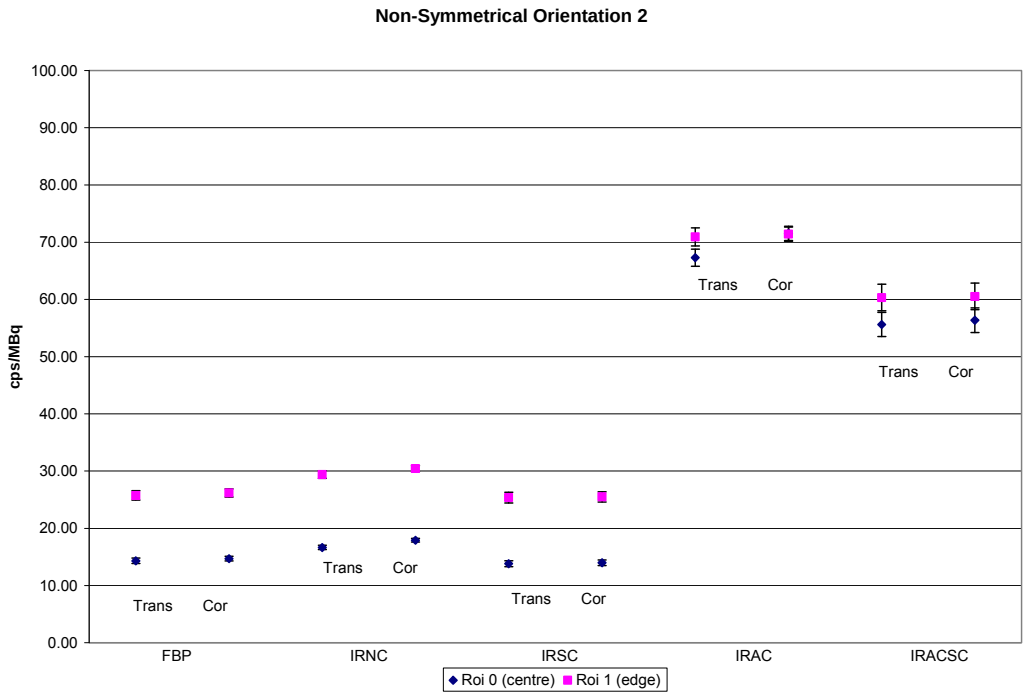

b)

Fig 5.18 a) CT image showing orientation of sources b) cps/MBq for Sources in Orientation (2)

Orientation (3)

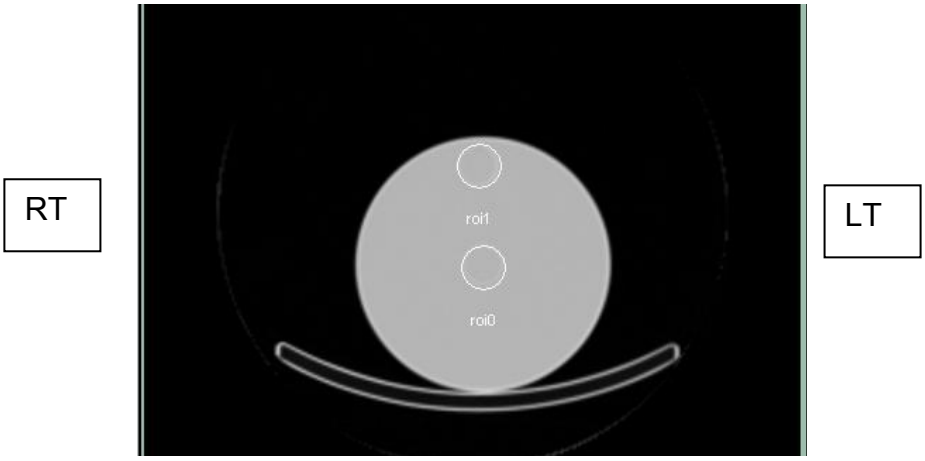

a)

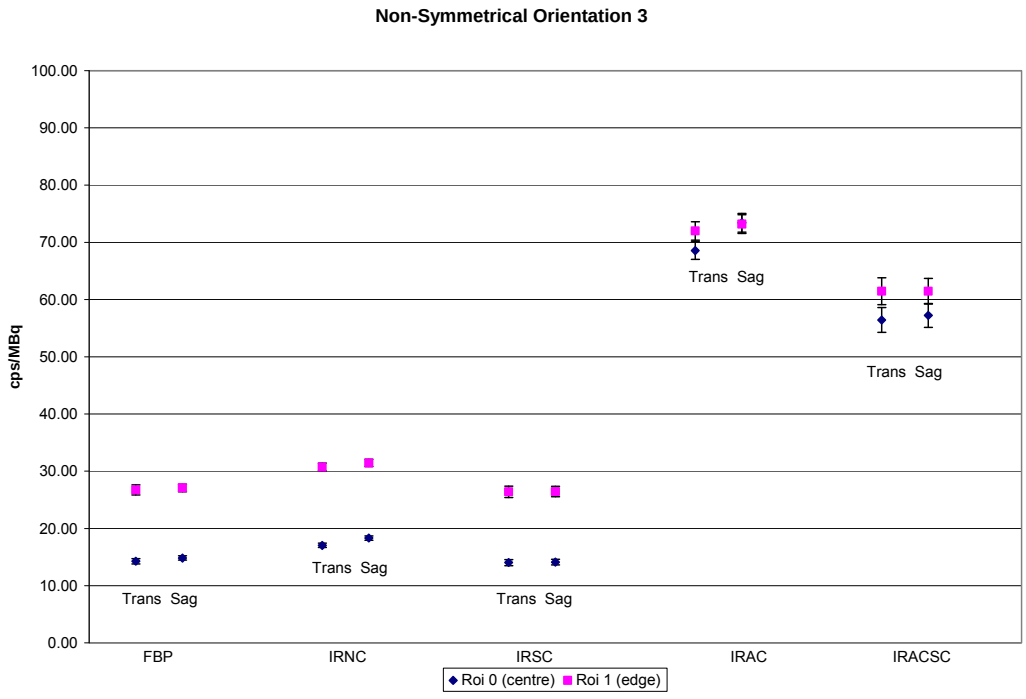

b)

Fig 5.19 a) CT image showing orientation of sources b) cps/MBq for sources in Orientation (3)

Orientation (4)

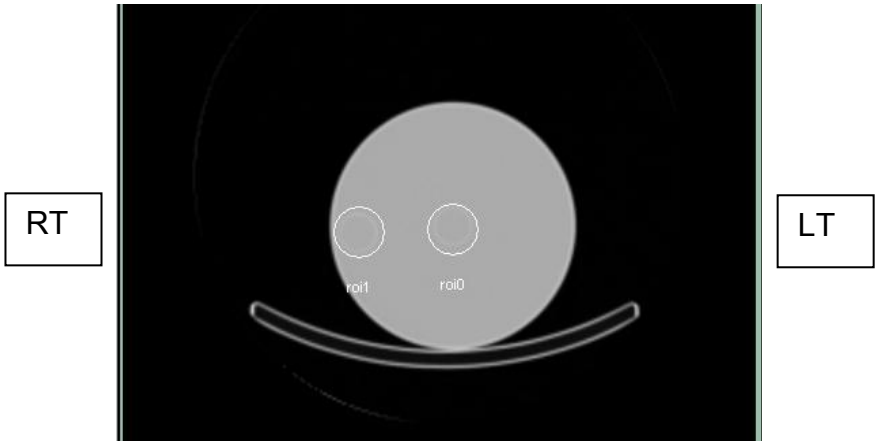

a)

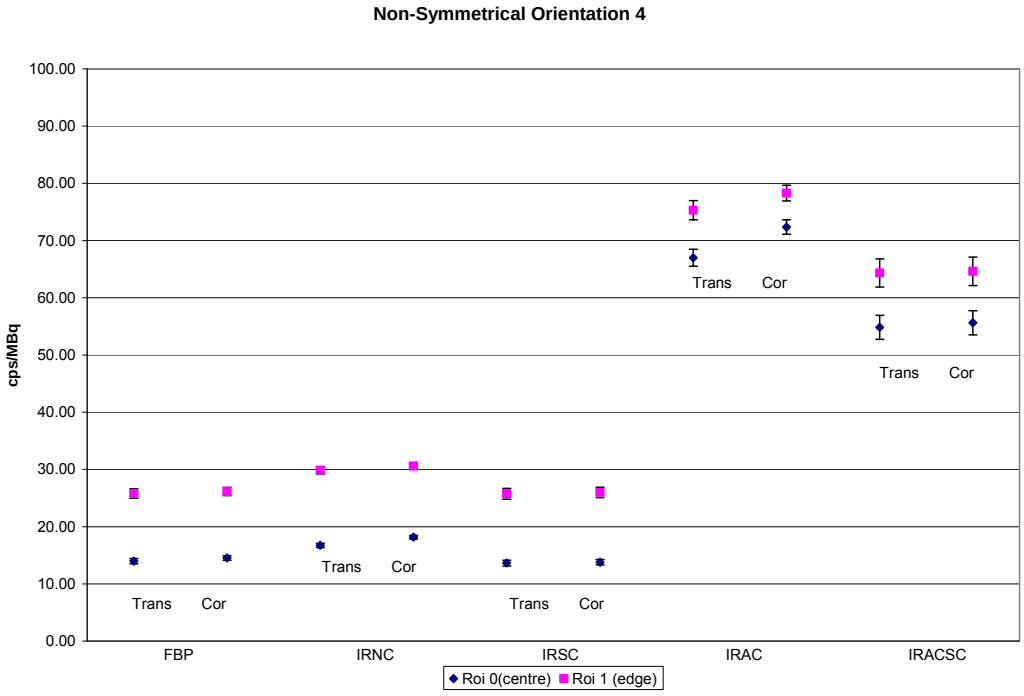

b)

Fig 5.20 a) CT image showing orientation of sources b) cps/MBq for sources in Orientation (4)

Orientation (5)

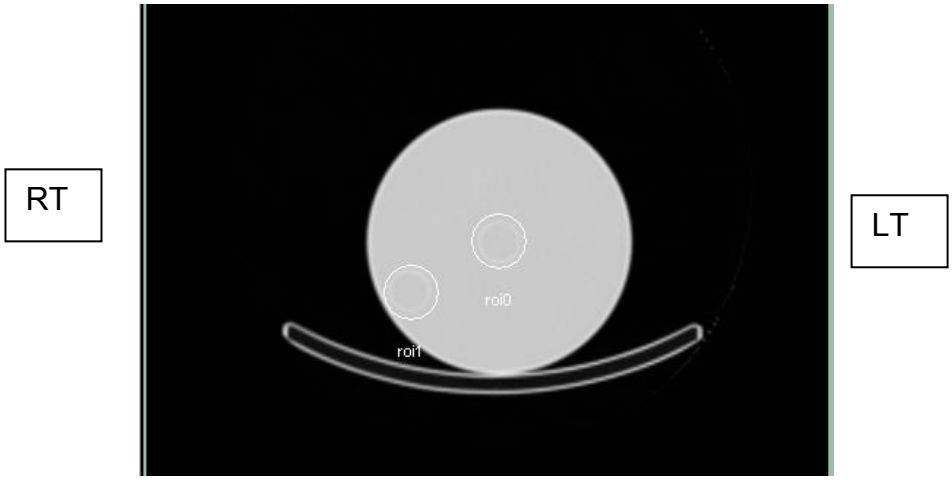

a)

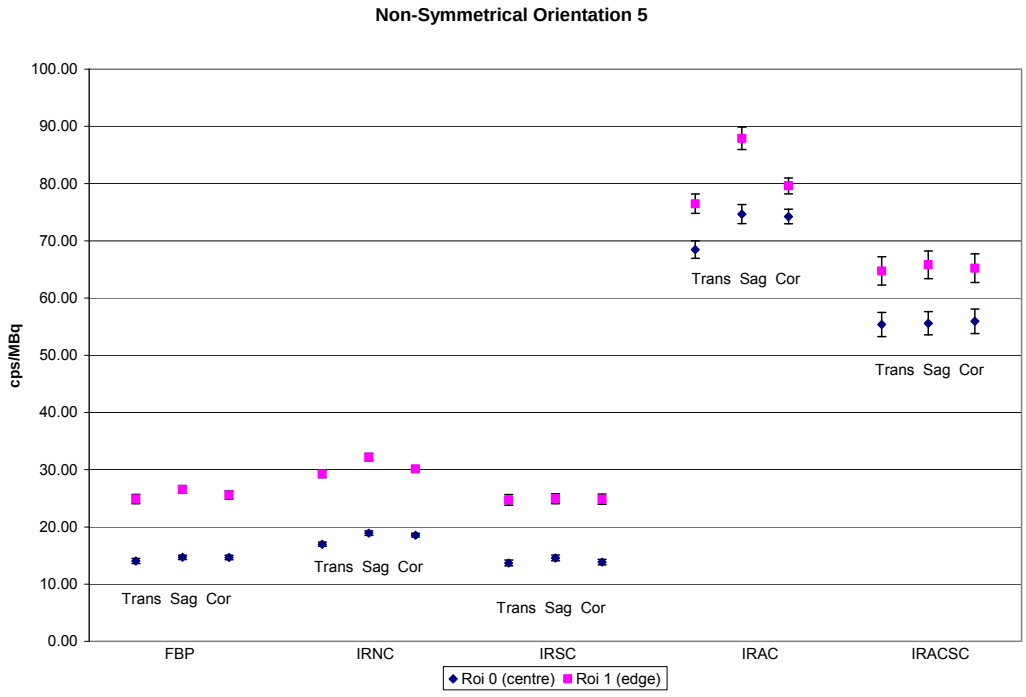

b)

Fig 5.21 a) CT image showing orientation of sources b) cps/MBq for sources in Orientation (5)

Orientation (6)

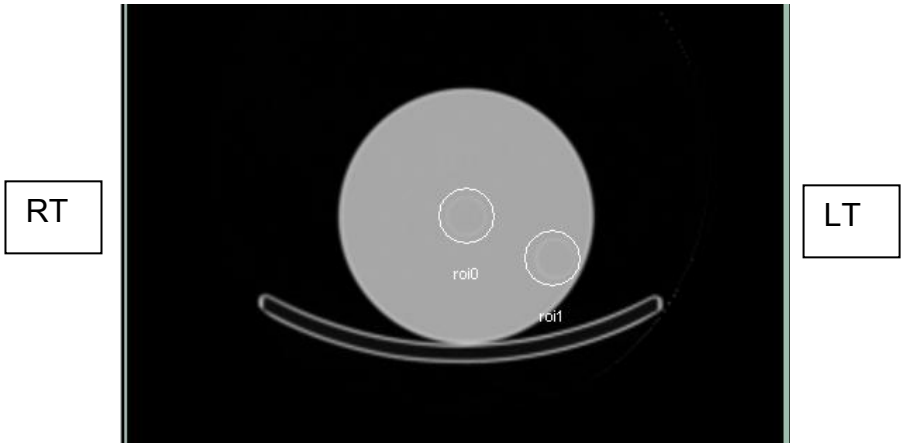

a)

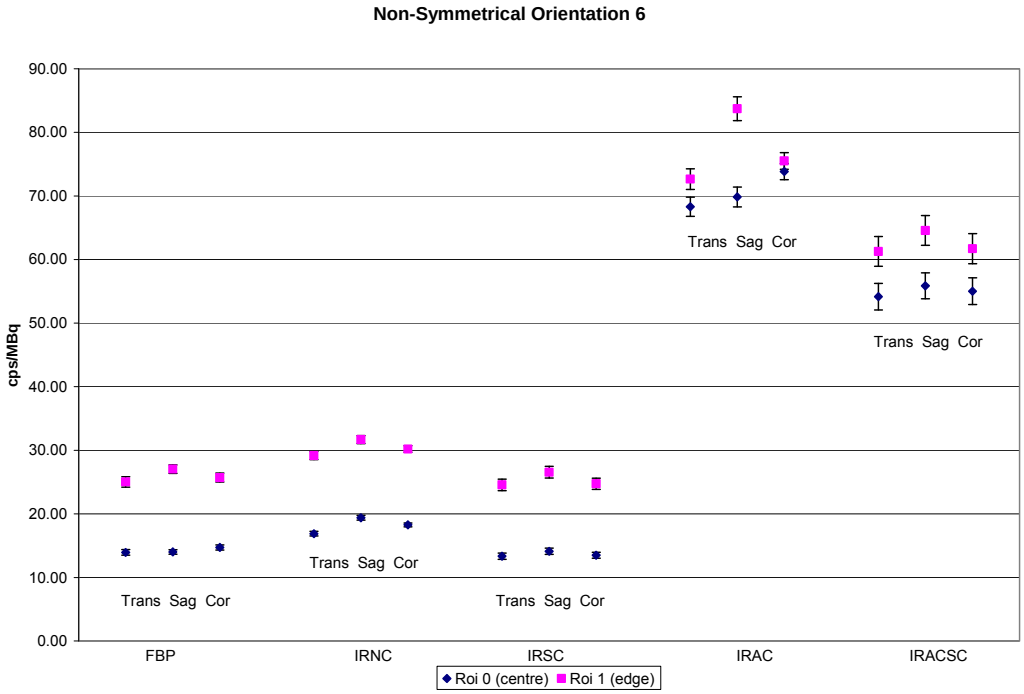

b)

Fig 5.22 a) CT images showing orientation of sources b) cps/MBq for sources in Orientation (6)

Orientation (7)

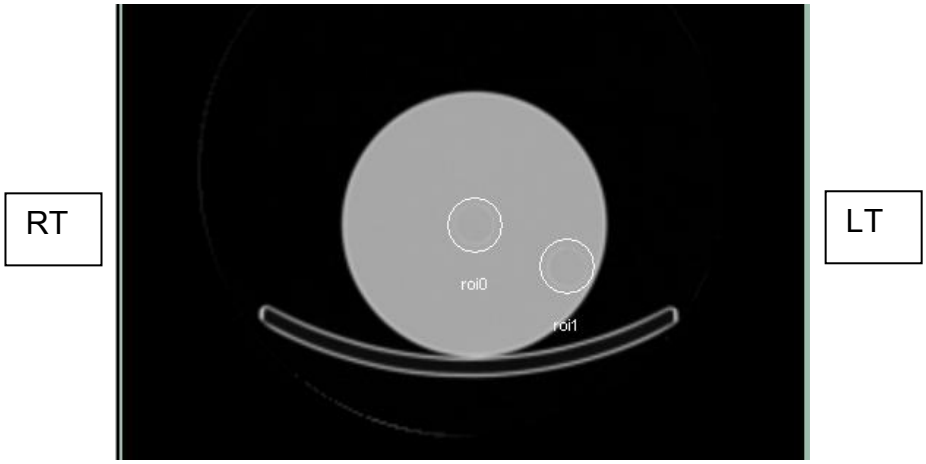

a)

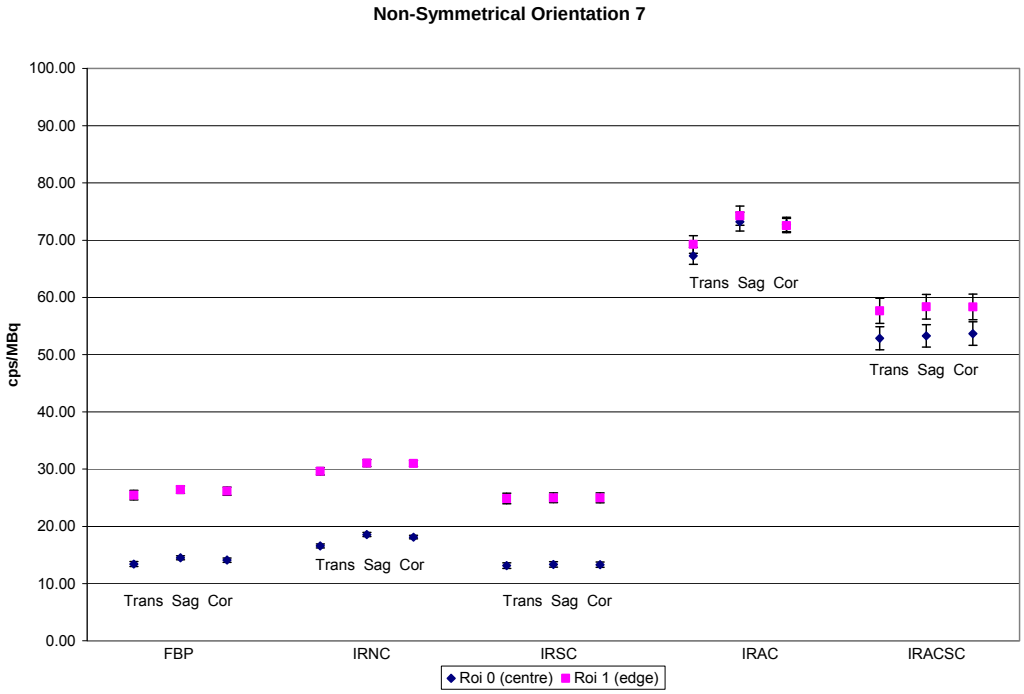

b)

Fig 5.23 a) CT image showing orientation of sources b) cps/MBq for sources in Orientation (7)

Orientation (8)

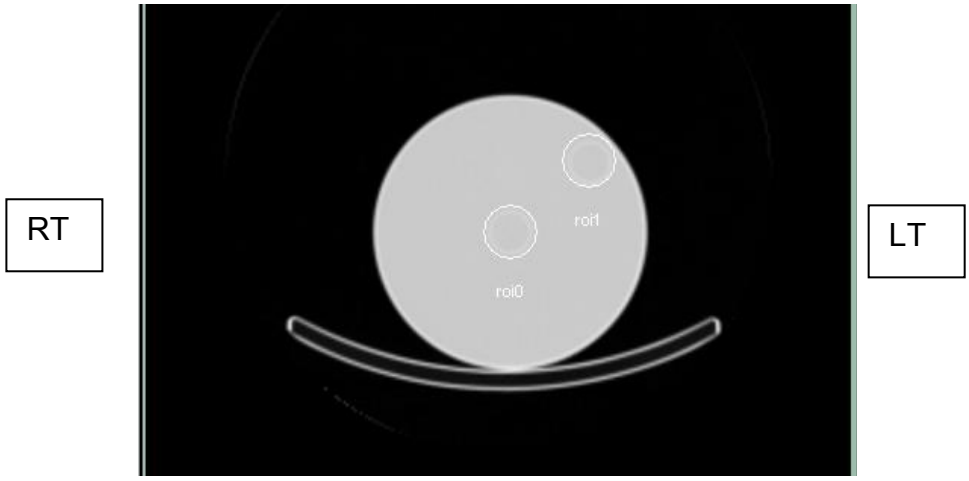

a)

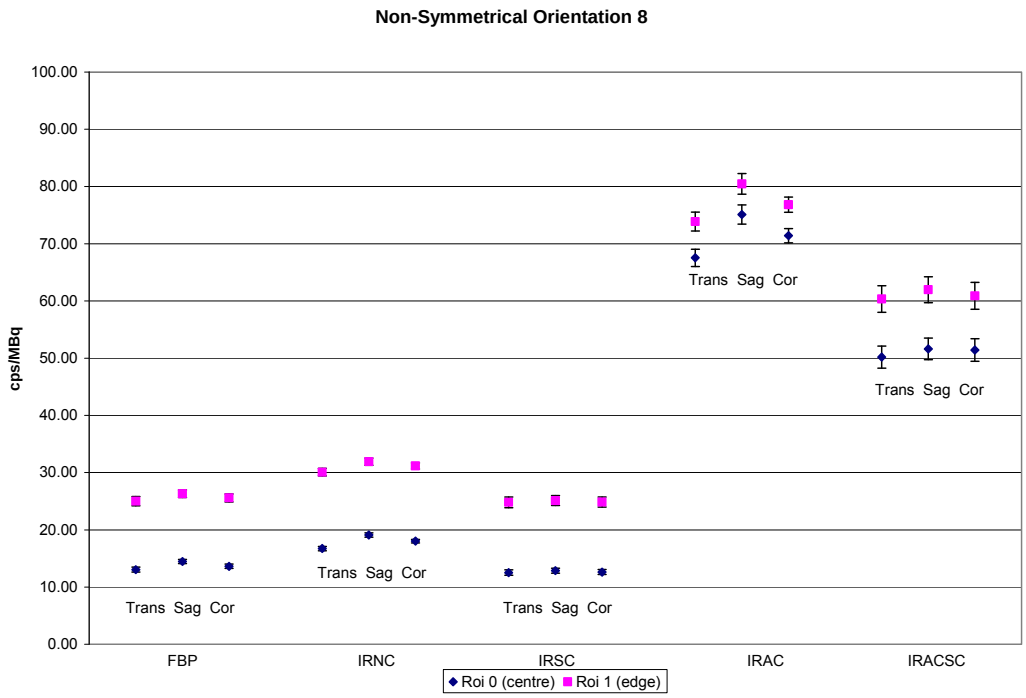

b)

Fig 5.24 a) CT image showing orientation of sources b) cps/MBq for sources in Orientation (8)

The effect of the rotational orientation is summarized for the transaxial reconstruction plane in Fig 5.25. Note that the results are expressed as cps/MBq in the edge source as a function of the angle of rotation, with the 0 degree position being taken as the 12 o'clock position.

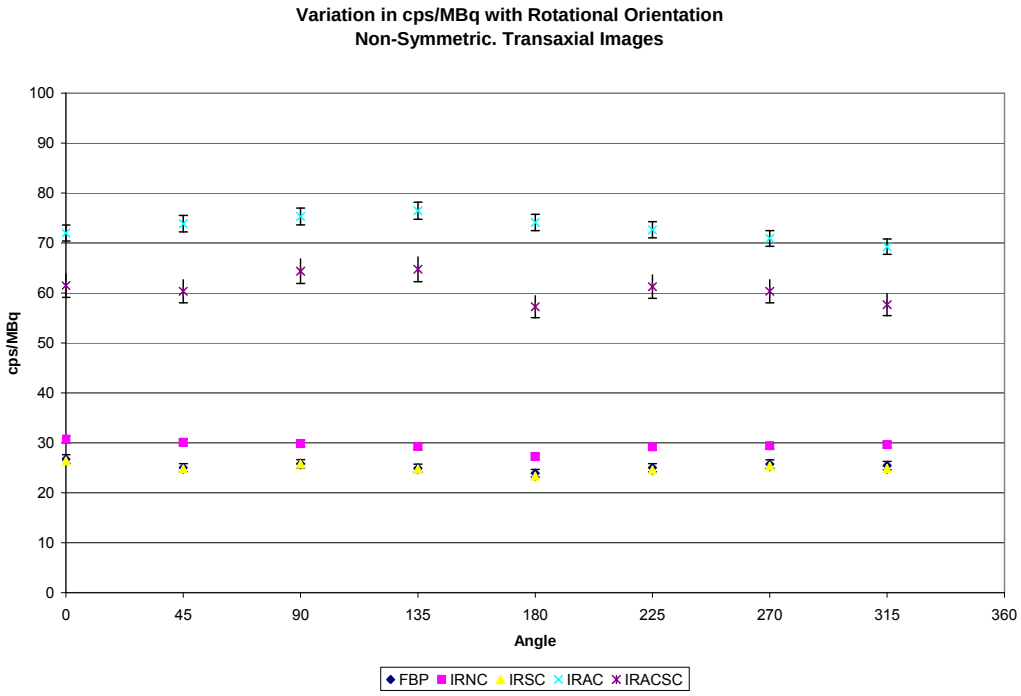

Fig 5.25 Variation with orientation for transaxial images

The ratio of cps/MBq between the edge and centre sources in the on axis (orientations 1 to 4) and off axis (orientations 5 to 8) rotational orientations are shown in Figs 5.26 and 5.27.

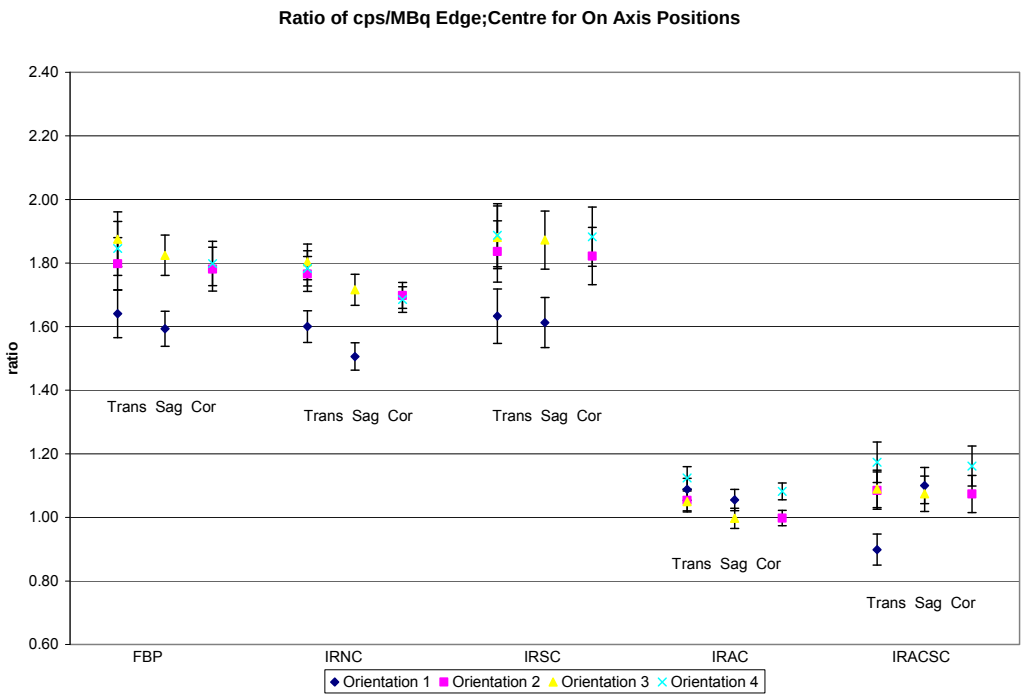

Fig 5.26 Ratio of cps/MBq edge:centre for on-axis positions

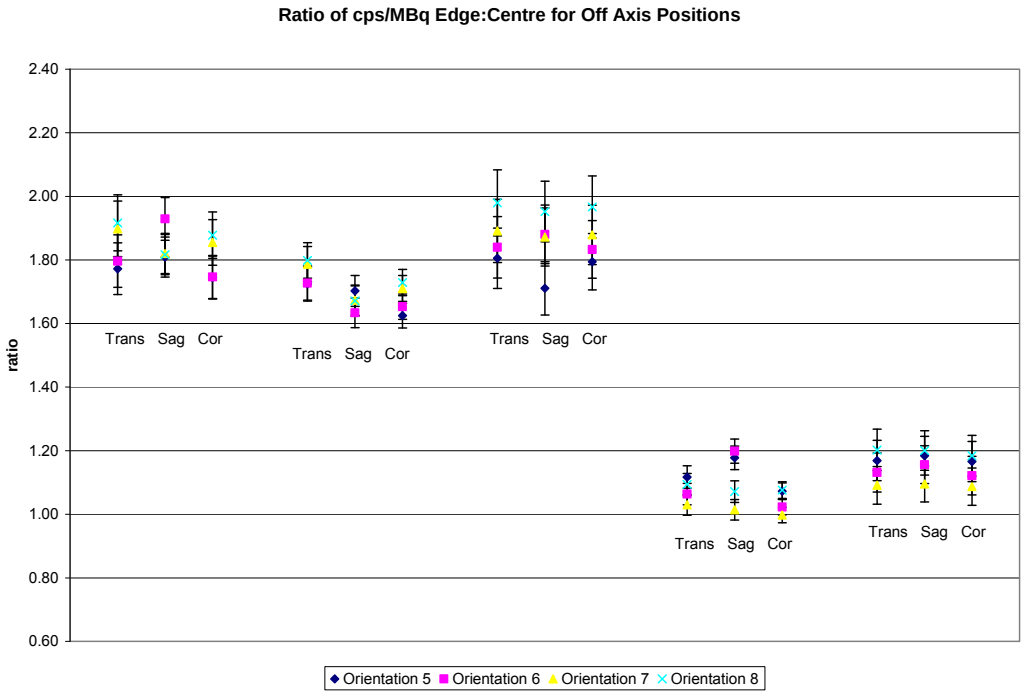

Fig 5.27 Ratio of cps/MBq edge:centre for off axis positions

Planar results are shown in Table 5.6 where ROI 0 refers to the centre region of interest, and ROI 1 that in the edge position. (Results are not shown for orientations 1 and 3 ie. the 0° and 180° positions, since planar

anterior and posterior imaging cannot discern between the two sources in these orientations.)

		Roi 0 cps/MBq	Roi 1 cps/MBq	Ratio 1:0
Orientation 2	Head 1	18.28	33.01	1.81
	Head 2	16.54	26.04	1.57
	Geometric mean	17.39	29.32	1.69
Orientation 4	Head 1	17.98	28.91	1.61
	Head 2	16.36	30.69	1.88
	Geometric mean	17.15	29.79	1.74
Orientation 5	Head 1	17.47	13.07	0.75
	Head 2	14.82	16.41	1.11
	Geometric mean	16.26	26.89	1.65
Orientation 6	Head 1	16.43	18.21	1.11
	Head 2	16.49	41.19	2.50
	Geometric mean	16.47	27.39	1.66
Orientation 7	Head 1	18.30	48.58	2.65
	Head 2	12.02	16.43	1.37
	Geometric mean	14.84	28.25	1.90
Orientation 8	Head 1	17.84	44.09	2.47
	Head 2	14.82	16.41	1.11
	Geometric mean	16.26	26.89	1.65

Table 5.6 Results of planar imaging in phantom orientations 2,4,5,6,7and 8

For the non attenuation corrected reconstructions (FBP, IRNC and IRSC) there is little difference between the groups of results. A marked difference can be seen between the values for the two sources, with the source in the centre of the phantom consistently measuring fewer cps/MBq than the source at the edge of the phantom. This applies to all orientations and is expected due to the effects of attenuation. When correction for attenuation is applied a much higher value of cps/MBq is detected as expected (approx 70-80 cf. approx 15-30 cps/MBq) with this being reduced slightly by the addition of scatter correction. The difference between the IRAC and IRACSC groups is statistically significant, when measured using a 2 tailed Students T test $p<0.05$ for Roi 0 and $p<0.01$ for Roi 1.There is little difference between the values for the two sources with results being largely within experimental error.

The ratio of cps/MBq for the two sources show that for SPECT the ratio varies from approximately 1.8 when no AC is used, to approximately 1.1 when AC is used (true ratio 1.0). The best results were achieved for AC reconstructions without scatter, where a best result of 1.0 was achieved. There was very little variation in results between the positional orientations with all differences being within experimental error.

For planar acquisitions, using the geometric mean method to take some account of depth dependence, the ratio of cps/MBq between the two sources (edge position:centre position) was found to be approximately 1.7.

5.6 Discussion

For reasons described in sections 5.2 and 5.3 of this chapter, it was decided that for subsequent quantitative measurements, the simple methodology of placing the phantom directly onto the scanning couch during acquisitions and drawing a manual region of interest around the reconstructed images would be suitable to use. An analysis of the errors inherent in this approach proved that there was an acceptable level of reproducibility in the results obtained.

There is a slight sinusoidal dependence on the angle of acquisition that is not eradicated with attenuation correction. By approximating a straight line fit to the results, the points that best fit the straight line were the horizontal orientations (orientations 2 and 4 in the non-symmetrical and orientation 2 in the symmetrical case.) For this reason it was decided that for subsequent measurements the phantom should be positioned in a horizontal orientation.

Chapter 6

Quantitation Measurements

6.1 Introduction

As stated in chapter 1, one of the overall aims of quantitation in nuclear medicine is to convert the countrate (in cps) detected in an image into a measure of the radioactivity (in MBq) present in the object of interest. In planar imaging, a relatively straightforward measurement can be made of counts per second per MBq using a sensitivity phantom as shown in chapter 4. This sensitivity value can be applied to subsequent planar images once corrections for background have been made.

In SPECT the situation is made more complicated by the difference in measured counts in an image caused by reconstruction method, volume of the object (as result of the partial volume effect) and its position within an attenuating medium. Given these differences, the question needs to be asked 'Is determining a single sensitivity factor for SPECT imaging a valid method of quantitation or does a specific sensitivity factor need to be calculated for every acquisition geometry encountered, which would be difficult in clinical practice?' The aim of this chapter is to establish sensitivity values for FBP, IRNC, IRSC, IRAC and IRACSC reconstruction methods and to investigate the accuracy and validity of using these to quantify activity for a range of SPECT acquisitions. This will be investigated for a single source object and for two source object situations with varying positional geometry, activity ratios, object volumes and background activities. The results of these variations will be expressed in terms of cps/MBq and deviation from the expected activity

taken as that measured on the radionuclide calibrator. Absolute and relative quantitation between the two sources will be considered, to determine the most accurate method for quantitation in SPECT imaging, with particular consideration given to the effect of attenuation.

6.2 Establishment of SPECT sensitivity

In order to convert measured count rates into activity in MBq for the range of SPECT acquisitions to be carried out in this study, sensitivity values were established for each of the reconstruction methods and acquisition geometries considered. It was then possible to make a decision on the most appropriate sensitivity value or values to be used in later stages of this study.

6.2.1 Method

In order to establish SPECT sensitivity in terms of counts per second per MBq, four geometries were considered;

- point source in air on and off centre of rotation,
- Source A (56 ml) in a cylindrical phantom with no background activity,
- Source B (112 ml) in a cylindrical phantom with no background activity,
- cylindrical phantom containing uniform activity.

The cylindrical phantom used was the Jaszczak phantom with no inserts. This has a volume of 6.5 litres as described in chapter 4. As before, for phantom acquisitions autocontouring was used. For the point source in air, a circular radius of 26 cm was used.

The point source was 0.1 ml of radioactive solution (activity 0.62 MBq) at the tip of a 1 ml syringe. This was imaged both at the centre of rotation and off axis by 7 cm.

Sources A and B were filled with Tc-99m at an activity concentration of approximately 0.1MBq per ml, resulting in activities of approximately 5.6 MBq and 11.2MBq respectively. Each source was imaged positioned at the centre of the cylindrical phantom.

The cylindrical phantom alone was imaged containing approximately 180 MBq in order to avoid count saturation, based on results found in chapter 4.

All geometries were acquired and reconstructed using the parameters listed in Table 5.1 and listed again here for ease of reference (Table 6.1). These parameters were used as standard protocol throughout this study.

Camera set up	H mode
Matrix	128 ×128
Frame time	30s
Zoom	1.0
Reconstruction	OSEM 2 iterations 16 sub sets
Data sets	FBP, IRNC, IRSC, IRAC, IRACSC

Table 6.1 Standard SPECT acquisition parameters

Effective volumes of interest were generated by summing the slices containing the radioactive phantom insert and generating a region of interest (ROI) on the summed image. For the phantom and source images, the ROI was drawn as a rectangle just large enough to include all

of the visible image as described in chapter 5. For the point source, a circular region of interest centred on the centre of the source was used.
For each geometry, the counts to activity conversion was determined by dividing the reconstructed counts per second within a ROI by the defined activity for that region.

Each of these sensitivity values were then used to calculate an estimate of activity in each of the other phantoms. In other words, each sensitivity calculated from a particular geometry was applied to acquisitions carried out with a different geometry, to investigate the inaccuracy that this introduces. The aim of this was to answer the question posed in the introduction to this chapter, ‘is a single sensitivity value valid in SPECT imaging, or does a separate sensitivity value need to be found for every geometrical orientation encountered?’ These results were expressed in terms of percentage deviation form the ‘true’ or expected activity, defined as that measured in the radionuclide calibrator.

6.2.2 Results

The sensitivities calculated for the geometries described are shown in Table 6.2. The errors quoted are estimates based on the reproducibility measurements carried out for Source A (section 5.4) and are likely to be underestimations for the point source measurements where the relative error in activity measurement is high and conversely overestimations for the cylindrical phantom where the relative error in activity measurement is lower.

	Sensitivity cps/MBq				
	Point source on axis	Point source off axis	Source A	Source B	Cylindrical phantom
FBP	89.08±5.82	87.55±5.72	12.57±0.82	13.63±0.89	20.65±1.35
IRNC	91.28±4.18	92.29±4.23	15.82±0.72	17.15±0.79	26.98±1.24
IRSC	87.44±7.33	87.63±7.35	12.01±1.01	13.59±1.14	20.15±1.69
IRAC	91.88±4.44	93.08±4.50	63.36±3.06	67.75±3.27	74.05±3.58
IRSCAC	87.10±7.66	89.24±7.84	48.46±4.26	54.39±4.78	55.99±4.92

Table 6.2 Sensitivity results for point source on and off axis, sources A and B and cylindrical phantom.

The sensitivities for the point source found on and off axis were found to be within the error range and so for the remainder of this chapter the on-axis sensitivities are used.

6.2.3 Calculated activities using point source sensitivity

The results of applying the point source sensitivity values to counts per second found from Sources A and B and the cylindrical phantom are shown in Figs 6.1 to 6.3.

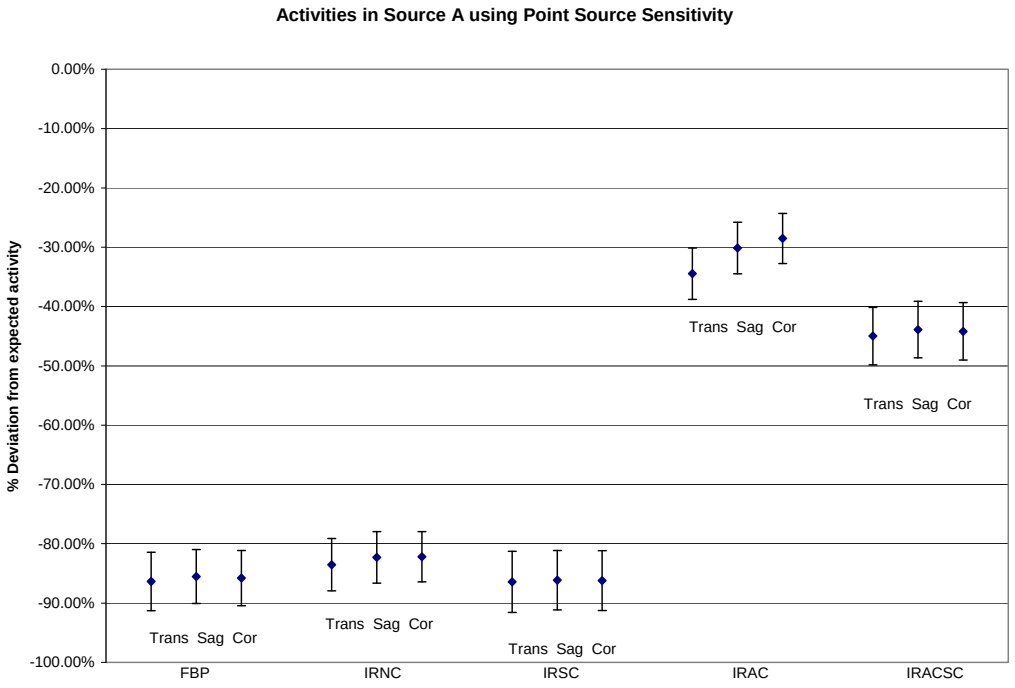

Fig. 6.1 Calculated activity in Source A using sensitivity from point source

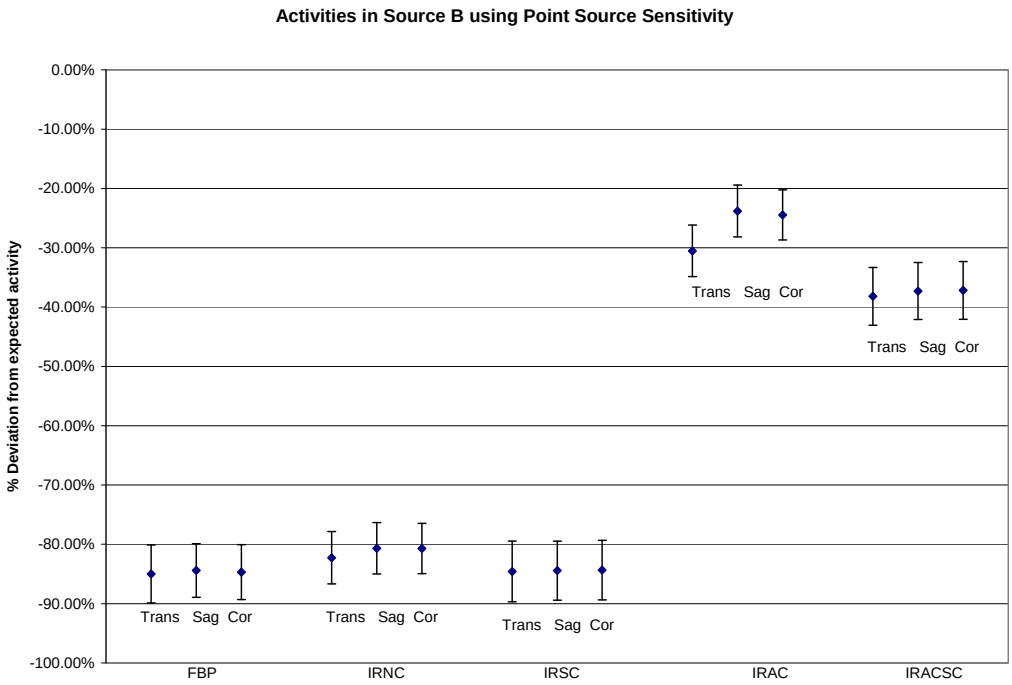

Fig. 6.2 Calculated activity in Source B using sensitivity from point source

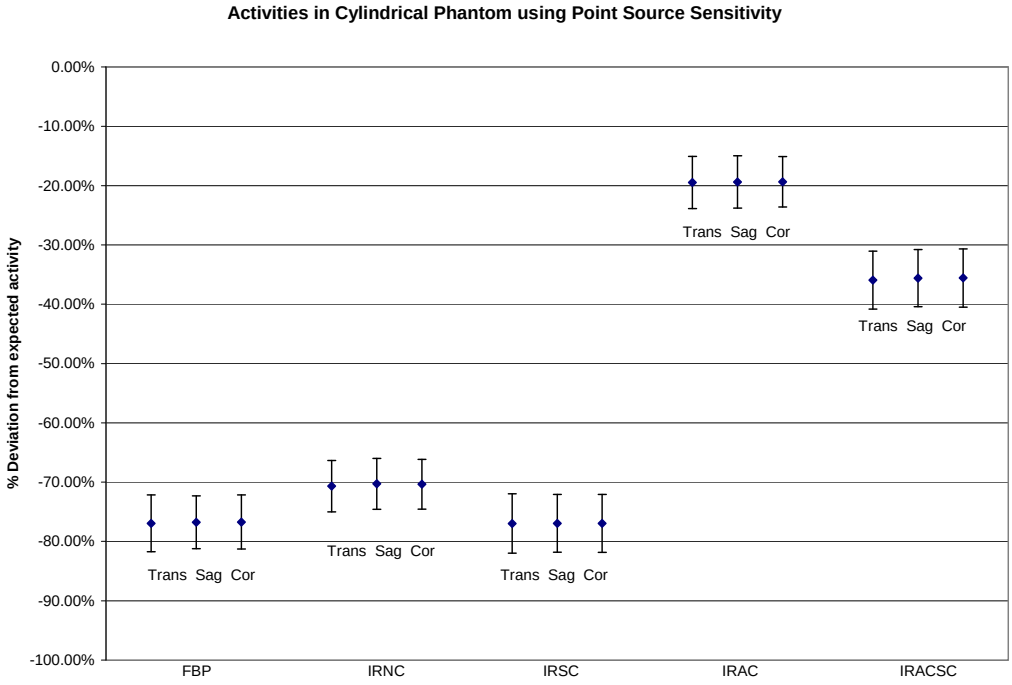

Fig. 6.3 Calculated Activity in cylindrical phantom using sensitivity from point source

6.2.4 Calculated activities using Source A sensitivity

The results of applying the Source A sensitivity values to counts per second found from the point source, Source B and the cylindrical phantom are shown in Figs 6.4 to 6.6.

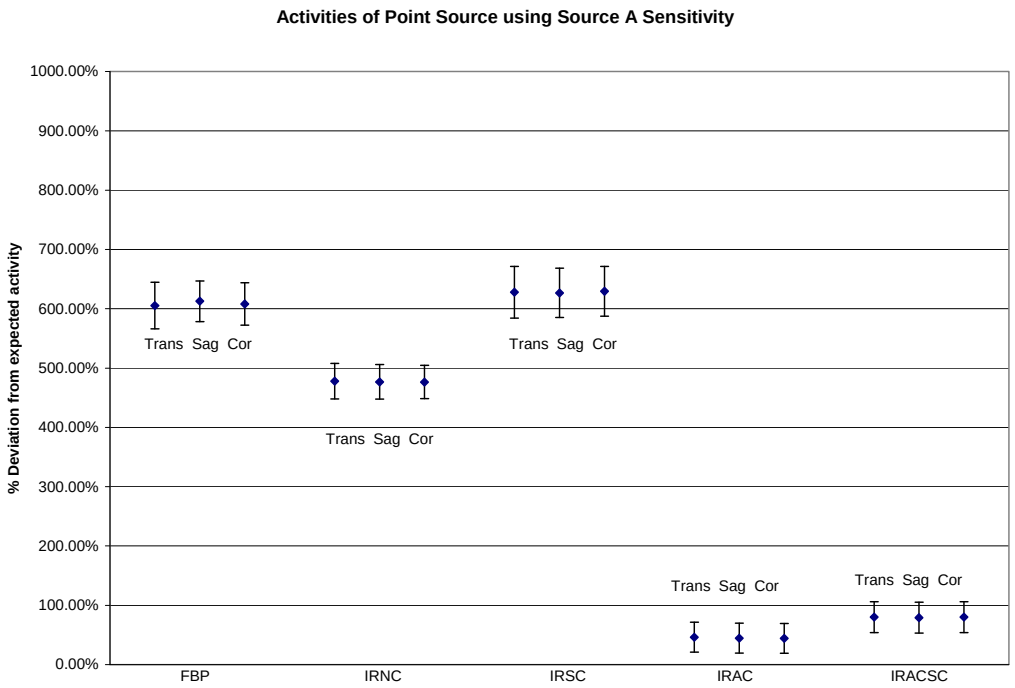

Fig. 6.4 Calculated Activity in point source using sensitivity from Source A

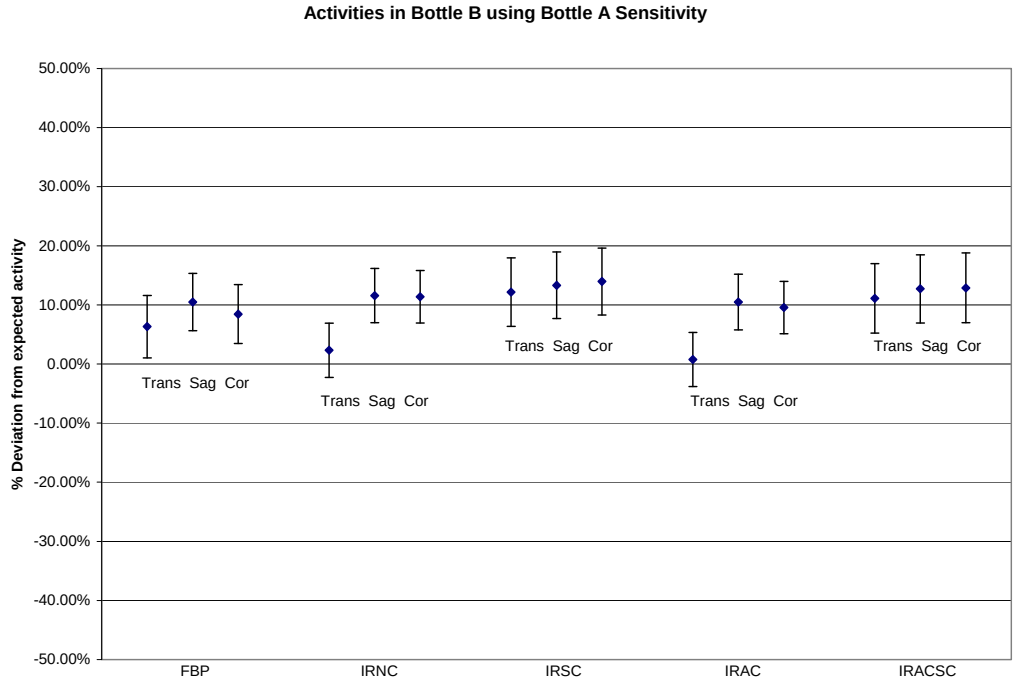

Fig. 6.5 Calculated Activities in Source B using sensitivity from Source A

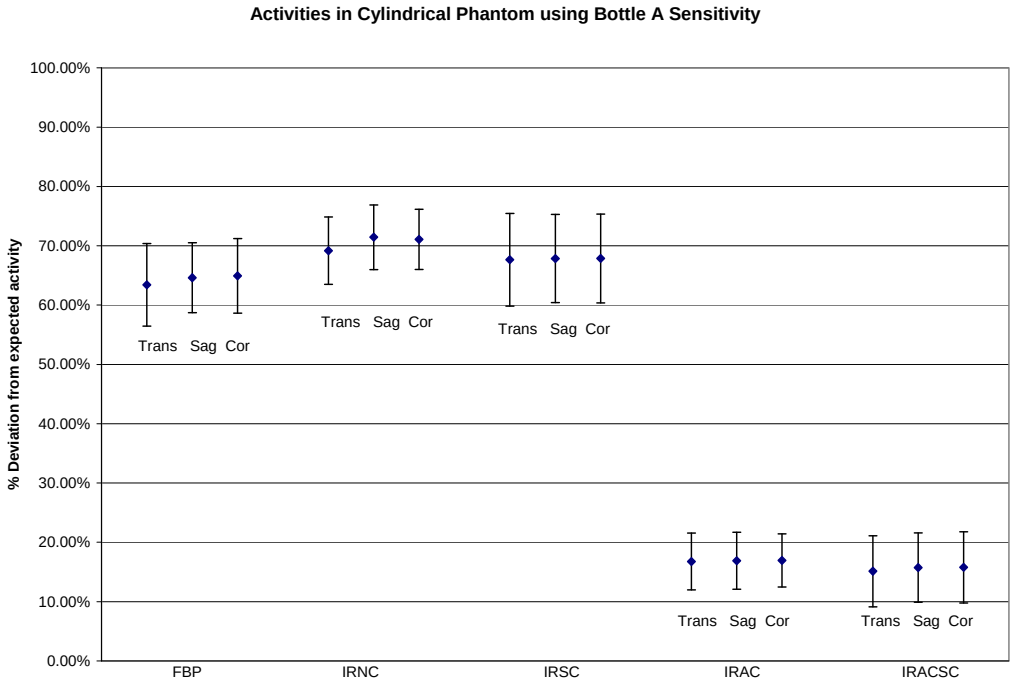

Fig. 6.6 Calculated Activities in cylindrical phantom using sensitivity from Source A

6.2.5 Calculated activities using Source B sensitivity

The results of applying the Source B sensitivity values to counts per second found from the point source, Sources A and the cylindrical phantom are shown in Figs 6.7 to 6.9.

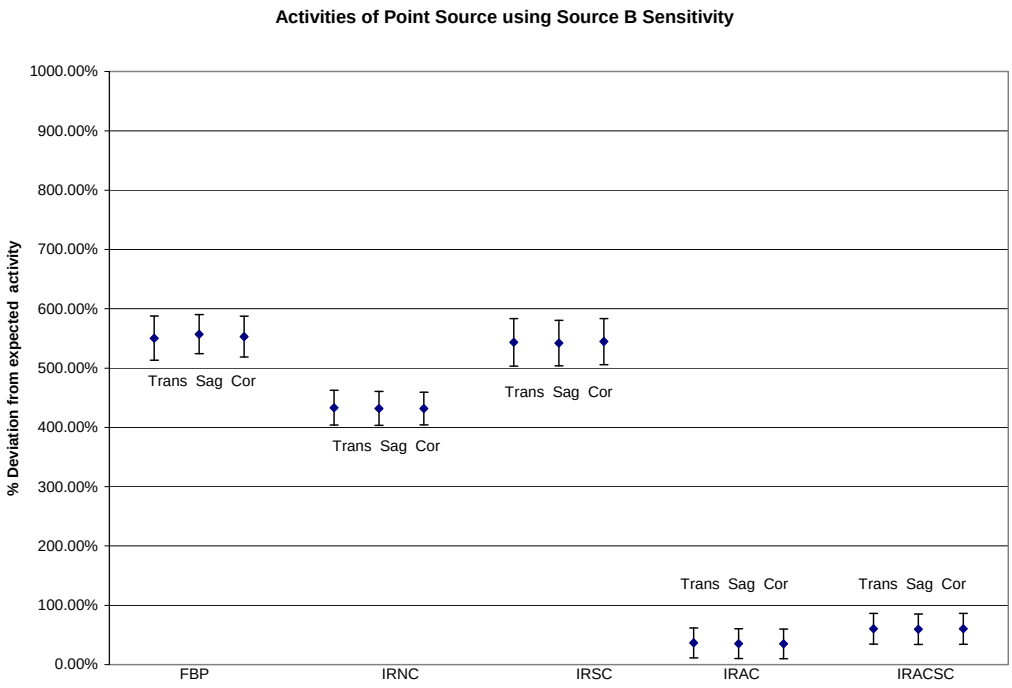

Fig. 6.7 Calculated activity in point source using sensitivity from Source B

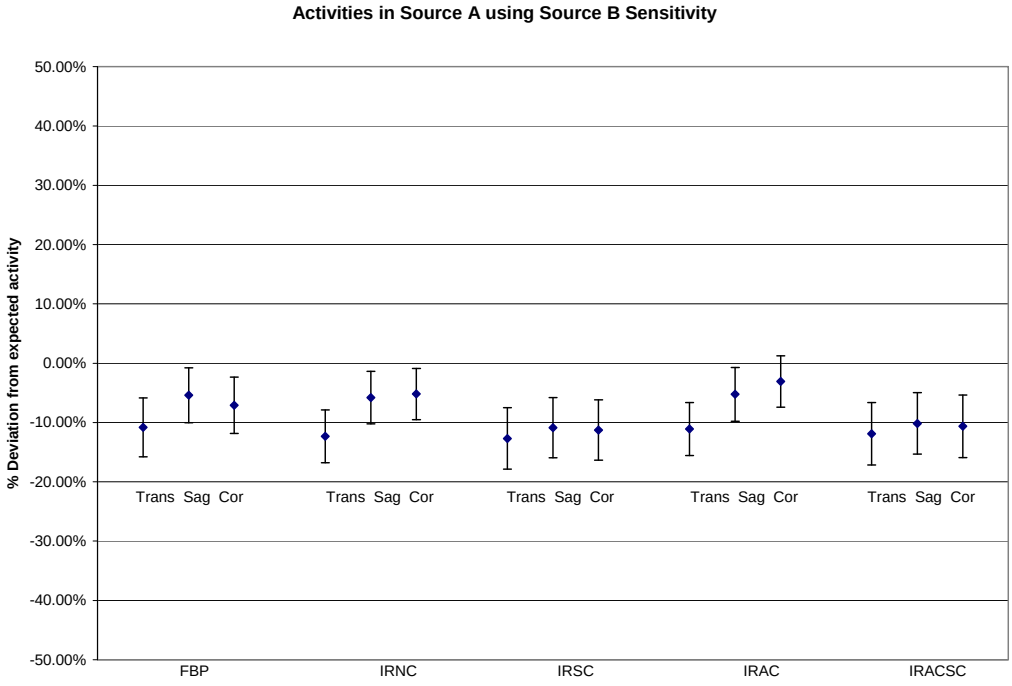

Fig. 6.8 Calculated activities in Source A using Sensitivity from Source B

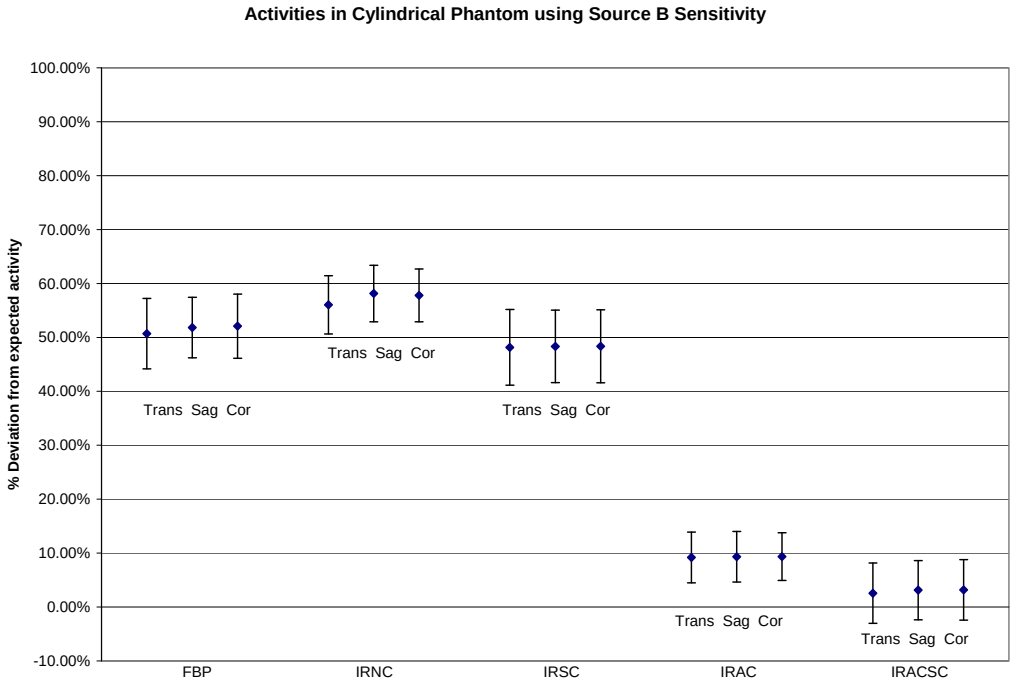

Fig. 6.9 Calculated activities in cylindrical phantom using Sensitivity from Source B

6.2.6 Calculated activities using cylindrical phantom sensitivity

The results of applying the uniform cylindrical phantom sensitivity values to counts per second found from the point source and Sources A and B are shown in Figs 6.10 to 6.12.

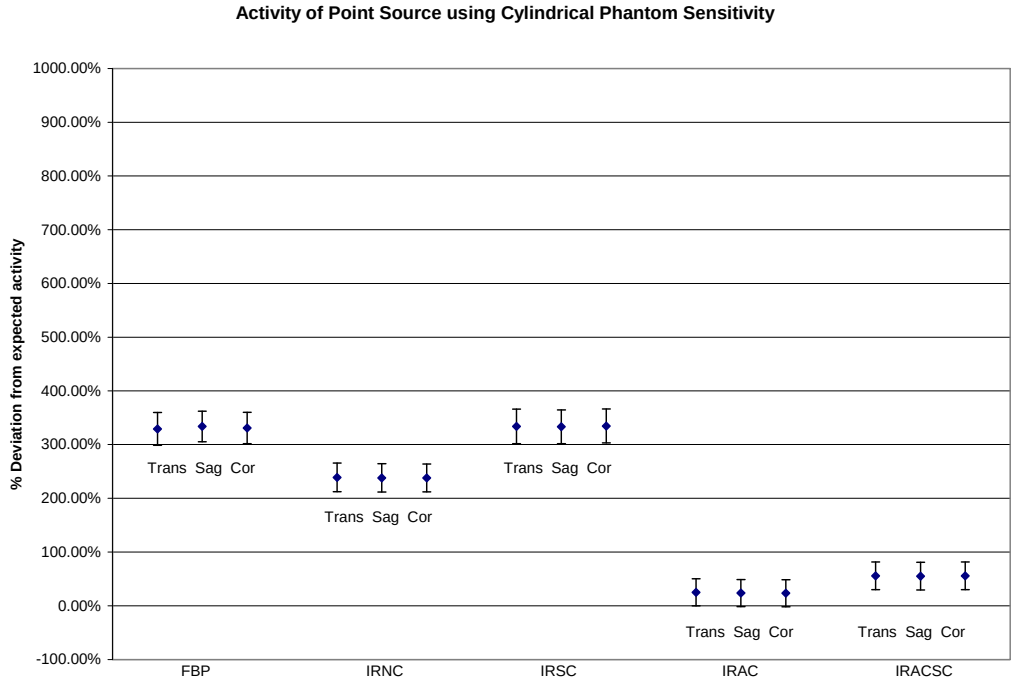

Fig. 6.10 Calculated activity in point source using sensitivity from cylindrical phantom

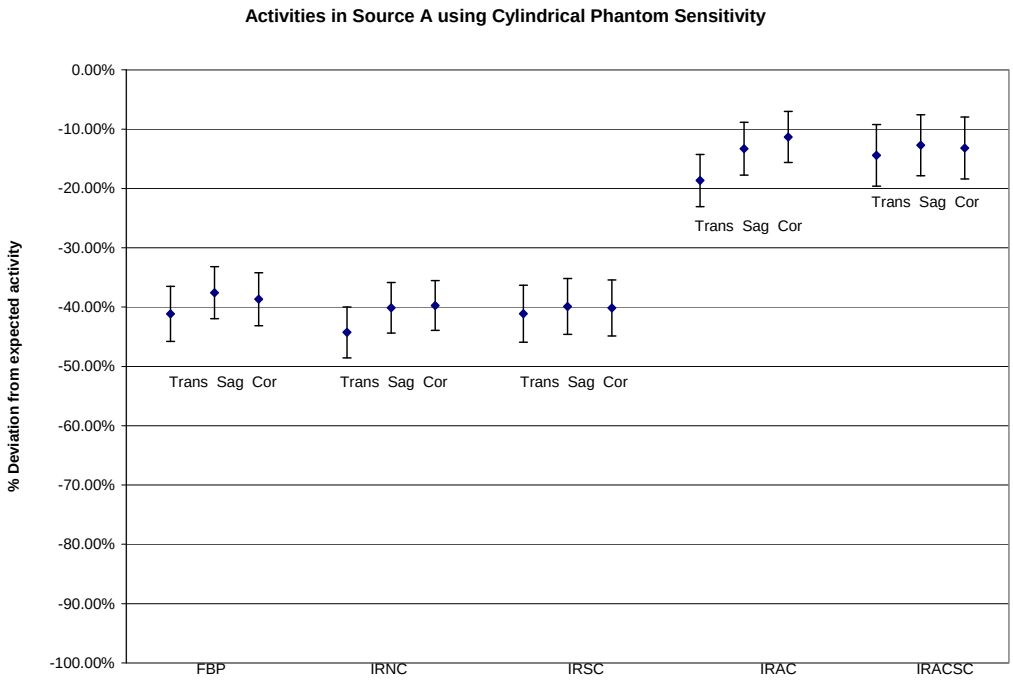

Fig. 6.11 Calculated activities in Source A using sensitivity from cylindrical phantom

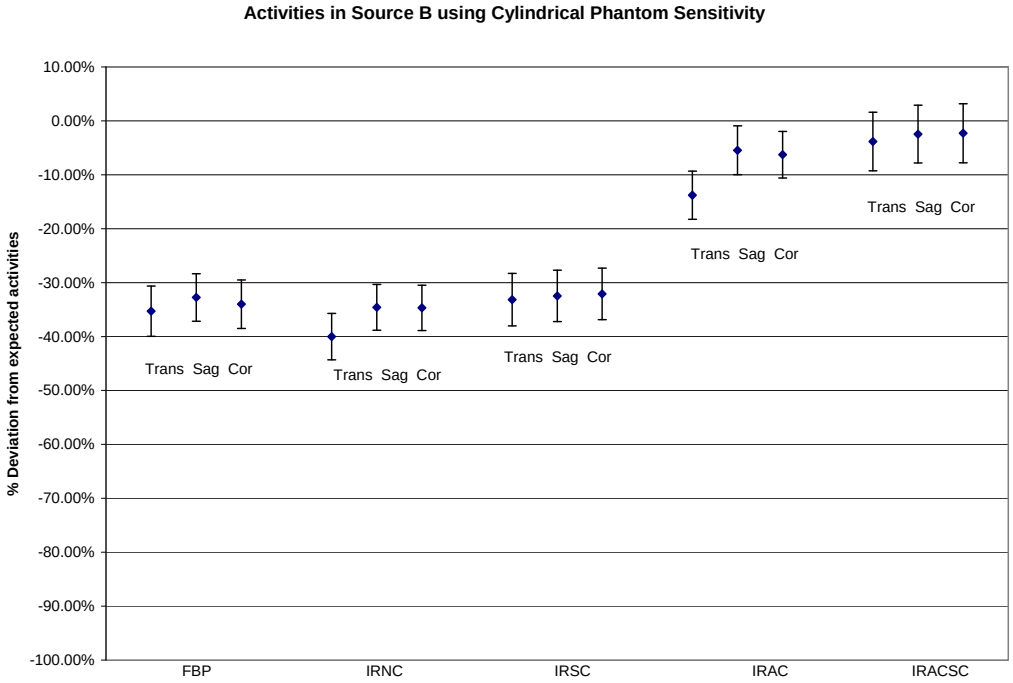

Fig. 6.12 Calculated activities in Source B using sensitivity from cylindrical phantom

6.2.7 Discussion on sensitivity values

It could be argued that measurement of a point source in air is the ‘truest’ way to measure the performance of the gamma camera in terms of sensitivity. These results however show that calculating sensitivity for a point source in air is not directly applicable to the situation of an extended source in an attenuating medium. This is as would be expected, since in the absence of attenuation, the counts measured by the gamma camera per MBq are higher than where attenuation is present. Therefore, as these results show, applying these sensitivities to a condition where attenuation is present results in a gross underestimation of the activity present. (Conversely, applying sensitivities calculated with attenuation present, leads to a gross overestimation of activity in a point source in air, if AC is not applied).For the point source in air, there was little difference between the measured sensitivities using the different reconstruction techniques. However, this situation was not the same for the extended source measurements in an attenuating medium, where measured sensitivities were lower when no AC was used by a factor of approximately 4 times for sources A and B and 3 times for the cylindrical phantom. These results are specific to the geometry used in this experiment, and show clearly that for accurate quantitation, the amount of attenuation present must be taken into account. When corrections for attenuation and scatter are included in the reconstruction, using AC alone results in a sensitivity value closest to that found in air, although still lower by approximately 25% as shown in Table 6.3.

	Sensitivity cps/MBq
Point Source IRAC	91.88 ± 4.44
Source A IRAC	63.36 ± 3.06
Source B IRAC	67.75 ± 3.27
Cylindrical phantom IRAC	74.05 ± 3.58

Table 6.3 Results of sensitivity measurements using IRAC

In these calibration measurements, no background activity was placed in the phantom, so 'in scatter' from the background into the region of interest would not need to be corrected for. The inclusion of scatter correction in this instance has lowered the sensitivity values measured still further from those measured in air.

The sensitivities measured for Sources A and B are very similar to each other as would be expected since the amount of attenuating material surrounding the source is similar in each case (9.25 cm vs 8.90 cm water). As a result, the most consistently accurately calculated activities when compared with the expected activity (i.e. that measured in the radionuclide calibrator) both with and without AC are those in sources A and B using sensitivities calculated for sources B and A respectively.

For the cylindrical phantom, the measured sensitivity is higher than for the smaller sources, despite self attenuation towards the centre of the phantom. The results of comparing measured activities with expected activities show that without attenuation correction, this leads to an underestimation in calculated activity for sources A and B. However, once attenuation correction is applied, very good results are achieved using the

cylindrical phantom calculated sensitivities. A minimum deviation from the expected activity of -2.27 % is achieved for calculating the activity in Source B using IRACSC. The converse is also true- for the cylindrical phantom the expected activity is most accurately reproduced using the sensitivity from Source B with IRACSC, giving a minimum deviation of +2.70 %.

In all cases, the results clearly show that there is little difference in using IR with no corrections or IR with scatter correction compared with using FBP, but that applying attenuation correction and using the corresponding sensitivity value, results in calculated activity measurements much closer to the expected value even for volumes as diverse as a point source or the 6.5 litre cylindrical phantom.

From these results it can be concluded that either the sensitivities from Sources A or B would be most suitable to use for the remainder of this study. It was decided to use the Source A (56 ml) results as this was the source size used in the determination of errors in chapter 5 and was chosen to be the source size used in the orientation, ratio and background experiments.

6.3 Effect of position on quantitation with a single phantom insert

The sensitivity results so far in this chapter have all been established with either a uniform source of activity or with the active source placed in the centre of a uniform attenuating medium. In order to investigate the effect of the depth of attenuating material on sensitivity, Source A was moved from the centre of the phantom to a position closer to the edge , where there would be an angular dependence on the amount of attenuating material for photons to pass through before reaching the camera during the SPECT acquisition. The lateral (lid to base) depth of the source was the same as for the central position.

6.3.1 Method

The effect of position on sensitivity was investigated by positioning Source A in Position 2 in the cylindrical phantom as shown in Fig 6.13. Based on the orientation measurements carried out in section 5.5, a horizontal orientation was used. An activity concentration of approximately 0.1 MBq per ml was used as previously, and images were acquired and reconstructed using the standard parameters in Table 6.1.

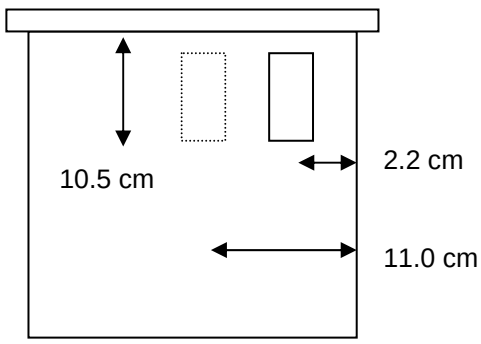

Fig 6.13 Cylindrical phantom with single insert at position 1 (central) or position 2 (edge)

6.3.2 Results

The results of calculating the sensitivity for Source A in positions 1 and 2 and deviation from expected activity are shown in Figs 6.14 and 6.15.

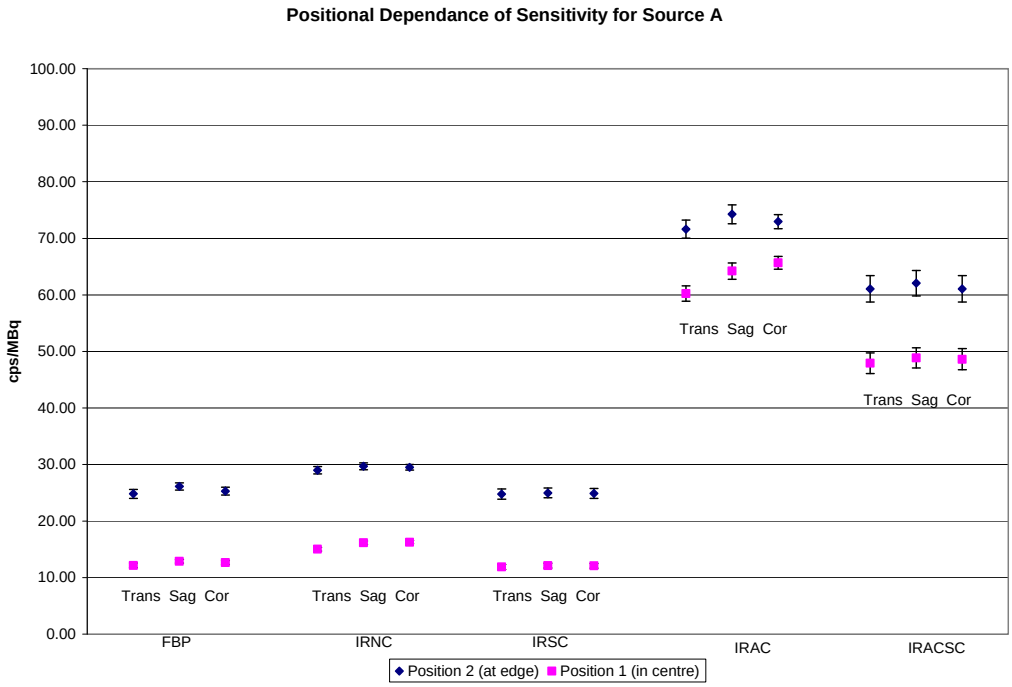

Fig. 6.14 Results of Calculating Sensitivity in Source A in Position 2

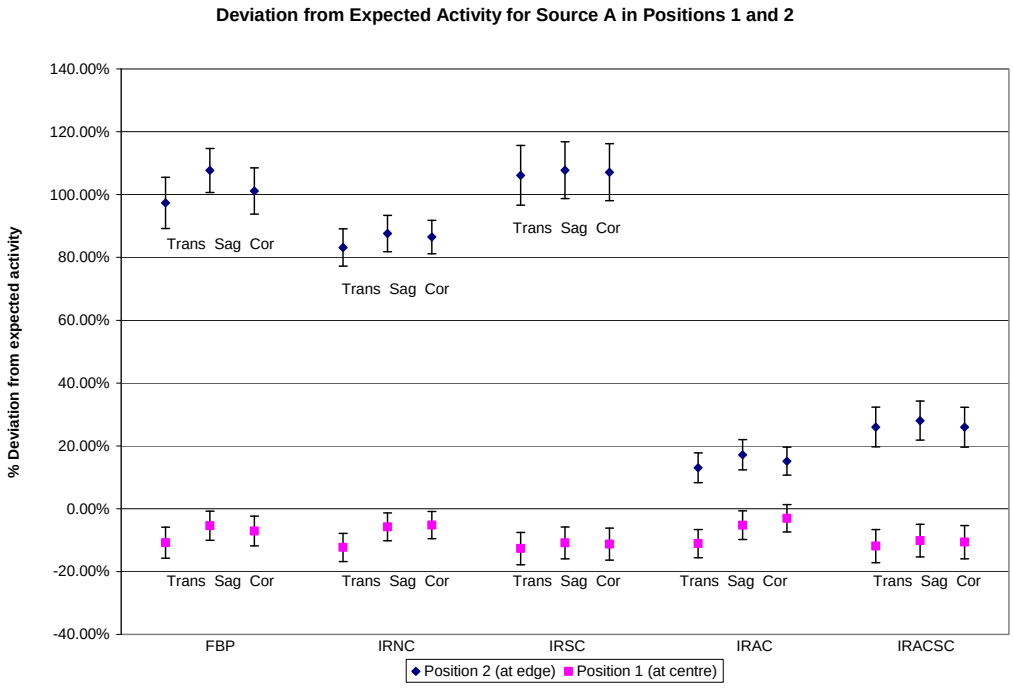

Fig. 6.15 Deviation from expected Activity for Source A in Positions 1 and 2.

Where attenuation correction is not used, the calculated activity is now overestimated by around 80%. The use of attenuation correction improves this, but calculated activities are still overestimated by approximately 10%. This implies that for SPECT imaging as well as for planar imaging, if accurate quantitation is required, the depth of an object within an attenuating material is highly relevant. The use of attenuation correction should therefore be recommended to minimise this effect.

6.4 Quantitation measurements with two sources

For some applications of clinical nuclear medicine (e.g. Tc-99m DMSA renal imaging), absolute quantitation is not required, but rather a measure of relative uptake of radiopharmaceutical between two organs. Two sources were therefore inserted into the cylindrical phantom to model this situation, allowing measurements of absolute activity and relative activity to be made. Two cases were modelled- the symmetrical with both sources positioned equally from the mid-line, and the non-symmetrical with one source in the centre and the other towards the edge of the cylindrical phantom.

Despite the widespread application of SPECT imaging, it is still routine practice to calculate relative renal Tc-99m DMSA uptake based on the geometric mean of planar anterior and posterior images. For this reason, planar anterior and posterior acquisitions were carried out for each phantom geometry and used to calculate relative activities based on the geometric mean. These were compared with the SPECT results with and without corrections for attenuation and scatter, to assess the impact of using SPECT imaging for relative quantitation measurements.

6.4.1 Method

The phantom was set-up as for the rotational orientation measurements in chapter 5 such that two sources could be inserted at positions 2 (edge) and 3 (edge) in the symmetrical case or positions 1 (centre) and 2 (edge) for the non-symmetrical case (See Fig 5. 8) SPECT acquisitions were carried out using the standard acquisition parameters as in Table 6.1, with the following variations:

- activity concentration ratio of Tc-99m between the sources changed to 2:1 with the higher activity concentration in position 2. Activity concentrations of approximately 0.2 MBq/ml and 0.1 MBq/ml were used resulting in activities of approximately 112 MBq and 56 MBq.
- relative volume of the sources changed by using Source B (112 ml) in position 2 and Source A (56 ml) in positions 3 for the symmetrical and 1 for non-symmetrical cases. An equal activity concentration of approximately 0.1 MBq/ml of Tc-99m was used in each case resulting in activities of approximately 112 MBq and 56 MBq respectively.
- background activity concentration changed to approximately 0.5% of Tc-99m resulting in an activity of approximately 32 MBq. Source A was used in both phantom positions for this measurement, filled with an activity concentration of 0.1 MBq/ml.

In all cases, the acquisitions were reconstructed using OSEM iterative reconstruction to yield FBP, IRNC, IRSC, IRAC and IRACSC data sets in the transverse, sagittal and coronal planes. Regions of interest were drawn manually as described in section 5.3. Where two regions were drawn, in the symmetrical case ROI0 was in the 90 degree position and in the non-symmetrical case ROI0 was the central region and ROI1 the edge region.

Planar images were also acquired as previously in the anterior and posterior positions.

SPECT results were expressed in terms of cps/MBq and the ratio of cps/MBq between the two sources. Using the sensitivity calculated in Section 6.2, the results were then converted to an activity and expressed in terms of percentage deviation from the expected activity, defined as that measured in the radionuclide calibrator. The planar images were used to calculate the ratio of cps/MBq between the two sources in anterior and posterior projections and using the geometric mean.

6.4.2 Results – Symmetrical phantom

6.4.2.1 Variation in activity ratio

The results of varying the activity ratio between sources to 2:1 with the sources in symmetrical orientation (2) are shown in Figs 6.16 and 6.17.

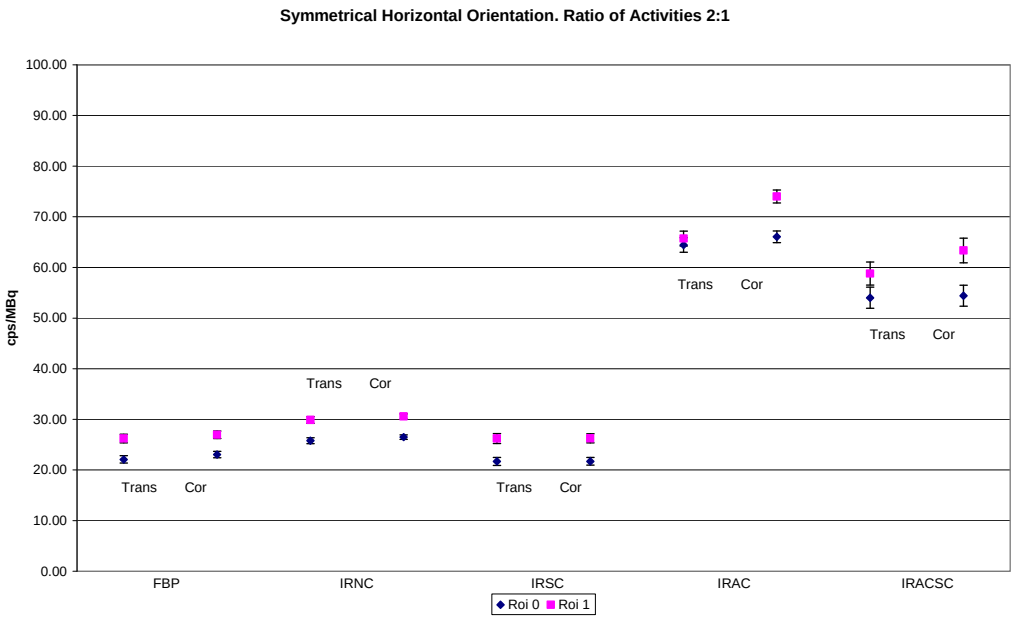

Fig 6.16. cps/MBq for ratio of activities 2:1

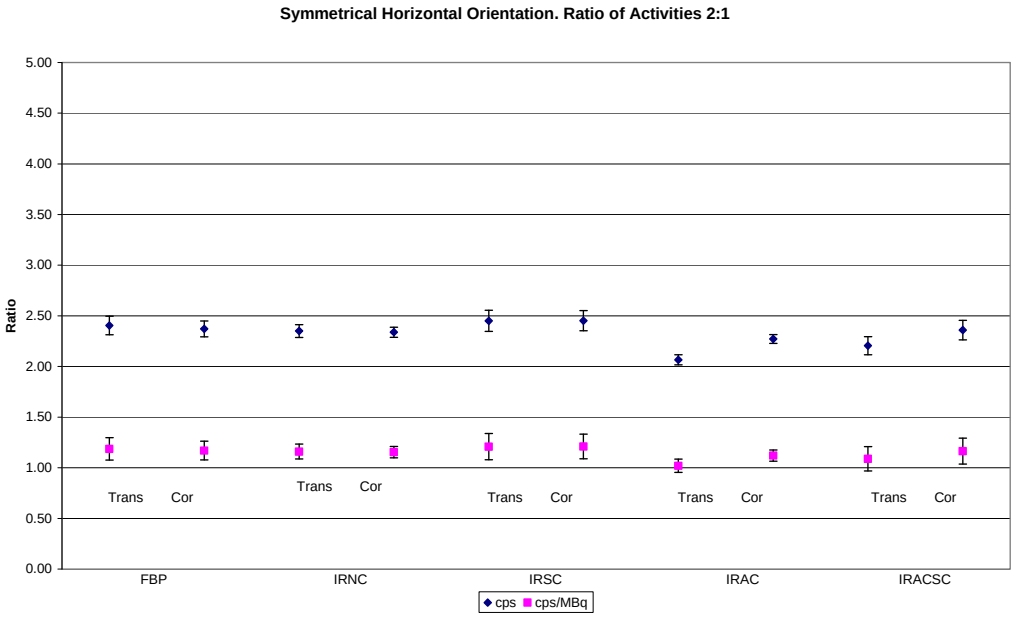

Fig 6.17. Ratios of cps and cps/MBq for ratio of activities 2:1

The planar results of changing the activity ratio are shown in Table 6.4

	Roi 0 cps/MBq	Roi 1 cps/MBq	Ratio 1:0
Head 1	28.12 (46.34%)	32.56 (53.66%)	1.16
Head 2	26.79 (46.89%)	30.34 (53.11%)	1.13
Geometric mean	27.45 (46.62%)	31.43 (53.38%)	1.14

Table 6.4 Planar results for activity ratio 2:1

The results show that unlike the non-symmetrical case, ratios close to the true ratios of 1.0 for cps/MBq and 2.0 for cps can be achieved even without the use of AC. This is as would be expected, since both phantom inserts are an equal distance from the edge of the phantom and therefore subject to an equal amount of attenuation. The planar results show that relative cps/MBq results of 45 -55% can be achieved in the symmetrical case without the need for SPECT. (This figure is significant, since in

clinical nuclear medicine this is taken as the normal relative uptake range in renal studies.)

The results of applying the calculated sensitivity values to these results are shown in Fig 6.18

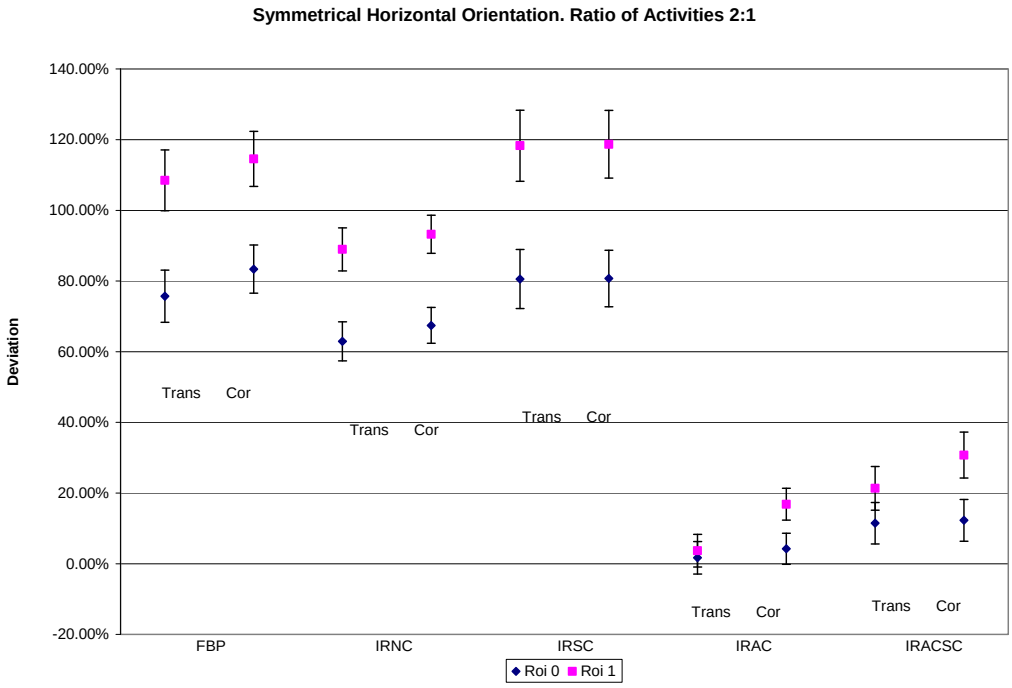

Fig 6.18 Deviation from expected activity for ratio of activities 2:1

The results show that as previously, the amount of activity is overestimated in groups where AC is not applied, due to the geometry of the phantom, but this effect is greatly reduced when AC is applied. For the lower activity source (ROI 0) the deviation is close to zero although in all cases the overestimation is slightly higher for the higher activity source (ROI 1).

6.4.2.2 Variation in volume of cylindrical sources

The results of measurements made with sources of two different volumes (56 ml and 112 ml) are shown in Figs 6.19 and 6.20

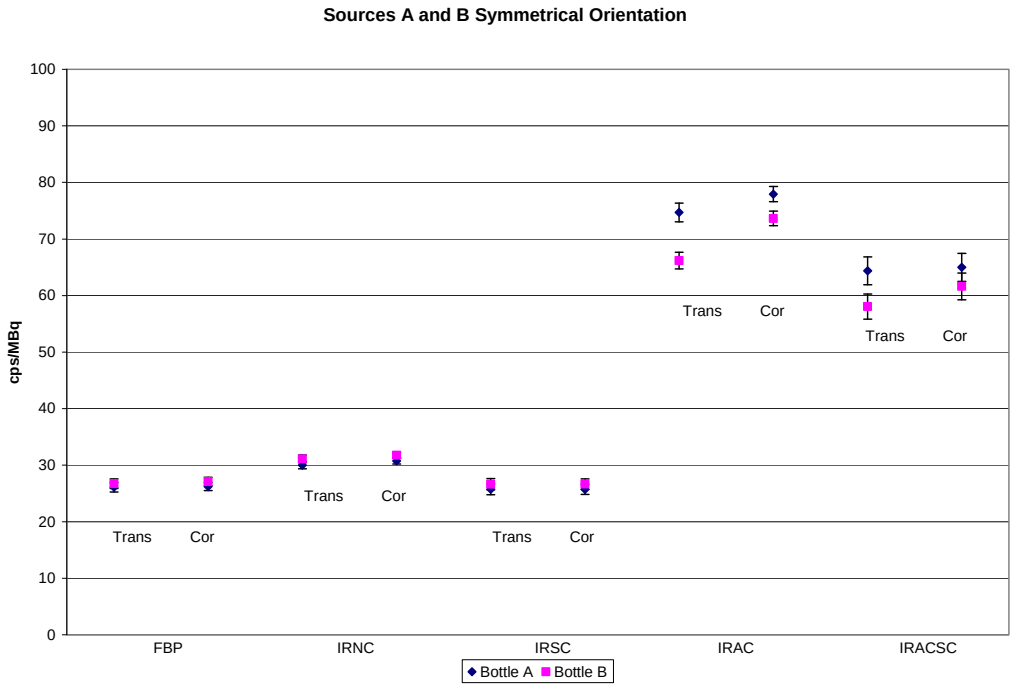

Fig 6.19 cps/MBq for Sources A and B.

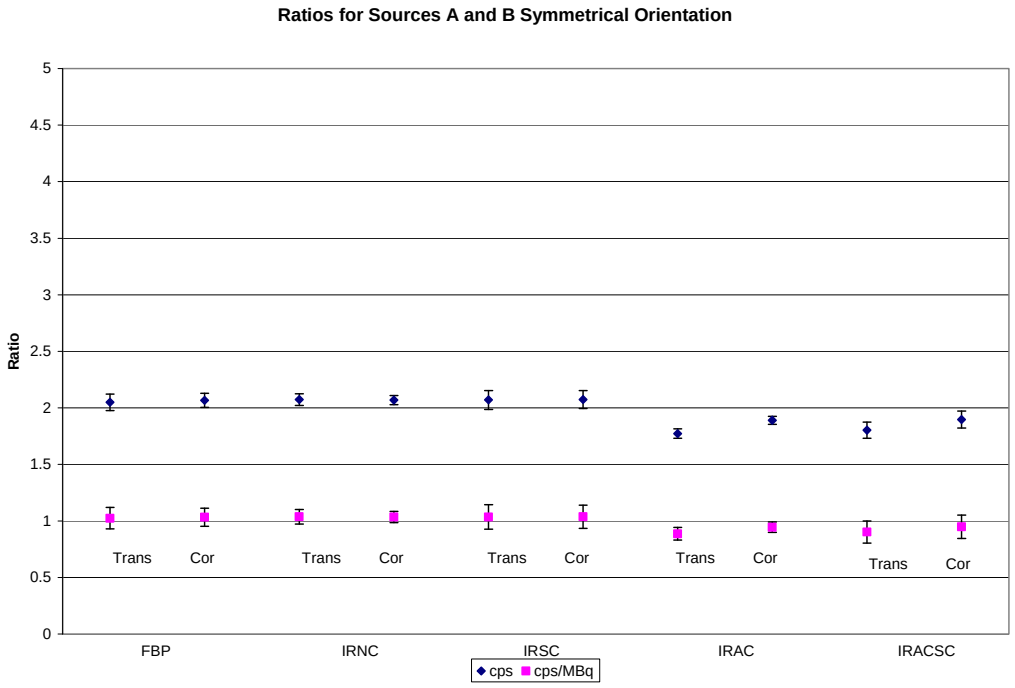

Fig 6.20 Ratios of cps and cps/MBq for Sources A and B.

The planar results for Sources A and B are shown in Table 6.5

	Roi 0 cps/MBq	Roi 1 cps/MBq	Ratio B:A
Head 1	34.25 (50.32%)	33.82 (49.68%)	0.99
Head 2	28.35 (46.75%)	32.29 (53.25%)	1.14
Geometric mean	31.16 (48.53%)	33.05 (51.47%)	1.06

Table 6.5 Planar results for Sources A and B

The results of applying the calculated sensitivity value to the SPECT results are shown in Fig 6.21

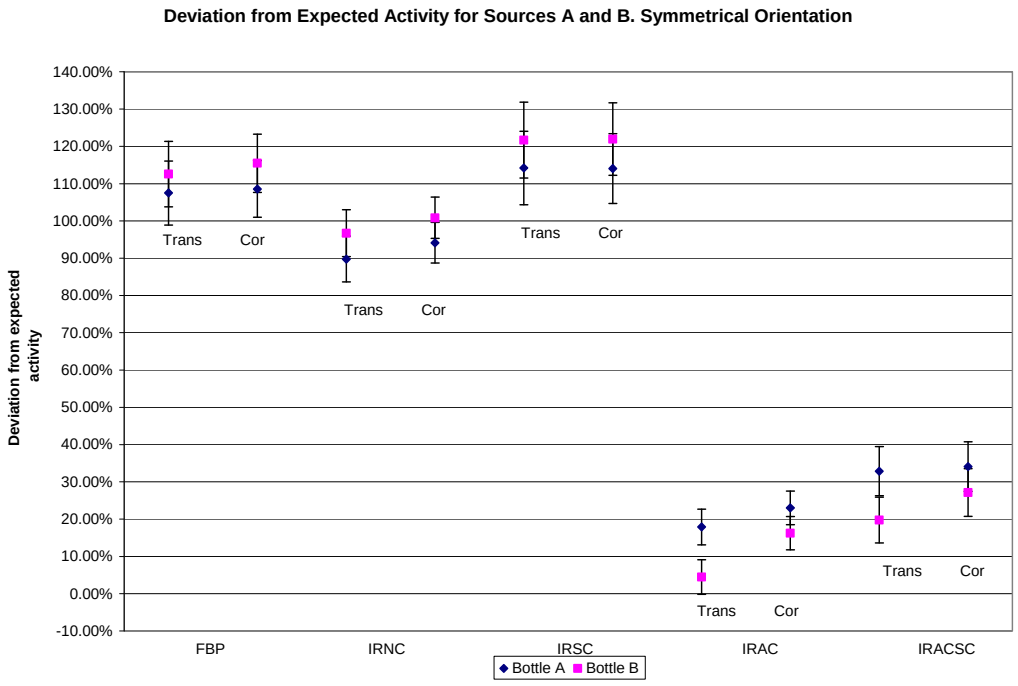

Fig 6.21 Deviation from expected activity for Sources A and B. Symmetrical Orientation.

With the two sources in a symmetrical orientation i.e. both effectively at the edge of the phantom, there is a large overestimation in calculated activity for each source when AC is not applied. With the use of attenuation correction the calculated activities are within approximately 30% of expected values in all reconstruction planes.

6.4.2.3 Variation in background concentration

The effect of adding a background concentration to the symmetrical phantom in terms of cps/MBq is shown in Fig 6.22

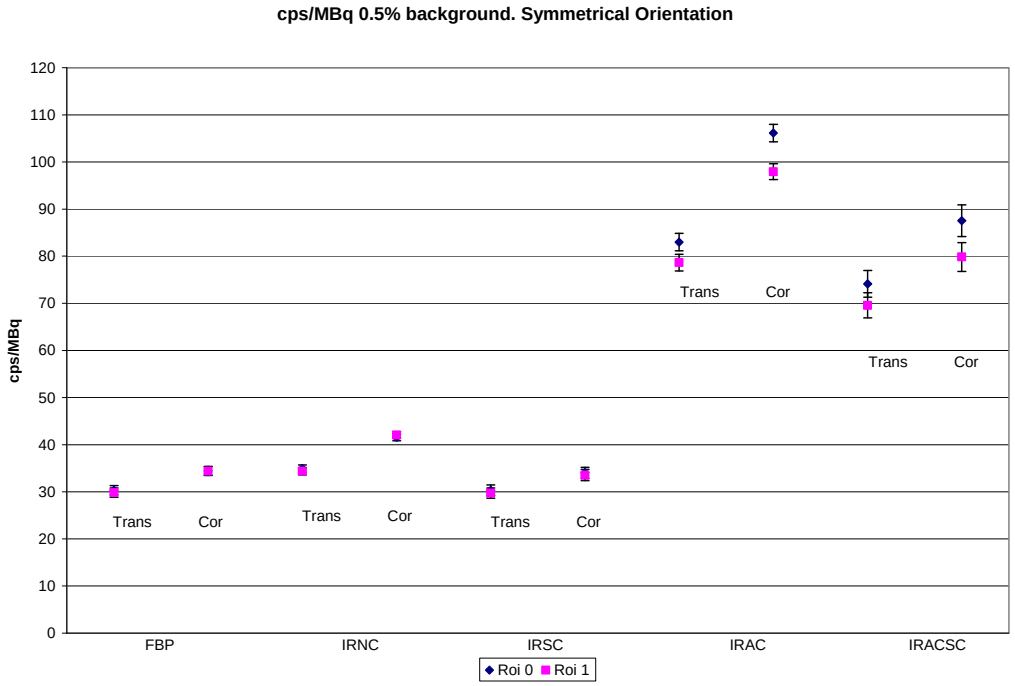

Fig 6.22 Results of cps/MBq with 0.5% background activity

To establish the proportion of counts due to scattered photons, these results were compared with data from the orientation study in chapter 5 (symmetrical orientation 2, Fig 5.12). For ease of comparison the results for ROI 0 were used. The results are shown in Table 6.6.

		No bgd cps/MBq	0.5% bgd cps/MBq	% Increase	Proportion due to scatter (%)
FBP	Trans	26.74	30.33	13.43	11.84
	Cor	27.11	34.46	27.11	21.33
IRNC	Trans	30.77	34.95	13.58	11.96
	Cor	31.36	41.54	32.46	24.51
IRSC	Trans	26.74	30.33	13.43	11.84
	Cor	26.78	34.02	27.04	21.28
IRAC	Trans	75.70	82.99	9.63	8.78
	Cor	79.27	106.12	33.87	25.30
IRACSC	Trans	66.02	74.40	12.69	11.26
	Cor	67.19	87.54	30.29	23.25

Table 6.6 Results of cps/MBq for Roi 0 with and without background.

With background, there is an increase in the number of cps detected as would be expected. The proportion of cps/MBq due to scattered photons ranges between 9% and 12% in the transaxial plane and 21% and 25% in the coronal plane. The addition of scatter correction to the reconstruction algorithm appears to have no effect on the proportion of scattered photons detected.

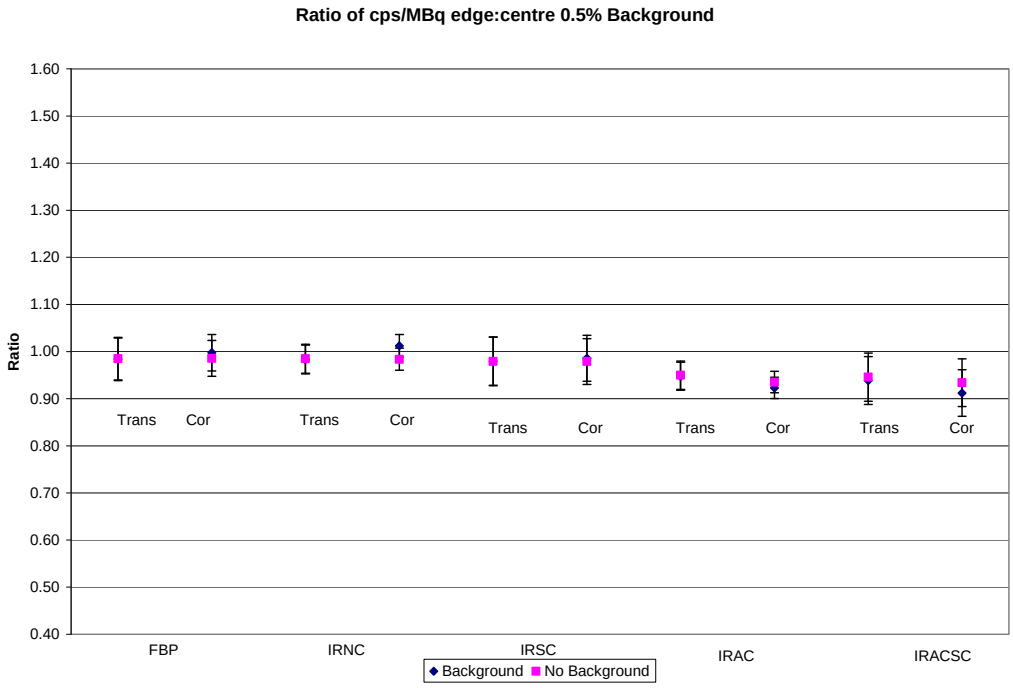

Fig 6.23 Ratio of cps/MBq edge:centre for background concentration 0.5% and no background

As with previous results in the symmetrical orientation, the results are very close to the true ratio of 1.0. This has not been degraded by the addition of background activity.

The planar results for the symmetrical orientation with background are shown in Table 6.7

	Roi 0 cps/MBq	Roi 1 cps/MBq	Ratio 1:0
Head 1	24.79	25.57	1.03
Head 2	22.72	22.53	0.99
Geometric mean	23.73	24.00	1.01

Table 6.7 Planar results for the symmetrical orientation with background

Once again ratios very close to 1.0 can be achieved with simple static acquisitions in the symmetrical orientation and this has not been affected by the addition of background activity.

The results of applying the calculated sensitivity value to these results are shown in Fig 6.24.

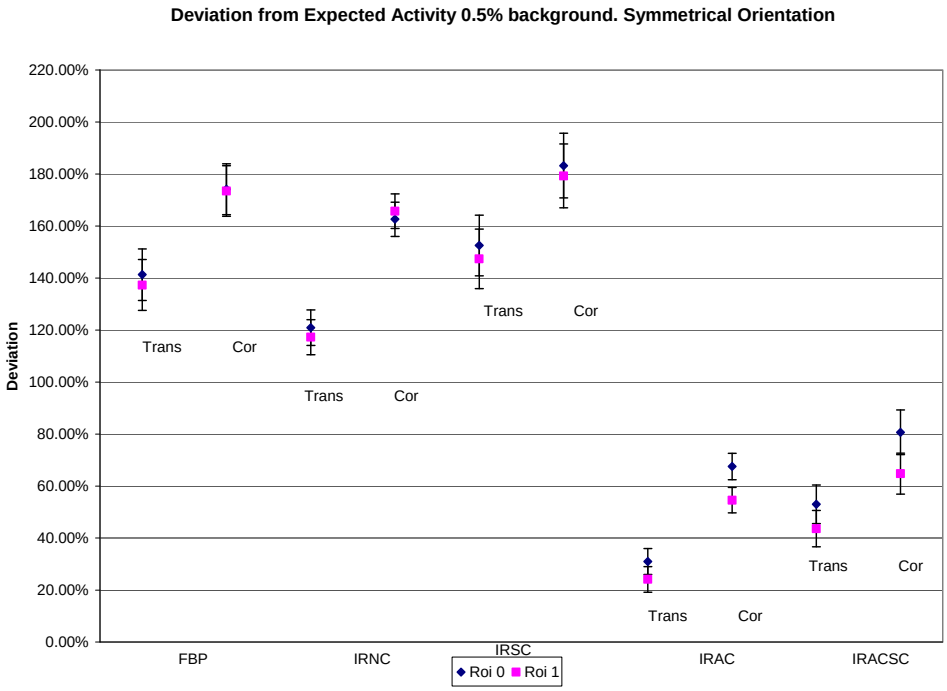

Fig 6.24 Deviation from expected activity with 0.5% background

The addition of background has exacerbated the overestimation of activity in all cases. As with previous results the addition of attenuation correction leads to the best results, but there is no improvement due to the addition of scatter correction alone.

6.4.3 Results – Non-symmetrical phantom

6.4.3.1 Variation in activity ratio

The results of varying the activity ratio between the Sources to 2:1 are shown in Figs 6.25 and 6.26

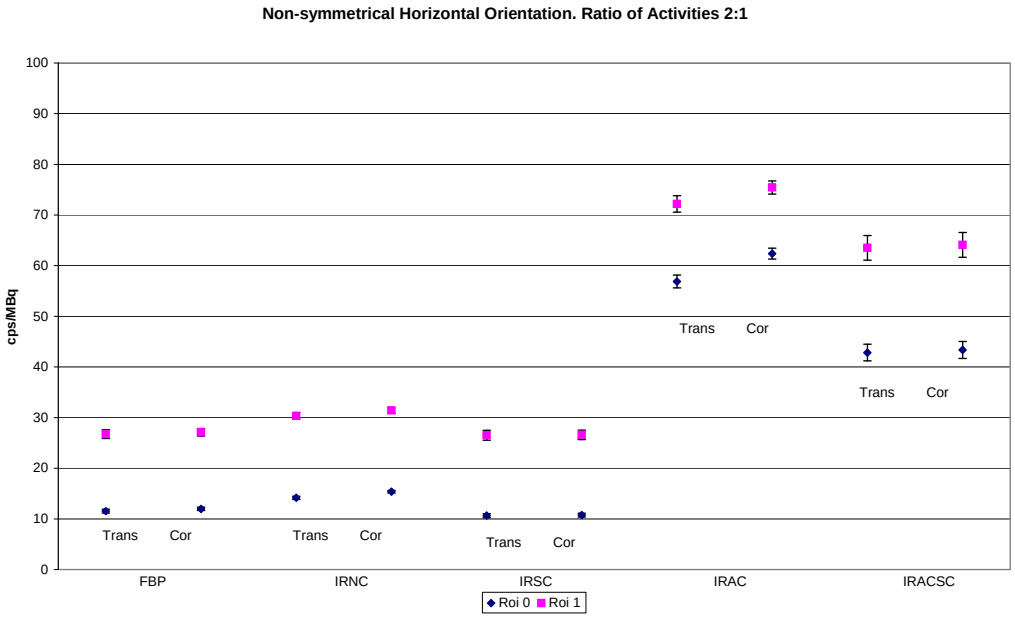

Fig 6.25 cps/MBq for activity ratio 2:1

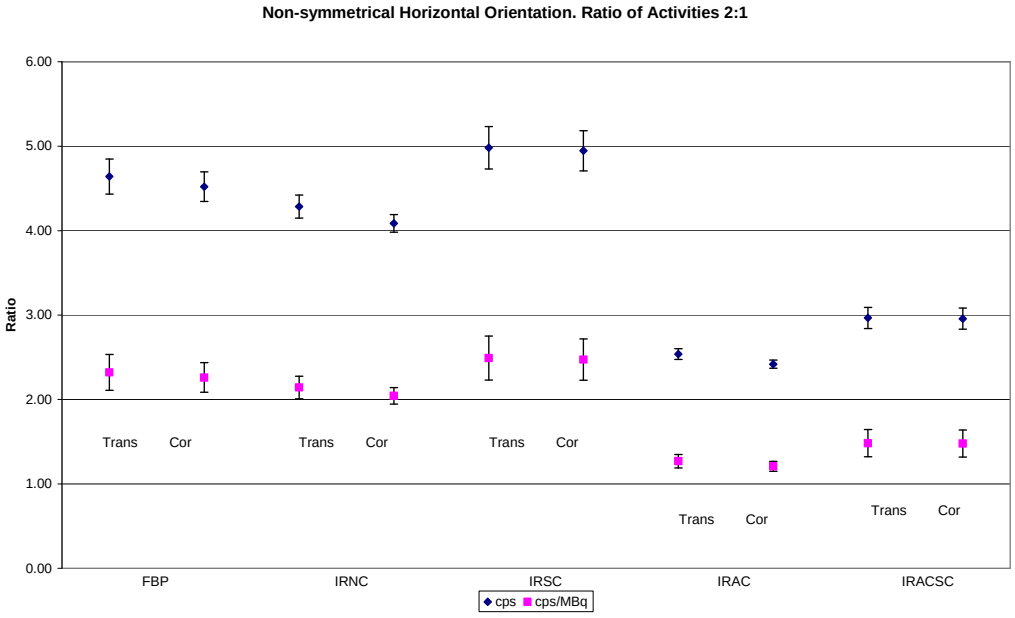

Fig 6.26 Ratio of cps and cps/MBq for activity ratio 2:1

When attenuation correction is added to the method of reconstruction the number of cps/MBq recorded is ~5 times higher for the lower activity source and ~ 2.5 times higher for the higher activity source. Of more relevance here are the ratio measurements. In terms of cps/MBq the true ratio is 1.0. The results show that when AC is not used, this ratio varies between 2.0 and 2.5, implying an overestimation of the proportion of counts in the source closer to the edge of the phantom, while when AC is used this ratio falls to 1.2. Again the results for IRAC are slightly better than those for IRACSC. When expressed in terms of cps the true ratio is 2.0. The results show that when AC is not used this ratio rises as high as 5.0, whilst with AC although there is still some overestimation of the edge source, the ratio falls to 2.5.

The planar results for varying the activity ratio are shown in Table 6.8

	Roi 0 cps/MBq	Roi 1 cps/MBq	Ratio Roi1:Roi0
Head 1	18.12 (34.40%)	34.56 (65.60%)	1.91
Head 2	15.68 (34.39%)	29.92 (65.61%)	1.91
Geometric mean	16.86 (34.39%)	32.16 (65.61%)	1.91

Table 6.8 Planar results for activity ratio edge:centre of 2:1

A ratio of 1.91 was measured in the anterior, posterior and geometric mean cases, again implying that more counts are measured from the source at the edge, relative to that in the centre.

The results of applying the calculated sensitivity values to these results are shown in Fig 6.27.

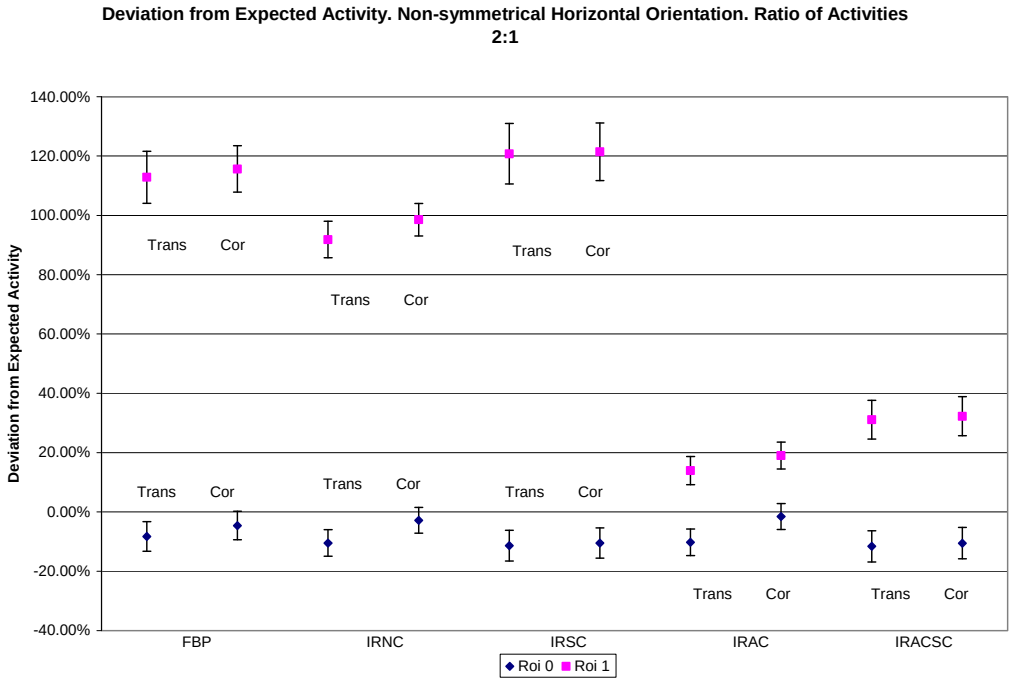

Fig 6.27 Deviation from expected activity for ratio of activities edge:centre of 2:1

Once again it can be seen that a more accurate calculation of activity can be made using AC during reconstruction of the data and using a corresponding sensitivity factor, even for objects at different depths within the phantom and therefore subject to a varying amount of attenuation.

6.4.3.2 Variation in volumes of phantom inserts

The results of imaging sources of two different volumes (56 ml and 112 ml) are shown in Figs 6.28 and 6.29.

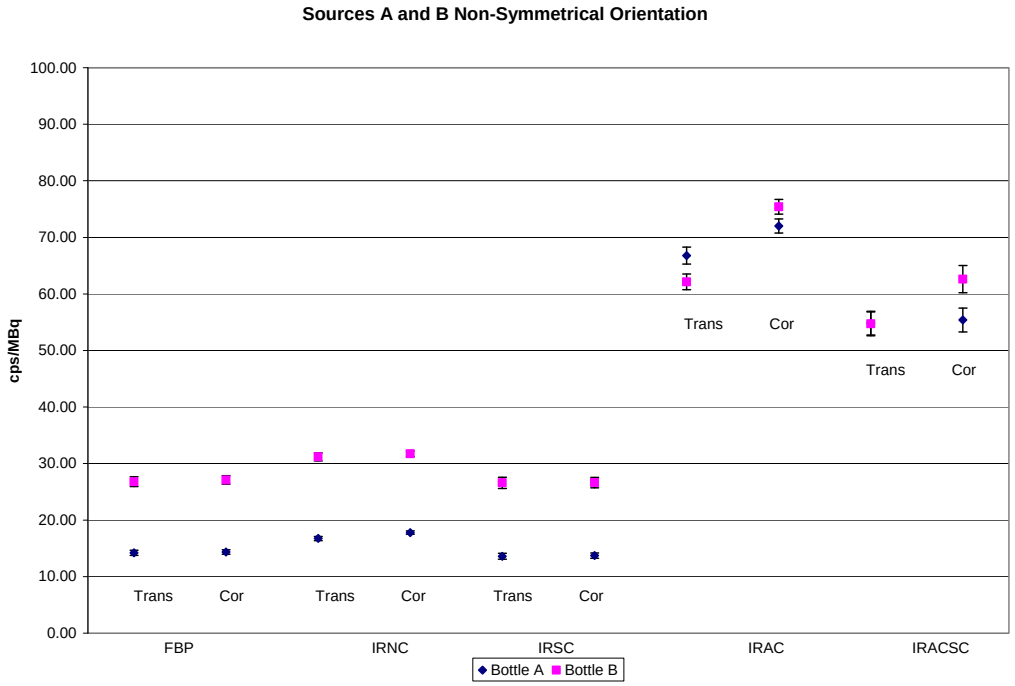

Fig 6.28 cps/MBq for Source A in the centre and Source B at the edge of the phantom

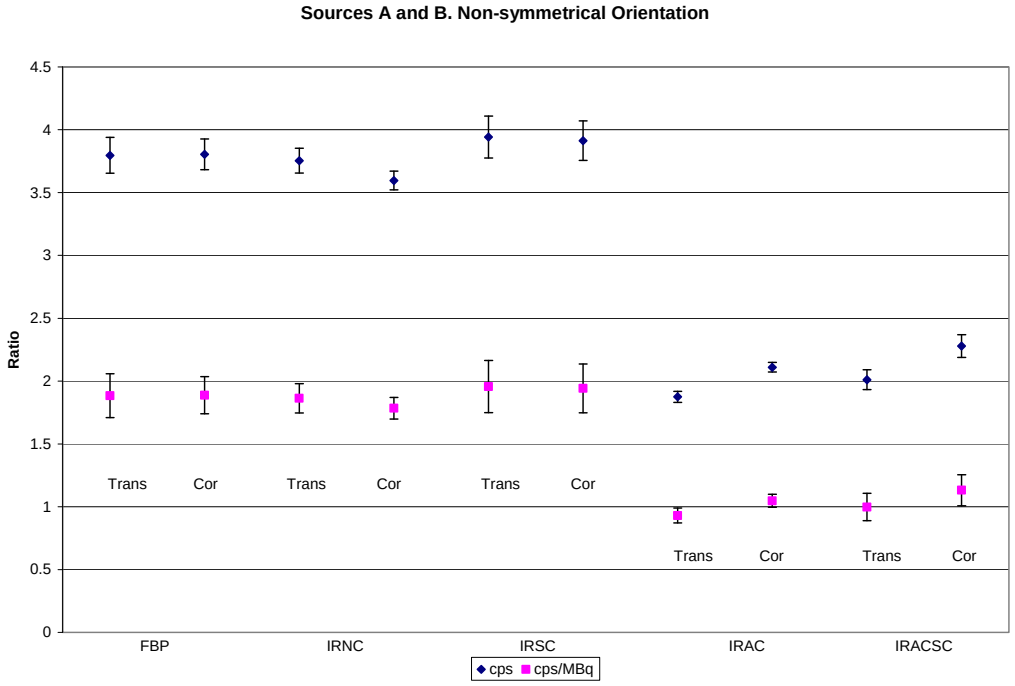

Fig 6.29 Ratios of cps and cps/MBq for Source A in the centre and Source B at the edge of the phantom.

When AC is used in the reconstruction, there is an approximately threefold increase in cps/MBq. It can also be seen that in the IRAC and IRACSC groups the values for both sources are within experimental error of each other, whereas when AC is not applied, higher cps/MBq are recorded for the source at the edge of the phantom, as would be expected from previous results. The ratio results show that when no AC is applied the ratio of cps/ MBq (true value1.0) approaches 2 (1.9 for the IRSC group), but a result of 1.0 is achieved with IRACSC. The ratio of cps which would be expected to be 2.0 given a linear response to activity, approaches 4 (3.9) for non-corrected groups but a ratio of 2.0 is achieved with IRACSC. These results again imply that the overestimation of counts at the edge of the phantom is greatly reduced by the use of AC.

The planar results of varying the volume of the phantom inserts are shown in Table 6.9

	Source A cps/MBq	Source B cps/MBq	Ratio B:A
Head 1	19.40 (35.52%)	35.21 (64.48%)	1.81
Head 2	16.70 (35.49%)	30.36 (64.51%)	1.82
Geometric mean	18.00 (35.50%)	32.70 (64.50%)	1.82

Table 6.9 Planar results for Sources A (centre) and B (edge)

The ratio of 1.82 for planar imaging implies that there is a large overestimation in cps/MBq for the source at the edge of the phantom that is not corrected for by use of the geometric mean.

The results of applying the calculated sensitivity values to the SPECT results are shown in Fig 6.30

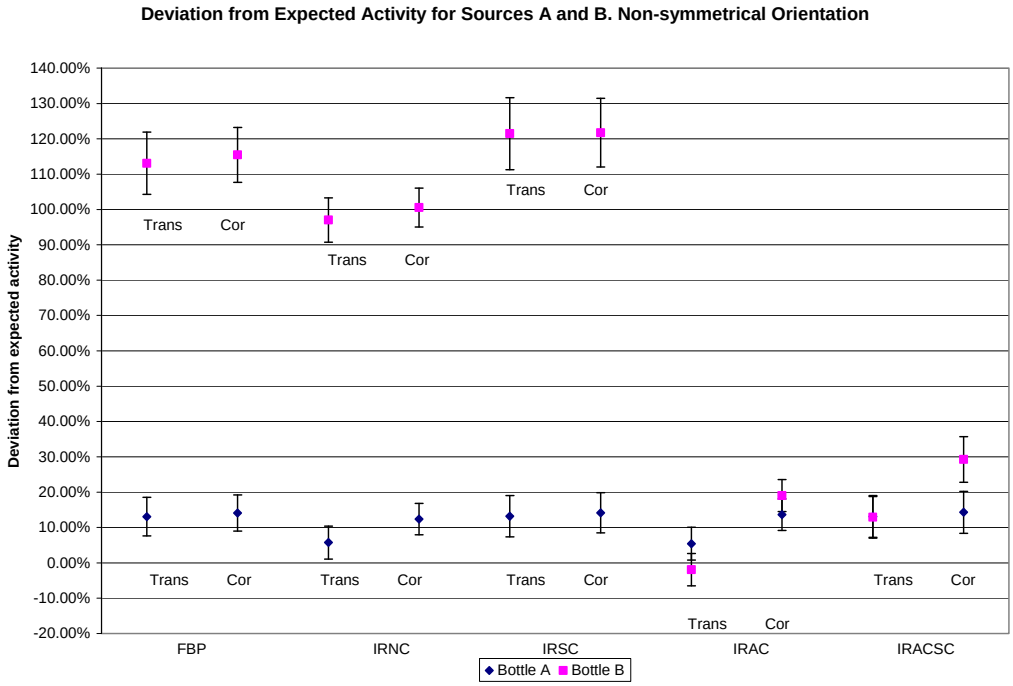

Fig 6.30 Deviation from expected activity for Sources A and B

As expected, there a gross overestimation in calculated counts for Source B (at the edge of the phantom) when no AC is applied, that is corrected for with AC.

6.4.3.3 Variation in background concentration

The effect of adding a background concentration of 0.005 MBq/ml (0.5%) to the phantom, on the measured cps/MBq in the sources is shown in Fig. 6.31. Source A was used in both positions for this measurement with an equal activity concentration ratio.

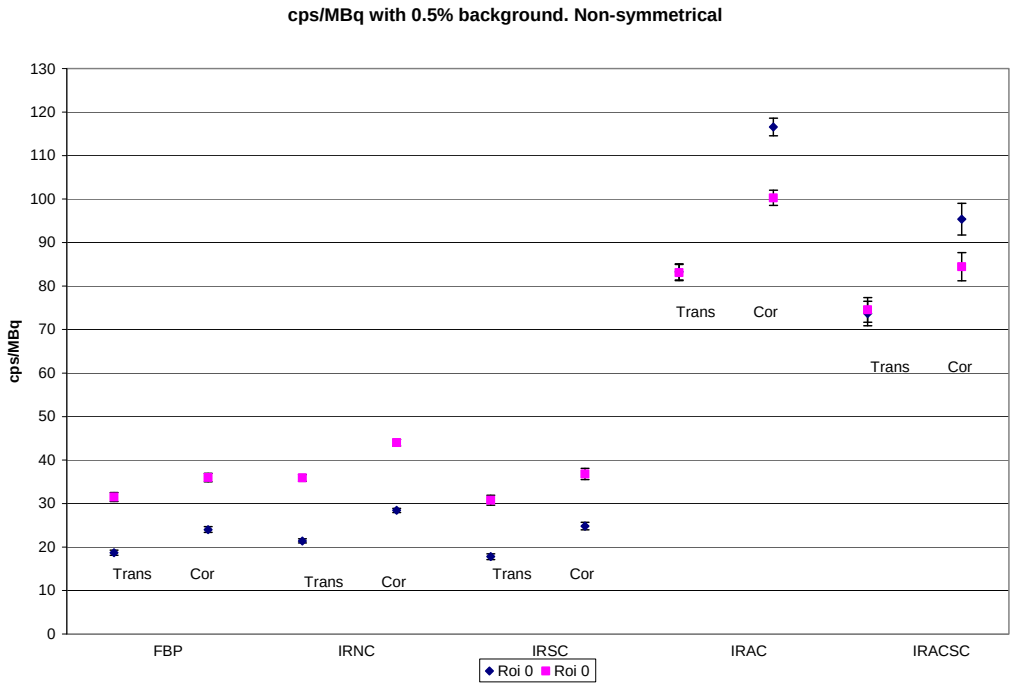

Fig 6.31 cps/MBq with 0.5% background. Non-symmetrical orientation.

These results can be compared with the equivalent geometrical set-up with no background present that was used in the orientation study in Chapter 5 – Fig 5.18 For ease of comparison the cps/MBq figures for the central source with and without background are shown in Table 6.10

		No bgd cps/MBq	0.5% bgd cps/MBq	% Increase	Proportion due to scatter (%)
FBP	Trans	14.32	18.69	30.52	23.38
	Cor	14.70	24.01	63.33	38.78
IRNC	Trans	16.65	21.40	28.53	22.20
	Cor	17.92	28.41	58.54	36.92
IRSC	Trans	13.82	17.78	28.65	22.27
	Cor	13.99	24.82	77.41	43.63
IRAC	Trans	67.29	83.26	23.73	19.18
	Cor	71.55	116.59	62.95	38.63
IRACSC	Trans	55.63	73.68	32.45	24.50
	Cor	56.37	95.38	69.20	40.90

Table 6.10 Comparison of cps/MBq in Roi 0 (centre) with and without background activity

For SPECT images reconstructed into the transaxial plane, there is an increase of approximately 30% in measured cps/MBq caused by scattered photons due to background activity. Another way of expressing these results is as the proportion of the cps/MBq in the final image when background is present that are therefore due to scatter. The results in Table 6.10 show that for transaxial slices this figure varies between 22% and 25% and for the coronal slices, between 37% and 41%. These figures are in good agreement with the recognised figure of 30% of counts in a planar image being due to scattered photons. Perhaps surprisingly, the addition of scatter correction to the reconstruction process does not seem to reliably improve this figure.

Fig 6.32 shows the edge;centre ratio of cps/MBq for both the non-background and with background cases.

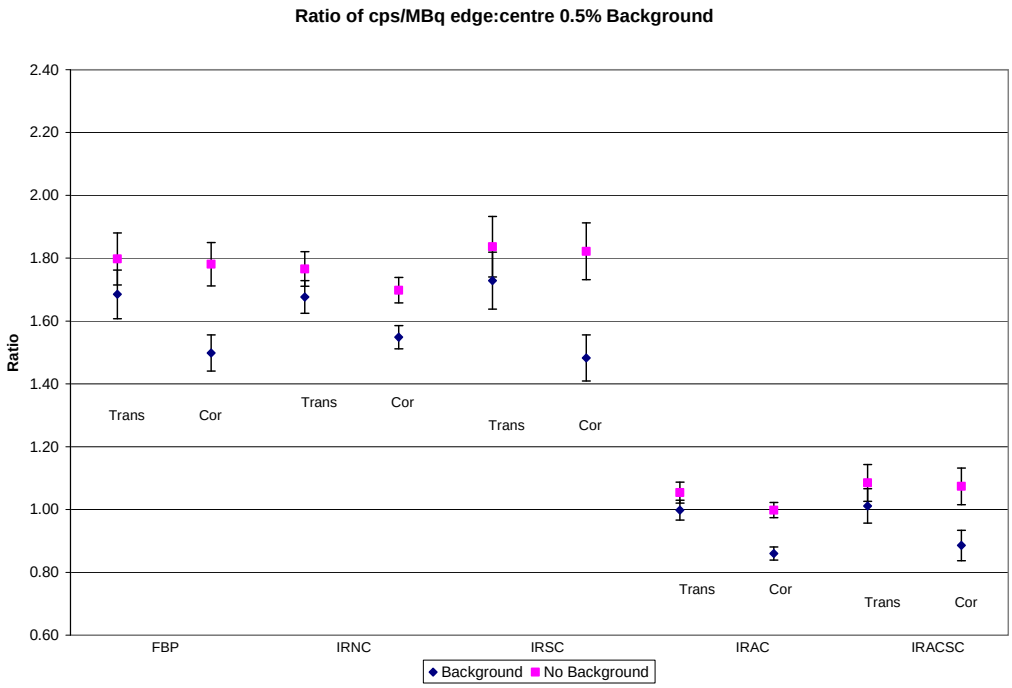

Fig 6.32 Ratio of cps/MBq edge:centre with and without background

In all cases, the ratio of cps/MBq between the source in the edge and that at the centre of the phantom is lower when background activity is present. This implies that scattered photons from the background activity have a proportionately higher influence on the source at the centre of the phantom to that at the edge. This is as would be expected, since the source at the centre is subject to a greater volume of surrounding background material than that at the edge. Again these results show no significant improvement due to scatter correction.

The planar results for the phantom with background activity are shown in Table 6.11

	ROI 0 cps/MBq	ROI 1 cps/MBq	Ratio 1:0
Head 1	14.73	27.45	1.86
Head 2	14.83	25.37	1.71
Geometric mean	14.78	26.39	1.79

Table 6.11 Planar cps/MBq results for 0.5% background

As with earlier planar results, the ratio of 1.79 implies an overestimation in cps/MBq for the source at the edge of the phantom that is not corrected for by use of the geometric mean.

The results of applying the calculated sensitivity value to the SPECT results are shown in Fig 6.33

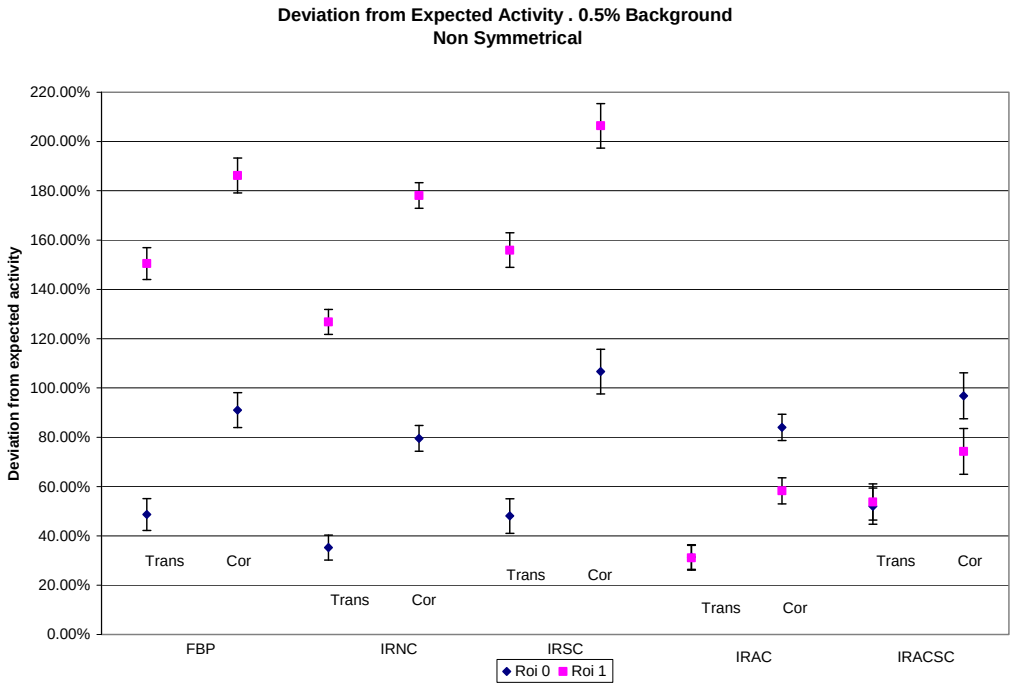

Fig 6.33 Deviation from expected activity with 0.5% background

There is a much larger deviation from the expected value than was found in non-background cases, even with the addition of attenuation and scatter correction. This is as may be expected due to the noted increase in measured cps due to scattered photons, which would translate into an increase in the calculated activity.

There is also a noticeable variation in the results between the transverse and coronal planes for these results. The reason for this is not clear and would warrant further investigation in this area.

6.5 Discussion

The aim of this chapter was to establish whether a single sensitivity value could be established for SPECT imaging in order to carry out accurate quantitation. As described in section 6.2 the sensitivity value calculated in terms of cps/MBq is dependent on the method of reconstruction, the volume of the source used and the amount of attenuation it is subject to. For this reason, it was shown that the use of attenuation correction (AC) is essential for accurate quantitation of a single source of differing acquisition geometries both in the establishment of the sensitivity value and the reconstruction of the data to which it is applied. The addition of scatter correction (SC) to AC has little effect and SC alone shows no improvement in quantitative accuracy over reconstructions using filtered back projection (FBP) and iterative reconstruction with no corrections (IRNC).

The results of the two source measurements also clearly show the influence of attenuation on quantitative results. When no correction for attenuation was made, there was a gross overestimation of calculated activity for sources subject to less attenuation than that inherent in the sensitivity measurements. This would imply that without AC a separate sensitivity value would need to be found for every geometrical situation. Although only water was used as an attenuating medium in these experiments, it would also hold true that quantitative results would vary with differing values of attenuation coefficient as are found in clinical situations. With AC, the deviation in calculated activity measurements

was improved to ~20-30%, for all, activity ratios, phantom sizes and background concentrations investigated.

The results of finding the ratios of cps/MBq for two sources in both symmetrical and non-symmetrical orientations showed that accurate results could be achieved in the symmetrical case even without the use of AC, since both sources were subject to the same amount of attenuation. In fact, in the symmetrical case accurate ratios (implying accurate relative counts) could be found using planar imaging and correcting for depth using the geometric mean. The same was not true in the non-symmetrical case where the two source were subject to a different amount of attenuation – a larger amount for that in the centre than for that at the edge. In this case, the use of AC was imperative in achieving accurate ratio results.

These results are significant for renal uptake measurements using Tc-99m DMSA where the standard method is to carry out planar imaging and calculate relative kidney uptake using the geometric mean method. These results show that if the kidneys are truly symmetrical in terms of being subject to the same amount of underlying and overlying tissue then this method is acceptable. However if there is a non-symmetrical distribution of attenuating background tissue then the use of SPECT with AC would give a more accurate measurement of relative uptake.

Chapter 7

Conclusions and Further Work

7.1 Conclusions

7.1.1 Introduction

Due to their well documented beneficial effect on image quality (Bockisch et al. 2009; Mariani et.al 2010), the use of attenuation correction and scatter correction in SPECT has become widely used in clinical Nuclear Medicine. All major manufacturers now supply the facility for doing this on most gamma camera systems, with no necessity for the user to understand the effect of these corrections on the actual count rate being recorded. Whilst this may be acceptable in qualitative imaging, there is a growing appreciation of the potential for accurate quantitation in nuclear medicine (Bailey and Willowson 2013), which requires a more thorough understanding of the effects of individual and combined corrections.

In recent years, a number of physical phantom based studies have been carried out to investigate absolute quantitation in SPECT using a variety of isotopes, correction techniques and methods for determination of absolute activity. A selection of these were summarised by Shcherbinin et al. (2008) and are shown in table 7.1 reproduced from their paper. Their own study investigated quantitative accuracy of SPECT/CT imaging for Tc-99m, In-111, I-123 and I-131 isotopes using the GE Infinia Hawkeye 4 slice SPECT/CT

system and incorporating corrections for attenuation, scatter, collimator blurring and collimator septal penetration. They achieved activity estimates with error levels of 3-5% for all of the isotopes when all of the above corrections were combined.

Study	Radiotracer	Camera	Results of absolute quantitation
He et al. (2005)	In-111	GE Discovery VG/Hawkeye	2-12% errors for 6 and 20 ml spheres
De Wit et al. (2006)	Ho-166	ADAC Vertex MCD	1-13% errors for 220 ml cylindrical containers
Du et al. (2006)	I-123	Siemens E-cam	2% errors for regions of brain phantom
Koral et al. (2007)	I-131	Prism 3000	1-24% errors for 7-135 ml spheres
Vandervoort et al. (2007)	Tc-99m	Siemens E-cam	4% errors for 18 ml heart chamber

Table 7.1 Parameters and results of sample quantitative SPECT studies with physical phantoms. (Shcherbinin 2008)

Due to the variety of gamma camera systems and methods of correction used in quantitative studies, the purpose of this project was to investigate a single SPECT/CT system – the GE Millennium VG Hawkeye gamma camera with single slice CT attenuation correction and dual window scatter

correction. The hypothesis to be tested was ***"accurate attenuation correction is essential for quantitative gamma camera imaging".***

The conclusions from this single system will support establishment of a more standard methodology for quantitative gamma camera imaging using any SPECT/CT system.

7.1.2 SPECT performance phantom measurements

The first conclusion to be drawn was that:

The addition of attenuation correction to SPECT images of a uniform SPECT performance phantom, increased the number of raw projection counts recorded by a factor of 2.2 (220%).

This result is consistent with reconstructed images of the same phantom which clearly showed that without correction, self attenuation leads to a reduction in counts towards the centre of the phantom compared with the edges. The results of measuring the uniformity of the images reinforced this point, with the uniformity of reconstructions carried out with AC being far superior to those reconstructions without AC – deviation from measured activity of 6.67% IRAC compared with 26.00% FBP.

The next point found was :

Scatter correction, removes counts from the raw data by a factor of 1.3 (23%).

In clinical planar imaging, it is accepted that ~30% of counts in a region of interest are due to scattered counts from outside the region (Hutton 2011). In this study, a lower figure was expected since scatter occurs only within the phantom in the absence of any external source of scattered photons. The lower count rate did prove to have an affect on image uniformity, with results for images reconstructed with scatter correction only (IRSC) being on average slightly worse than those reconstructed with FBP. (~27.0% vs. 26.0%). The addition of scatter correction to attenuation correction also had a negative impact on uniformity, which may be a cause to question the use of scatter correction at all in nuclear medicine imaging. However, scatter correction was seen to have a positive impact in contrast measurements. The results of measuring the contrast between the myocardial wall and cavity in the cardiac insert of the anthropomorphic phantom, showed that scatter correction had more impact on the results than attenuation correction and led to an increase in contrast when added to AC alone (64.99% IRACSC vs. 58.51% IRAC). The best contrast measurements were found with FBP alone (72.23%). The results suggest that although AC has a significant and positive effect on uniformity which makes its use in quantitative studies essential, it has a detrimental effect on image contrast, which can to some

extent be compensated for by the use of scatter correction. These findings agree with those of El Fakhri et al (2000) who also found attenuation correction to be the most significant correction for uniformity, where-as scatter correction had the most impact on contrast measurements. It can be concluded that:

The use an iterative reconstruction algorithm including attenuation correction and scatter correction is to be recommended for all SPECT imaging.

7.1.3 Establishment of s SPECT sensitivity value

The results of establishing a sensitivity value for use in quantitative SPECT imaging showed that:

Unlike planar imaging, it is not feasible to calculate one sensitivity value in cps/MBq using a standard set of acquisition parameters and apply this to all imaging situations.

Sensitivity values calculated in SPECT imaging are highly dependent on the volume of the source, due to the partial volume effect for small sources (diameter <2 times FWHM) and the effect of self attenuation for large sources such as the Jaszczak phantom. In this study, values varied from 89.08 cps/MBq for a point source to 12.57 cps/MBq for source A, when no corrections were applied. Sensitivity values also varied hugely with the use of attenuation correction and to a lesser extent with scatter correction in the

reconstruction algorithm, as would be expected from the known effect that these corrections have on the number of counts recorded. For source A, values varied from 12.01 cps/MBq with scatter correction only, to 63.36 cps/MBq with attenuation correction only.

This method of establishing sensitivity values was similar to that used by Dewaraja et al. (2005) in their I-131 therapy dosimetry study. They considered three calibration geometries: a) a point source in air, b) an elliptical tank with uniform activity and c) a hot sphere centred in an elliptical tank with background activity. They found that quantitation with the sphere based sensitivity was superior to that using the uniform tank. Although there was little difference between results using the sphere and point source based sensitivity, results with the point source were very dependent on the size of ROI drawn around the reconstructed images and so the sphere based sensitivity value was chosen for the remainder of the quantitative study. In contrast, Zeintl et al. (2010) carried out an investigation into quantitative accuracy of Tc-99m SPECT/CT using a sensitivity value base on a large cylindrical phantom (diameter 216 mm, height 186 mm), whilst Shcherbenin et al. (2008) carried out their study using a sensitivity value found from planar images. Despite these differences in methodology, these authors were all able to report good quantitative accuracy when corrections for attenuation, scatter and collimator response were applied.

7.1.4 Quantitative Measurements

In this present study, when the range of sensitivity values found for the different geometries were used for absolute quantitation, the dependence on attenuation correction was clear. Quantitative results were expressed in terms of percentage deviation of the calculated activity from the activity in the phantoms as measured on the radionuclide calibrator (referred to as the expected activity). Without attenuation correction, deviations reached >100% where-as when attenuation correction was included all deviations were <30%. The addition of scatter correction made only a small difference to these results - repeated measurements are now needed to establish the statistical significance of this difference.

It can be concluded from these results that:

The best way of achieving accurate quantitation in SPECT imaging is to reconstruct all images using an iterative reconstruction algorithm including attenuation correction and possibly scatter correction.

Absolute activities should be calculated using a sensitivity value found using attenuation correction in the SPECT reconstruction of calibration phantom images where the phantom is large enough to avoid the partial volume effect. This calibration phase is essential for quantitation and should be carried out locally on any SPECT/CT system where quantitative results are required.

The dependence of accurate quantitation on attenuation correction is also clear from the results of the relative uptake measurements. It was found that:

For a completely symmetrical orientation i.e. when both bottles were subject to the same amount of surrounding attenuating medium, planar measurements in the anterior and posterior projections gave relative count rate results comparable with SPECT imaging when corrected for background and using the geometric mean method to compensate for depth. For the non-symmetrical orientation i.e. when the two bottles are subject to differing amounts of attenuation, the most accurate relative count rate results were found using SPECT reconstruction with attenuation correction.

7.1.5 Clinical applications of quantitation

If these results are extended to a clinical situation where relative uptake is of importance, for example static renal cortex imaging using Tc-99m DMSA, it can be surmised that:

If the kidneys are known to be lying symmetrically within the body (as shown by ultrasound for example), there is little to be gained from using SPECT with CT attenuation correction.

The decision to use this would have to be weighed up against the longer scanning time for the patient and the extra radiation dose from the CT. The effective dose from an abdomen-pelvis scan using the Hawkeye has been

found to be 1.5 mSv (Sawyer et. al. 2008) although the exact figure would obviously depend upon the number of slices needed. Compared with the effective dose from a Tc-99m DMSA scan of 0.7 mSv however, it can be seen that the addition of CT to kidney imaging represents a significant increase in patient dose, which would be difficult to justify in the simple case, especially for paediatric patients. Current BNMS guidelines for renal cortical scintigraphy recommend the use of planar anterior and posterior views rather than SPECT imaging (BNMS 2011), citing a lack of consensus in current literature on the usefulness of SPECT, (with no corrections) in this application (EANM 2011, Piepsz et al. 1999, De Sadeleer et al. 1996). However, the results of this study have suggested that:

If the kidneys are known or suspected to be in an abnormal position within the body, then SPECT with attenuation correction would give more accurate relative uptake results and the extra radiation burden to the patient may be justified.

Brain imaging of the dopaminergic system using I-123 labelled ioflupane (DaTSCAN) is another area where relative uptake between the left and right striata could be a useful clinical indicator and further studies are required to investigate this. Here however, previous studies have found that because of the small size of the striata the partial volume effect becomes significant and correction for this must be included for accurate quantitation (Buvat et al. 2000, Soret et al. 2003).

Despite the potential of quantitative SPECT imaging and the widespread availability of SPECT/CT systems, in their review of 2013 Bailey and Willowson concluded that “Few clinical applications of quantitative SPECT exist today because SPECT has generally been developed without routine application of corrections for attenuated and scattered radiation. The major application of attenuation correction in SPECT to date has been in the area of removing attenuation artefacts in SPECT myocardial perfusion imaging (Heller 2004) but the emphasis has not been on quantitative assessment” (Bailey and Willowson 2013). It is the opinion of the author that:

With careful establishment of sensitivity calibration factors for the imaging system used and with application of corrections for attenuation and scatter in the SPECT reconstruction process, quantitation in nuclear medicine will prove to be accurate and reliable and its use in clinical applications, particularly dosimetry for targeted radionuclide therapy, will continue to grow.

7.2 Further work

7.2.1 Incorporation of resolution recovery

This study used simple phantom measurements to investigate the quantitative effects of attenuation correction and scatter correction on images acquired using the GE Millenium Hawkeye gamma camera with single slice CT. Attenuation and scatter are not the only factors affecting accuracy of quantitation, 3D resolution recovery (RR) also has a part to play

and several phantom studies have already been published with the inclusion of this (Shcherbinin et al. 2008, Zeintl et al.2010). In Shcherbinin's study, resolution recovery was included in all reconstructions and corrections for attenuation and scatter were sequentially added. Errors in calculated activity of a source of Tc-99m placed centrally in an anthropomorphic phantom varied from 84.3% with RR and no other corrections to 21.4% with the addition of attenuation correction and 2.9% with the further addition of scatter correction (Shcherbinin et al. 2008). Zeintl's group carried out a quantitative phantom study with corrections for attenuation, scatter and resolution recovery and then carried out an in vivo validation using SPECT/CT datasets from patients undergoing Tc-99m diphosphonate examinations of the pelvis including the bladder. The radioactivity in the patients' urine served as the gold standard. Their results showed a mean accuracy of 3.6% (SE 8.0%) for the phantom studies and 1.1% for the patient studies (Zeintl et al. 2010). Resolution recovery could not be included in this current study, as the facility is not available on the gamma camera system used. However, manufacturers are now making resolution recovery software available on many systems, so the first phase of follow on work from this study would be to carry out further phantom measurements, with the addition of resolution recovery. The relative impact of the three types of correction could then be established. A further question to be asked is, 'In a clinical setting, could the appropriate use of corrections lead to a lower amount of radiopharmaceutical being administered to the patient?'

This may be particularly relevant in light of recent worldwide shortages of Mo-99. It should also be noted that the Hawkeye system used for this study utilises single, 10 mm thick CT slices, where-as the more recent SPECT/CT systems utilise 4 or more slice CT. The quantitative effect of using higher resolution attenuation correction maps also needs to be investigated.

7.2.2 Use of Monte Carlo modelling

This study was carried out using physical phantoms with a limited number of geometrical orientations. A more flexible way of modelling a wide variety of situations would be to use the statistical method of Monte Carlo modelling. This method has been applied to date in many areas of nuclear medicine including; detector modelling and systems design, image correction and reconstruction techniques, internal dosimetry and pharmokinetic modelling (Ljungberg 2002; Ljungberg 2003; Haidi 2003; Ljungberg 2011; Saeedzadeh 2012). A detailed consideration of Monte Carlo modelling is outside the scope of this study, but a review of Monte Carlo techniques in nuclear medicine can be found by Zaidi (1999).

7.2.3 Clinical studies

From phantom measurements the benefit of SPECT imaging with attenuation and scatter correction for sources in a symmetrical geometry remains unclear. To investigate this in a clinical setting, a study could be carried out on patients undergoing static renal imaging using Tc-99m DMSA,

to assess relative kidney function. Results found using SPECT imaging with the addition of attenuation correction, scatter correction and where available resolution recovery, could be compared with results from the standard geometric mean method to assess whether there is a significant difference in results and whether this would have an impact on patient management. In terms of absolute uptake, quantitative results could be compared with the common laboratory criteria for kidney function: serum creatinine and creatinine clearance. In their work on individual kidney function, Groshar et al.(1991) found a good correlation between the uptake of Tc-99m-DMSA measured by quantitative SPECT with renal function measured by serum creatinine (r = 0.89) and creatinine clearance (r= 0.76) even though corrections for attenuation and scatter were not included.

7.3 Summary

In summary, this study has proved the hypothesis that:

Accurate attenuation correction is essential for quantitative gamma camera imaging.

Scatter correction and 3D resolution recovery also improve overall accuracy. Sensitivity values for conversion of cps into MBq should be found locally prior to beginning quantitative work, using the same acquisition parameters and corrections as to be used for the clinical study and using a phantom large enough to avoid the partial volume effect. In terms of relative

quantitation studies, the reliance on attenuation correction is less clear and further clinical studies are needed to establish the benefit of carrying out CT attenuation correction when weighed against the increased radiation dose to the patient. The widespread availability of SPECT/CT gamma cameras now means that in addition to improved localisation capabilities leading to improved detection ability (Bockisch et al. 2009), accurate quantitation in nuclear medicine is now feasible and of benefit in an increasing number of clinical applications.

References

Amro H.W., Dewaraja S.J., Roberson Y.K. et al. (2010). "Methodology to incorporate biologically effective dose and equivalent uniform dose in patient specific 3 dimensional dosimetry for non-Hodgkin lymphoma in patients targeted with I-131 tositumomab therapy." Journal of Nuclear Medicine **51**(4): 654-9.

Anagnostopoulos C., Harbinson M. et al. (2003). "Procedure guidelines for radionuclide myocardial perfusion imaging." Nuclear Medicine Communications **24**: 1105-1119.

Anger H. O. (1958). "Scintillation camera." Review of Scientific Instrumentation **29**: 27 - 33.

Anger H. O. (1964). "Scintillation camera with multichahnnel collimators." Journal of Nuclear Medicine **5**: 515 - 31.

Armstrong I., Arumugam P. et al. (2012). "Reduced-count myocardial perfusion SPECT with resolution recovery." Nuclear Medicine Communications **33**(2): 121-129.

Bailey D. L., Hutton B. F. et al. (1987). "Improved SPECT using simultaneous emission and transmission tomography " Journal of Nuclear Medicine **28**: 844 -51.

Bailey D. ,Willowson K. (2013). "An evidence-based review of quantitative SPECT imaging and potential applications." Journal of Nuclear Medicine **54**: 83-89.

Barwick T.D., Dhawan R.T., Lewington V. (2012). "Role of SPECT/CT in differentiated thyroid cancer." Nuclear Medicine Communications **33**: 787-98.

Beekman F. J., Kamphuis C. et al. (1998). "Half-fanbeam collimators combined with scanning point sources for simultaneous emission -transmission imaging." Journal of Nuclear Medicine **39**: 1996- 2003.

Ben Younes R., Mas J. et al. (1988). "A fully automated contour detection algorithm the preliminary step for scatter and attenuation compensation in SPECT " Journal of Nuclear Medicine **14**: 586 - 589.

Benamer T. P., Grosset J et al. (2000). "Accurate differentiation of parkinsonism and essential tremor using visual assessment of I-123- FP-CIT SPECT imaging; the I-123-FP-CIT study group." Movement Disorders **15**: 503-510.

Blackenspoor S. C., Xu X., et al. (1996). "Attenuation correction of SPECT using x-ray CT on an emission-transmission CT system: myocardial perfusion assessment." IEEE Trans Nucl. Sci. **43**: 2263 - 2274.

BNMS (2004). "Gamma camera, PET scanner and data processor system tender questionnaire. Version 3.1.4."
http://www.bnms.org.uk/imsges/stories/downloads/documents/bnmscameratenderparta.doc Accessed Dec. 2012.

BNMS (2011). "Renal cortical scintigraphy guidelines "
http://www.bnms.org.uk/images/stories/Procedures_and_Guidelines/Renal_Cortical_Scintigraphy_Guidelines_2011a.

Bocher M., Balan A. et al. (2000). "Gamma camera-mounted anatomical X-ray tomography: technology, system characteristics and first images." European Journal of Nuclear Medicine **27**(6): 619-27.

Bockisch A. F., Schmidt L., Kuwert D. et al. (2009). "Hybrid imaging by SPECT/CT and PET/CT: proven outcomes in cancer imaging." Seminars in Nuclear Medicine **39**: 276-289.

Bolster A. (2003). Quality control of gamma camera systems. York, Institute of Physics and Engineering in Medicine.

Borgstrom L. N., Weisz S., Moren A. et al. (1992). "Pilmonary deposition of inhaled terbutaline: comparison of scanning gamma camera and urinary excretion methods." Journal of Pharmacological Science **81**: 753-755.

British Thyroid Association (2007) "Guidelines for the management of thyroid cancer.2nd edition." http://www.british-thyroid-association.org. Accessed Aug. 2012.

Bruyant P. (2002). "Analytic and Iterative Reconstruction Alogorithms in SPECT." The Journal of Nuclear Medicine **43**(10): 1343-1358.

Butterworth S. (1930). "On the theory of filter amplifiers." Experimental Wireless and Wireless Engineer **7**: 536-541.

Buvat I., Todd-Pokropek H., Di Paola A. et al. (1994). "Scatter correction in scintigraphy: the state of the art." European Journal of Nuclear Medicine **21**: 675-694.

Buvat I. S., Hapday M., Riddell S. et al. (2000). "Respective importance of scatter, attenuation, collimator response and partial volume effect corrections for accurate quantification in I-123 dopamine receptor imaging." IEEE Medical Imaging Conference Proceedings **serial on CD-ROM**: 13-15-13-19.

Buvat I. and Castiglioni I. (2002). "Monte Carlo simulations in SPECT and PET." The Quarterly Journal of Nuclear Medicine **46**: 48-61.

Case J. A., Licho R. et al. (1999). "Bone SPECT of the spine: a comparison of attenuation correction techniques." Journal of Nuclear Medicine **40**(4): 604-13.

Catafau A. (2001). "Brain SPECT of dopaminergic neurotransmission: a new tool with proved clinical impact." Nuclear Medicine Communications **22**: 1059-60.

Celler A., Sitek A. et al. (1998). "Multiple line source array for SPECT transmission scans; simulation, phantom and patient studies." Journal of Nuclear Medicine **39**: 2183 - 2189.

Chang L. (1978). "A method for attenuation correction in radionuclide computed tomography." IEEE Transactions on Nuclear Science **25**: 638 - 43.

Chesler D. A. and Reiderer S. J. (1975). "Ripple suppression during reconstruction in transverse tomography." Physics in Medicine and Biology **20**: 632-636.

Chouker M. T., Linke K., Pogarell R. et al. (2001). "Striatal dopamine transporter binding in early to moderately advanced Parkinson's disease: monitoring of disease progression over 2 years." Nuclear Medicine Communications **22**: 721-725.

Corbett J. R. and Ficaro E. P. (1999). "Clinical review of attenuation-corrected cardiac SPECT." Journal of Nuclear Cardiology **6**(1 Pt 1): 54-68.

Darcourt J. B., Tatsch J., Varrone K. et al. (2009). "EANM procedure guidelines for brain neurotransmission SPECT using I-123 labelled dopamine transporter ligands, version 2." European Journal of Nuclear Medicine and Molecular Imaging.

De Sadeleer C. B., Goes A., Piepsz E. et al. (1996). "Renal technetium-99m DMSA SPECT in normal volunteers." Journal of Nuclear Medicine **37**: 1346-1349.

de Wit T. C. X., Nijsen J., van het Schip J. F. W. et al. (2006). "Hybrid scatter correction applied to quantitative holmium-166 SPECT." Physics in Medicine and Biology **51**: 4773-87.

Dendy P. P. and Heaton B. (2012). Physics for Diagnostic Radiology. Boca Raton, Florida, CRC Press.

Dewaraja Y., Wilderman K., Kaminski S.J. et al.(2009). "Use of integrated SPECT/CT imaging for tumor dosimetry in I-131 radioimminotherapy: a pilot patient study." Cancer Biother Radiopharm **24**(4): 417-26.

Dewaraja Y., Koral K.F. (2001). "Monte Carlo evaluation of object shape effects in iodine-131 SPECT tumour activity quantification." European Journal of Nuclear Medicine **28**: 900-906.

Dewaraja Y., Karminski S.J., Avram A.M. et al. (2010). "I-131 tositumomab radioimmunotherapy: inital tumour dose response results using 3 dimensional dosimetry including radiobiologic modelling." Journal of Nuclear Medicine **51**(7): 1155-62.

Dewaraja Y., Ljungberg M.S., Koral K.F. et al. (2005). "Accurate dosimetry in I-131 radionuclide therapy using patient specific 3 dimensional methods for SPECT reconstruction and absorbed dose calculation." Journal of Nuclear Medicine **46**(5): 840-849.

Dieudonne A. G., Laffont S, Rolland Y. et al. (2011). "Clinical feasability of fast 3 dimensional dosimetry of the liver for treatment planning of heptocellular carcinoma with Y-90 microspheres." Journal of Nuclear Medicine **52**(12): 1930-7.

Dolovich M. S., Rossman C., Newhouse M. (1976). "A sensitive index of peripheral airways obstruction." Journal of Applied Physiology **40**: 468-471.

Du, Y. T., Frey E. C. (2006). "Model based compensation for quantitative I-123 SPECT imaging." Physics in Medicine and Biology **51**: 1269-82.

EANM (viewed Feb 2011). "Guidelines on Tc-99m DMSA scintigraphy in children." http://www.eanm.org/scientific_info/guidelines_intro.php.

El Fakhri G., Buvat I., et al. (2000). "Relative impact of scatter, collimator response, attenuation, and finite spatial resolution corrections in cardiac SPECT." Journal of Nuclear Medicine **41**(8): 1400-8.

Esteves F. R., Folks R., Keidar Z. et al. (2009). "Novel solid-state detector dedicated cardiac camera for fast myocardial perfusion imaging: mulicentre comparison with standard dual detector cameras." Journal of Nuclear Cardiology **16**: 927-34.

Fahn S. O., Shoulson I., Kieburtz K. et al. (2004). "Parkinson sudy group. Levodopa and the progression of Parkinson's disease." New England Journal of Medicine **351**(24): 2498-508.

Ficaro E. P. (2002). "Should SPET attenuation correction be more widely employed in routine clinical practice? For.[see comment]." European Journal of Nuclear Medicine & Molecular Imaging **29**(3): 409-12.

Ficaro E. P. and Fesslar J. A. (1996). "Simultaneous transmission/emission myocardial perfusion tomography. Diagnostic accuracy of attenuation-corrected Tc-99m sestamibi single-photon emission computed tomography." Circulation **93**: 463- 473.

Ficaro E. P., Shreve P. et al. (1996). "Evaluation of attenuation corrected cardiac SPECT perfusion imaging in women [abstract]." Circulation **94**: I-13.

Fisher D. (2000). "Internal dosimetry for systemic radiation therapy semin." Radiation oncology **10**: 123-132.

Fleming J. S. (1998). "A technique for using CT images in attenuation correction and quantification in SPECT." Nuclear Medicine Communications **10**: 83 - 97.

Fleming J. S. and Perkins A. C. (2000). Targeted Radiotherapy. York, Institute of Physics and Engineering in Medicine.

Fleming J.S., Conway J.H., Bolt L., Holgate S.T. (2003). "A comparison of planar scintigraphy and SPECT measurement of total lung deposition of inhaled aerosol." Journal of Aerosol Medicine **16**:9-19.

Flux G. B., Monsiers M., Savolainen S. et al. (2006). "The impact of PET and SPECT on dosimetry for targeted radionuclide therapy." Z. Medical Physics **16**: 47-59.

Frey E. C., Tsui B. M., et al. (1992). "Simultaneous acquisition of emission and transmission data for improved Tl-201 cardiac SPECT imaging usinf a Tc-99m transmission source." Journal of Nuclear Medicine **33**: 2238 - 45.

Front D., Ioselevsky G., et al. (1987). "In vivo quantitation using SPECT of radiopharmaceutical uptake by human meningiomas." Radiology **164**: 93-96.

Gadd R., Baker M., et al. (2006). "Protocol for establishing and maintaining the calibration of medical radionuclide calibrators and their quality control." Measurement Good Practice Guide No. 93.

Garcia E. V., Van Train K. F. et al. (1985). "Quantification of rotational thallium-201 myocardial tomography." Journal of Nuclear Medicine **26**: 17-26.

Garin E. l., Rolland Y., Edeline J. et al. (2012). "Dosimetry based on Tc-99m macroaggregated albumin SPECT/CT accurately predicts tumour response and survival in heptocellular carcinoma patients treated with Y-90 loaded glass microspheres: prelimainary results." Journal of Nuclear Medicine **53**(2): 255-63.

General Electric Healthcare, Training in Partnership (2002)."Nuclear medicine Millennium VG operators reference manual."P.N. 2194378 100 Rev. 4.

Giubbini R., Gabanelli S. et al. (2011). "The value of attenuation correction by hybrid SPECT/CT imaging on infart size quantification in male patients with previous mypocardial perfusion infarct." Nuclear Medicine Communications **32**(11): 1026-1032.

Greaves C. (2011). "Mathematical techniques in nuclear medicine." IPEM Report 100.

Grimes J., Celler, A., Sherbinin, S., Puworskka-Bilska, H., Birkenfield, B. (2012) "The accuaracy and reproducibility of SPECT target volumes and activities estimated using an iterative adaptive thresholding technique." Nuclear Medicine Communications **33**:1254-66.

Groshar D. E., Frenkel A., Front D. (1991). "Renal function and technetium-99m-dimercaptosuccinic acid uptake in single kidneys: the value of in vivo SPECT quantitation." Journal of Nuclear Medicine **32**(5): 766-768.

Grossman G. B., Garcia E. V. et al. (2004). "Quantitative Tc-99m sestamibi attenuation-corrected SPECT: development and multicenter trial validation of myocardial perfusion stress gender-independent normal database in an obese population.[see comment]." Journal of Nuclear Cardiology **11**(3): 263-72.

Haidi H. S. (2003). "Therapeutic applications of Monte Carlo calculations in nuclear medicine." IOP Publishing, Bristol and Philadelphia.

He B. D., Song X., Segars W. P., Fre E. C. (2005). "A Monte Carlo and physical phantom evaluation of quantitative In-111 SPECT." Physics in Medicine and Biology **50**: 4169-85.

Heller G. V., Bateman T. M. et al. (2004). "Clinical value of attenuation correction in stress-only Tc-99m sestamibi SPECT imaging.[see comment]." Journal of Nuclear Cardiology **11**(3): 273-81.

Hendel R. C., Corbett J. R., et al. (2002). "The value and practice of attenuation correction for myocardial perfusion SPECT imaging: a joint position statement from the American Society of Nuclear Cardiology and the Society of Nuclear Medicine." Journal of Nuclear Cardiology **9**(1): 135-43.

Herbert R., Kulke W., et al. (1965). "The use of technetium 99m as a clinical tracer element." Postgraduate Medical Journal **41**(481): 656-662.

Herbert T. J., Gopal S. S., et al. (1995). "Fully automated optimization algorithm for determining the 3-D patient contour from photopeak projection data in SPECT." IEEE Trans Med Imaging. **14**: 122 - 131.

Hoffman E. J., Huang G., Phelps M. E. (1979)."Quantitation in positron emission computed tomography: 1. effect of object size." Journal of Computational Assisted Tomography **3**: 299-308.

Hosoba M., Wani H., et al. (1986). "Automated body contour detection in SPECT; effects on quantitative studies." Journal of Nuclear Medicine **27**: 1184 - 1191.

Hudson H. M. and Larkin R. S. (1994). "Accelerated image reconstruction using ordered subsets of projection data." IEEE Trans Med Imaging. **13**: 601-609.

Hutton B.F. and Osiecki A. (1998). "Correction of partial volume effects in myocardial SPECT." Journal of Nuclear Cardiology **5**:402-13.

Hutton B. F., Buvat I., Beekman F. (2011). "Review and current staus of SPECT scatter correction." Physics in Medicine and Biology **56**: R85-R112.

Hutton B. F., Braun M. et al. (2002). "Image registration: an essential tool for nuclear medicine." Eur. J. Nuc. Med.(29): 559 - 577.

Itoh H. S., Swift D.L., Wagner H.N. (1985). "Quantitative measurement of total aerosol lung deposition: comparison of three different techniques." Journal of Aerosol Science **16**: 367-371.

Jarrit P. H., Whalley D. R. et al. (2002). "UK audit of single photon emission tomography reconstruction software using software generated phantoms." Nuclear Medicine Communications **23**: 483-491.

Jaszczak R. J., Coleman R. E. et al. (1981). "Physical factors affecting quantitative measurements using camera based single photon emission computed tomography (SPECT)." IEEE Trans Nuclear Science. **NS 28**: 69-80.

Jaszczak R. J., Gilland G. R. et al. (1993). "Fast transmission CT for determining attenuation maps using collimated line source, rotatable air-copper-lead attenuators and fan beam collimation." Journal of Nuclear Medicine **34**: 1577 - 86.

Jaszczak R. J., Greer K. L. et al. (1984). "Improved SPECT quantification using compensation for scattered photons." Journal of Nuclear Medicine **25**: 893 - 900.

Kalantari F. R., Saghari M. (2012). "Quantification and reduction of the collimator-detector response effect in SPECT by applying a system model during iterative image reconstruction: a simulation study." Nuclear Medicine Communications **33**: 228-38.

King M.A., Haedemenos G. J., Glick S.J. (1992). "A dual photopeak window method for scatter correction." Journal of Nuclear Medicine **33**:605-12.

Kojima A., Ohyama Y. et al. (2000). "Quantitative planar imaging method for measurement of renal activity by using a conjugate-emission image and transmission data." Medical Physics **27**: 608-616.

Koral K. F. , Dewaraja Y. et al. (2007). "Recovery of total I-131 activity within focal volumes using SPECT and 3D OSEM." Physics in Medicine and Biology **52**: 777-90.

Lee Z. B., Nelson D., Heald D. (2001). "The effect of scatter and attenuation on aerosol deposition as determined by gamma scintigraphy." Journal of Aerosol Medicine **14**: 167-183.

Links J. M., Becker L. C. et al. (2004). "Clinical significance of apical thinning after attenuation correction." Journal of Nuclear Cardiology **11**(1): 26-31.

Links J. M., DePuey E. G. et al. (2002). "Attenuation correction and gating synergistically improve the diagnostic accuracy of myocardial perfusion SPECT." Journal of Nuclear Cardiology **9**(2): 183-7.

Ljunberg M. and Sjogreen-Gleisner K. (2011). "The accuracy of absorbed dose estimates in tumours determined by quantitative SPECT; a Monte Carlo study." Acta Oncol. **50**(6): 981-9.

Ljunberg M., Sjogreen K., Liu X. et al. (2002). "A 3-dimensional absorbed dose calculation method based on quantitative SPECT for radionuclide therapy: Evaluation for I-131 using Monte Carlo simulation." Journal of Nuclear Medicine **43**: 1101-1109.

Ljunberg M. S., Liu X., Frey E. et al. (2003). "3D absorbed dose calculations based on SPECT: evaluation for In-111/Y-90 therapy using Monte Carlo simulations." Cancer Biother Radiopharm **18**: 99-107.

Loke K.S., Padhy A.K., Ng D.C., Goh A.S., Divgi C. (2011). "Dosimetric considerations in radioimmunotherapy and systemic radionuclide therapies; a review." World Journal of Nuclear Medicine **10**: 122-38.

Mariani G., Bruscelli L. et al. (2010). "A review on the clinical uses of SPECT/CT." Eur. J. Nuc. Med.

Meller J., Becker W. (2002) "The continuing importance of thyroid scintigraphy in the era of high -resolution ultrasound." European Journal of Nuclear Medicine **29**;S425-S438.

Meredith R., Buschbaum D. (2006). "Pretargeted radioimmunotherapy." Oncol Biol Phys **66 (2 suppl)**: S57-S59.

Metz C. E. (1980). "The geometric transfer function component for scintillation camera collimators with straight parallel holes." Physics in Medicine and Biology **25**(6): 1059-1070.

National Electrical Manufacturers Association (1980). "Standards for performance measurements of scintillation cameras." NEMA publication No. NU 1-1980.

Newman S. S., Hooper G., Kallen A. et al. (1995). "Comparison of gamma scintigraphy and pharmokinetic technique for assessing pulmonary deposition of terbutaline sulfate delivered by pressurized metered dose inhaler." Pharm. Res.(12): 231-236.

NIST (1996) "X-ray mass attenuation coefficients." http://www. physics.nist.gov/PhysRefData/XrayMassCoef/tab4 Accessed Feb.2012.

Nowak D. J., Eisner R. L., et al. (1986). "Distance weighted backprojection: A SPECT reconstruction technique ." Radiology **159**: 531-536.

Nunez M., Prakash V., Vial R., Mut F. Alonso O., Hutton B.F. (2009)."Attenunation correction for lung SPECT: evidence of a need and validation of an attenuation map derived from the emission data." European Journal of Nuclear Medicine and Molecular Imaging. **36**:1076-89.

O'Connor M. K., Kemp B., et al. (2002). "A multicentre evaluation of commercial compensation techniques in cardiac SPECT using phantom methods." Journal of Nuclear Cardiology **9**: 361-376.

Ogawa K., Harata H. et al. (1991). "A practical method for position dependent Compton-scatter correction in single photon emission CT." IEEE Trans Med Imaging. **10**: 408-412.

Okuda K., Nakajima K. et al. (2011). "Cause of apical thinnig on attenuation-corrected myocardial perfusion SPECT." Nuclear Medicine Communications: 1033-1039.

Pacini F., Castagna M.G., Brilla L., Jost L. ESMO guidelines working group.(2008) "Differentiated thyroid cancer: ESMO clinical recommendations for diagnosis, treatment and follow up."Annals of Oncology **Supp2**:99-101.

Pan T. S., King M. A. et al. (1997). "Estimation of attenuation maps from scatter and photopeak window single photon emission computed tomographic images of Tc-99m labeled sestamibi." Journal of Nuclear Cardiology **4**: 42 -51.

Piepsz A. B., Gordon I., Granerus G. et al. (1999). "Consensus on renal cortical scintigraphy in children with urinary tract infection." Seminars in Nuclear Medicine **29**: 160-174.

Pitcairn G. R., Newman S. (1997). "Tissue attenuation corrections in gamma scintigraphy." Journal of Aerosol Medicine **3**: 187-198.

Pretorius P. H., van Rensburg A.J., van Aswegen A., Ltitter M. G.,Serfontein D. E., Herbst, C.R. (1993). "The channel ratio method of scatter correction for radionuclide image quantitation." Journal of Nuclear Medicine **34**: 330-5.

Radon J. (1917). "On the determination of functions from their integrals along certain manifolds." Beriche Sachsisiche Akadamie der Wissenschaaften, Liepzig Math-Phys. Kl. **69**: 262-277.

Rousset O. M., Leger G.C., Gjedde A.H. et al. (1993). "Correction for partial volume effects in PET using MTI-base 3D simulations of human brain metabolism." Quantification of Brain Function: Tracer Kinetics and Image Analysis in Brain PET: Elsevier Science Publishers: 113-123.

Saeedzadeh E. S., Tehrani-Fard A., Ay M.R., Khosravi H.R., Loudos G. (2012). "3D calcualtion of absorbed dose for I-131 targeted radiotherpay: a Monte Carlo study." Radiation Protection Dosimetry **150**(3): 298-305.

Sawyer L. and Starritt H. (2008). "Effective doses to patients from CT acquisitions on the GE Infinia Hawkeye: a comparison of calculation methods." Nuclear Medicine Communications **29**(2): 144-149.

Schillaci O. P., Filippi L., Manni C. et al. (2005). "The effect of levodopa therapy on dopamine transporter SPECT imaging with I-123-FP-CIT in patients with Parkinson's disease." European Journal of Nuclear Medicine and Molecular Imaging **32**(12): 1452.

Segre E. and Seaborg G. (1938). "Nuclear isomerism in element 43." Physical Review **54**(9): 772-772.

Sharir T., Slomka P., Berman D. (2010). "Solid state SPECT technology: fast and furious." Journal of Nuclear Cardiology **17**: 890-896.

Sharp P., Gemmell H., Murray A., (2005)."Practical Nuclear Medicine 3rd Edition." Springer, London.

Shcherbinin S. C., Belhocine T., Vanderwerf R., Driedger A. (2008). "Accuracy of quantitative reconstructions in SPECT/CT imaging." Physics in Medicine and Biology **53**: 4595-4604.

Sheehy N., Tretault T. et al. (2009). "Pediatric Tc-99m DMSA SPECT performed by using iterative reconstruction with isotropic resolution recovery: improved image quality and reduced radiopharmaceutical activity." Radiology **251**(2): 511-516.

Shepp L. A. and Logan B. F. (1974). "The Fourier Reconstruction of a head section." IEEE Trans Nucl.Sci. **NS-21**: 21-43.

Shepp L. A. and Vardi Y. (1982). "Maximum likelihood reconstruction for emission tomography." IEEE Trans Med Imaging. **MI-1**: 113-122.

Siegel J. A., Wu R. K. et al. (1985). "The build-up factor: effect of scatter on absolute volume determination." Journal of Nuclear Medicine **26**: 390- 394.

Sorensen L. and Archambault M. (1963). "Visualisation of the liver by scanning with Mo99 (molybdate) as tracer." The Journal of Laboratory and Clinical Measurement **62**: 330-340.

Soret M., Bacharach S. et al. (2007). "Partial-volume effect in PET tumour imaging." Journal of Nuclear Medicine **48**(6): 932-945.

Soret M. K., Darcourt J. (2003). "Quantitative accuracy of dopaminergic neurotransmission imaging with I-123 SPECT." Journal of Nuclear Medicine **44**: 1184-1193.

Stabin M. (2008). "Update: the case for patient specific dosimetry in radionuclide therapy." Cancer Biother Radiopharm **23**(3): 273-84.

Stansfield E., Sheehy N. et al. (2010). "Pediatric Tc-99m-MDP bone SPECT with ordered subset expectation maximisation iterative reconstruction with isotropic 3D resolution recovery." Radiology **257**(3): 793-801.

Starck S. A., Ohlson J. et al. (2003). "An evaluation of reconstruction techniques and scatter correction in bone SPECT of the spine." Nuclear Medicine Communications **24**(5): 565-570.

Stewart R., Ponto R. et al. (1995). "In-vivo validation of simultaneous transission-emission protocol (STEP) for Tc-99m-sestamibi SPECT - quantitative comparison with N-13 ammonia PET." Journal of the American College of Cardiology **25**: 217A.

Sudbrock F. S., Simon T., Eschner W. et al. (2010). "Dosimetry for I-131-MIBG thepapies in metastatic neuroblastoma, phaeochromocytoma and paragangliona." European Journal of Nuclear Medicine **37**(7): 1279-90.

Tan P., Bailey D. L. et al. (1993). "A scanning line source for simultaneous emission and transmission measurements in SPECT." Journal of Nuclear Medicine **34**: 1752 - 60.

Tomitani T. (1987). "An edge detection algorithm for attenuation correction in emission CT." IEEE Trans Nucl.Sci. **34**: 309 - 312.

Tonge C., Ellul M. et al. (2006). "The value of registration correction in the attenuation correction of myocardial SPECT studies usig low resolution computed tomography images." Nuclear Medicine Communications **27**: 843-852.

Tonge C., Manoharan M. et al. (2005). "Attenuation correction of myocardial SPECT studies using low resolution computed tomography images. ." Nuclear Medicine Communications **26**: 231-237.

Tsougos I. L., Georgoulias P., Theodorou K., Kappas C. (2010). "Patient specific internal radionuclide dosimetry." Nuclear Medicine Communications **31**: 97-106.

Tsui B. M. W. and Gullberg G. T. (1990). "The geometric transfer-function for cone and fan beam collimators." Physics in Medicine and Biology **35**(1): 81-93.

Van Laere K., Koole M. et al. (2001). "Image filtering in single photon emission computed tomography: principles and applications." Computerised medical Imaging and Graphics **25**: 127-133.

Van Train K. F., Areeda J. et al. (1993). "Quantitative same-day rest-stress technitium-99m sestamibi SPECT: definition and validation of stress normal limits and criteria for abnormality." Journal of Nuclear Medicine **34**: 1494 - 502.

Van Train K. F., Garcia E. V. et al. (1994). "Multicentre trial validation for quantitative analysis of same-day rest-stress technetium-99m-sestamibi myocardial tomograms." Journal of Nuclear Medicine **35**: 609 - 18.

Vandervoort E., Cellar A., Harrop R. (2007). "Implementation of an iterative scatter correction, the influence of attenuation map quality and their effect on absolute quantitation in SPECT." Physics in Medicine and Biology **52**: 1527-45.

Vanzi E., Genovesi D., Di Martino F. (2009). "Evaluation of a method for activity estimation in Sm-153 EDTMP imaging." Medical Physics **36**(4): 1219-29.

Vidal R. and I. Buvat (1999). "Impact of attenuation correction by simultaneous emission/transmission tomography on visual assessment of Tl-201 myocardial perfusion images." Journal of Nuclear Medicine **40**: 1301 - 1309.

Vlaar A., van Kroonenburg M., Kessels A. et al. (2007). "Meta-analysis of the literature on diagnostic accuracy of SPECT in parkinsonian syndromes." BMC Neurology **7**: 27.

Wackers F. J. (1999). "Attenuation Correction, or the Emperor's New Clothes?" The Journal of Nuclear Medicine **40**(8): 1310 - 1312.

Walker Z. C., Walker R.W.H. et al. (2002). "Differentiation of dementia with Lewy bodies from Alzheimers disease using a dopaminergic presynaptic ligand." Journal of Neurological Neurosurgical Psychiatry **73**: 134-140.

Wallis J. W., Miller T. R. et al. (1995). "Attenuation correction in cardiac SPECT without a transmission measurement." Journal of Nuclear Medicine **36**: 506-512.

Willowson K., Bailey D.L., Baldcock C. (2008). "Quantitative SPECT reconstruction using CT derived corrections." Physics in Medicine and Biology **53**:3099-112.

Willowson K., Bailey D.L., Baldock C et al. (2010). "In vivo validation of quantitative SPECT in the heart." Clinical Physiology and Functional Imaging **30**: 214-219.

Wiseman G. K., Leight B., Erwin W. et al. (2003). "Radiation doismetry results and safety correclations from Y-90 ibrutumomab tiuxetan radioimmunotherapy for relapsed or refractory non-hodgkins lymphoma: combined data from 4 clinical trials." Journal of Nuclear Medicine **44**: 465-474.

Wong K. D., Marzola M.C., Grasseto G. et al. (2011). "Molecular imaging in the management of thyroid cancer." Quarterly Journal of Nuclear Medicine and Molecular Imaging **55**(5): 541-59.

Wu R. K. and Siegel J. A. (1984). "Absolute quantification of radioactivity using the build-up factor." Medical Physics **11**: 189 - 192.

Yani K. (2005). "Accurate dosimetry in I-131 radionuclide therapy using patient specific 3-dimensional methods for SPECT reconstruction and absorbed dose calculation." Journal of Nuclear Medicine **46**: 840-849.

Zaidi H. (1999). "Relevance of accurate Monte Carlo mdelling in nuclear medical imaging." Medical Physics **26**: 574-608.

Zaidi H. (1999). "Relevance of accurate Monte Carlo modelling in nuclear medicine imaging." Medical Physics **26**: 574-608.

Zaidi H. (2006). "Quantitative analysis in nuclear medicine imaging." Springer science and business media.

Zeintl J. V., Yahil A. et al. (2010). "Quantitative accuracy of clinical Tc-99m SPECT/CT using ordered subsets expectation maximisation with 3-dimensional resolution recovery, attenuation and scatter correction." Journal of Nuclear Medicine **51**: 921-928.